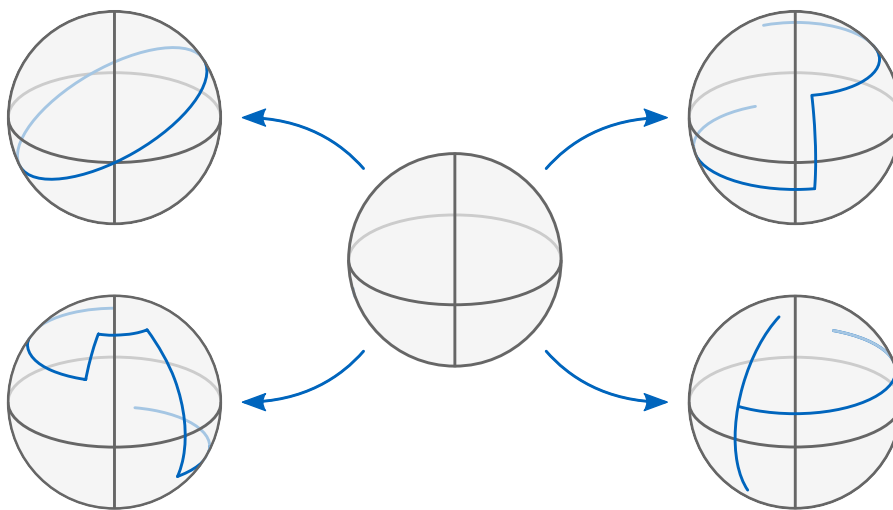# Trajectory Optimization for Sparsely Sampled Computed Tomography

Fabian Bauer

Vollständiger Abdruck der von der TUM School of Engineering and Design der Technischen Universität München zur Erlangung des akademischen Grades eines

Doktors der Ingenieurswissenschaften

genehmigten Dissertation.

Trajectory Optimization for Sparsely Sampled Computed Tomography

Fabian Bauer

Vollständiger Abdruck der von der TUM School of Engineering and Design der Technischen Universität München zur Erlangung des akademischen Grades eines

Doktors der Ingenieurswissenschaften (Dr.-Ing.)

genehmigten Dissertation.

Vorsitzender:
>   Prof. Dr. rer. nat. Rudolf Neu

Prüfende der Dissertation:
>   1. Prof. Dr.-Ing. habil. Christian U. Große
>   2. Prof. Dr. rer. nat. Franz Pfeiffer

Die Dissertation wurde am 14.04.2022 bei der Technischen Universität München eingereicht und durch die TUM School of Engineering and Design am 19.07.2022 angenommen.

FÜR MEINE ELTERN

Acknowledgments

This thesis would not have been possible without the help, motivation and professional support of many people. First of all, I want to thank Prof. Christian Große for giving me the opportunity to pursue a PhD at the Chair of Non-Destructive Testing, his support and helpful suggestions over the course of this work. Notably, I want to thank Matthias Goldammer for supervising this work, his support, advice, and continuous encouragement during the ups and downs of my doctorate. Further, I would like to acknowledge Claudio Laloni for the exceptional freedom and flexibility that I enjoyed while working for his department and Professor Pfeiffer for taking the role of the co-referee for this thesis.

I want to express my gratitude to the entire department at Siemens and in particular Christian Watzl and Karsten Schörner for their technical advice, our students Fehmi Bouhaouel and Ruben Burger for their valuable and manifold contributions and my PhD student colleagues Lukas Bergbreiter, Jan-Carl Grager, and Julia Frisch for the interdisciplinary exchange. Special thanks go to Eik Arnold for manufacturing support with the test parts and Claudia Zeiser for competently facilitating my daily struggle with the Kafkaesque Siemens bureaucracy. Moreover, I would like to thank the PhD students from our machine vision group Sergey Zakharov, Haowen Deng, Adrian Haarbach, Tolga Birdal, Mira Slavcheva and Mai Bu for welcoming work atmosphere. I am deeply grateful to Agnieszka Tomczak, Roman Kaskman, and Ivan Shugurov for an infinite number of related and unrelated discussions and support with the software implementation.

Many thanks also to my colleagues at the chair and in particular to Thomas Schromm, Jochen Kollofrath, and Isabelle Stüwe for their proofreading support as well as lively discussions concerning X-ray technology and far beyond. I am indebted to Nicole Maass (Siemens Healthineers) for helpful annotations concerning reconstruction algorithms and Daniel Forndran (BMW Group) for providing the RoboCT measurements. Last but not least I would like to thank my family, friends, and way too many further people to ever fit here for their endless support and for keeping me sane during the Corona pandemic and in particular the work on this thesis.

Abstract

Industrial computed tomography (CT) setups traditionally implement circular or helical acquisition trajectories owing to their mechanical simplicity and the availability of specialized reconstruction methods. Such sampling patterns are inherently inefficient since they are applied independently of the inspection task. Contrary, the use of part-specific orbits in combination with modern iterative reconstruction algorithms has demonstrated great potential for advances beyond the limits of conventional CT scans. Notably, maintaining high image quality with fewer projections becomes feasible which might be a remedy that counteracts the significant scan times which still pose a major barrier to large-scale application of CT-based imaging concepts in industrial practice. However, while modern and highly versatile systems that allow for such novel sampling patterns are emerging, no satisfactory systematic approach currently exists to leverage these capabilities towards said enhancements.

To overcome these limitations this thesis provides a framework for optimization and evaluation of the acquisition trajectory with respect to the imaging task and the inspected object. Related simulation-based findings are validated by an experimental lab setup as well as a robot-guided CT platform in a shop floor environment to demonstrate the practicability of the approach. Furthermore, several fundamental properties are identified which are imperative to guarantee for efficient and stable trajectory optimization. The influence of setup geometry and object are investigated and various tools and methods are provided for systematic analysis of inspection scenarios with respect to achievable improvements.

Kurzfassung

Industrielle Computertomografieanlagen verwenden typischerweise kreis- oder helixförmige Aufnahmetrajektorien, da diese mechanisch einfach umzusetzen und zudem angepasste Rekonstruktionsverfahren für diese Spezialfälle verfügbar sind. Solche einfachen Abtastmuster sind jedoch in der Regel ineffizient, da sie ohne Berücksichtigung der jeweiligen Prüfaufgabe festgelegt wurden. Im Kontrast dazu haben bauteilspezifische Trajektorien in Verbindung mit modernen iterativen Rekonstruktionsalgorithmen das Potential zu deutlichen Verbesserungen verglichen zu konventionell durchgeführten Aufnahmen. Mit solchen Anpassungen ist es insbesondere möglich, eine hohe Bildgüte mit einer kleineren Anzahl an erforderlichen Projektionsbildern als bisher zu erreichen, was zu kürzeren Messzeiten führt und die Einführung von CT-basierter Bildgebung in großem industriellen Maßstab erleichtert. Während jedoch zunehmend moderne und vielseitig konfigurierbare Anlagen zur Verfügung stehen, welche die freie Festlegung von Bahnkurven ermöglichen, existiert derzeit noch kein zufriedenstellender und systematischer Ansatz, der in der Lage ist, diese neu gewonnene Flexibilität auch gewinnbringend umzusetzen.

Die vorliegende Arbeit zielt darauf ab, diese bestehenden Einschränkungen zu überwinden. Hierfür wird ein Ansatz zur Optimierung und Bewertung von Aufnahmetrajektorien unter Berücksichtigung des untersuchten Bauteils sowie individueller Anforderungen an die Bildgebung bereitgestellt. Erkenntnisse, welche mittels Simulationen generiert wurden, wurden hierfür sowohl mit einem experimentellen Laboraufbau als auch einer robotergestützten Plattform in einer Fertigungsumgebung validiert, wodurch ein Nachweis der praktischen Anwendbarkeit des Verfahrens erbracht werden konnte. Des Weiteren wurden mehrere grundlegende Voraussetzungen identifiziert, die erfüllt sein müssen, um eine wirkungsvolle und stabile Trajektorienoptimierung gewährleisten zu können. Schließlich wurde der Einfluss der Anlagen- und Bauteilgeometrie untersucht sowie verschiedene Methoden und Verfahren entwickelt, welche eine systematische Analyse der Prüfaufgabe im Hinblick auf das erreichbare Verbesserungspotential ermöglichen.

Table of Contents

1 | Introduction and Motivation

Whilst already well-established in medical disciplines, X-ray computed tomography (CT) has also increasingly expanded to the industrial field for many decades. Since the first applications focusing on non-destructive testing (NDT) in the 1980s [1] and the introduction of commercially available scanners in 2005 [2] these methods have nowadays turned into a valuable tool for a large variety of applications, such as metrology or quality control [3]. Other relevant areas range from material analysis to the food industry [4] and driven by recent advancements in additive manufacturing new use cases are emerging [5–7] with the number of potential applications increasing further on. The inspected objects are manifold and comprise small items, such as electronic devices or carbon composite fibers [4, 8], as well as larger assemblies or even entire vehicles [9], turning industrial CT into a much broader-ranged field than its medical counterpart.

Most advances in CT imaging over the last decades have focused on improvements to the hardware or the reconstruction method. While the luminosity of X-ray tubes is approaching the limits dictated by fundamental physics, X-ray detectors have reached a quantum efficiency where only limited gains can still be expected using conventional technology. On the other side, with the advent of fast graphical processing units and efficient implementations, modern algorithms allow for reconstruction in real time with sufficient room to spare for more sophisticated techniques. As a consequence, it has become necessary to explore unusual concepts off the beaten track to achieve further progress in this field. As such, concentrating on the most informative data and acquiring only the projections that are related to those appears to be a viable concept.

In practice, sampling patterns are determined by the number of projections and the trajectory implemented by the CT system. For the course of this work a trajectory is defined as the composition of all considered acquisition positions, specified by the relative spatial position of the imaging system to the test object. In this thesis, these poses are located in three-dimensional space and do not necessarily need to be connected by a smooth path. While the influence of reducing the total number of projections has been investigated [10–12], several designs with various drawbacks and advantages have also been proposed with the planar (partial) circle and the helix being today by far the most commonly applied trajectories owing to their mechanical simplicity and the availability of specialized reconstruction algorithms. However, these standard approaches are highly inefficient, since the particular geometry of the inspected object is not taken into account. Furthermore, it has been demonstrated that not every projection carries the same degree of informative value and that the choice of acquisition poses, especially

in cases where only few projections are available, can drastically influence the attainable image quality of the reconstructed volumes [13–15] and the reliability of further metrological analysis [16–19].

For industrial CT, two recent advancements can be identified that allow the adjustment of the acquisition trajectory in such a way that performance improvements can be achieved. For one, the broader availability of highly adaptive or even robot-based platforms, which allow the free positioning of X-ray source and detector in space, has enabled the inspection of larger and more complex components than the conventional, granite-based installations that are restricted by a more limited test volume. However, the high flexibility of such setups has barely been exploited in practice and common planar circle trajectories or laminographic methods are still most frequently applied. A second important driver is the high impact of approaches related to compressed sensing (CS), which are now feasible due to technological advances in computation speed in very recent years. The amount of data required can be greatly reduced with CS-based methods, provided certain side conditions are met to compensate for the missing information. Such approaches can even generate reasonable results with fewer projections than defined by the Nyquist-Shannon theorem, which is considered the lower bound of required information by conventional methods. Following similar concepts and ideas to those used in compressed sensing, acquisition patterns with a projection count significantly below this threshold, which are referred to as sparsely sampled trajectories [20], bear considerable potential for improvements, but may also result in severe reconstruction artifacts if not handled properly. Both technologies complement each other well: while many degrees of freedom are required to leverage the potential of CS-inspired sampling patterns, each projection is particularly expensive in case of flexible CT setups, since the offset between source and detector is often larger than in conventional systems, so that long exposure times are required owing to the inverse-square law. Thus, scan time reduction by sparse acquisition methods becomes highly attractive [21] and this work will focus on concepts to leverage the choice of the trajectory towards more efficient imaging and obtaining a higher visual quality.

While most trajectory optimization approaches were initially developed in the medical field, industrial setups are considered even more promising due to the fundamental differences in the inspection task and the system properties. One advantage lies in the typical objects that are inherently better suited due to their particular shape, which can be expressed well in a sparse Fourier basis (see sec. 4.3). Furthermore, most objects are industrial parts, for which the detailed geometry is readily available in form of computer-aided design (CAD) data or blueprints [22], while such information can only occasionally be provided (e.g., from previous scans) for medical investigations. Furthermore, industrial setups themselves are better suited for the requirements of optimized acquisition protocols. Due to the high number of typically required projections, the scans can take relatively long and the unproductive positioning time for each position of the source-detector system is practically negligible [23]. Since the setup movements are typically slower, inertial forces are low and significant deviations from a circular path can easily be realized from a mechanical point of view. Furthermore, possible time savings are substantially higher if expressed in absolute numbers. This work deals with industrial CT from a non-destructive testing (NDT) point of view, for which a lower image quality is rather satisfactory compared to typical requirements for metrology. As result, the total number of projections can be even lower and fast scan times become feasible in return [12]. However, the choice of an appropriate trajectory is

2

always a trade-off with other important scan properties such as imaging quality, arising artifacts or resolution, which that have to be determined and assessed individually. In contrast to medical CT, the inspection task is typically well-defined and often consists only of a decision related to the occurrence of certain features (e.g., cracks or voids) in a restricted volume of interest (VOI).

Even though trajectory optimization is a relatively young field of active research, it has demonstrated great potential beyond the limit of conventional CT imaging which is based on planar acquisition patterns and has increasingly attracted attention in recent years. A direct advantage deriving from fewer acquired projections is the reduction of the required scan time, which is still considered to be the most significant bottleneck for the examination of multiple parts [12, 24]. This can lead to cost savings due to a higher part throughput and may enable the broader applicability of related concepts such as inline-CT for future mass inspection. For automatic defect recognition systems a good data quality is required to ensure its reliable function [25]. In such cases trajectory optimization can improve the image fidelity for a predefined time budget and increase the performance of involved algorithms. Dynamic imaging of very fast processes, which has increasingly gained interest in recent years [26], might also benefit from such methods, since typically only few projections can be provided due to the limited recording speed [27]. Furthermore, not only versatile systems benefit from trajectory optimization approaches, but also such where the source positions are limited and fixed by design (i.e., improved arrangement of the setup) [28] or their firing sequence can be adapted [29]. While this work focuses on the industrial application of CT, medical systems can also greatly benefit from sparse sampling patterns, leading to fewer motion artifacts by faster acquisition and less radiation delivered to the patient [30]. So far, these methods have even shown more promising results for dose reduction than lowering the X-ray tube current [31–33], which is – for instance in form of automatic exposure control mechanisms [34] – already applied since decades.

This work is structured in four logical parts as follows: first, important preliminary considerations and properties are outlined in part I. This comprises the fundamentals of CT (sec. 2) and signal detection theory (sec. 3), the state of the art (sec. 5) and a discussion of the problem itself and its implications (sec. 4). Next, in part II, a trajectory optimization framework is proposed and the related evaluation methodology is defined (sec. 6). The subsequent variation of model parameters allows to investigate the problem further and leads to the definition of core properties that need to be fulfilled to assure high image quality and improve the acquisition trajectory (sec. 7). In part III the framework is applied experimentally, which allows verification of the findings of the previous part (sec. 8) and to demonstrate the practical feasibility of the approach (sec. 9). Last, in part IV, the influence of object and setup geometry is investigated (sec. 10), an outlook towards future work is provided (sec. 11) and a conclusion is drawn (sec. 12).

Part I

Theoretical Background

2 | Fundamentals of Computed Tomography

2.1 Basic Principles

In 1895, Wilhelm Conrad Röntgen discovered X-rays – highly energetic radiation that can pass through objects appearing opaque to the human eye and reveals their inner structure without having to open or destroy them. This finding, which was awarded the first Nobel prize in physics in 1901, forms the basis for all radiographic techniques that evolved in the following years. Planar radiography was the first application of X-rays [35]. Unfortunately, as a projection method, its usage comes with a loss of depth information since only a two-dimensional projection is obtained. Furthermore, the resulting image is a summation over all layers of the object, which limits the achievable contrast [36, p. 75].

Subsequently, there has been strong interest in overcoming these limitations and probably the first tomographic method was invented by the Polish radiologist Karol Mayer in 1914. After 1921 it was independently reinvented by at least ten different individuals and finally advanced into the first commercially available clinical CT system in 1971 [37]. Most of these early setups did not rotate the source-detector system in relation to the object but used a translational movement instead. Modern versions of such a method are usually referred to as laminography or tomosynthesis [38, p. 2] and are in principle special cases of a limited angle CT (see also sec. 7.3).

Figure 2.1 illustrates schematically the principle of a typical industrial CT system. An X-ray source (left) emits radiation which gets attenuated by interaction with the specimen. The remaining beam intensity is measured at the detector stage (right) and stored in form of a projection image. The sample is rotated during the scan, thus resulting in multiple measurements (commonly in the order of several hundred or thousand) that are typically distributed over 360° circumference. This is in contrast to medical systems where the source-detector setup moves around the stationary patient. The recorded image sequence of projections can finally be processed by a reconstruction algorithm (sec. 2.3) that generates the desired volumetric representation of the part. According to the interception theorem, the projected specimen at the detector can be scaled by varying source-detector distance (SDD) and source-object distance (SOD), leading to a magnification factor $M = \frac{\text{SDD}}{\text{SOD}}$. Since the measured object appears enlarged on the detector, a nominal resolution M-times smaller than the pixel size can be obtained [2].

If the detector consists only of a single one-dimensional array as depicted in fig. 2.1, it is called a line detector and the setup is operated with a fan beam geometry. The reconstruction yields only one horizontal slice of the object and to acquire the entire
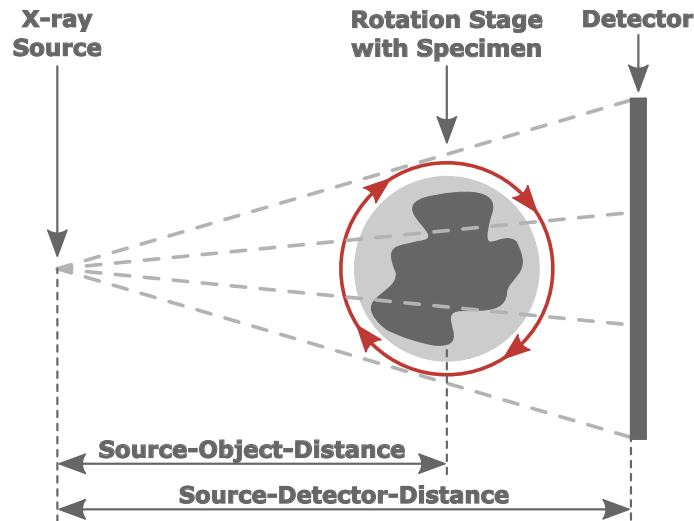
Figure 2.1: Schematic top view of an industrial CBCT setup. The source emits X-rays that are attenuated by interaction with the specimen and captured by the detector. After each measurement, a projection image is created and the object is rotated into the next position. The system used for this work is depicted in fig. 8.1.

volume the source-detector system needs to be lifted to the next plane, where the scan process is repeated. Fan beam configurations typically improve the image quality but require very long scan times due to the repetitive workflow. If the detector resembles a plane, the method is referred to as cone-beam computed tomography (CBCT) and the entire reconstructed volume can be swiftly scanned in a single rotation [2]. For the sake of simplicity the discussions in this chapter and in particular sec. 2.3 are based on a parallel beam setup, while the adaption to cone beam geometry can be derived analogously [39, 40].

Besides moving the specimen instead of the source-detector system, industrial CT also differs in several other aspects from medical setups. While X-ray sources for diagnostic scanners typically operate with acceleration voltages below 150 eV, industrial versions can currently be equipped with linear accelerators that reach up to 9 MeV [36, 41, p. 16]. Furthermore, dose considerations are much less relevant compared to medical diagnostics and instead, the achievable precision, accuracy, and scan resolution is of more concern. As a consequence, significantly higher beam intensities are used which results in better achievable image quality compared to medical systems. Since the investigated objects are often much denser (for instance steel parts as opposed to tissue) comparably long scan times are required, which is, however, usually still acceptable since the parts do not move or alter their shape during the acquisition [38, p. 16f]. Additionally, metrological scanners are equipped with temperature control measures [2]. Further important differences can be found in the system price and the feasible sample size [42].
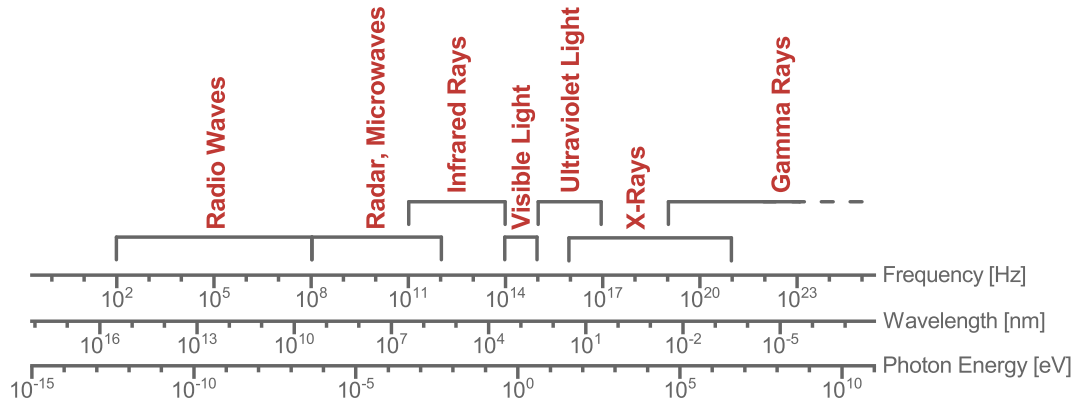
Figure 2.2: Overview of the electromagnetic spectrum. Approximate ranges are adapted from [36, 44, p. 16f].

2.2 X-Ray Physics

2.2.1 Nature and Generation of X-Ray Photons

X-rays are electromagnetic waves with typical wavelengths ranging roughly between 10^{-8} m and 10^{-13} m [36, p. 16]. Figure 2.2 provides an approximate overview of the electromagnetic spectrum and relevant ranges. While several different methods such as synchrotron sources or free-electron lasers [43, p. 155f] are available to produce X-rays, in industrial CT systems typically X-ray tubes are used to reach peak photon energies up to approx. 600 keV, while linear accelerators are necessary for higher values of up to 9 MeV. In an X-ray tube, within a vacuum chamber, a cathode filament is heated up until the temperature is sufficient to overcome the binding energy of the contained electrons to the filament material. As a result, electrons are boiled off by thermionic emission and are accelerated towards the anode as a result of the applied potential difference. The beam is shaped by electron optics (a so-called Wehnelt cylinder) and directed towards a small focal spot at the metallic target. Subsequently, the abrupt deceleration of the charge carriers generates a spectrum of X-ray photons that leave the tube [36, p. 16f].

The formation of X-rays is achieved by the interaction of the incident electrons with the orbital electrons and the atomic nucleus of the target material, where the deceleration of the charged particles leads to an electric dipole that radiates off electromagnetic waves in form of X-ray photons. In the extreme case, the entire energy of an electron gets converted into a single photon, which carries the maximum obtainable energy $E_{\max} = eU_a$, which equals the acceleration voltage U_a of the tube times the elementary charge e. However, typically one incident electron leads to the formation of several photons, and the deceleration process is realized as a cascade of interactions, therefore leading to a continuous emission spectrum known as bremsstrahlung. If fast electrons interact with the shells of the target material an electron can be removed due to the kinetic energy of the collision and another electron from a higher shell filling the vacant position. The potential difference between the shells is then released by the emission of photons of a particular wavelength that is referred to as the characteristic peaks of the spectrum that depend on the target material. Figure 2.3a shows the typical emission spectrum of an X-ray tube. The characteristic peaks $K_{\alpha_1}, K_{\alpha_2}$ (transition of L-

(a) X-ray Tube Emission Spectrum

(b) Absorption Coefficients of Iron
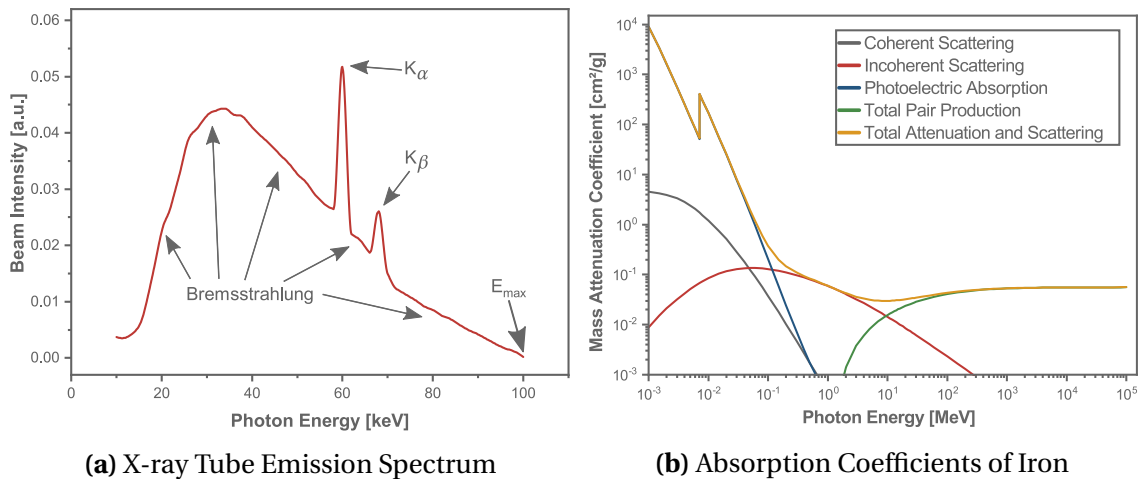
Figure 2.3: X-ray tube emission spectrum (fig. 2.3a) obtained via experimental measurements [45]. Shown is the bremsstrahlung, the superimposed characteristic target material peaks K_α and K_β, as well as the maximum photon energy E_{max}. The energy-dependent mass attenuation coefficients of elementary iron are shown in fig. 2.3b. Depicted are separately coherent and incoherent scattering, photoelectric absorption, and combined nucleus and electron pair production together with the combination of all these processes. Experimental attenuation data were obtained from the XCOM database [46].

shell electrons to the innermost K-orbital) and K_{β_1}, K_{β_2} (transition of M-shell electrons to K-orbital) of the tungsten target are not distinguishable in the depicted resolution. Alternatively, the energy can be transferred to a weakly bound electron, which leaves the atom as so-called Auger electron. The probability for this effect decreases with increasing atomic number [36, p. 16f].

By this method of X-ray generation typically over 99 % of the incident electron energy is converted into heat, resulting in a high thermal load to the target. To prevent damage to the material, the photon output (or, equivalently, the electron power) for a given focal spot needs to be restricted. The maximum permitted beam intensity can be increased if the focal spot size is enlarged, therefore allowing a better heat distribution on the anode. However, this measure comes at the cost of a decreased image quality since the point-spread function (PSF, see sec. 3.3) becomes wider [36, p. 22f].

2.2.2 Interactions and Attenuation in Matter

The photons emitted by the X-ray source interact with the material in the beamline with respect to several physical effects. In general, the radiation intensity of a monoenergetic photon beam passing through matter can be described by the Lambert-Beer law as

$$I(x) = I_0 \cdot e^{-\mu x}, \tag{2.1}$$

with I_0 being the initial beam intensity, $I(x)$ the intensity at position x and μ the material-specific attenuation coefficient, where the object is assumed to be homogeneous [36, p. 32f]. Equation 2.1 is simplified since scattered photons are neglected and treated as lost signal; however, in reality, multiple subsequent scattering events are possible leading to photons hitting the detector nevertheless and therefore contributing to the measured intensity. Additionally, here the spectrum is assumed to contain only a

single wavelength, which is not realistic for real X-ray sources; instead, the wavelength-dependency of the attenuation coefficient leads to the formation of beam hardening artifacts. The attenuation coefficient is composed of several separate physical effects that depend themselves on the material the beam is passing through and the wavelength of the incident photon λ_p, so that

$$\mu(\lambda_p) = \mu_{cs}(\lambda_p) + \mu_{is}(\lambda_p) + \mu_{pa}(\lambda_p) + \mu_{pp}(\lambda_p) \tag{2.2}$$

holds. Here, $\mu_{cs}(\lambda_p)$ and $\mu_{is}(\lambda_p)$ refer to coherent and incoherent scattering, while $\mu_{pa}(\lambda_p)$ and $\mu_{pp}(\lambda_p)$ are the attenuation coefficients of photoelectric absorption and pair production, respectively. To obtain a polychromatic pendant to eq. 2.1 it is necessary to integrate eq. 2.2 with respect to the photon energy spectrum [36, p. 32f]. These most important physical mechanisms contributing to the attenuation coefficient are also shown in fig. 2.3b and will be briefly summarized in the following while less frequent interactions (e.g., the photonuclear effect) are neglected since they are of minor relevance for this work.

Coherent Scattering　In this process a photon scatters in an elastic event, i.e., its energy (and consequently wavelength) is preserved. The photon typically interacts either with a quasi-free (Thomson scattering) or a strongly bound electron (Rayleigh scattering). The effect is mostly relevant for lower energies [47, p. 239, 291].

Incoherent Scattering　A photon can also interact inelastically with a loosely bound electron and transfer a fraction of its energy to it. As a result, the electron is ejected from the atom, while the photon is scattered under a certain angle that can reach values between 0° (forward scattering) and 180° (backscattering). Since the energy is not preserved, its wavelength is shifted to higher values. The angular probability of incoherent scattering also referred to as Compton scattering, can be calculated via the Klein-Nishina equation. After the collision both – the released electron and the photon – might possess enough energy to undergo further interactions [47, p. 297f]. Industrial computed tomography applications typically operate in the range between 100 keV and 9 MeV, which makes incoherent Compton scattering the dominant attenuation effect (see also fig. 2.3b).

Photoelectric Absorption　If the binding energy of a tightly bound electron (in contrast to the quasi-free electron of the Compton effect) is lower than the energy carried by an incident photon, the photon can be entirely absorbed, while the electron is either excited or removed from the atom. The ejected electron is called a photoelectron and the vacant position will subsequently be filled by an electron from a higher shell; the released energy in this process is either transferred to an Auger electron (see sec. 2.2.1) or results in the emission of a photon of a characteristic wavelength or [47, p. 336f].

Pair Production　For very high energies of the incident photon, its interaction with the Coulomb field of the nucleus can lead to the formation of an electron-positron pair. In practice, the positron always recombines with another electron after a short traveling distance, which results in the emission of two photons in approximate opposite directions. This effect is called the pair annihilation process and is utilized in positron

emission tomography (PET). To occur, the incident photon needs to carry at least the rest energy of both particles, which leads to a threshold of 1.022 MeV under which pair production is physically not possible. For very high energies over 10 MeV the effect becomes dominant [36, p. 39f]. Pair production is also feasible, but typically much less likely to appear in the electric field of an electron, which is then referred to as triplet production [48, p. 189].

2.2.3 Detection

After passing through the object of investigation a detector is necessary to measure and quantify the remaining intensity of the X-ray beam. While historically gas-filled ionization chambers (e.g., the famous Geiger-Mueller-counter) or films have been applied [48, p. 215f], today typically digital flat-panel detectors are used. These can be separated into systems using direct and indirect conversion. In direct conversion detectors incident X-ray photons hit a photoconductor (consisting of amorphous selenium for instance) where they are converted into electrical charge without any intermediate steps. Under this layer, a thin-film transistor array is placed, which is subsequently used to detect the generated charge. In detectors using an indirect conversion setup X-rays first strike a scintillator layer typically consisting of cesium iodide or gadolinium oxysulfide, which emits visible light proportional to the incident energy. This light is then detected by a photodiode array [49]. For all integrated circuit based detectors it is important to calibrate the system properly, since each separate detector element may differ in amplification gain and mean dark signal. If not taken into account, these variations lead to a systematic bias, the so-called fixed-pattern noise, which is superimposed onto the measurements [50, p. 1091].

2.3 Image Reconstruction

2.3.1 Radon Transform and the Fourier Slice Theorem

In sec. 2.2.2 the Lambert-Beer law (eq. 2.1) was introduced, which can be used to describe the attenuation of X-rays in matter. If the condition of homogeneous matter is relaxed to an arbitrary spatial distribution of attenuation values it becomes necessary to integrate over all infinitesimal path elements $\mathrm{d}l$ along the photon path L [36, p. 156f]:

$$-\ln\left(\frac{I_\mathrm{m}}{I_0}\right) = \int_L \mu(l)\mathrm{d}l, \tag{2.3}$$

where I_m denotes the measured intensity at the detector. For a given setup the straight X-ray path L can be fully defined without loss of generality by the rotation angle ϕ of the source-detector system relative to the object coordinate system and its lateral offset ξ as indicated in fig. 2.4. The expression on the left side is then the angle-dependent one-dimensional Radon transformation p_ϕ of the imaged object. However, in practice not a single pixel but a detector array is used, so that the left side becomes a function depending also on ξ, turning the expression into [36, p. 156f]

$$p_\phi(\xi) = \int_L \mu(\xi, \phi)\mathrm{d}l. \tag{2.4}$$
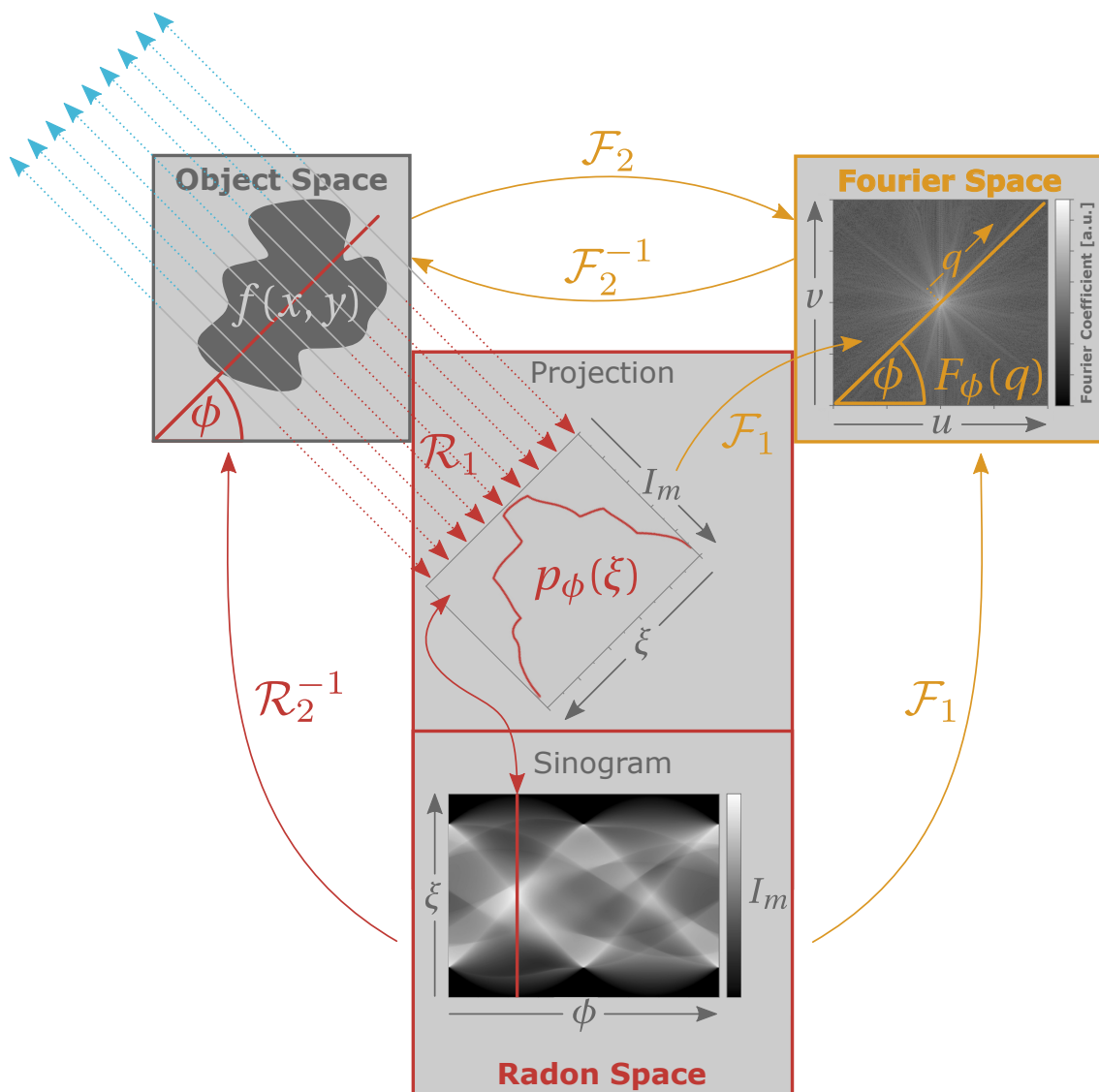
Figure 2.4: Relation between object, Fourier and Radon space. A projection of the object $f(x,y)$ is acquired by the one-dimensional Radon transform $\mathcal{R}_1$. The projections $p_\phi(\xi)$ originating from all angles ϕ together form the sinogram and the inverse two-dimensional Radon transform $\mathcal{R}_2^{-1}$ is necessary to recover the original image. In theory, this can be accomplished by applying the inverse Fourier transform $\mathcal{F}_2^{-1}$ to the sum of all Fourier-transformed projections, which is referred to as the Fourier slice theorem. In practice, this is accomplished by analytic (sec. 2.3.2) or iterative (sec. 2.3.3) methods. The unfiltered backprojection that plays a fundamental role in the former is schematically indicated in light blue.

Note that while such a detector array is separated into discrete pixel elements in reality in this section, it is assumed to be continuous; this condition will be relaxed in sec. 2.3.3. By comparing eq. 2.3 with eq. 2.4 it becomes obvious that the Radon transform denoted as $\mathcal{R}$ of an object is nothing else than its (logarithmically normalized) measured intensity values of the projection onto a coordinate system rotated by an angle ϕ. Figuratively speaking, the Radon transform does not need to be computed at all, since the image formation process in CT acts as a physical Radon transform.

By expressing the object as the more general function $f(x, y)$ with Cartesian spatial coordinates x, y instead of representing it via its attenuation values the coordinate systems are linked via

$$p_\phi(\xi) = p_\phi(x\cos(\phi) + y\sin(\phi)), \tag{2.5}$$

and the integral of eq. 2.4 can be calculated as

$$\mathcal{R}\left(f(x, y)\right) = f(x, y) * \delta(L) = p_\phi(\xi), \tag{2.6}$$

$$p_\phi(\xi) = \iint_{-\infty}^{\infty} f(x, y)\delta(x\cos(\phi) + y\sin(\phi) - \xi)\mathrm{d}x\mathrm{d}y, \tag{2.7}$$

where the Dirac delta function δ is used and the operator $*$ denotes a convolution [36, p. 160f]. The representation of all angles ϕ in a single plot is called the sinogram of $f(x, y)$ and contains, in theory, all information necessary to reconstruct $f(x, y)$ via the inverse Radon transform (see sec. 2.3.2).

The Fourier slice theorem which is depicted in fig. 2.4 is one of the most important principles for many reconstruction methods [36, p. 167]. It states that the one-dimensional Fourier transform of the Radon-transformed object (i.e., the projection) equals a radial line in the two-dimensional Fourier transform of the object where the respective angles coincide. A proof can be found in the literature [36, p. 165f] and the theorem is summarized as:

$$F(u, v) \bullet\!\!\overset{\mathcal{F}}{-}\!\!\circ f(x, y) \circ\!\!\overset{\mathcal{R}}{-}\!\!\bullet p_\phi(\xi) \bullet\!\!\overset{\mathcal{F}}{-}\!\!\bullet F_\phi(q), \tag{2.8}$$

where the Fourier space $F(u, v)$ is gradually filled by $F_\phi(u, v)$ with each added projection, whose representation in Cartesian and polar coordinates is given via

$$F_\phi(u, v)|_{\substack{u=q\cos(\phi) \\ v=q\sin(\phi)}} = F_\phi(q), \tag{2.9}$$

with radial coordinate q [36, p. 166].

2.3.2 Analytic Solution and Filtered Backprojection

While the radiographic imaging process is given by the Radon transformation described in sec. 2.3.1, the reconstruction of $f(x, y)$ from projections in CT is an inverse problem and a closed expression for the inverse Radon transformation $\mathcal{R}^{-1}$ is required. While such an inversion formula has been proposed by Radon in 1917 from a theoretical point of view [51], it has turned out to be practically not feasible. First, to yield a unique solution of relative attenuation coefficients, it requires to sample with infinitely small angular steps, which is obviously not possible in reality. While this condition can be relaxed, due to the discretization into voxels a certain sampling rate is nevertheless necessary to avoid aliasing artifacts, which will be discussed in sec. 4.1. Furthermore, the formula is sensitive to noise, which is an inherent property of each projection caused for instance by the underlying photon statistics [52, p. 37f]. While a reconstruction algorithm based on the Fourier slice theorem (sec. 2.3.1) could be applied instead a regridding step is necessary between the polar representation of the Fourier space and the object space given in Cartesian coordinates. Unfortunately, the required interpolation step produces deviations that are particularly large at high spatial frequencies and lead to severe degradation of image quality so that this method is practically also not feasible [36, p. 169f].

Instead, the most frequently used approach is based on the filtered backprojection (FBP), which is typically used in form of the reconstruction algorithm proposed by Feldkamp, Davis, and Kress (the so-called FDK algorithm [53]). It can be shown that this method is equivalent to the original solution suggested by Radon [36, p. 191]. Essentially, the obtained projections are convoluted with a filter kernel and backprojected in the volume, where the attenuation values are smeared out over the entire photon path. This is schematically indicated (without the filtering step) in fig. 2.4.

The backprojection of the filtered projection $h_\phi(\xi)$ to obtain the reconstruction $\tilde{f}(x, y)$ of the object $f(x, y)$ can be written as [36, p. 179f]

$$\tilde{f}(x, y) = \int_0^\pi h_\phi(\xi) \mathrm{d}\phi. \tag{2.10}$$

While integrating over π instead of 2π is sufficient to describe the entire object space, in practice projections are typically obtained from more than 180°. For one, this is due to the use of cone-beam setups that violate the condition of parallel X-ray beams that is inherently assumed during this entire chapter. Furthermore, the SNR of a reconstructed voxel improves with the number of backprojected rays through this element [23], which essentially means that more measurements reduce the effective noise by averaging.

The filtering step acts edge-enhancing on the image and is realized by applying a high pass filter in the frequency domain [36, p. 179f]:

$$h_\phi(\xi) = \mathcal{F}^{-1}\left(F_\phi(q) \cdot |q|\right). \tag{2.11}$$

In practice, eq. 2.11 can only be approximated due to undesirable properties of the filter kernel. In consequence, several alternatives have been suggested with the proposal of Shepp and Logan [54] being today the most commonly used version [36, p. 242f].

2.3.3 Iterative Approaches

While the backprojection-based method outlined in the last section is by far the most frequently used reconstruction algorithm for X-ray CT, it is only of minor importance for this work. Instead, iterative reconstruction methods will be primarily used, which are known to perform better in case of irregular sampling or sparse data [36, 55, p. 201]. So far, all considerations in sec. 2.3 were based on continuous values and distributions. However, in reality, the detector is composed of a pixel grid and the reconstructed volume is typically given in form of a discrete scalar field in a voxel grid. As a result, the continuous representation via the Radon transform can be replaced by a system of equations [36, p. 205] and

$$p_\phi(\xi) = \mathcal{R}\left(f(x, y)\right) \tag{2.12}$$

$$\text{becomes} \qquad \mathbf{p} = \mathbf{A}\mathbf{f}. \tag{2.13}$$

The vector $\mathbf{p} \in \mathbb{R}^m$ contains all values of the sinogram, i.e., all obtained $p_\phi(\xi)$ given as measured pixel values of the sampled object $\mathbf{f} \in \mathbb{R}^n$ given in its attenuation values. The matrix $\mathbf{A} \in \mathbb{R}^{m \times n}$ is called the system matrix and connects both vectors to each other. Typically, the inversion of $\mathbf{A}$ is not trivial or even possible, since it is almost singular and very large. Furthermore, eq. 2.13 can only be approximately solved since the data contains noise so that an exact solution cannot be provided. Depending on the number

of measurements m conducted, $\mathbf{A}$ is usually over-determined by design; however, in this work the number of projections is typically low, which turns it into an under-determined problem [36, p. 205]. In general, a solution to eq. 2.13 is given by

$$\tilde{\mathbf{f}} = \arg\min_{\mathbf{f}} \left(\|\mathbf{A}\mathbf{f} - \mathbf{p}\|^2 \right), \tag{2.14}$$

which satisfies the least-squares minimum norm [36, p. 206f]. This is equivalent to the definition of the Moore-Penrose pseudo-inverse, which can in theory be computed by the singular value decomposition (SVD). Unfortunately, in practice, this approach is not achievable except for very small dimensions of $\mathbf{A}$. Given typical parameters used in this work, $\mathbf{A}$ would contain in the order of 10^{15} elements, which is clearly not feasible even for modern computers so that iterative approaches have to be used instead.

The basic idea of such methods will be briefly derived in the following. First, expanding the objective function in equation 2.14 gives

$$\tilde{\mathbf{f}} = \arg\min_{\mathbf{f}} \left((\mathbf{A}\mathbf{f} - \mathbf{p})^{\mathrm{T}} (\mathbf{A}\mathbf{f} - \mathbf{p}) \right), \tag{2.15}$$

$$= \arg\min_{\mathbf{f}} \left((\mathbf{f}^{\mathrm{T}}\mathbf{A}^{\mathrm{T}} - \mathbf{p}^{\mathrm{T}})(\mathbf{A}\mathbf{f} - \mathbf{p}) \right), \tag{2.16}$$

$$= \arg\min_{\mathbf{f}} \left(\mathbf{f}^{\mathrm{T}} \underbrace{\left(\mathbf{A}^{\mathrm{T}}\mathbf{A}\mathbf{f} - \mathbf{A}^{\mathrm{T}}\mathbf{p} \right)}_{\to 0, \text{ for eq. } 2.18} - \mathbf{p}^{\mathrm{T}} \underbrace{\left(\mathbf{A}\mathbf{f} - \mathbf{p} \right)}_{\text{eq. } 2.14} \right), \tag{2.17}$$

where the last term can be identified again as part of the objective function of eq. 2.14 that is to be minimized. The residual error is assumed to be negligibly small in the following as indicated and the normal equation is given by

$$\mathbf{A}^{\mathrm{T}}\mathbf{A}\mathbf{f} = \mathbf{A}^{\mathrm{T}}\mathbf{p}, \tag{2.18}$$

$$\left(\mathbf{I} - \left(\mathbf{I} - \mathbf{A}^{\mathrm{T}}\mathbf{A} \right) \right) \mathbf{f} = \mathbf{A}^{\mathrm{T}}\mathbf{p}, \tag{2.19}$$

$$\mathbf{f} - \left(\mathbf{I} - \mathbf{A}^{\mathrm{T}}\mathbf{A} \right) \mathbf{f} = \mathbf{A}^{\mathrm{T}}\mathbf{p}, \tag{2.20}$$

$$\mathbf{f} = \mathbf{f} - \mathbf{A}^{\mathrm{T}} \left(\mathbf{A}\mathbf{f} - \mathbf{p} \right), \tag{2.21}$$

where $\mathbf{I}$ denotes the identity matrix [43, p. 702f]. While eq. 2.21 defines the update step of the fixed point iteration schema, it can also be interpreted as a series of back- and forward projections. Starting from an initial guess for the solution it is possible to calculate related projections using eq. 2.13. The difference to the measured projection can then be back-projected to the volume by $\mathbf{A}^{\mathrm{T}}$ and used to update the n-th iteration solution $\mathbf{f}^{(n)}$. The algorithm stops after a termination condition is reached, for instance when the projection error is lower than a predefined threshold or after a certain number of iterations. More formal, eq. 2.21 is expressed as

$$\mathbf{f}^{(n)} = \mathbf{f}^{(n-1)} - \underbrace{\frac{\overbrace{\mathbf{A_i}\mathbf{f}^{(n-1)} - \mathbf{p_i}}^{\text{Projection Error}}}{\mathbf{A_i}\mathbf{A_i}^{\mathrm{T}}} \mathbf{A_i}^{\mathrm{T}}}_{\text{Backprojected Error}}, \tag{2.22}$$

where $\mathbf{A_i}$ denotes the i-th row of $\mathbf{A}$, i.e., the part associated with $\mathbf{p_i}$. The term $\mathbf{f}^{(n)}$ after n iterations is an estimate for the desired solution $\tilde{\mathbf{f}}$. The pixel $\mathbf{p_i}$ to which the volume is

projected and compared to in each iteration is typically selected randomly or according to a statistical distribution [36, p. 213f]. This method, where only one projection pixel value per iteration is considered is referred to as the algebraic reconstruction technique (ART).

The objective function in eq. 2.14 can be modified to include further properties, which leads to other iterative approaches such as the maximum likelihood [36, p. 230f], the conjugate gradient least-squares [43, p. 703] or the total variation minimization [56]. Furthermore, regularization terms reflecting prior knowledge of the object can be included as well [43, p. 703]. One possible choice is a weighted least-squares norm that is given by

$$\left\|\mathbf{Af} - \mathbf{p}\right\|_{\mathbf{R}}^2 = \left(\mathbf{Af} - \mathbf{p}\right)^{\mathrm{T}}\mathbf{R}\left(\mathbf{Af} - \mathbf{p}\right), \tag{2.23}$$

where $\mathbf{R} \in \mathbb{R}^{m \times m}$ is a diagonal matrix whose entries are defined as $\mathbf{R_{ii}} = 1/\sum_{j=0}^{n}\mathbf{A_{ij}}$. This definition of $\mathbf{R}$ assigns a higher weight to rays that intersect the reconstructed part volume only for a small length and vice versa [43, p. 702f]. Analogous to eq. 2.22, the update step can then be derived as

$$\mathbf{f}^{(n)} = \mathbf{f}^{(n-1)} - \frac{1}{\sum_{i=0}^{m}\mathbf{A_{ij}}}\sum_{i=1}^{m}\left(\frac{\mathbf{A_i}\mathbf{f}^{(n-1)} - \mathbf{p_i}}{\sum_{j=1}^{n}\mathbf{A_{ij}}}\mathbf{A_i}^{\mathrm{T}}\right). \tag{2.24}$$

This algorithm is termed the simultaneous iterative reconstruction technique (SIRT) and is known to be more stable in the presence of noise, but for the price of a slower convergence [43, p. 702f]. It also deals well with uneven distributions of projection directions [57]. While ART processes each projection pixel value separately in different iterations, SIRT uses all available information (i.e., all pixels of all projections) in each step as indicated by the summation over m elements.

As a compromise between both algorithms, the simultaneous algebraic iteration algorithm (SART) was proposed in 1984 [58], which will be used primarily in this work. The algorithm comprises several minor adjustments that will be omitted here for the sake of clarity and tries to combine the advantages of ART and SIRT [59, p. 285]. The update formula is equivalent to eq. 2.24, but instead of all projections only the values associated with an angular direction ϕ (i.e., all pixel values in one single projection) are considered so that the expression is given by

$$\mathbf{f}^{(n)} = \mathbf{f}^{(n-1)} - \frac{1}{\sum_{i \in I_\phi}\mathbf{A_{ij}}}\sum_{i \in I_\phi}^{m}\left(\frac{\mathbf{A_i}\mathbf{f}^{(n-1)} - \mathbf{p_i}}{\sum_{j=1}^{n}\mathbf{A_{ij}}}\mathbf{A_i}^{\mathrm{T}}\right), \tag{2.25}$$

where I_ϕ denotes the set of indices related to the same projection angle ϕ [43, p. 702f]. This change in the considered subset for each iteration leads to faster convergence of SART in comparison to SIRT, while being relatively robust towards streak artifacts and noise at the same time [60].

3 | Signal Detection Theory and Model Observer

While the most important physical principles relevant to X-ray imaging and the foundations of CT have been covered in the previous chapter 2, the following sections aim to provide further concepts that are necessary for this work. First, basic properties of noise and imaging systems are introduced in sec. 3.1 to 3.3. An important concept for this work will be statistical signal detection theory (sec. 3.4), which was originally developed for radar surveillance [61, 62, p. 151] and subsequently lead to further important tools, such as the receiver operating characteristic (sec. 3.5) and model observers (MOs) that will be discussed in sec. 3.6. This chapter ends with a contemplation concerning noise statistics (sec. 3.7) and detection performance criteria (sec. 3.8).

3.1 Signal-to-Noise Ratio

The signal-to-noise ratio (SNR) is defined as the ratio of the average power $\langle P_{\text{signal}} \rangle$ of a signal (i.e., meaningful information) $s(t)$ to the average power $\langle P_{\text{noise}} \rangle$ of the background noise (i.e., the unwanted, disturbing signal) $n(t)$, with t being the time for a time-dependent signal [63, p. 191]:

$$\text{SNR} = \frac{\langle P_{\text{signal}} \rangle}{\langle P_{\text{noise}} \rangle}, \tag{3.1}$$

where the operator $\langle \cdot \rangle$ denotes the statistical average. The average power P_x of a stationary signal $x(t)$ is then generally defined as

$$\langle P_x \rangle = \lim_{T \to \infty} \frac{1}{T} \int_{-T/2}^{T/2} |x(t)|^2 \mathrm{d}t, \tag{3.2}$$

with T being the observation interval [63, p. 7]. As indicated, the power calculated according to eq. 3.2 is equal to its expectation value if the signal is ergodic[1] which is inherently assumed in the following [50, p. 367f, p. 387]. The expression simplifies for a constant (i.e., time independent) real-valued signal $s(t) = s$ to

$$\langle P_{\text{signal}} \rangle = \lim_{T \to \infty} \frac{1}{T} \int_{-T/2}^{T/2} |s|^2 \mathrm{d}t = s^2. \tag{3.3}$$

---

[1]Ergodicity denotes the property of a random process that each particular realization carries the identical statistical information, which is closely related to the law of large numbers. For the detailed background the interested reader is referred to the literature [50, p. 387f].

The noise can be modeled as a stationary and random process, so that

$$\langle P_{\text{noise}} \rangle = \lim_{T \to \infty} \frac{1}{T} \int_{-T/2}^{T/2} |n(t)|^2 \mathrm{d}t = \lim_{T \to \infty} \frac{1}{T} \int_{-T/2}^{T/2} n(t)^2 \mathrm{d}t, \tag{3.4}$$

where it is assumed again that the noise is real-valued. The variance $\text{Var}(X)$ of a continuous random variable X is defined as [64, p. 1476]

$$\text{Var}(X) = \int_{-\infty}^{\infty} (X - \mu)^2 f(X) \mathrm{d}X = \sigma_X^2, \tag{3.5}$$

with μ being the expectation value, $f(X)$ the probability density and σ_X the standard deviation. Since it is assumed that the signal does not exist (or is not of interest due to being constant) outside the observation interval, the limits can be adjusted accordingly. Furthermore, if the density function is assumed to be a constant scalar value given by $f(X) = \lim_{T \to \infty} \frac{1}{T}$ it can be removed from the integral. Note that this assumption equals the discrete case with constant but infinitely high sampling rate. If the noise is also additive with mean $\mu = 0$ this results in

$$\sigma_n^2 = \lim_{T \to \infty} \frac{1}{T} \int_{-T/2}^{T/2} (n(t) - 0)^2 \mathrm{d}t, \tag{3.6}$$

which can be identified as the expression in eq. 3.4, so that $\sigma_n^2 = P_{\text{noise}}$. Together with the equations 3.1 and 3.3 one finally obtains an expression for the SNR as

$$\text{SNR} = \frac{\langle P_{\text{signal}} \rangle}{\langle P_{\text{noise}} \rangle} = \frac{s^2}{\sigma_n^2}. \tag{3.7}$$

The definition of the SNR provided by eq. 3.7 is often used in engineering disciplines. However, several alternative definitions are sometimes utilized [65] and in imaging sciences the SNR is typically defined as the square root of eq. 3.7, which is given by [36, p. 421]

$$\text{SNR} = \frac{s}{\sigma_n}. \tag{3.8}$$

One reason for this definition is that the values in an image are usually generated by a detector, which is typically not detecting single photons or events, but the incident energy integrated over the exposure time, which is just a process as described by eq. 3.2. Consequently, both definitions are linked and express the same fundamental law.

3.2 Noise Equivalent Quanta and Detective Quantum Efficiency

Assuming a mono-energetic X-ray spectrum and an ideal linear detector, the signal strength is proportional to the number of incident photons N. Furthermore, photons are considered to follow a Poisson distribution, i.e., the variance equals the mean value, which is the desired signal. Considering eq. 3.8, the equation simplifies further into [36, 66, p. 421f]

$$\text{SNR} = \frac{s}{\sigma_n} = \frac{\langle N \rangle}{\sqrt{\langle N \rangle}} = \sqrt{N}. \tag{3.9}$$

For an ideal detector every single photon is captured and the SNR is given as

$$\text{SNR}_{\text{ideal}} = \frac{\langle N_{\text{ideal}} \rangle}{\sqrt{\langle N_{\text{ideal}} \rangle}} = \sqrt{\langle N_{\text{ideal}} \rangle}, \tag{3.10}$$

while in reality its efficiency is limited so that only

$$\text{SNR}_{\text{real}} = \frac{\langle N_{\text{real}} \rangle}{\sqrt{\langle N_{\text{real}} \rangle}} = \sqrt{\langle N_{\text{real}} \rangle} < \sqrt{\langle N_{\text{ideal}} \rangle}, \tag{3.11}$$

can be obtained [66]. This is part of the reason why an increasing number of projections leads to an improvement in image quality that follows a square-root law as discussed in sec. 4.3. The number of quanta that actually contribute to the image for the real case is given as

$$\langle N_{\text{Real}} \rangle = \text{SNR}_{\text{real}}^2 = \text{NEQ}, \tag{3.12}$$

with NEQ being called the noise-equivalent quanta. The ratio of the NEQ to the available photons that could theoretically be detected provides a figure of merit for the quality of the detecting device that is referred to as detective quantum efficiency (DQE), which is defined as [66]

$$\text{DQE} = \frac{\text{SNR}_{\text{real}}^2}{\text{SNR}_{\text{ideal}}^2} = \frac{\text{NEQ}}{\langle N_{\text{ideal}} \rangle}. \tag{3.13}$$

It shall be noted that the DQE for a particular spatial frequency u is proportional to the modulation transfer function (MTF) and the noise power spectrum (NPS), which will be introduced in the next sections, so that

$$\text{DQE}(u) \propto \frac{\text{MTF}(u)^2}{\text{NPS}(u)} \tag{3.14}$$

holds [66]. Comparing with eq. 3.3 and 3.6 this equation can be interpreted as a frequency-dependent SNR of the detection stage. By weighting with the relevant frequency components a task-specific figure of merit – the so called model observers (MOs) – can be defined, which will be introduced in sec. 3.6 [50, p. 866].

3.3 Modulation Transfer Function

An one-dimensional image $f'(x)$ of an object $f(x)$ is considered, which is produced by a linear and shift invariant imaging system with x being the spatial coordinate in object space. The resulting image is then given as

$$f'(x) = \int f(x - x')\text{PSF}(x')\text{d}x', \tag{3.15}$$

where $\text{PSF}(x)$ denotes the so called point spread function (PSF), which describes the resolution properties of the imaging system. It is defined as the response to a Dirac impulse $\delta(x)$ [66]. Note that eq. 3.15 describes a convolution with the PSF as kernel function. The Fourier transform of the PSF is the optical transfer function (OTF):

$$\text{OTF}(u) = \mathcal{F}(\text{PSF}(x)), \tag{3.16}$$

with u being the frequency coordinate in Fourier space. The magnitude of the OTF is referred to as the modulation transfer function (MTF) denoted as MTF(u), which is usually normalized by its zero-frequency value to enforce MTF(0) = 1 so that [66]

$$\text{MTF}(u) = \frac{|\text{OTF}(u)|}{|\text{OTF}(0)|}. \tag{3.17}$$

The MTF is closely related to the spatial resolution, which indicates how close two objects (e.g., two lines) that are seen through an imaging system can be to each other to be still observed as two separate objects. A linked parameter is the contrast C (also called modulation), which is defined as the quotient of the gray value variation interval of an image normalized by its mean, which is given as [36, p. 404]

$$C\big(f(x)\big) = \frac{\max(f(x)) - \min(f(x))}{\max(f(x)) + \min(f(x))}. \tag{3.18}$$

The contrast can be interpreted as a metric for the discriminability of a bright feature to the dim background in an image or vice versa [67, p. 38]. Since eq. 3.15 describes a convolution in image space, the MTF can be used as transfer function; i.e., it describes the frequency-dependent ratio $C(f'(x))/C(f(x))$, which can be calculated as multiplication of $f(x)$ with the MTF in Fourier space. Note that the discussion in this section is restricted to an one-dimensional MTF. However, since CT is volumetric imaging method, the related MTF comprises three spatial dimensions and the integral in eq. 3.15 has to be adjusted to cover the entire volume [68].

3.4 Basic Concepts of Statistical Decision Theory

A continuous object f is considered, which is discretely represented by a vector $\mathbf{f}$ in the Hilbert space of square-integrable functions. The image formation process of an arbitrary imaging system can then be expressed as

$$\mathbf{g} = \mathcal{H}\big(\mathbf{f}\big) + \mathbf{n}, \tag{3.19}$$

with $\mathcal{H}$ being an appropriate imaging operator and $\mathbf{g}$ the resulting (i.e., measured) data. The vector $\mathbf{n}$ denotes noise that is added during the image formation process, which is assumed to be additive, stationary and zero-mean in the following. Consequently, the noise in a particular measurement can be defined as the difference between the expected data and the actually resulting data as

$$\mathbf{n} \equiv \mathbf{g} - \langle \mathbf{g} \rangle = \mathbf{g} - \mathcal{H}\big(\mathbf{f}\big), \tag{3.20}$$

where $\langle \cdot \rangle$ again denotes the statistical average for a certain amount of acquired data, which is equivalent to the expectation value of $\mathbf{g}$ [50, p. 806f].

The process described in the last passage can be referred to as data acquisition. In practice, $\mathcal{H}$ is non-invertible since it maps the continuous data f of the real world onto a discrete detector, so that only a finite set of measurements can be conducted [69, p. 150]. Furthermore, for the special case of computed tomography it is worthwhile to point out that the result of the imaging process is typically not the image itself (unlike in some other disciplines, like e.g., microscopy or two-dimensional radiography) but the entire projection data. To obtain the desired image, which is represented by a

three-dimensional volume $\tilde{\mathbf{f}}$, an intermediate step – the reconstruction operation $\mathcal{Z}$ as introduced in sec. 4.4 – is required, which can be considered an approximation for the discrete inversion of $\mathcal{H}$. Due to the influence of noise in the acquisition process and properties of the reconstruction, the image (which is referred to as reconstruction or reconstruction result from now on for convenience) is typically not exactly identical but only an estimate of the object. Additionally, the reconstruction problem is ill-posed (see sec. 2.3), so that the obvious choice of $\mathcal{Z} = \mathcal{H}^{-1}$ is usually not feasible. However, for the sake of simplicity it is continued with $\mathbf{g}$ instead of $\tilde{\mathbf{f}}$, but the derivation can be performed analogously. The imaging process is typically performed with a certain (decision) task in mind, which will be the decision if a certain signal is present or not in the following. The means by which this task is performed is called the decision-maker or the observer. While the observer can be, for instance, a human operator assessing the image and trying to make a decision, this work focuses on mathematical observer models [50, p. 802f]. An overview of psychophysical methods can be found in the literature [70, p. 7f].

3.5 Receiver Operation Curve

If the object consists of a non-random background signal $\mathbf{s_b}$ and a known, superimposed signal of interest which is produced by some feature $\mathbf{s_f}$ the task is referred to as signal known exactly/background known exactly (SKE/BKE). Consequently, the noise $\mathbf{n}$ is the only source of randomness for this model. The binary detection task that the observer is supposed to handle can then be formulated as a decision if the signal is present or not, i.e., as the two possible hypotheses

$$H_0 : \mathbf{g} = \mathbf{s_b} + \mathbf{n}, \tag{3.21}$$
$$H_1 : \mathbf{g} = \mathbf{s_b} + \mathbf{s_f} + \mathbf{n}, \tag{3.22}$$

with H_0 being the signal absent and H_1 the signal present case [71, 72]. Due to eq. 3.19, the feature signal can also be defined as

$$\mathbf{s_f} = \left\langle \mathcal{H}\left(\mathbf{f}|H_1\right)\right\rangle - \left\langle \mathcal{H}\left(\mathbf{f}|H_0\right)\right\rangle, \tag{3.23}$$

where the average operator is required since the image formation is a statistical process due to the additive noise. From now on, all signals are considered to be real-valued, which is a reasonable assumption for absorption contrast based CT. The decision maker calculates then a test statistic $t(\mathbf{g})$, which is a random variable since it depends on $\mathbf{g}$. Consequently, the conditional probability density functions on $t(\mathbf{g})$ can be expressed as

$$p(t|H_i) = \int_\infty p(t|\mathbf{g})p(\mathbf{g}|H_i)\mathrm{d}g, \tag{3.24}$$

with $p(\mathbf{g}|H_i)$ as the probability density of $\mathbf{g}$ given that the hypothesis H_i is true and the scalar test statistic $p(t|\mathbf{g})$, given the data $\mathbf{g}$. The expression $p(\mathbf{g}|H_i)$ is sometimes referred to as likelihood function, since it expresses how likely it is to obtain the data $\mathbf{g}$, given that the hypothesis H_i holds [50, 72, p. 807f]. For the case of CT, the uncertainty to obtain this particular data even in the absence of noise can also be explained by the fact that the image formation is not a deterministic process per se, but obeys the law of Poisson photon statistics.
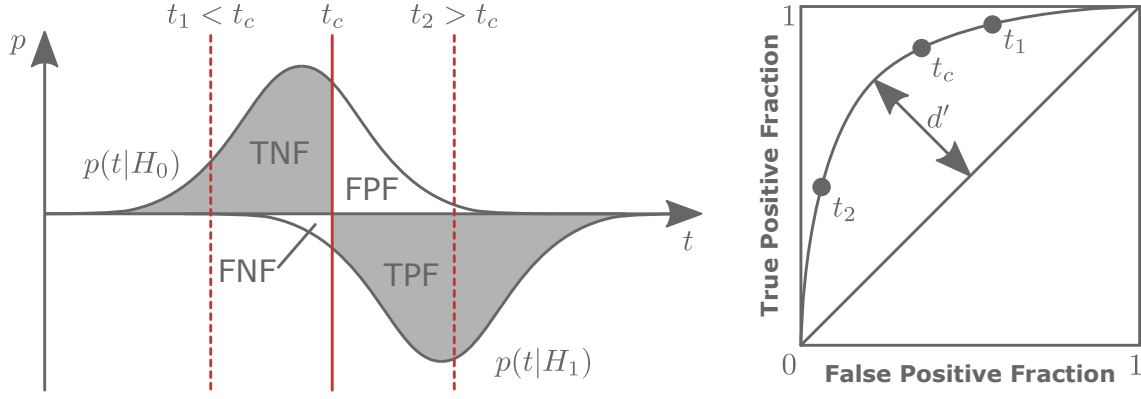
Figure 3.1: Probability density functions of both hypotheses with the fractions TPF, FPF, TNF, FNF and the resulting ROC curve.

The result of the detection task is obtained by comparing the test statistic to a previously defined scalar threshold t_c. If $t(\mathbf{g}) > t_c$ holds, the null hypothesis H_0 is rejected and vice versa. This results in four possible decision outcomes: if H_0 is true and correctly classified as true, it is termed a true positive, if it was falsely classified it is referred to as a false positive. Analogous, if H_1 is correctly classified it is true negative and if it is falsely classified as H_1 it is called false negative [50, p. 813f]. Assuming an infinite number of decisions made with the criterion t_c the fractions of each possible outcome are obtained as integral under the curve as illustrated in fig. 3.1 as

$$\text{TPF} = P(t \geq t_c|H_1) = \int_{t_c}^{\infty} p(t|H_1)\mathrm{d}t, \tag{3.25}$$

$$\text{FPF} = P(t \geq t_c|H_0) = \int_{t_c}^{\infty} p(t|H_0)\mathrm{d}t, \tag{3.26}$$

$$\text{FNF} = 1 - \text{TPF} \quad = \int_{-\infty}^{t_c} p(t|H_1)\mathrm{d}t, \tag{3.27}$$

$$\text{TNF} = 1 - \text{FPF} \quad = \int_{-\infty}^{t_c} p(t|H_0)\mathrm{d}t, \tag{3.28}$$

with $P(t \geq t_c|H_i)$ being the probability (i.e., the integral over the respective probability density function) to come to each conclusion given the threshold criterion t_c and the underlying hypothesis H_i [50, p. 813f]. The true positive fraction (TPF) is often called sensitivity, while the true negative fraction (TNF) is referred to as specificity. It is apparent from both, the equations and fig. 3.1, that the choice of the threshold criterion influences the decision of the observer. Low values of t_c favor accepting H_1 and vice versa. Connected to this is a rise in TPF, but also the false positive fraction (FPF), i.e., a present feature is more readily detected, but for the price of a higher fraction of falsely detected signals. At the same time TNF and the false negative fraction (FNF) decrease. Nevertheless, in practice, the consequences of each outcome are typically not identical. For instance, it is desirable to reliably detect a cancer tumor in a medical CT scan and accept a higher number of false alarms. A frequently used method to depict this trade-off are the so called receiver operating characteristic curves (ROCs, see right graph in fig. 3.1), where the TPF and FPF (or similar entities) are compared against each other for different choices of t_c. By varying t_c, it is possible to move to another working point on the ROC [50, p. 814f].

For given probability density functions it is not possible to change the shape of the ROC, since it is a representation of the underlying nature of the task and the decision strategy, i.e., the model to compute $p(t|H_i)$. Consequently, metrics can be derived that express how hard the decision task actually is. As such, the SNR of the test statistic SNR_t is defined analogous to eq. 3.8 as the ratio of the expectation value of the signal (which is the difference between the expectation values of both hypotheses) and the average of the variances of the conditional test statistics [50, p. 819f]:

$$\text{SNR}_t = \frac{\langle t|H_1 \rangle - \langle t|H_0 \rangle}{\sqrt{\frac{1}{2}(\sigma_0^2 + \sigma_1^2)}}. \tag{3.29}$$

From now on it is assumed that the test statistic follows a Gaussian distribution, which can be motivated by empirical findings being often in the same shape, the central limit theorem (i.e., the distributions originate from different but similar sources which are combined), and generally for the sake of easier mathematical handling [73, p. 19f]. For further simplification, the variances of signal and noise are considered to be identical. In this particular case, SNR_t is given the special name detectability index d' [50, p. 819].

Note, that if the variance is set to be equal to one and shift accordingly, the distributions $p(t|H_0) = \mathcal{N}(0,1)$ and $p(t|H_1) = \mathcal{N}(d',1)$ are obtained with $\mathcal{N}(\mu,\sigma)$ denoting the Gaussian distribution with mean μ and standard deviation σ, i.e., the detectability d' can be interpreted directly from the plot of the probability densities as the difference of their means [73, p. 20]. If both assumptions hold, the ROC curve is symmetric with respect to the diagonal from upper left to lower right and d' can be found in the diagram as the distance between the intersection point with this diagonal to the equality line defined as TPF = FPF as indicated in fig. 3.1. For $d' = 0$ the enumerator of eq. 3.29 is required to be zero, so $p(t|H_0) = p(t|H_1)$ holds and the corresponding ROC would be just a straight line, which represents the worst case of two totally indistinguishable distributions. In the best case that both distributions are perfectly separable, they need to be an infinite distance apart from each other, since the normal distribution has no intersection point with the x-axis and infinity is obtained in the enumerator, yielding $d' = \infty$ for the optimal case (see fig. 3.2). The detectability index is related to the integral over the ROC curve (typically referred to as area under the curve denoted as AUC), which is another frequently used performance metric by

$$\text{AUC} = \frac{1}{2} + \frac{1}{2}\,\text{erf}\left(\frac{d'}{2}\right), \tag{3.30}$$

with $\text{erf}(x)$ denoting the error function defined as $\text{erf}(x) = \frac{2}{\sqrt{\pi}}\int_0^x e^{-x'^2}\,\mathrm{d}x'$ [50, p. 817f]. Another interpretation is given by the formula $d' = \text{erf}(\text{TPF}) - \text{erf}(\text{FPF})$ [73, p. 24]. It shall further be noted that the ROC is related to the concept of probability of detection (POD) curves, which can be used to determine the likelihood of detecting a flaw of a certain characteristic parameter (usually its length, size or volume) reliably. Further information concerning the POD can be found in the literature [8, 74].
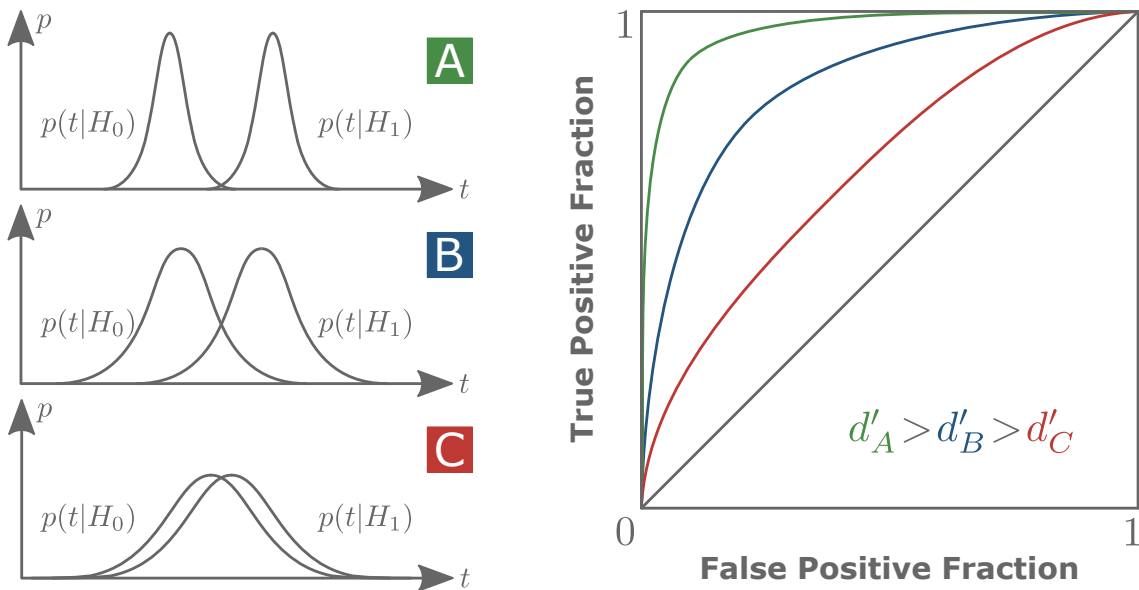
Figure 3.2: The shape of the test statistics influences the ROC-curve, which is independent of the selected t_c.

3.6 Ideal Bayesian Observer

The goal is now to define a test statistic which results in the best possible outcome with respect to some prerequisite. For this, the classification task is performed by computing the ratio

$$\Lambda(\mathbf{g}) = \frac{p(\mathbf{g}|H_1)}{p(\mathbf{g}|H_0)} > \Lambda_c, \tag{3.31}$$

and comparing the outcome to a threshold criterion Λ_c. If $\Lambda(\mathbf{g}) > \Lambda_c$ holds, one decides for H_1 and vice versa. The expression $\Lambda(\mathbf{g})$ is called the likelihood ratio. Since it it is often more convenient to work with sums instead of fractions, the log-likelihood-ratio is defined as $\lambda(\mathbf{g}) = \log(\Lambda(\mathbf{g}))$. Note that the data-dependent part in eq. 3.31 is formulated on the left side, while the right one only holds a certain threshold that is defined by some external assumption. This means that the ROC curve expressed by the equation is always identical, but with a different operating point and typical examples for the choice of Λ_c are the maximum a posteriori and the maximum likelihood criterion [50, p. 825f]. A test that can be formulated in the form of eq. 3.31 is called likelihood-ratio test and any observer performing this test is referred to as an ideal observer. It includes all information that is necessary to compute $p(\mathbf{g}|H_j)$ (e.g., noise statistics or the measurement process itself) and is supposed to be optimal in all possible operating points, i.e., it yields the maximum TPF, AUC and d' [50, p. 828f]. However, this does not mean that the ideal observer always decides correctly (since this is also dependent on the obtained measurements) but it achieves the minimal estimator variance and maximizes the TPF for a given FNF [75].

26

3.7 Noise Statistics

3.7.1 Uncorrelated Gaussian Noise

It is now assumed that the noise $\mathbf{n}$ is zero-mean, stationary, independent and following a Gaussian distribution with standard deviation σ. As expressed in eq. 3.21 and 3.22 the noise is also considered to be purely additive and identically distributed for both hypotheses. Then, the probability density for each of the M vector elements g_m is given by

$$p(g_m|H_0) = \frac{1}{\sqrt{2\pi\sigma^2}}\exp\left(-\frac{\left(g_m - s_{bm}\right)^2}{2\sigma^2}\right), \tag{3.32}$$

$$p(g_m|H_1) = \frac{1}{\sqrt{2\pi\sigma^2}}\exp\left(-\frac{\left(g_m - s_{bm} - s_{fm}\right)^2}{2\sigma^2}\right), \tag{3.33}$$

with s_{bm}, s_{fm} being the m-th vector component of $\mathbf{s_b}$ and $\mathbf{s_f}$, respectively. Due to the statistical independence, $\mathbf{g}$ can be expressed as the product of its elements g_m. From this point, it is straightforward to define the likelihood ratio of eq. 3.31 as [50, p. 835f]

$$\Lambda(\mathbf{g}) = \frac{p(\mathbf{g}|H_1)}{p(\mathbf{g}|H_0)} = \frac{\prod_{m=1}^{M}\frac{1}{\sqrt{2\pi\sigma^2}}\exp\left(-\frac{\left(g_m - s_{bm} - s_{fm}\right)^2}{2\sigma^2}\right)}{\prod_{m=1}^{M}\frac{1}{\sqrt{2\pi\sigma^2}}\exp\left(-\frac{\left(g_m - s_{bm}\right)^2}{2\sigma^2}\right)}. \tag{3.34}$$

After canceling out the common terms, the exponential function can be removed by applying the natural logarithm on both sides of the equation, which yields the log-likelihood $\lambda(\mathbf{g})$ introduced in sec. 3.6 and changes the multiplication into an addition. Since the signal and background are known exactly by definition, the second fraction in eq. 3.35 is constant since it only depends on those and can be included in the threshold criterion instead, so that $\lambda(\mathbf{g})$ is adjusted. This gives a modified expression $\lambda'(\mathbf{g})$ that is also referred to as the matched-filter discriminator (for detailed derivation see [50, p. 835f]):

$$\lambda(\mathbf{g}) = \ln\left(\Lambda\left(\mathbf{g}\right)\right) = \sum_{m=1}^{M}\left(\frac{\left(s_{bm} + s_{fm} - s_{bm}\right)g_m}{\sigma^2} - \frac{\left(s_{bm} + s_{fm}\right)^2 - s_{bm}^2}{2\sigma^2}\right), \tag{3.35}$$

$$\lambda'(\mathbf{g}) = \sum_{m=1}^{M} s_{fm}g_m = \mathbf{s_f}^{\mathrm{T}}\mathbf{g}. \tag{3.36}$$

3.7.2 Correlated Gaussian Noise and Noise Power Spectrum

The expressions for $p(g_m|H_j)$ in equation 3.33 can be generalized by introducing the noise covariance matrix $\mathbf{K_n}$, whose entries are given by

$$\mathbf{K_{ij}} = \langle(g_i - \langle g_i\rangle)(g_j - \langle g_j\rangle)^{\mathrm{T}}\rangle. \tag{3.37}$$

The covariance matrix is self-adjoint with the diagonal entries being the variances of the entries of $\mathbf{g}$. If an off-diagonal entry K_{ij} is zero, it follows that g_i and g_j are statistically independent [50, p. 368f]. Since the noise is assumed to be zero-mean, it is described

entirely by its covariance matrix[2]. For the given case the expected signal is already known since a SKE/BKE case is assumed, so by use of eq. 3.20 one obtains [50, p. 368f]:

$$\mathbf{K_{n}}_{,j} = \langle (\mathbf{g} - \langle \mathbf{g} \rangle)(\mathbf{g} - \langle \mathbf{g} \rangle)^{\mathrm{T}} | H_j \rangle = \langle \mathbf{nn}^{\mathrm{T}} \rangle. \tag{3.38}$$

Since in eq. 3.21 and 3.22 the noise was defined to be independent of the signal, the covariance matrix does not depend on the underlying hypothesis as well and the index j is from now on omitted for convenience.

Similar to the covariance, the noise correlation matrix $\mathbf{C_{n}}_{,j}$ is defined as

$$\mathbf{C_{n}}_{,j} = \langle \mathbf{gg}^{\mathrm{T}} | H_j \rangle = \mathbf{K_{n}}_{,j} = \langle \mathbf{nn}^{\mathrm{T}} \rangle, \tag{3.39}$$

which is equal to the covariance matrix in case of zero-mean random vectors like the noise definition used in this work [50, p. 268]. Here, it was again used that the covariance and correlation matrices are identical for both hypotheses as described above.

According to the Wiener–Khinchin theorem, which can be derived directly as a special case from the cross-correlation theorem [76, p. 51f], the power spectrum $P_x(u)$ with frequency u of the signal $x(t)$ is given by the Fourier transform of its autocorrelation function [50, p. 390] which is given as the diagonal values of the correlation matrix, since both matrices are identical according to eq. 3.39. If applied only to the noise part of the signal this frequency-dependent signal power is referred to as the noise power spectral density, Wiener spectrum or the noise power spectrum NPS(u), which is defined as [69, 77, p. 148]

$$P_{\mathrm{noise}}(u) = \mathrm{NPS}(u) = \frac{1}{M} \sum_{m=1}^{M} \left(\mathcal{F}(\mathbf{n}) \right)^2. \tag{3.40}$$

or alternatively in its continuous form analogous to eq. 3.4 as [50, p. 390]

$$\mathrm{NPS}(u) = \lim_{T \to \infty} \frac{1}{T} \mathcal{F}\left(n(t)^2 \right). \tag{3.41}$$

The integration of eq. 3.41 over all frequencies gives an expression for $\langle P_{\mathrm{noise}} \rangle$, occasionally also referred to as Parseval's theorem, which states that the power of a signal is preserved if it is Fourier-transformed. The reason for this is that the Fourier transform is a unitary transform, which is invariant of scalar products and norms, like the ℓ_2 norm in this case [50, p. 117].

Equation 3.32 and 3.33 can be generalized towards a multivariate normal random vector as [50, p. 836f]:

$$p(\mathbf{g}|H_0) = \frac{1}{\sqrt{(2\pi)^M \det(\mathbf{K_n})}} \exp\left(-\frac{1}{2} (\mathbf{g} - \mathbf{s_b})^{\mathrm{T}} \mathbf{K_n^{-1}} (\mathbf{g} - \mathbf{s_b}) \right), \tag{3.42}$$

$$p(\mathbf{g}|H_1) = \frac{1}{\sqrt{(2\pi)^M \det(\mathbf{K_n})}} \exp\left(-\frac{1}{2} (\mathbf{g} - \mathbf{s_b} - \mathbf{s_f})^{\mathrm{T}} \mathbf{K_n^{-1}} (\mathbf{g} - \mathbf{s_b} - \mathbf{s_f}) \right), \tag{3.43}$$

---

[2]Generally speaking, this is not exactly true since $\mathbf{K_n}$ only captures first and second order correlations (i.e., connections of sets with three points or more are neglected). However, since additive and zero-mean Gaussian noise is assumed, this information is sufficient to describe the distribution entirely [70, p. 13].

with det($\cdot$) denoting the determinant. After intermediate steps (see [50, p. 836f]) a more general expression for eq. 3.36 is given by

$$\lambda'(\mathbf{g}) = \mathbf{s_f}^\mathrm{T} \mathbf{K_n}^{-1} \mathbf{g}. \tag{3.44}$$

Note that under the assumption of uncorrelated data (i.e., the previous case of sec. 3.7.1), the autocovariance function is zero for all times $t \neq 0$ [76, p. 342f] and the covariance matrix becomes diagonal with the standard deviations as diagonal elements [50, p. 368f]. This is equivalent to the definition of white noise[3] used by some sources [76, p. 342]. As a consequence, for identical standard deviations $\det(\mathbf{K_n}) = \sigma$ holds and $\mathbf{K_n}^{-1}$ becomes a scaling with $\frac{1}{\sigma}$ since all entries of the matrix are uncorrelated [64, p. 1443], which can also be expressed by the combination of eq. 3.4 and 3.6 for the continuous case.

3.7.3 Prewhitening Filter

If $\mathbf{K}$ is non-singular, eq. 3.44 can be rewritten as

$$\lambda'(\mathbf{g}) = \mathbf{s_f}^\mathrm{T} \mathbf{K_n}^{-1} \mathbf{g} = \left(\mathbf{K_n}^{-\frac{1}{2}} \mathbf{s_f} \right)^\mathrm{T} \left(\mathbf{K_n}^{-\frac{1}{2}} \mathbf{g} \right). \tag{3.45}$$

Comparing this with eq. 3.36 this can be interpreted as a multiplication of the expected signal and the data with the same matrix before computing the scalar product analogous to the case of uncorrelated Gaussian noise (eq. 3.36); this method is sometimes referred to as prewhitening [50, 72, p. 839].

The use of applying the prewhitening filter $\mathbf{K_n}^{-1/2}$ onto the measurements becomes particularly apparent if the covariance matrix of the filtered measurements $\mathbf{K_n}^{-1/2}\mathbf{g}$ is calculated. Using the definition of the covariance matrix in eq. 3.38 one obtains [50, p. 839]

$$\mathbf{K_z} = \left\langle \left(\mathbf{K_n}^{-\frac{1}{2}} \mathbf{g} - \left\langle \mathbf{K_n}^{-\frac{1}{2}} \mathbf{g} \right\rangle \right) \left(\mathbf{K_n}^{-\frac{1}{2}} \mathbf{g} - \left\langle \mathbf{K_n}^{-\frac{1}{2}} \mathbf{g} \right\rangle \right)^\mathrm{T} \right\rangle \tag{3.46}$$

$$= \mathbf{K_n}^{-\frac{1}{2}} \left\langle (\mathbf{g} - \langle \mathbf{g} \rangle) (\mathbf{g} - \langle \mathbf{g} \rangle)^\mathrm{T} \right\rangle \mathbf{K_n}^{-\frac{1}{2}} \tag{3.47}$$

$$= \mathbf{K_n}^{-\frac{1}{2}} \mathbf{K_n} \mathbf{K_n}^{-\frac{1}{2}} = \mathbf{I}, \tag{3.48}$$

where the definition of the covariance matrix $\mathbf{K_z}$ of eq. 3.38 is used again in eq. 3.47. This means that the covariance matrix of the filtered data becomes the identity matrix $\mathbf{I}$, which is diagonal and therefore corresponds to white noise.

The question arises now, why the observer performance is actually maximized if the data noise is uncorrelated. To explain this, it is necessary to go one step back to the beginning of sec. 3.5 where the general test statistic $t(\mathbf{g})$ was introduced. If $t(\mathbf{g})$ is a linear function, i.e., of the form

$$t(\mathbf{g}) = \mathbf{w}^\mathrm{T} \mathbf{g}, \tag{3.49}$$

with discriminant $\mathbf{w}$, the resulting ideal observer is called the Hotelling observer. It was shown in sec. 3.7.2 that for the case of a SKE/BKE task with identical Gaussian

---

[3]It shall be noted that the concept of white noise is generally problematic for real-world applications, since an infinite spectrum with constant power does not converge but instead diverge towards infinity, which holds even for finite observation intervals. To avoid this problem, often a band-limited white noise is used as an approximation [76, p. 343]

covariances the prewhitening observer defined in eq. 3.36 equals the Hotelling observer with $\mathbf{w} = \mathbf{s_f}$, since the only source of randomness is given by the noise vector $\mathbf{n}$. The proof and further extensions to tasks with statistically varying signal $\mathbf{s_f}$ (i.e., the signal and background is not know precisely like in the SKE/BKE case) can be found in the literature [50, 850f]. For the Hotelling observer and the SKE/BKE case, it can be shown that the SNR is proportional to the trace[4] of the inverse noise covariance matrix [50, p. 853]

$$\text{SNR}^2 \propto \text{tr}(\mathbf{K_n}^{-1}), \tag{3.50}$$

with $\text{tr}(\cdot)$ denoting the trace, which is maximized by the choice of eq. 3.48 if the covariance matrix is similar for each hypothesis [50, p. 855].

Summing up, applying a matched filter to the measured data as defined by eq. 3.36 yields the best results with respect to the performance metrics defined via the ROC-concept, given that white noise is present. A proof that this procedure also maximizes the SNR of the signal is provided in the literature [80, p. 238f]. If the noise is correlated, the optimal test statistic is given by performing a prewhitening operation before applying the matched filter. Further details concerning the matched filter concept is provided in the literature [81].

It is critically important to point out that the strategy of the ideal observer as derived in the last equations relies on an invertible covariance matrix $\mathbf{K_n}$. However, the inverse does not exist unless the number of measurements (i.e., the size of $\mathbf{g}$) equals or exceeds the dimension of $\mathbf{K_n}$ [72]. In reality it is almost never feasible to perform such a high number of measurements. For instance, if $\mathbf{g}$ represents a $(1{,}024 \times 1{,}024)$ pixel image, approx. 10^6 measured projections would be necessary to allow for matrix inversion. A possibility to overcome this problem is the introduction of frequency channels that reduce the dimensionality of $\mathbf{K_n}$ significantly, which leads to channelized observer models that are beyond the scope of this work [82].

3.8 Observer Performance

The signal-noise-ratio defined in eq. 3.29 can be used to provide a figure of merit to quantify how difficult the classification task described by eq. 3.21 and 3.22 is. This is possible since the data are assumed to be normally distributed and the formation of the decision variable is a linear transform. For the enumerator of this expression, the mean values $\langle \lambda(\mathbf{g}|H_j)\rangle$ given by eq. 3.44 and variances σ_λ^2 defined by eq. 3.38 of the conditional probability density functions are required, which are given by

$$\langle \lambda'(\mathbf{g})|H_j\rangle = \langle \mathbf{s_f}^{\text{T}}\mathbf{K_n}^{-1}\mathbf{g}|H_j\rangle, \tag{3.51}$$

$$\sigma_{\lambda'}^2 = \langle \left(\lambda'(\mathbf{g}) - \langle \lambda'(\mathbf{g})|H_j\rangle\right)^2 |H_j\rangle = \cdots = \mathbf{s_f}^{\text{T}}\mathbf{K_n}^{-1}\mathbf{s_f}. \tag{3.52}$$

The skipped intermediate steps can be found in the literature [50, p. 837]. Since related terms are subtracted from each other in the enumerator of the SNR, constant terms

---

[4]In general, this metric is called the Hotelling trace, which describes the inter- and intra class scattering properties as a generalized class separability metric [50, p. 853] and has also been used to quantify imaging system performance [78]. Note that this metric is based on the trace of the (inverse) covariance matrix, while usually (e.g., in eq. 3.42) the determinant is used instead. These different scatter expressions are referred to as total and generalized variance, respectively [79, p. 81f].

can be omitted (i.e., such that do not depend on the data $\mathbf{g}$), which yields together with eq. 3.29

$$\mathrm{SNR}^2_{\lambda,\mathrm{PW}} = \mathrm{SNR}^2_{\lambda',\mathrm{PW}} = \frac{\left(\langle\lambda'(\mathbf{g})|H_1\rangle - \langle\lambda'(\mathbf{g})|H_0\rangle\right)^2}{\mathbf{s_f}^{\mathrm{T}}\mathbf{K_n}^{-1}\mathbf{s_f}} \tag{3.53}$$

$$= \frac{\left(\langle\mathbf{s_f}^{\mathrm{T}}\mathbf{K_n}^{-1}\mathbf{g}|H_1\rangle - \langle\mathbf{s_f}^{\mathrm{T}}\mathbf{K_n}^{-1}\mathbf{g}|H_0\rangle\right)^2}{\mathbf{s_f}^{\mathrm{T}}\mathbf{K_n}^{-1}\mathbf{s_f}} \tag{3.54}$$

$$= \frac{\left(\mathbf{s_f}^{\mathrm{T}}\mathbf{K_n}^{-1}(\mathbf{s_f}+\mathbf{s_b}) - \mathbf{s_f}^{\mathrm{T}}\mathbf{K_n}^{-1}\mathbf{s_b}\right)^2}{\mathbf{s_f}^{\mathrm{T}}\mathbf{K_n}^{-1}\mathbf{s_f}} \tag{3.55}$$

$$= \frac{\left(\mathbf{s_f}^{\mathrm{T}}\mathbf{K_n}^{-1}\mathbf{s_f}\right)^2}{\mathbf{s_f}^{\mathrm{T}}\mathbf{K_n}^{-1}\mathbf{s_f}} = \mathbf{s_f}^{\mathrm{T}}\mathbf{K_n}^{-1}\mathbf{s_f}, \tag{3.56}$$

where it was used that $\langle\mathbf{s_f}|H_0\rangle = \mathbf{0}$, i.e., the expected feature signal is not present in the data if the zero hypothesis holds (see eq. 3.21) [50, p. 837]. This derivation is valid for the case where a prewhitening filter (sec. 3.7.3) can be applied to the data as indicated by the index PW. For the case without the filtering step or when uncorrelated Gaussian noise is present eq. 3.36 has to be used instead of eq. 3.44. Starting again from eq. 3.53 this results in

$$\mathrm{SNR}^2_{\lambda,\mathrm{NPW}} = \mathrm{SNR}^2_{\lambda',\mathrm{NPW}} = \frac{\left(\langle\lambda'(\mathbf{g})|H_1\rangle - \langle\lambda'(\mathbf{g})|H_0\rangle\right)^2}{\mathbf{s_f}^{\mathrm{T}}\mathbf{K_n}^{-1}\mathbf{s_f}} \tag{3.57}$$

$$= \frac{\left(\langle\mathbf{s_f}^{\mathrm{T}}\mathbf{g}|H_1\rangle - \langle\mathbf{s_f}^{\mathrm{T}}\mathbf{g}|H_0\rangle\right)^2}{\mathbf{s_f}^{\mathrm{T}}\mathbf{K_n}^{-1}\mathbf{s_f}} = \frac{\left(\mathbf{s_f}^{\mathrm{T}}\mathbf{s_f}\right)^2}{\mathbf{s_f}^{\mathrm{T}}\mathbf{K_n}^{-1}\mathbf{s_f}}, \tag{3.58}$$

where $\mathrm{SNR}_{\lambda,\mathrm{NPW}}$ denotes the SNR of the non-prewhitening (NPW) model observer [66]. Note that according to this definition the SNR solely depends on the signal strength and noise properties but not the background signal that is identical for both hypotheses. For the special case of uncorrelated noise outlined in sec. 3.7.1 and uniform variance the covariance matrix is diagonal with identical entries and eq. 3.56 simplifies to

$$\mathrm{SNR}^2_{\lambda} = \frac{\mathbf{s_f}^{\mathrm{T}}\mathbf{s_f}}{\sigma^2}, \tag{3.59}$$

which is equivalent to eq. 3.7 [50, p. 838]. With eq. 3.56 and eq. 3.58 two expressions for the SNR in given projection or volume data are available. They consider the particular imaging task in form of the discriminant $\mathbf{s_f}$ and differ only in their assumptions concerning the statistical nature of the additive noise. So far, due to the expressions in eq. 3.21 and eq. 3.22, the expected signal was defined directly in the measured data domain and all further discussions in this chapter concentrated on the noise component. However, for practical applications the signal difference of interest is given in the object domain. As a consequence, the influence of the imaging operator $\mathcal{H}$ becomes relevant, which has been neglected so far for the sake of a more convenient and clear discussion. In order to include this effect, the signal difference $\Delta\mathbf{s}$ in the object domain[5] is defined analogously to the one given in sec. 3.4 and 3.5 as

$$\Delta\mathbf{s} = \left(\mathbf{f}|H_1\right) - \left(\mathbf{f}|H_2\right), \tag{3.60}$$

---

[5]Due to practical considerations $\Delta\mathbf{s}$ is in this work either defined mathematically or obtained by estimates for $\mathbf{f}$ that are generated by the reconstruction of the maximum feasible measurements as described in sec. 6.4.1. See also the discussion concerning the signal template definition in sec. 11.2.1

which is in contrast to the definition of $\mathbf{s_f}$ of eq. 3.23 that was given in the imaging domain. Note, however, that $\mathbf{s_f} \neq \mathcal{H}(\Delta \mathbf{s})$, since the imaging operator is not necessarily linear. Furthermore, it is often more convenient to work in the frequency domain instead of the image domain, since the matrix of the noise power spectrum is diagonal for stationary noise and easier to handle than the autocorrelation function. This is possible, since, according to Parseval's theorem, the value of the SNR of a signal does not change if it is Fourier-transformed as outlined in sec. 3.7.2. Since these formulas are also typically encountered in their continuous form, for convenience this switch will also be performed in the following without further discussion. The correspondences for the most important variables in sec. 3.4 are then given as [70, p. 51f]

$$\Delta \mathbf{s} \circ\!\!\xrightarrow{\mathcal{F}}\!\!\bullet \omega, \quad \mathbf{K_n} \circ\!\!\xrightarrow{\mathcal{F}}\!\!\bullet \mathrm{NPS}, \quad \mathcal{H} \circ\!\!\xrightarrow{\mathcal{F}}\!\!\bullet \mathrm{OTF}, \tag{3.61}$$

with the noise power spectrum NPS introduced in sec. 3.7.2 and signal template ω. The variable OTF denotes the optical transfer function (OTF), which describes the frequency-dependent image degradation by the acquisition system [70, p. 51f] as discussed in sec. 3.3. Since X-ray detectors usually operate by integrating the incoming photon energy, only the amplitude of the OTF is relevant, which is given by the MTF as defined in eq. 3.17.

This makes also intuitively sense, if one considers an extremely poor imaging system (i.e., the MTF drops to zero almost instantly) that leads to a reconstruction image where all voxels have the identical value. This result would have zero noise, since no derivations from the average value occur, but would also be clearly useless in practice. Together with eq. 3.56 and 3.58 this finally yields the frequency-dependent form for the detectability of the PW and NPW model observer as

$$\mathrm{SNR}_{\mathrm{PW}}^2 = d'_{\mathrm{PW}} = \iiint \frac{(\mathrm{MTF}(u,v,w) \cdot \omega(u,v,w))^2}{\mathrm{NPS}(u,v,w)} \mathrm{d}u\mathrm{d}v\mathrm{d}w, \tag{3.62}$$

$$\mathrm{SNR}_{\mathrm{NPW}}^2 = d'_{\mathrm{NPW}} = \frac{\left(\iiint (\mathrm{MTF}(u,v,w) \cdot \omega(u,v,w))^2 \mathrm{d}u\mathrm{d}v\mathrm{d}w\right)^2}{\iiint \mathrm{NPS} \cdot (\mathrm{MTF}(u,v,w) \cdot \omega(u,v,w))^2 \mathrm{d}u\mathrm{d}v\mathrm{d}w}, \tag{3.63}$$

with u, v, w being the frequencies in the three-dimensional Fourier space. The integral is justified, since the frequencies of the NPS are independent for stationary noise [70, p. 52] and the index λ is omitted for convenience. Essentially, the prewhitening step aims toward reducing the impact of frequencies with strong noise, while the matched filter increases the importance of the frequencies that contain the expected signal and the MTF models the image degradation by the acquisition system [70, p. 52]. This is also apparent from eq. 3.62, which is equivalent to eq. 3.14 if the enumerator is weighted with the expected signal difference.

While the DQE introduced in sec. 3.2 has established itself as the standard metric to quantify detector performance [43, p. 364], the model observers aim to provide an index that is specific to the considered imaging task. So far, model observers have been used for a wide variety of applications, for instance to quantify image quality[6] of CT setups and protocols [83–86] and to optimize existing systems, for instance with respect to the

---

[6]Observer models are also frequently used to assess image quality with respect to the perception of a human observer, which is particularly relevant in medical disciplines, where the data are usually assessed by trained specialists instead of algorithms. For this particular task, several modifications for the NPW have been proposed to correlate better with human perception. In contrast, the PW model observer is usually used to assess the maximum possible system performance as baseline.

used regularization, tube current modulation [87, 88] or further parameters [89]. Other use cases comprise the assessment of single photon emission computed tomography (SPECT) compensation algorithms [90], optimization of tomosynthesis parameters [91], loss function for machine learning based denoising [92] or task-based modeling [93]. For the course of this work the MOs will act as a figure of merit for the optimization framework (chapter 6), since it is an expression that combines the desirable properties of a high SNR with the Fourier transformed expected signal, which is important for the optimization task as outlined in sec. 4.3.

4 | Outline of the Problem

4.1 Data Sufficiency

An important property of a trajectory implementation is its completeness of the sampled Fourier space (see also sec. 7.3), since otherwise characteristic artifacts (e.g., the well-known cone-beam artifacts) arise, which lead to a degradation of image quality and a loss of geometrical information. An illustrative formulation of this requirement is given by the Tuy-Smith sufficiency condition that states that all surfaces intersecting the object of investigation also need to intersect the trajectory of the X-ray source at least once [94]. Designs that fulfill this condition are also referred to as theoretical exact since the reconstruction for noiseless data is feasible with a unique solution [23]. Strictly speaking, the Tuy-Smith condition cannot be fulfilled in practice, since a CT trajectory typically consists of a finite number of points instead of a continuous curve [95]. In fact, the transition to discrete poses is still an unsolved problem [23] and only approximate formulations to express the extent to which data completeness is achieved are currently available [95].

According to the Nyquist-Shannon theorem [97, 98] the maximum obtainable frequency in a projection image is given as $\nu_{\max} = 1/(2\Delta\xi)$ with $\Delta\xi$ being the pixel pitch in the detector line. Since high frequencies are located far from the origin of the coordinate system, $\nu_{\max}$ can be identified as a circle line in Fourier space as indicated in fig. 4.1. The Fourier slice theorem, which was discussed in sec. 2.3.1, states that measurements conducted under a particular acquisition angle with parallel beam geometry correspond to a line in Fourier space. Assuming that the detector has t pixel elements, such a line will also consist of t entries. Furthermore, since no spatial separability in beam direction (i.e., the depth information) can be provided, the line is exactly one pixel wide in angular direction which equals the zero-spatial-frequency (i.e., the averaged value in this direction). The size of each of this isotropic elements ν_q can then easily be calculated as [96]

$$\nu_q = \frac{\nu_{\max}}{t/2} = \frac{2}{t}\frac{1}{2\Delta\xi} = \frac{1}{t\Delta\xi}, \tag{4.1}$$

where the expression for the maximum frequency of above is used. As indicated in fig. 4.1, the Fourier space is now increasingly sampled by obtaining a growing number of projections that are $\Delta\phi = 2\pi/N$ apart, with N being the number of projections. Due to point symmetry, the Fourier space can be completely filled without gaps if only a half circle is sampled. Since the diameter of the highest frequency circle is given with $2\pi\nu_{\max}$, the number of equiangularly over a half circle arranged projections that need to be provided is given by [96]

$$N = \frac{\pi\nu_{\max}}{\nu_q} = \pi\frac{t\Delta\xi}{2\Delta\xi} = \frac{\pi}{2}t. \tag{4.2}$$
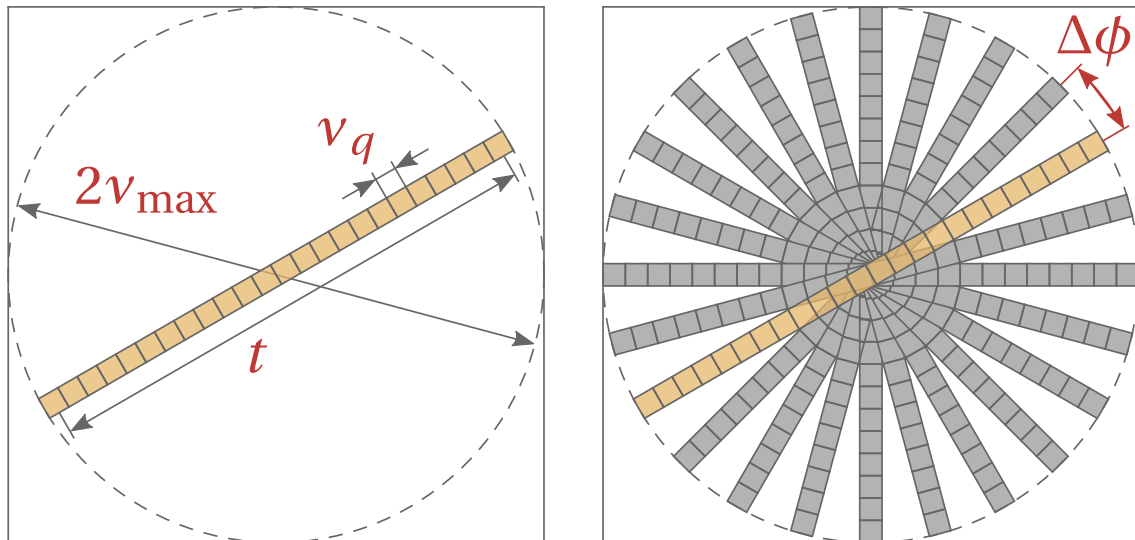
35

Figure 4.1: Illustration of the sampling of the Fourier space with an increasing number of projections. Left: according to the Fourier slice theorem (sec. 2.3.1) each projection corresponds to t entries located on a line in Fourier space with maximum obtainable frequency v_{max}. Right: By acquiring more projections from different scan angles the Fourier space is increasingly filled and the sufficient number of projections is reached when no gaps are left between the separate measurements. Graphic adapted from [96].

In practice, as a rule of thumb instead of eq. 4.2, the projection number N is often chosen to fit approximately the number of horizontal detector elements t [36, p. 261]. This can be justified if the high-frequency content in the image is superpositioned by strong noise. Also, typically cone beam CT setups are used, where a single projection does not correspond to a particular line but a wedge having the same opening angle as the cone beam [99], which will be discussed in sec. 10.4.2. It shall be noted that it is in fact possible in practice to acquire a complete reconstruction from only 180° rotation[1] which is referred to as short-scan CT and contains the minimum degree of redundancy [43, p. 684f]. If more projections are available, the additional information is used to reduce interpolation-related errors and noise [100]. Data sufficiency conditions for short scans are beyond the scope of this work and are provided in the literature [101]. Recently, it has also been shown that in practice most operators select a number of projections that is clearly lower than required by the Nyquist-Shannon sampling theorem, which is probably primarily driven by economic considerations [26].

Sometimes a different formulation of eq. 4.2 is encountered. The largest object that fits onto the detector screen has the same size as the detector itself, which equals $D = t\xi$. According to the Nyquist-Shannon theorem the smallest resolvable feature d has the size of twice the pixel spacing so that $d = 2\xi$ holds. By using these relations eq. 4.2 can be rewritten as [96]

$$N = \frac{\pi}{2}t = \frac{\pi t \xi}{2\xi} = \pi \frac{D}{d}. \tag{4.3}$$

---

[1] For CBCT setups the minimal rotation angle increases to 180° plus the cone beam angle. If a short scan is performed with such a system, some parts of the Fourier space are sampled more often than others and a weighting function is necessary to prevent severe artifacts. Typically a so called Parker window is used to compensate for these redundant data [43, p. 684f].

This relation is also known as the Crowther criterion, which was originally derived for electron tomography in 1970 [102]. For more detailed discussions of data sufficiency and information content in the light of the Shannon-Nyquist criterion the interested reader is referred to the literature [103–105]. It shall also be mentioned that, as apparent from fig. 4.1, the density of projections is higher at the low-frequency domain in the image center and increases then linearly to higher frequencies. This is the reason why a ramp-shaped filter is used to compensate for this effect in reconstruction algorithms of the FBP type (see sec. 2.3.2) [96].

A particular intuitive perception of the problem can be obtained if the reconstruction task is perceived as solving of a system of equations, which is the fundamental idea of all iterative reconstruction methods as outlined in sec. 2.3.3. Referring to eq. 2.13 it becomes clear that the system is underdetermined if the dimension of $\mathbf{f}$ is smaller than $\mathbf{p}$, i.e., the number of projections must be higher than the number of voxels in the volume divided by the number of pixels in a projection. However, this is a clearly simplified point of view, since the system matrix is sparse and not all voxels are sampled equally well. In fact, for very few projections some information cannot be obtained since related parts of the Fourier space are not sampled at all. In the extreme case of a detector with very high resolution and a small volume this relation might yield that one or two projections are already sufficient to properly reconstruct the object, which is clearly not realistic. Last, iterative reconstruction methods are simplifications for themselves, since they are based on the representation of the image in form of a voxel grid, while it can be shown that continuous objects can in general not be uniquely determined by a finite number of projections [52, p. 283f].

4.2 Sparsity and Compressibility of Signals

In section 4.1 considerations based on signal theory and data completeness conditions lead to an estimate for the minimal number of projections. However, this leaves the question why it should be feasible at all to reduce the projection count under this lower threshold and still expect a proper outcome in terms of image quality of the reconstructed volume. According to compressed sensing (CS) theory it is nevertheless possible to obtain useful results, even for acquisition patterns that include significantly fewer projections than required by Nyquist and Shannon's sampling theorem, if additional constraints are introduced that compensate for the missing data. The fundamental idea of such approaches is basically very similar to data compression algorithms and relies on the fact that many signals can be stored more efficiently if they are transformed into a more appropriate basis in which they appear sparse. While the Nyquist-Shannon theorem establishes an upper bound for the required sampling rate, its application is – strictly speaking – only appropriate if the original signal has a broadband frequency content. However, signals encountered in practice are typically only broadband if they have been previously compressed and under some conditions the requirements stated in sec. 4.1 can be relaxed [106, p. 91]. The case where only such a low projection number is available is referred to as sparse-view CT [20]. The related theoretical background will be briefly covered in the following:

A vector $\mathbf{s} \in \mathbb{R}^n$ is called sparse of degree $m \leq n$ if at most m entries differ from zero. Since sparsity itself is a strong constraint for real data often the weaker concept of compressibility is more convenient which requires that the number of its components

that are larger than a certain threshold is relatively small [107, p. 41f]. For convenience, in the course of this work both terms will mostly be used synonymously. A sparsifying transform basis $\mathbf{\Psi} \in \mathbb{R}^{n \times n}$ is a basis that expresses the vector $\mathbf{x} \in \mathbb{R}^n$ in the sparse vector $\mathbf{s}$:

$$\mathbf{x} = \mathbf{\Psi}\mathbf{s}. \tag{4.4}$$

Typical examples for $\mathbf{\Psi}$ are the singular value decomposition (SVD), the wavelet transform or the Fourier transform. Such transforms can often be realized in a computationally efficient way, for instance in case of the fast Fourier transform (FFT). Storing only the $m \ll n$ relevant values (and their position) of $\mathbf{s}$ is the fundamental concept of many compression methods, including well known algorithms like JPEG or MPEG [106, p. 84f]. Related to these concepts, some work based on the wavelet transform has been performed to compress CT-scans [108].

The inversion of this idea forms the central concept of compressed sensing. Instead of acquiring all values of $\mathbf{x}$ only a partial quantity of measurements $\mathbf{g} \in \mathbb{R}^p, p \ll n$ is performed, which can be used to reconstruct the original signal [106, p. 89f]:

$$\mathbf{g} = \mathbf{\Phi}\mathbf{x} = \mathbf{\Phi}\mathbf{\Psi}\mathbf{s}, \tag{4.5}$$

where the measurement matrix $\mathbf{\Phi} \in \mathbb{R}^{p \times n}$ describes the sampling scheme to select the subset $\mathbf{g}$ of $\mathbf{x}$. While eq. 4.5 is generally underdetermined, it is assumed that the required solution leads to a sparse $\mathbf{s}$. Under appropriate choice of $\mathbf{\Phi}$ this can be expressed as the solution that minimizes the norm $\ell_1(\mathbf{s})$ as side condition. It shall be noted that nevertheless CS is rarely used for images due to the high computational costs [106, p. 92]. However, the fact that for medical CT fewer measurements correspond to the particularly valuable benefits of lowering the dose to the patient and less movement artifacts due to the faster acquisition speed have turned CS-based reconstruction methods into an active field of research [109, 110]. Further related applications can be found, for instance, in scatter estimation [111] or magnetic resonance imaging (MRI) [112, 113].

These considerations show that the sampling conditions derived in sec. 4.1 are oversimplified for practical problems, since they provide a part-independent upper threshold for the necessary number of projections. As improvement, a modification of eq. 4.2 was proposed that includes information on the sparsity of the gradient magnitude image of the object [114]. For CS (i.e., eq. 4.5) particularly the choice of the sampling strategy $\mathbf{\Phi}$ plays an important role. Assuming a Gaussian measurement matrix, the required number of samples N to obtain an accurate representation of $\mathbf{x}$ with high probability is given by

$$N \le cm\log\left(\frac{n}{m}\right), \tag{4.6}$$

where the constant c depends on the coherence between $\mathbf{\Psi}$ and $\mathbf{\Phi}$ [106, p. 90]. In fact, it has been shown in the case of a CS-based reconstruction method that under certain conditions objects can even be reconstructed *exactly* with a low number of projections that follow eq. 4.6 [115]. Further sufficient sampling conditions for CS are discussed in the literature [116]. In addition to incoherence it was shown in an experimental study that the sampling density of the acquired projections influences the final image quality [30]. While a Gaussian choice of $\mathbf{\Phi}$ is generally believed to provide the recovery strategy with the fewest samples (a property referred to as near-optimal sampling strategy), Jørgensen and Sidky implied that non-random measurement matrices might be preferable under certain conditions. Their results suggest that equidistantly sampling

a planar trajectory is equal or better to drawing random samples, even though the measurement matrix for such a strategy is highly structured [117]. These findings are valid for a generic basis like the one provided by the Fourier transform. If the application scenario is clearly defined, a tailored basis $\mathbf{\Psi_t} \in \mathbb{R}^{r \times n}$ with $r \ll n$ can be used, which is specialized for the task and provides a particular low-rank representation for $\mathbf{s}$ and for such bases efficient sampling strategies are known [118]. Nevertheless, the physically performed Radon transform cannot be avoided so that an arbitrary choice of $\mathbf{\Phi}$ and $\mathbf{\Psi}$ is not feasible in practice, which will be discussed in sec. 4.3.

For the applications discussed in this section the fundamental assumption is the existence of a sparse representation in an appropriately selected basis. This concept will be illustrated with an example in the following, for which a gray value image with a certain resolution is considered. Given the assumption that each pixel is statistically independent it would be necessary to measure each element separately. In such a case, the Nyquist-Shannon criterion would be justified and not even an average value could be given by measuring less than every pixel element, since each unmeasured value might be an extreme outlier. However, to minimize its autocorrelation the image would basically need to be pure white noise, which is typically not encountered in practical applications. Considering a natural image instead, it seems more reasonable to assume that adjacent pixels often do not differ significantly, e.g., if they belong to the same object with rather homogeneous properties. This means that the separate pixel values are not independent from each other anymore and less degrees of freedom are required to describe the image compared to the white noise case. Under those circumstances it can be justified to sample just a random subset to obtain an approximation of the imaged object. In a certain sense, thumbnails (i.e., images with reduced resolution compared to the original version) in computer graphics can be considered a practical everyday application. Similar examples can be found in other domains. For instance, acoustic signals like music are typically sparse in a Fourier basis since they consist of air vibrations that are particularly well represented by a basis that relies on sinusoidal waves. In contrast, approximating such oscillations with a basis composed of step functions would intuitively appear inappropriate and inefficient.

Even though the reasoning outlined in the previous paragraphs explains why trajectory optimization as such is actually feasible, it must be stressed that the methods used in this work cannot be counted towards compressed sensing in a strict sense, even though many used concepts are very similar. Typically CS is an approach to efficiently and accurately determine the image vector $\mathbf{x}$ from few measurements $\mathbf{g}$. On the contrary, the goal of this work is to propose an as efficient $\mathbf{\Phi}$ as possible with the provided a priori information (i.e., in form of $\mathbf{x}$) and using the Fourier transform as sparse basis $\mathbf{\Psi}$ while the side condition to favor the sparsest solution (e.g., via calculation of the $\ell_1(\mathbf{s})$ norm) is not explicitly used[2], even though some reconstruction algorithms might include similar properties. However, in both cases the difference for a given m between the estimate for $\mathbf{x}$ and its true value should be minimized, which will be formalized in sec. 4.3.

---

[2]However, in section 10 the Gini coefficient will be used to quantify the sparsity of $\mathbf{s}$, but for the sake of assessing the optimizability instead of performing the optimization itself.

4.3   Practical Implications

In section 2.3.1 the Fourier slice theorem was introduced, which relates the Radon and the Fourier representation of an object to each other, while sec. 4.2 referred to the Fourier transform acting as a generic basis, meaning that most natural signals are sparse if expressed in its modes as basis functions [106, p. 85]. These considerations are linked and have a pictorial explanation that will be illustrated in the following. As simplification, parallel beam geometry will be assumed for this section (this condition will be relaxed towards CBCT in sec. 10). While laminography is not explicitly covered in this work, it shall be noted that an empirical study relating the achievable image quality to the acquired number of projections has been performed as well [119].

First, a grid pattern is assumed as depicted in fig. 4.2 together with its power spectrum in Fourier space. The Fourier transform acts as sparsifying transform so that most entries of the transformed object correspond to zero. Considering the Fourier slice theorem by comparing this result to fig. 2.4, it becomes apparent that these coefficients can be measured with only a single projection located at $\phi = 0°$. This observation makes intuitively sense: The pattern can be fully resolved by one view obtained in vertical direction and the maximal contrast in Radon space can be obtained. For this particular example all information of the object is contained in a single sample as indicated in the Fourier space and the original object can be exactly recovered. For all other choices of ϕ the relevant part of the Fourier space is not sampled. For the horizontal case (i.e., $\phi = 90°$) the contrast becomes minimal in the reconstruction since it contains only a single value which corresponds to the zero frequency (i.e., a single entry) in Radon space. On the other hand, the power spectrum of the Fourier transform reveals salient edges of the object it is applied to, which results in high values for the power and amplitude spectrum at angles perpendicular to the ones in object space as illustrated exemplarily in fig. 4.3. This property is independent to linear shifts of the object [120, 328f]. Combining these two findings yields that valuable image information can be retrieved if a projection tangential to the corresponding edge of the imaged object is obtained (see also optimization approach 1 in sec. 5.2). A more mathematical derivation of this intuitive explanation can be found in the literature [121]. It shall be noted that this also means that theoretically an infinite number of projections is required to image smooth transitions or continuous free-form lines (e.g., the orange curve in fig. 4.3). However, in practice this is not the case due to the voxel discretization of the volume – which can be considered as introducing very small edges into the object – so that a finite (but relatively high) number of projections can often be considered to be sufficient.

These considerations have several important direct consequences. A study [122] based on equiangular distributed poses suggests that reconstructions with few projections show a particularly high direction dependency with respect to the acquisition poses. This seems reasonable, since the high coefficients can easily be missed if they need to be covered with few samples. It was also shown that the dependency decreases if a ring structure is added around the part, while it increases if instead a rectangular geometry is used. This can directly be explained with the Fourier space as well, since the first geometry is highly symmetric and invariant to the projection poses (assuming an equidistant planar trajectory) since in each direction features of the same signal power amplitude are added. In contrast, a square-shaped object results unavoidably in distinct streaks in Fourier space that need to be covered with the acquired projections. However, while this makes the ring-surrounded object less direction-dependent, it is also more
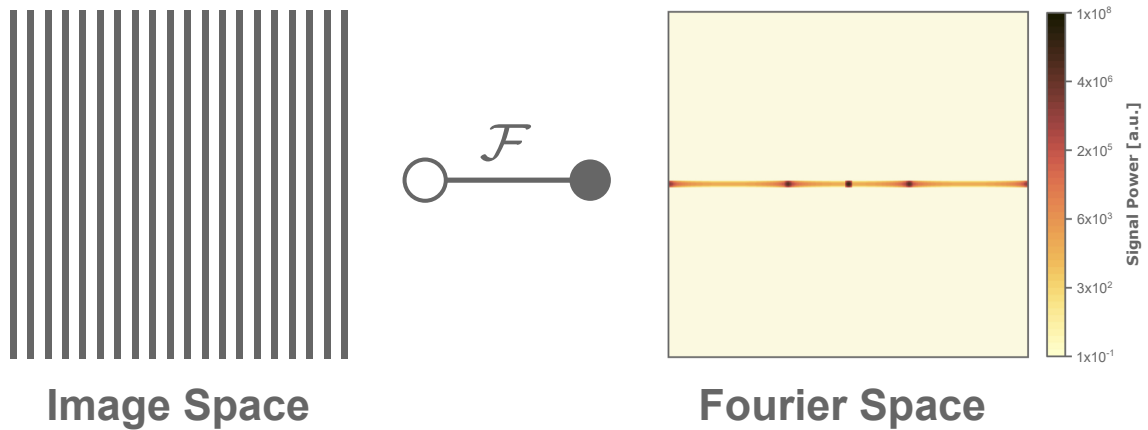
Image Space

Fourier Space

Figure 4.2: The Fourier transform of a grid pattern is sparse. Strictly speaking this example only holds qualitatively for an infinite large object with smoothly varying but different grid distances. Since the shown pattern is uniform the Fourier transform would typically result in only a single peak (i.e., two peaks due to the point symmetry to the origin). This image could be reconstructed using only a single, appropriately selected projection.

difficult to image since more projections are required to sample the relevant part of Fourier space, since all directions carry a certain amount of information in this case and in fact it was determined that the image quality of this structure is worse compared to the object without the surrounding structure. The authors conclude that more complex objects are less dependent on the choice of acquisition angles [122]. According to the considerations outlined above, this is just a different phrasing of the fact that for such objects the Fourier space appears to be less sparse (see also sec. 10.1). In the light of these findings it is also not surprising that for trajectory optimization the biggest improvements have been reported if the part has only few preferential directions, while such with many salient features can hardly be properly reconstructed with few projections [123]. Furthermore, the imaging of a continuous object with compact support can be formulated as a continuous-to-discrete mapping followed by a Fourier transform, whose coefficients form a matrix of infinite size. Trying to recover the relevant parts of this matrix (i.e., its dominant Fourier coefficients) lead to discrete sufficiency conditions for CBCT, which are beyond the scope of this work [124].

While the examples provided in fig. 4.2 and 4.3 may suggest that trajectory optimization is a relatively simple and straightforward problem, it is in fact much more demanding in practice. For one, the provided two-dimensional examples have unique solutions if they contain a finite number of edges, but an infinite amount of possible ones if the problem is extended to three spatial dimensions. The reason for this is that a line in 2D – which has a unique tangent – corresponds to a plane in 3D, for which an arbitrary number of parallel viewing directions can be defined. As direct result, for a given geometry several solutions for an optimized trajectory can be found and in many cases completely different acquisition positions lead to a very similar image quality. Fortunately, experiments have shown that beneficial scan angles are at least unaffected by the choice of varying X-ray tube settings, even though low power setups can benefit most from the avoidance of projections associated with a low SNR.

Opposed to the simplifications in this chapter, in reality the parallel beam geometry is nowadays not used anymore; instead, the rays diverge and form the cone-beam geometry of the setup. As a consequence, a single projection does not correspond to
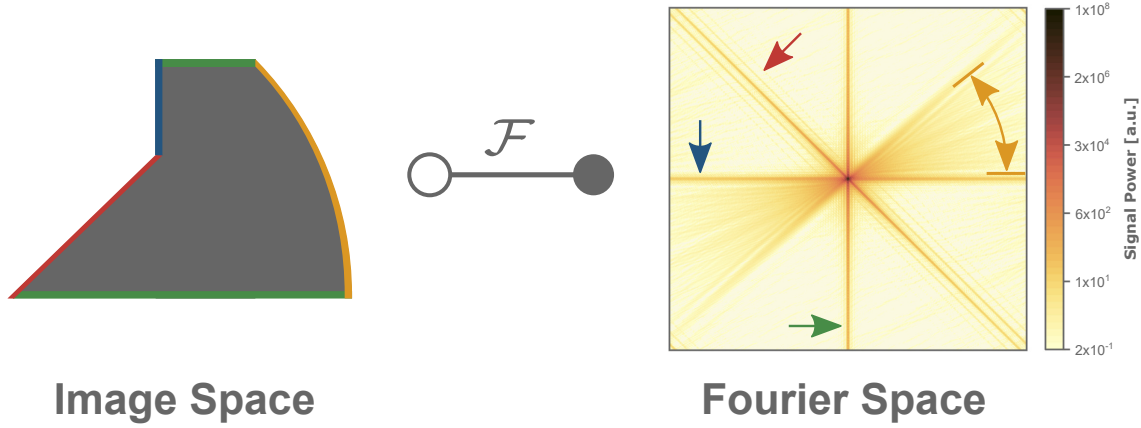
41

Figure 4.3: The Fourier transform of a simple object. Dominant streaks corresponding to high coefficients can be identified as salient edges in the original image as indicated.

a line in Fourier space but forms a segment instead (see sec. 10.4.2). Furthermore, a projection can in theory be tangent to more than one edge, which makes it particularly valuable. However, in practice this can typically not be achieved if the rotation center and SOD are fixed, but it might provide additional improvements if these parameters can also be freely selected, which was not investigated in this work due to parameter space restrictions. Also, a poor SNR can reduce the information content of some projections drastically, and even the loss of entire parts of Fourier space due to photon starvation can occur in the worst case. Geometric constraints of the setup and further similar limitations have to be considered as well. These aspects were not covered in this section but also need to be taken into account to obtain a practically feasible optimization framework.

4.4 Problem Definition and Formal Optimization Criterion

Bearing these preliminary considerations in mind it is now possible to define a formal definition of the trajectory optimization problem. In eq. 4.5 a relation between the image and the related data acquisition was given. Unfortunately, due to the unavoidable physical Radon transform it is not possible to measure arbitrary components, e.g., of a Fourier-based sparsifying or tailored transform $\mathbf{\Psi}$ or $\mathbf{\Psi_t}$. Instead, using the Fourier slice theorem of eq. 4.5 and the iterative formulation of the problem in eq. 2.13 the measurement process can be expressed for the particular case of trajectory optimization as

$$\mathbf{g_{CT}} = \mathbf{\Phi p} = \mathbf{\Phi A f} = \mathbf{\Phi A \mathcal{F}^{-1} s} = \mathbf{\Phi \Psi_{CT} s}, \qquad (4.7)$$

where $\mathcal{F}^{-1}$ denotes the matrix associated with the discrete inverse Fourier transform and $\mathbf{\Psi_{CT}}$ the sparsifying transform related to the angular projection selection problem. Note that the vector of measured projections $\mathbf{g_{CT}}$ is not equivalent to $\mathbf{g}$, since the entries of $\mathbf{f}$ cannot be observed directly via CT. Since quantifying the necessary number of projections for this particular problem is not trivial and beyond the scope of this work the interested reader is directed to the related literature [125].

The goal of performing a trajectory optimization is to define a selection of measurements that minimize the deviations between the reconstructed solution and the actual object. Using the notation introduced in eq. 4.7, the reconstruction operator $\mathcal{Z}(\mathbf{g_{CT}}) = \tilde{\mathbf{f}}$ can be defined as a mapping from a subset of the projection measurements $\mathbf{g_{CT}}$ to an estimate for the image $\tilde{\mathbf{f}}$ (see also sec. 2.3.3). The reconstruction step is typically very complex and nonlinear, so that no matrix representation is possible. For the course of this work $\mathcal{Z}(\cdot)$ serves as an abstract operator that describes the reconstruction process without having to specify its detailed implementation explicitly. The aim is then to find an optimized measurement strategy $\mathbf{\Phi_{N,opt}}$ for a predefined number of projections N so that the achievable image quality is maximized:

$$\mathbf{\Phi_{N,opt}} = \underset{\mathbf{\Phi} \in \mathbf{\Phi_N}}{\arg\max}\left(\left\|\tilde{\mathbf{f}}\right\|\right), \tag{4.8}$$

$$= \underset{\mathbf{\Phi} \in \mathbf{\Phi_N}}{\arg\max}\left(\left\|\mathcal{Z}\left(\mathbf{g_{CT}}\right)\right\|\right), \tag{4.9}$$

$$= \underset{\mathbf{\Phi} \in \mathbf{\Phi_N}}{\arg\max}\left(\left\|\mathcal{Z}\left(\mathbf{\Phi Af}\right)\right\|\right), \tag{4.10}$$

where the norm $\|\cdot\|$ denotes an appropriately selected image quality measure that will be introduced in sec. 6.5.1 and $\mathbf{\Phi_N}$ is the set of all measurement matrices that contain N projections. Quantifying image quality is generally a very hard task, which can, however, be facilitated if a reference-based measure is applied. Analogous to eq. 4.8 this can be formulated as

$$\mathbf{\Phi_{N,opt}} = \underset{\mathbf{\Phi} \in \mathbf{\Phi_N}}{\arg\min}\left(\left\|\tilde{\mathbf{f}}, \mathbf{f}\right\|\right), \tag{4.11}$$

$$= \underset{\mathbf{\Phi} \in \mathbf{\Phi_N}}{\arg\min}\left(\left\|\mathcal{Z}\left(\mathbf{\Phi Af}\right), \mathbf{f}\right\|\right), \tag{4.12}$$

where the norm $\|A, B\|$ indicates the image quality of A with respect to the reference B. Unfortunately, this formulation is typically also not feasible in practice since $\mathbf{f}$ is often unknown or a continuous function. Instead, the goal of this work will be to provide a measure that brings the solution as close as possible to the reconstruction of all available projections:

$$\mathbf{\Phi_{N,opt}} = \underset{\mathbf{\Phi} \in \mathbf{\Phi_N}}{\arg\min}\left(\left\|\mathcal{Z}\left(\mathbf{g_{CT}}\right), \mathcal{Z}\left(\mathbf{p}\right)\right\|\right), \tag{4.13}$$

$$= \underset{\mathbf{\Phi} \in \mathbf{\Phi_N}}{\arg\min}\left(\left\|\mathcal{Z}\left(\mathbf{\Phi Af}\right), \mathcal{Z}\left(\mathbf{Af}\right)\right\|\right), \tag{4.14}$$

which is an ill-posed problem and not solvable in practice due to the size of its components and the properties of $\mathcal{Z}$. This definition also assumes that the reconstruction with all projections yields the result that approximates $\mathbf{f}$ best. This simplification will be outlined in sec. 4.5 and discussed later in sec. 6.5.1. In theory, eq. 4.14 can be solved – for instance via brute force – by variation of $\mathbf{\Phi}$ until the error becomes minimal. Unfortunately, this is not feasible in practice due to the huge dimensionality of the measurement strategy (i.e., many different projection combinations exist) and the very high computational costs to compute $\mathcal{Z}\left(\mathbf{\Phi Af}\right)$, in particular for high values of N. For instance, a single reconstruction using approx. 2,500 projections with the typical

parameters, volumes, projection sizes and hardware (for specifications see sec. 6.4) used in this work can easily take over 40 min. Additionally, the computation to evaluate the image quality metric can become expensive as well, depending on the choice of the measure and the size of the considered volume. Because of this, a heuristic methodology outlined in sec. 6, which is based on the imaging properties of the CT system, will be used for the course of this work.

4.5 Projection Ranges

If a reconstructed volume originates from a sufficiently high number of projections (i.e., at least the recommended number of sec. 4.1 is reached) the question arises how the image quality changes if a smaller subset of projections is used instead. Intuitively, one might assume that a higher number of projections corresponds to more information and therefore must also lead to a better result. Surprisingly, it has been found that this is not necessarily the case.

Zhao et al [126] gives a particular illustrative example at low projection numbers. The authors describe how the image quality improves by actually reducing the projection number in an equidistant planar scan from 40 to 39, since the odd number breaks the symmetry and leads to an improved filling of the Fourier domain (see also sec. 7.3). However, this effect decreases very quickly with increasing projection numbers due to improved sampling conditions. The authors also propose that – assuming a fixed time budget for the entire scan – a projection region that leads to particular good image quality exists. This is due to two conflicting effects: the exposure time per projection has to decrease with an increasing number of samples, which leads to a decreased SNR in each image due to an inherent electronic noise component, while view sampling effects decrease with more projections [126]. It shall be noted that the latter observation is probably much less pronounced for industrial CT due to different detector properties, exposure times and photon energies. This is supported by findings, where it was observed for a CS-based reconstruction method that acquiring many high-SNR images is clearly preferable to few low-SNR ones [127]. For constant exposure times, it was also shown that – depending on the particular imaging task and the inspected geometry – an increase in the projection number or the total sampling angle does not necessarily lead to image quality improvements. Instead, a complex interplay of aliasing artifacts, noise effects and the relevant part of the object frequency spectrum was observed, where high frequency tasks benefit to a certain degree from finer angular sampling and low frequency ones are improved by covering a broader acquisition range if properly balanced with occurring noise [128].

Considering the image quality over a broad range of projection numbers it has been shown that the first few projections contribute most to the image and often every single added projection visibly changes the reconstruction [10, 122, 129, 130], which is also valid for other imaging modalities [131]. The reason is that every projection contributes a relatively high fraction to the image if few projections are used, but also the SNR is proportional to the square root of the projection number, since the photons follow a Poisson-distribution and as a result the quality curves (see e.g., sec. 3.2) generally follow approximately the shape of a square root function [12].

For industrial CT it has been shown that over a broad range of projections very few improvements can be obtained [12], while increasing over a certain threshold holds

no further benefits and only increases scan time [11, 132]. Focusing on metrological applications, Buratti et al. proposed three distinct definitions for projection numbers that they consider to be ideal with respect to different cost functions: the metrological optimum aims to minimize the measurement uncertainty, while the technical optimum is supposed to minimize acquisition time and obtaining a similar uncertainty at the same time. Last, the industrial optimum is defined to minimize the tomographic time, while sustaining results that fulfill the minimum required measurement uncertainty [10, 11]. In the course of this work these considerations will essentially be avoided by investigating the quality over a broader range of projections and leaving the optimal projection number open to the definition of the respective imaging task. However, a method to identify valuable projection ranges will be proposed in sec. 10.

Based on considerations of the previous sections, two relevant projection ranges can be identified: for very low projection numbers every projection adds a relatively large proportion of information to the reconstructed image. Consequently, avoiding redundancy can lead to a clear improvement in image quality. In particular, sampling important parts of the Fourier domain efficiently by adapting the acquisition positions is believed to improve image fidelity at a faster pace than a standard scheme like the equiangular planar circle trajectory. The low-projection space is highly relevant for many applications as outlined in sec. 1 and this work will primarily focus on this range of low projection numbers.

The advantages of an optimized trajectory gets relativized for higher projection numbers as the Fourier space is increasingly sampled and after a certain, part-dependent threshold no benefit can be observed anymore. Since optimized trajectories are mechanically more demanding and comprise less productive exposure time, the use of standard trajectories appears more appropriate in this range. Since industrial parts often exhibit a predominant direction where more material is present in the X-ray path it is reasonable to assume that some projections are inherently more noisy than others. For very high projection numbers where the Fourier space is mostly filled including such projections can act disadvantageous since it actually increases the noise level without adding relevant information. Because the SNR of a given voxel depends on the acquired poses that project this particular voxel onto the detector plane [23] this effect can vary spatially and does not necessarily affect the entire volume.

However, while the linked image degradation is supposed to be typically small in absolute numbers and therefore difficult or even impossible to detect for a human observer it might be relevant for automatic software-based evaluation in the context of NDT or metrological investigations as indicated by the projection number definitions in this section. Furthermore, even if the quality differences in this region are not significant for a particular application, the scan time can be reduced without drawbacks to a certain extent. It is assumed that location, influence and shape of both regions are generally part dependent [12], which will be exemplarily shown in section 10.6 based on in silico experiments.

The original intention for this work was to reduce the amount of projections that are necessary for a meaningful output. The reason behind this is that a certain minimal required image quality is necessary to detect a flaw reliably. However, it often seems reasonable to prefer referring to image quality enhancement for a given, predefined number of projections instead, since two reconstructed volumes with the same quality value are typically not identical and may exhibit different kinds of artifacts which can lead to confusion and is interpreted subjectively.

It shall further be noted that the results presented in this work are mostly generated by an iterative reconstruction method while related work in the literature concerning the influence of the projection number is typically based on FBP type algorithms (see sec. 2.3). While being neglected for further discussions, it can generally be assumed that the choice of the particular reconstruction method and the used filter kernel influences the results to a certain extent [12, 126].

5 | State of the Art

5.1 Part-Independent Trajectory Designs

For most applications to date the planar circle (PC) trajectory is used due to the relatively easy mechanical setup that requires only one degree of freedom (DOF) in the most restricted case. However, many other trajectories have been proposed over time and an overview of such is given in tab. 5.1. While particularly helical designs have gained some relevance in the medical field, most of these approaches are limited to special cases or primarily of academical interest. Additionally, inspired by pseudorandom sampling methods with low discrepancy for Monte-Carlo-methods a further design, the low-discrepancy spherical trajectory (LDS), is introduced in sec. 6.5.2.2, which is considered to be particularly well suited for benchmarking. Laminographic approaches or methods with dynamic offset are beyond the scope of this work and the interested reader is referred to the literature [133–135] for further details about such.

Since according to the Tuy-Smith condition (see sec. 4.1) the completeness of the Fourier space requires movement of the X-ray source into a third dimension it is clear that the PC trajectory cannot be theoretical exact. However, adding additional degrees of freedom to the trajectory is not trivial since an improper choice can lead to decreased image resolution uniformity or a higher degree of data redundancy, which needs to be compensated by apodization or window functions [23]. To achieve an as efficient as possible uniform sampling of the Fourier space, the so called space filling trajectory has been proposed [23, 150], which fulfills a discrete pendant of the Tuy-Smith condition. However, this design is – although universally applicable – also not optimal, since the shape of the object is not considered so that less relevant parts of the Fourier space are assigned the same importance than more relevant ones (see sections. 4.2 and 4.3). Approaches to overcome this limitation and define the trajectory with regard to the part geometry are outlined in section 5.2.

Due to practical reasons of the implementation (sec. 6) and typical geometric constraints of available setups, this work focuses on spherical trajectories, for which all positions of the X-ray source are located on the surface of a sphere centered around the object. Furthermore, in each individual considered case SOD and SDD are kept constant to reduce the complexity, while effects linked to widening the cone beam angle are discussed in sec. 10.4.2. It was shown that this type of trajectory holds several advantages when compared to the conventional circle trajectory, e.g., for the imaging of flat objects and limited or large cone beam angles [155].

Table 5.1: Non-exhaustive overview of CT trajectory designs proposed in the literature. This table was previously released as part of a separate work [136].
*Depends on detailed realization.

Trajectory Design	Theoretically Exact	Source
Planar/Inclined Circle	No	[53]
(Partial) Circle + Arc/Line(s)	Yes	[137–140]
Two Orthogonal Circles	Yes	[94]
Two Circles + Line	Yes	[141]
Ellipse-Line-Ellipse	Yes	[142]
Dual Ellipse Cross Vertex	Yes	[143]
Two Concentric Arcs	Yes	[144]
(Reverse) Helix	Yes	[145, 146]
Rotate-Plus-Shift	No	[147, 148]
Closed Sinusoidal	Yes	[149]
Space Filling	Yes	[23, 150]
Multiple Line Segments	Yes/No*	[151]
Straight Line	No	[152–154]
Low-Discrepancy Sphere	Yes	[136]

5.2   Trajectory Optimization Approaches

5.2.1   Conventional Computed Tomography

The common trajectory designs outlined in sec. 5.1 are calculated independently from the actual shape of the measured specimen. However, for a robot-based medical CT setup (see sec. 5.3) adjusting the trajectory from a circular towards an elliptical shape was found to reduce the influence of scatter effects [156] and further investigations aiming particularly towards minimizing the dose delivered to the patient with regards to the trajectory design have been performed [157, 158]. More importantly, several mostly heuristic approaches have been proposed in the literature to improve the acquisition trajectory for classical CT. In the following, these methods will be specified and a coarse classification is suggested, while it needs to be stressed that many algorithms can be counted towards more than one category or combine several concepts. A more detailed overview is provided in tab. 5.2. As apparent from the table trajectory optimizations is a relatively young field of active research since most approaches have been developed in the last 5 years and no system implementing a trajectory optimization algorithm is yet commercially available or in practical routine use.

5.2.1.1   Capture Tangential to Object Edges

1. In order to reconstruct an edge of a part correctly, projections with X-rays tangent to this edge are necessary [121], which is essentially just a different formulation of Tuy's sufficiency condition [159] as discussed in sec. 4.3. Therefore, by obtaining projections from these angles, the object's shape is better reconstructed than otherwise. Based on the part geometry as input, a method for identifying these valuable projection angles based on the Hough transform of the preliminary

known object has been proposed that shows good results under certain conditions [160].

2. Recently another approach was suggested by Matz et al., which uses a wavelet transform to detect the object edges in the projections [161]. The method also uses additional weights to exclude opposite projections and prevents projection clustering (see sec. 6.4.3) [161].

5.2.1.2 Avoid Highly Attenuating Directions

3. For very dense objects so called photon starvation artifacts can arise due to the low signal-noise ratio [162], while also the formation of beam hardening artifacts is facilitated [163]. Consequently, a simple and frequently used method to improve image quality is to adjust the trajectory or position of the part in such a way that long X-ray path lengths and very dense materials are avoided, which reduces or even entirely avoids such artifacts. While this is typically done manually and based on the experience of the operator, also computational methods were developed [18, 163–167] to automatize the search of beneficial acquisition poses. Similarly, instead of separate projections, also entire scans obtained from different positioning angles can be combined to reduce the influence of these artifacts [168] and some work has been done to determine optimal alignment angles based on previous scans [169].

4. Based on similar considerations, another approach aims particularly towards the avoidance of metal artifacts. From few initial scout views a machine learning framework predicts the location of dense materials, like screws, in the volume. Given these information, for each possible view the difference between the respective line integrals for a mono- and polyenergetic X-ray source is calculated, which is supposed to quantify the severity of beam hardening artifacts. Based on the inconsistency of this property, referred to as spectral shift, an objective function is defined that can be minimized in order to obtain an optimized trajectory. As alternative, another objective function based on the accumulated attenuation values has been suggested, which aims to minimize photon starvation artifacts [170, 171].

5.2.1.3 Tuy-Smith Completeness

5. The incompleteness of Fourier space in cone beam computed tomography (CBCT) leads to the formation of characteristic artifacts [172] (see also sec. 2.3.1) and some approaches have been made to quantify the extent to which Tuy's condition (see sec. 4.1) is fulfilled with respect to a specific voxel [173] or volume of interest (VOI) [174]. Based on this preliminary work, an approach [175] aims to maximize the Fourier space completeness for a particular VOI, where projections with intensity values lower than a predefined threshold are not considered. The latter condition includes part-specific information (since projection data are per definition part-specific) and reflects consideration 3, since very noisy projections can generally be treated as missing parts in Fourier space [176]. An alternative expression for the local Tuy criterion is given by the percentage of surface area lost or underrepresented in Radon space, which has recently been used in combination with metrics related to the X-ray pathlength [19] (approach 3) and a metric for its variance to reduce beam hardening artifacts [177] in similar work.

6. A similar method to approach 5 was used to avoid metal artifacts for medical CT. The algorithm is also based on the local Tuy completeness and treats metal artifacts as lost parts of the Fourier space. For this purpose, a dense sphere, which aims to generate such artifacts, was introduced into the volume and the trajectory was optimized for good image quality at several sampling points in its close proximity. Since it was assumed that the location of the metal is initially not known, its position was varied and the trajectory design adjusted to perform similarly well for each. Consequently, the result is independent of the shape of the object and the dense matter location [176, 178]. However, in theory the method can be adapted for more complex scenarios so that it is counted to the optimization approaches instead of the proposed trajectory designs of sec. 5.1. Nevertheless, contrary to the information provided in tab. 5.2, such changes would require more knowledge concerning the imaging task.

5.2.1.4 Image Quality of the Reconstructed Object

7. An optimization method based on the information content of adding an additional projection has been proposed: first, based on all previously selected projections the volume is reconstructed, where the first projection is chosen manually. Next, for each projection candidate the volume is reconstructed under consideration of all projections that are already in the solution set. The difference between both reconstruction results is compared; high differences are assumed to be an indicator of a high amount of information in the next projection and the respective image is chosen subsequently [179].

8. Similar to approach 7 but adapted for medical C-arm CBCT, Hatamikia et al. used a greedy algorithm to select the best reconstruction using pose combinations from a predefined set of feasible arcs with respect to an objective function. As image quality quantifying function the structural similarity index (SSIM, see sec. 6.5.1.2) is used. In the second iteration, the arc candidates are re-evaluated under consideration of the already selected part trajectory and a second arc is chosen. Even though reconstructions are necessary, this pre-definition of trajectory segments and the relatively simple objective function reduces the computational costs considerably with respect to comparable approaches. The authors report a similar image quality to the standard trajectory with just a quarter of the number of projections [180]. In a variation of the heuristic algorithm, the SSIM as objective function was exchanged by the full-width at half maximum (FWHM) of the one-dimensional point-spread function (PSF, see sec. 3.3) that is obtained by averaging over the three-dimensional expression [181]. In a later version, the condition of previously defined arcs was modified and augmented by a more sophisticated search pattern, which further reduced the calculation time. Additionally, the objective function was changed again and the feature similarity index (FSIM) was used [182]. The newest development is able to consider kinematic constraints on-the-fly [183].

9. Brierley et al. used an approach based on the visibility of defects in industrial 2D-radiography. For this method, a certain number of predetermined flaws are digitally introduced to the three-dimensional model of the part (e.g., a computer-aided design (CAD) file). Subsequently, for the original and flawed geometry, a set

of projections is calculated via radiographic simulation. Subsequently, considering both datasets, a detectability index based on the visible defect size and the local contrast-to-noise ratio (CNR) is computed for each separate flaw. Based on these information, preferable projection angles are recommended [184, 185]. While this approach is designed for radiographic projections, an augmentation of a similar algorithm towards CT has recently been performed by Suth et al., which additionally considers the achieved surface sharpness in its figure of merit [186].

5.2.1.5 Model Observer

10. Of particular interest for this work is the approach of Stayman et al. that is based on the use of model observers (MOs, see sec. 3) to quantify the value of each projection with respect to the imaging task. The necessary image information – the noise power spectrum (NPS, sec. 3.7.2) and the modulation transfer function (MTF, sec. 3.3) – are efficiently approximated by predictor functions. To obtain the necessary task information an additional, preliminary scan was conducted. The projection selection is performed by a greedy algorithm for each iteration, taking previously selected projection choices into account [187–189]. The method was later augmented with improvements comprising continuous acquisition trajectories and an adjusted figure of merit [190, 191].

11. Recently, this algorithm was supplemented using machine learning methods by another group. The new approach does not require predictor functions and generates a closed trajectory path. In contrast to all other methods listed here, the algorithm requires training data for the scenario, so that it is not generally applicable for all objects by default. However, it is one of few sophisticated methods that are able to optimize the trajectory on-the-fly in real time, which is a highly desirable property for practical application [192, 193].

12. Another adaptation of approach 10 was performed earlier by Fischer et al. for industrial CT. The reachable projection poses are generated by a simulation framework in combination with the previously known geometry. While the approach was adapted to several VOIs, the template function for the model observer was in some cases selected to be uniform[1] [22]. The method proposed and investigated in this work is related to this approach and the most important improvements comprise a non-uniform template analogous to the approaches of 10 and a geometrical weighting function. Both adjustments will be discussed in detail in sec. 7. The method was later adapted for anisotropic dark-field CT [194].

13. Recently, a combination of model observers (approach 10) and a Tuy-based metric (approach 5) was proposed [195]. This method is essentially almost identical to the one used in this thesis and differs only in the use of a completeness metric instead of a geometric weighting function (sec. 6.4.3). However, both implementations aim towards fulfilling the same purpose.

---

[1]It will be shown in the course of this work that both of these choices in fact strongly decrease the capabilities of the method and the performance of the optimization algorithm.

Table 5.2: Overview of trajectory optimization methods for conventional CT applied in medical or industrial context. Indicated methods require a wide-sense image reconstruction (including forward-projection algorithms) or detailed a priori information (typically concerning the part geometry) about the imaging task, with the classification being ambiguous in some cases. The indicated year refers to the earliest proposal for each separate approach.

Approach	Reconstruction	Preknowledge	Origin	Year	Source
1	No	Yes	Medicine	2011	[160]
2	No	Yes	Industry	2022	[161]
3	No	Yes	Industry	2010	[18, 163–167]
4	Yes	No	Medicine	2020	[170, 171]
5	No	Yes	Industry	2020	[19, 175, 177]
6	No	No	Medicine	2020	[176]
7	Yes	No	Medicine	2013	[179]
8	Yes	Yes	Medicine	2020	[180–183]
9	Yes	Yes	Industry	2022	[186]
10	No	Yes	Medicine	2013	[187–191]
11	No	Yes	Medicine	2019	[192, 193]
12	No	Yes	Industry	2016	[22]
13	No	Yes	Industry	2021	[195]
14	No	No	Medicine	2013	[179]
15	No	Yes	Medicine	1991	[14, 15, 196]
16	Yes	No	Industry	2000	[197]
17	Yes	No	Medicine	2017	[198]
Own	No	Yes	Industry	2020	[129, 130, 199]

5.2.1.6 Further Concepts

14. Haque et al. proposed a method based on a property they call the spectral richness of the projection: a single projection is (unfiltered) backprojected and subsequently the obtained volume Fourier-transformed. Based on considerations derived from the Fourier slice theorem (see sec. 2.3.1), the absolute values of all points in the Fourier space that are located on a line (which is rotated around the origin with the projection angle) are added up, which yields the figure of merit (higher values are better) [179].

15. Kazantsev defined a metric for the projection information content based on the approximation of the actual image by functions spanned by a projection subset [196]. It can be calculated via the Gram determinant and projection images, so that no reconstruction is required [15]. It was later adapted by other researchers as quality criterion for different modalities [131]. The approach was further extended and successfully evaluated using computer simulations [14].

16. For elliptically shaped objects a genetic algorithm was developed. The next best projection is chosen randomly according to an angular distribution that is calculated from a fitness function, while projections close to already chosen angles are avoided [197]. This method is complex and restricted to very few application scenarios.

17. Barkan et al. proposed a method that does not require any a priori information of the object. In an initial iteration, equidistantly spaced projections are taken from the object and reconstructed to obtain an updated guess of the part geometry. Subsequently, a Ridgelet transformation is performed and the directions corresponding to the highest coefficients added the solution set. These angles are then measured and the workflow is repeated until a termination criterion is met. This approach is roughly similar to the observer models used in other work, but instead of the Fourier transformation a Ridgelet transformation is used and the SNR is not taken into account [198].

5.2.2 Discrete Tomography

The field of discrete tomography contemplates with CT images that comprise very few different gray values [200]. In the extreme case, only two different attenuation values are considered, which is referred to as binary tomography. These special disciplines of CT reconstruction become relevant in cases where it is only of interest to separate few materials or objects from each other; e.g., in geophysical tomography [201] or medical imaging with contrast markers [202]. Since the dynamic range of the gray values is usually known (or defined) previous to the reconstruction, this information can be exploited so that proper results are achievable with much fewer images than typically necessary for conventional CT [203, 204]. However, as for their continuous counterpart, the particular choice of projections is also highly relevant [200] and several optimization approaches have been proposed. This task is significantly easier for discrete tomography since the problem usually comprises much lower dimensions and said extensive simplifications have been made. In fact, the reconstruction of discrete tomography data can be considered a sparse signal recovery problem [205]. Even though these methods are not directly applicable for industrial CT, some examples will be presented in the following for the sake of completeness.

18. Varga et al. [206, 207] proposed a relatively simple algorithm to find the best set and number of projections for a given part that is similar to the approach of Hatamikia et al. [180] (see approach 8). In a first step, different sets of projections are provided; these sets differ in the number of involved equidistant projections and the offset-angle for the first projection. Next, the reconstructed image from each of these sets is compared to the image of the original object (i.e., the ideal solution of the reconstruction) and the set with the highest similarity is considered to be the best, where the relative mean error is used to quantify the image quality. Alternative to this greedy algorithm, an approach using simulated annealing was proposed, which was later [208] supplemented by further selection strategies. The algorithm is computationally very expensive since each possible combination of projections has to be considered separately [206, 207]. To improve calculation speed, a significantly faster modification was proposed that replaces parts of the framework by a neural network and can operate without reconstruction in the optimization loop [209].

19. Another approach for discrete tomography is based on the concept of the so called information gain, which is obtained by computing how much a particular additional projection would restrict the space of possible solutions, based on the projections chosen before. The calculation is performed by determining the

53

metric space diameter for each possible projection set candidate, which acts as a figure of merit for the similarity of possible solutions of the equation system and quantifies how much the choice of a particular additional projection reduces the uncertainty of the reconstruction result. While no knowledge of the imaged object is required, the algorithm is computationally very expensive [210]. The approach was later augmented to be applicable for conventional gray value CT [123].

20. For binary CT, a method based on the so called global uncertainty has been proposed, which also does not require previous knowledge of the part and is similar to the idea of approach 19. It measures voxel-wise how many possible solutions for each binary case exist and calculates from those an entropy-like metric that was previously introduced in a separate work [211]. This number is summed up over the entire volume and used as figure of merit by a modified greedy algorithm. Again, the approach is computationally very demanding so that approximations are necessary to turn the method practically applicable [212, 213].

5.2.3 Further Related Disciplines

Furthermore, also for other related imaging modalities some approaches have been developed:

21. Vogel et al. proposed an algorithm for freehand single photon emission computed tomography (SPECT), that could be adapted for CT applications. The approach does not incorporate prior knowledge (except motion restrictions by the setup, i.e., feasible and impossible projection poses) and runs in real time. Parallel to the data acquisition, potential pose candidates are assessed with respect to several possible figures of merit that are derived from the numerical condition of the system matrix that would result if the related projection would be picked and subsequently the one with the highest value is selected. The performance was validated with simulations and experiments [214].

22. For electron paramagnetic resonance imaging, an algorithm to determine the next best acquisition pose was developed. Initially, projections are acquired from four equidistantly spaced angles. Depending on the distribution of gray values in these, an entropy-like metric used as figure of merit is assigned to each projection. Subsequently, the next projection between the two previously obtained projections is iteratively selected as the one with the highest difference in their entropy metric until a termination condition is reached. No precomputing or a priori knowledge of the object is necessary and the next projection can be computed on-the-fly due to very low computational costs. As result it was possible to reduce the number of projections by 30 % without any loss of information [131].

23. A – in comparison to Brierley et al. – highly simplified approach for 2D-radiography was later proposed, which solely considers the contrast in a predefined VOI. The algorithm was combined with a pose estimation framework to allow for fast inline inspection [215–217].

24. Also for radiography, a method has been suggested that particular focuses on dimensional measurements. The approach aims towards finding a perpendicular projection to the features to be measured and uses a two-step registration method in combination with a radiographic simulation tool [218].

25. Based on similar considerations, several methods have been developed for coronary X-ray angiography. While the detailed implementation and workflow differs to some extent, they all try to optimize a cost function that is built up by combining metrics for vessel foreshortening and overlap as apparent from the projections corresponding to potential acquisition poses [219–223]. Furthermore, also an approach aiming to minimize only the vessel foreshortening has been proposed that essentially aims towards acquiring projections in which the relevant coronary segment appears parallel to the detector [224], which is comparable to approach 1 for CT.

5.3   Versatile Computed Tomography Installations

In order to achieve the maximal flexibility concerning the choice of the acquisition trajectories, it is necessary to be able to position X-ray source and detector freely around the object of investigation. Common CT systems usually utilize a mostly fixed source-detector system and therefore restrict themselves to rotation and translation of the probe, resulting in a limited number of degrees of freedom (DOF). As an approach to mitigate the space and flexibility limitations of such standard configurations, more versatile or robot-based systems have emerged in the recent years, where at least one component (X-ray source, workpiece or detector) is attached to a robotic arm that can be positioned freely in space [225]. Even though new challenges related to positioning accuracy [226], calibration [227, 228] or the reconstruction method [229, 230] are connected to these setups, the newly gained abilities and DOFs turn them into well-suited hardware counterparts for trajectory optimization and related adaptation methods. The benefits of trajectory optimization for such setups has been confirmed by simulative investigations [231].

Since the technology is relatively young, only few robot-based CT systems have been installed so far, for instance at the car manufacturer BMW in cooperation with the Fraunhofer institute [225, 232], with the latter also operating own systems [233] or at the French Alternative Energies and Atomic Energy Commission [230, 234]. A further setup exist in the veterinary [235] field and recently a comparable medical system has become commercially available [236]. While these approaches are based on several manipulators, also some configurations [237–239] have been proposed that only rely on a single industrial robot and allow rapid scan times down to 8 s [43, p. 939].

However, apart of experimental setups [240, 241] several conventional configurations already offer the adaptiveness necessary for optimized or non-standard trajectories. Examples for such comprise radiotherapy setups [43, p. 907f], mobile C-arms and angiography suites [43, p. 557f] for medical applications or robot-based radiography and laminography [242, 243] installations in the industrial field.

Part II

Optimization and Evaluation Approach

6 | Trajectory Optimization and Evaluation Approach

6.1 Overview

As mentioned in sec. 5, trajectory optimization is a relatively young field of active research and few practical viable and sophisticated methods were available when the investigations for this thesis started in 2018. In fact, during the course of this work, almost half of the approaches shown in tab. 5.2 were suggested in addition to own developments. Model observer based methods were one of the most promising concepts that were early available and reported good results for medical (approach 10) and industrial (approach 12) applications while their practical feasibility was not solely verified by simulations but additionally validated with real measurements. Based on this preliminary work, the choice of a MO-based backbone for own developments appeared reasonable. The proposed framework used for this work is depicted in fig. 6.1 and will be briefly outlined in the following. Further details are provided as part of separate publications [136, 199].

To reduce the complexity of the problem trajectory optimization can be formulated as a selection task: a number of m reachable acquisition poses are predefined and projections from these angles are simulated. The objective is now to identify for a number of projections $n < m$ a combination of positions that maximizes the image quality (see eq. 4.14). The images related to feasible acquisition poses are provided by a simulation (or a previous scan as in the experimental measurements of part III), which needs to be carried out only once and is described in sec. 6.3. Further information concerning the test object for most investigations of this work can be found in sec. 6.2. Furthermore, for efficient determination of the image properties during the optimization loop the reconstruction is avoided and an image quality prediction pipeline is employed instead that updates and recomputes estimates for MTF and NPS in each step as described in sec. 6.4.2. However, to increase computational performance the so called Fisher information matrices (FIMs, see sec. 6.4.2) will be computed before the optimization loop and reused in each iteration as shown in fig. 6.1.

Zheng et al. refered to this particular formulation of the selection task as so called set cover problem, where a group of projections is identified as a set and the task is to cover the important information in the image, which is represented by its salient edges [160]. The set cover problem is well-studied and many algorithms for its solution are available. Examples for such being used by similar approaches are, for instance, ant colony optimization [160], the covariance matrix adaptation evolution strategy [190] or simulated annealing [206]. For this work a greedy algorithm was selected for the
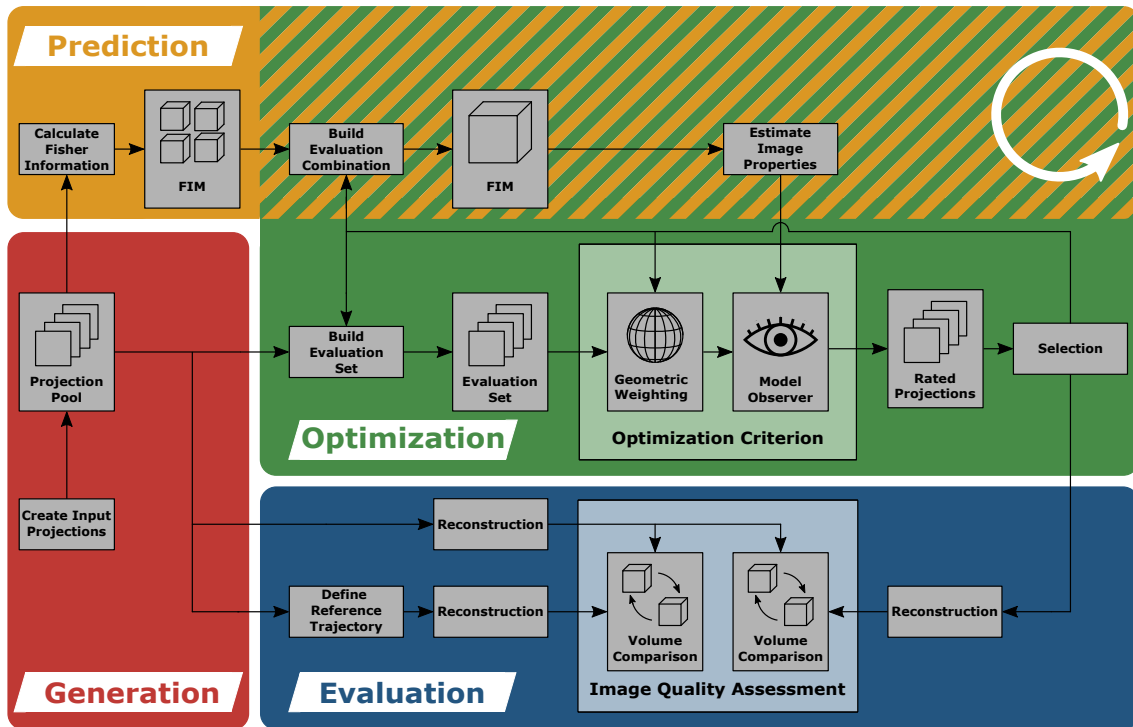
Figure 6.1: Simplified overview of the proposed trajectory optimization framework. Four general parts can be identified: the data generation stage prepares the input projections that are gradually selected by a greedy algorithm in the optimization algorithm. To avoid the computational burden of the reconstruction for each separate evaluation combination, predicted image quality properties are used, which are provided in each iteration by the prediction framework. Before the optimization process the Fisher information matrices need to be calculated in a separate preprocessing step to allow efficient calculation of the estimated data. At predefined iteration steps the calculated trajectory is passed over to the evaluation pipeline where it is reconstructed and compared to previously specified reference trajectories.

optimization stage due to its simple implementation, the proven feasibility for the given problem [22, 206], and the deterministic results. While this method is generally only capable of finding a local maximum, this drawback was neglected since the problem is expected to have several solutions that perform similarly well as described in sec. 4.3. In the first iteration all projections form together the projection pool and a figure of merit is calculated for each pose. The projection with the highest value is removed from the evaluation set and added to the solution set (see fig. 6.1). The quality indicator is then computed again for all remaining items in the evaluation set under consideration of all objects that are already in the solution. With progressing iterations fewer positions are contained in the evaluation set and need to be calculated; however the complexity for each single computation increases since more poses are already in the solution set, which makes the prediction step computationally more expensive. The steps performed during optimization and the figure of merit is described in sec. 6.4. Adaptions and refinements concerning the greedy algorithm have been proposed for trajectory optimization but are omitted for this work due to the higher complexity and computational effort [212].

The optimization part and in particular the composition of the figure of merit utilized in the greedy algorithm form the most crucial part of the entire framework. For
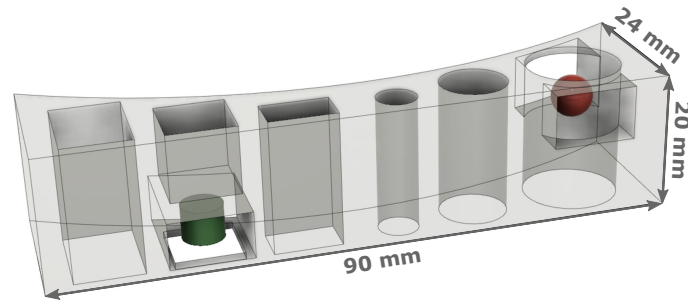
Figure 6.2: The bat phantom used for most investigations in this work. Shown are also the cylinder (green) and sphere feature (red).

an easier understandable approach several configurations of the latter will be described and evaluated using simulated data in the separate chapter 7. This structuring allows to simultaneously identify and outline fundamental properties that need to be fulfilled for a successful trajectory optimization and a good reconstruction. However, for assessing the results and success of the trajectory optimization framework an evaluation method needs to be implemented and the question needs to be addressed what a "good" reconstruction is actually supposed to mean. To achieve this, the projections contained in the solution set are passed over at predefined iterations to a reconstruction pipeline and the resulting volumes are compared to reference trajectories using appropriate image quality metrics as described in sec. 6.5.

6.2   Test Artifact

The bat phantom test part used for most investigations in this work is depicted in fig. 6.2 with technical details being provided in sec. B.3. The approximate geometry and name were derived from the artifact of a related work [244]. Within the part two VOIs are defined that hold a cylinder and a sphere as primitives; all further investigations will concentrate only at these two local object as detectable signals. The sphere was selected since it features per definition no clearly preferred direction, while the cylinder differs only slightly by the existence of two parallel planes. The features are of particular simple shape since model observers (see sec. 3) are typically used for such geometries.

The main intention for the design was to determine angles that will clearly correspond to a high SNR and good visibility. To achieve this, the objects are placed outside of the main body, so that a high contrast between the attenuation values of the feature and the surrounding air can be assured from a suitable angle. Furthermore, the main part contains windows of missing material next to the VOIs, so that projections obtained from this direction are supposed to result in a particularly high contrast. Furthermore, the object is significantly longer in one direction and features a concave edge to generate particular long X-ray penetration lengths to the direction of the edges due to the higher amount of material, which leads to a decreased SNR in this direction. The bat phantom is simulated to be made of elementary iron and is otherwise mostly symmetric with clearly defined edges and holes, which can similarly be found in typical industrial items. Furthermore, the part was constructed to be relatively flat to avoid cone-beam effects given planar reference trajectories.

6.3   Simulation Framework

The first step depicted in the framework in fig. 6.1 comprises the generation of the projection dataset, for instance via a simulation framework. Since geometry information of the parts to be scanned are often available for industrial CT [22] the use of CAD files or similar sources does not pose a significant drawback in practice. While the image stack can theoretically also stem from experimental measurements instead, this approach was selected for several reasons. First, a CT installation with the necessary degrees of freedom was originally not available for this work. While measurements were nevertheless facilitated by augmenting the setup with two tilting tables as presented in sec. 8.1, this method is very laborious which makes it difficult to investigate new scenarios. Furthermore, even with such a setup, additional geometrical restrictions are unavoidable and the manipulator itself biases the dataset by introducing an additional obstacle in the beam path for some angles. Additionally, the positioning error and further inaccuracies of the mechanical setup were avoided by using a simulation-based approach. This is particularly relevant, since no further software-based alignment correction was used in the framework and the positioning accuracy for flexible installations is often of concern if left uncompensated due to its influence on the measurement accuracy [226, 245]. Last, the use of simulations allows to assume a mono-energetic X-ray spectrum and no additional sources of noise, which obviates many artifacts (e.g., beam-hardening by a polychromatic source spectrum). While this reduces the impact of the optimization approach since it is not possible to suppress artifacts (they are already avoided per design), it guarantees a good image quality for the reference dataset and a proper comparison and evaluation. Furthermore, it allows to isolate the influence of the trajectory choice onto the image quality, since the focal spot size and other effects (like scattering) are entirely avoided. However, since many simplifications are made for the simulation step, it is important to perform additional experiments using real measurements in order to verify the findings made with artificial data. This was performed in sec. 8 as well as sec. 9 and these further setups are introduced in the related sections, respectively.

For all simulations in this work the proprietary radiographic simulation tool aRTist (*Bundesanstalt für Materialforschung und -prüfung (BAM), Berlin, Germany*) was used, which utilizes an analytical process model and a ray tracing method [246]. Source-detector distance (SDD) and source-object distance (SOD) were kept constant, while the source position moves on the surface of a sphere surface centered around the test object. The polar angle ϕ describes the movement in-plane around the object, while the azimuthal angle θ refers to shifting the source position in vertical direction, so that $\theta = 0°$ corresponds to a planar trajectory and negative values indicate an inclined source position. The part was sampled in 5° steps each, ranging from $\phi = [0°, 5°, \ldots, 355°]$ and $\theta = [-85°, -80°, \ldots, 85°]$, where $\theta = \pm 90°$ was left out to prevent the same image being generated several times in rotated versions. This results in 72 arcs in horizontal direction containing 35 projections each and 2,520 poses in total. While being relatively simple to describe and handle, this definition leads to the clustering of projections at the proximity of both poles ($\theta = \pm 90°$), which poses a systematic error. However, this definition is necessary to allow for all trajectory designs introduced in sec. 6.5.2. This is important, since it is a central property of the evaluation framework that the optimized and all reference trajectories are defined from the same selection set and no projections (which are associated with new information) exclusive to some designs are introduced.

It shall be noted that geometrical restrictions of the acquisition setup can be taken into account by excluding unreachable projections from the simulated image stack.

6.4 Optimization Loop

6.4.1 Figure of Merit

In every iteration of the optimization loop the figure of merit is calculated for each projection in the evaluation set. This is accomplished in three steps: first, the prediction part of the framework estimates MTF and NPS for the projection combination under consideration, which is explained in sec. 6.4.2. Based on these data, the selected observer model, template and regularization the detectability index d'^2 is calculated according to eq. 3.62 (PW MO) or eq. 3.63 (NPW MO). Last, the selection criterion is computed by multiplication of d'^2 with the geometric weighting value of the respective projection, which is calculated after each iteration as described in sec. 6.4.3. These three steps take approx. 7 ms on the test system used for this work with 256 GB memory, two Xeon E5-2640 processors (each 6 cores with 2.5 GHz) and a Nvidia Geforce Titan X GTX graphics card. The figure of merit is calculated for each possible projection combination in the evaluation set. Subsequently, the combination with the highest value is added to the solution set and all parts of the framework including the weighting map are updated and prepared for the next iteration. The entire optimization framework is formulated in sec. C.2 as pseudocode.

The observer models are of fundamental importance for this work and are explained more thoroughly in chapter 3. The sphere and cylinder template functions in sec. 7 are relatively simple and were defined mathematically directly in the voxel grid. For all other investigations the full projection set was first reconstructed using the SART method. Next, the VOI was then extracted from the volume, parts not belonging to the feature were removed manually and finally the template was converted into binarized form using a single threshold value that was determined individually for each feature.

6.4.2 Image Quality Prediction

To compute the detectability d', numerical values for the pixel-wise (i.e., the *local*) MTF and NPS are required by the model observer. Theoretically, these expressions have to be determined from the reconstructed volumes. The NPS can be calculated by evaluating several VOIs and averaging the result. However, this assumes that the image properties are stationary over the entire domain and this approach does only permit to compute the *global* NPS. To obtain a local expression, it is necessary to determine an invertible covariance matrix (see sec. 3.7.2), which requires a vast number of reconstructions and measurements[1]. Computing the local MTF can be performed by introducing a dirac impulse into the originally imaged object and calculating the point-spread function (see sec. 3.3) [247], which is demanding in practice and particularly if measured data are used instead of simulated ones. These practical limitations also prevent the use of model observers as evaluation criterion so that alternative metrics, which are introduced in

---

[1]However, the dimensionality of the covariance matrix can be reduced by the use of channelized MOs so that considerably fewer measurements are required and the matrix inversion becomes practically feasible [82].

sec. 6.5.1, are used in this work. More detailed discussions related to the practical determination of local MTF and NPS can be found in the related literature [68, 247–250].

Instead of measurements, predictor functions will be used to compute the required expressions. In general, in order to obtain the image properties of the reconstructed image, it is necessary to solve the estimator for the image defined by eq. 2.14. Unfortunately, this estimator is given in implicit form, so that the solution cannot be obtained analytically but has to be found via iterative approaches. However, it was shown that by use of the implicit function theorem, the Taylor expansion, and the chain rule, approximations for the mean and variance of such implicitly defined estimators can be found that only rely on partial derivatives of the objective function [251]. Based on this finding, an estimate for the local impulse response can be expressed which depends solely on the measurement mean[2] and the objective function derivatives [252]. Further work finally yielded expressions valid for transmission tomography [253] and allowed for the efficient calculation of MTF and NPS at a particular position j within the volume by solving [254]

$$\mathbf{MTF_j} \approx \frac{\mathcal{F}\left(\mathbf{A}^{\mathrm{T}}\mathbf{DAe_j}\right)}{\mathcal{F}\left(\mathbf{A}^{\mathrm{T}}\mathbf{DAe_j} + \beta\mathbf{Re_j}\right)}, \tag{6.1}$$

$$\mathbf{NPS_j} \approx \frac{\mathcal{F}\left(\mathbf{A}^{\mathrm{T}}\mathbf{DAe_j}\right)}{\left|\mathcal{F}\left(\mathbf{A}^{\mathrm{T}}\mathbf{DAe_j} + \beta\mathbf{Re_j}\right)\right|^2}, \tag{6.2}$$

with the system matrix $\mathbf{A}$ introduced in eq. 2.13, Fourier transform $\mathcal{F}$, a diagonal vector $\mathbf{D}$ containing the measured pixel values of the respective projection and $\mathbf{R}$ being a quadratic regularization matrix as proposed in the literature [254]. The division is supposed to be performed element-by-element-wise and the regularization parameter β is typically determined empirically [190]. Note that the formulas here are discrete, while the equations describing the model observers are provided in continuous form in sec. 3.8. In the final implementation a trapezoidal approximation was used to calculate the integrals; see also sec. C.2 for the implementation of the optimization framework in pseudocode. The proper choice of β is dependent on many parameters (e.g., the number of projections, the object geometry, etc.) and important to obtain reasonable results. The selection of a suitable β is as far as possible avoided for the course of this work by performing a parameter sweep with subsequent selection of the best results according to the achieved image quality as described in sec. 6.5. The use of the PW MO is independent of the used regularization, which can be shown by plugging eq. 6.1 and 6.2 into eq. 3.62. The vector $\mathbf{e_j}$ encodes the evaluated voxel position, which is located at the center of the VOI, as a Kronecker delta function, i.e., the desired location entry is given as one and all other values are set to zero. Since the image properties are assumed to vary only minimally in close proximity to the evaluated position, the result is considered to be valid within the entire VOI. It shall be noted that a vast number of measures – in particular such concerning the explicit implementation – are necessary to facilitate the calculation of eq. 6.1 and 6.2. While a detailed discussion would lead

---

[2]For most investigations, including this work, instead of the actual measurement mean only a single measurement is conducted as estimate for the mean value. This can be justified since the applied combination of projection- and backprojection ($\mathbf{A}$ and $\mathbf{A}^{\mathrm{T}}$) acts in a smoothing fashion on the data, which makes the approach relatively robust towards noise [252].

very far and is therefore omitted at this point, a thorough derivation and analysis is provided in the literature [190, 254].

The expression $\mathbf{A}^\mathrm{T}\mathbf{D}\mathbf{A}$ is referred to as Fisher information matrix (FIM), which is precomputed with respect to the considered VOI for each projection before the actual optimization loop is entered. Since the FIM is essentially build by projecting a voxel on the detector screen, weighting it with the measured intensity values and projecting it back to the volume, it can be represented as a volume as illustrated in fig. 6.1. The implementation is based on projection models provided by the commercially available CERA 6.0 reconstruction framework (*Siemens Healthineers AG, Erlangen, Germany* [255]) and make extensive use of graphic card based computing. To obtain the FIM related to several projections in the solution, the respective single-projection Fisher information matrices can be summed up, which has to be performed in each optimization loop separately.

It shall be noted that the discussion provided here is highly simplified. For instance, the approximations were originally derived for penalized likelihood SPECT reconstructions that (unlike to eq. 2.14) include an additional regularization parameter [254]. Many further assumptions and simplifications are required to justify the use of eq. 6.1 and 6.2, which are beyond the scope of this work and discussed elsewhere [251, 252, 254]. The validity of the predictor functions have been further investigated for transmission-CT using simulations [247] and experimental measurements [256]. These estimates have been used in most MO-based trajectory optimization methods (i.e., approaches 10 , 12, and 13 in sec. 5.1) and other applications, for instance to improve spatial image properties by locally adjusting reconstruction parameters [247]. It needs to be stressed that the predictions are strictly speaking only valid for penalized likelihood reconstruction methods, while a SART algorithm is considered for this work. However, based on the considerations of sec. 4 it is assumed that valuable angles are mostly independent of the applied reconstruction approach, so that the use of predictor functions – even though they estimate the outcome for a different reconstruction technique – is still justified.

6.4.3   Geometrical Weighting

The geometric weighting step acts as the second part of the optimization criterion. Since dominant preferential directions can lead to optimized trajectories with very clustered acquisition poses, this method tries to enforce spreading out over larger parts of the available positions resulting in a higher coverage of the entire Fourier space. This property is referred to as angular variety for the course of this work and several implementation methodologies will be discussed in sec. 7.4.3. Sampling as much as possible of the Fourier space is usually necessary to prevent limited angle artifacts [244]. The weighting achieves a uniform sampling, which is considered to result in a more homogeneous image quality. A detailed discussion related to the consequences of sampling with reduced discrepancy is provided by Kingston et al. [23, 150]. Similarly, it has been suggested that for a fixed number of projections a sampling scheme with uniform sampling density and high data incoherence yields the most promising results [30]. Furthermore, projections located opposite to already picked ones are penalized by the algorithm to break symmetry effects, which reduces data redundancy and is known to improve the achievable image quality [126] (see also sec. 4.5). The criterion is implemented as a weighting map that assigns every projection a certain weighting factor $0 < \gamma < 1$, which is updated after each iteration of the optimization loop. The

multiplication of this weighting map with the result of the MO yields the final figure of merit.

The weighting map is initialized with $\gamma = 1$ for each projection. After the first iteration the weights are updated according to the following scheme: the picked projection itself is noted with a weighting factor of $\gamma = 0$, since it should not be added a second time to the solution set. All projections located within a 15° angle section are weighted with $\gamma_{\text{adjacent}} = 0.8$ and all projections in the opposed region (i.e., in an angular range of 172.5° to 187.5°) to the selected pose (including the directly opposed one) is weighted by a factor of $\gamma_{\text{opposed}} = 0.9$. This leads to a much lower clustering of projections and a higher angular variety. Furthermore, projections located directly at opposite sides of the object are less likely to be chosen in the subsequent optimization iterations. Additionally, a weighting factor of $\gamma_{\text{close}} = 0.2$ is assigned to very close projections in an one-sided angular range of 1°. All weights can only be overwritten if the new assigned value is lower than the old one. The respective weights were determined empirically and the pseudocode describing this part of the framework is provided in sec. C.1.

The last weighting factor γ_{close} was introduced to stabilize the results for experimental data sets. Since simulated projection sets are defined to have an angular spacing of 5° (sec. 6.3), this factor has no influence on these data. However, the acquisition pattern of real setups can lead to position clustering in other directions due to mechanical restrictions of the system, e.g., in the horizontal plane in case of the tilting table (see sec. 8.2). Selecting several of these very close projections would equal including essentially identical projection (just rotated around the SDD-axis) to the solution, which would lead to poor optimization results.

6.5 Evaluation Method

To quantify the performance of the solution, the optimized trajectory is reconstructed at predefined projection numbers, which are defined in sec. 6.5.2. As reconstruction algorithm a modified SART approach is used, which is implemented and provided via CERA. The algorithm is outlined in sec. 2.3.3 and alternatives for future use are discussed in sec. 11.2.4. The method was selected due to its good performance in the presence of noise, undersampled data, and irregular sampling conditions [36, 55, p. 201] as well as its property to only yield positive voxel values which is relevant for evaluations using the structural similarity index (sec. 6.5.1.2). The volume sizes are provided in sec. B. The proposed evaluation framework has been published in detail in a separate work [136].

The image quality of the optimized trajectory is then calculated with respect to the quality measures defined in sec. 6.5.1 and compared to the performance of standard trajectories, which are introduced in sec. 6.5.2 and act as baseline reference. It is important to highlight at this point, that for the sake of a more robust comparison several representative trajectories of each design are computed and averaged, while the optimized trajectory is determined by computing several optimized trajectories with different regularization parameters and selecting the best performing one among them. While this could in theory be viewed as a brute force approach, where several random trajectories are generated and only the highest rated one is considered to be the solution, in practice typically only few or even just one regularization is sufficient to obtain the optimized trajectory for a certain projection range. However, the ideal regularization strength is not known before the optimization of new datasets, which

makes the parameter sweep necessary. Furthermore, the parameter selection can be considered to be a part of the optimization algorithm itself and can improve the results, since the optimized trajectory for a given number of projections can be different but do not need to include the poses of such with lower projection numbers (see for a similar discussion also the definition of PC and LDS trajectory in sec. 6.5.2). For this work the influence of the regularization is therefore neglected for convenience and treated as computational demanding but necessary step in the optimization framework.

6.5.1 Image Quality Metrics

In order to quantify the performance of different trajectories and their influence on the image quality of the reconstructed volume the use of appropriate image quality metrics is necessary as indicated in the problem formulation in eq. 4.14. Generally, the selection of suitable metrics depend on the purpose of the investigation and no criterion exhibits universal explanatory power for all applications and circumstances. Therefore, for this work two different measures are used to evaluate different aspects of the image assessment task: the root-mean-square error (RMSE, sec. 6.5.1.1) will be used as well-established, objective method to express the difference between two volumes while the structural similarity index (SSIM, sec. 6.5.1.2) is a simple criterion and aims to relate the results to the subjective human image perception. This choice of the metrics intends to establish a relationship to manual flaw detection as performed by a human observer while still assuring objectivity and comparability.

Both metrics directly operate on the voxel information and have been widely used for the image assessment of volumetric CT data. Furthermore, RMSE and SSIM are difference-based figures of merit that require a reference volume to relate to, which is the reconstruction generated by including all available projections as apparent from the right term in eq. 4.14, which is supposed to become minimal. This reference, which will be referred to as the full reconstruction from now on, is consequently considered to achieve the maximum obtainable image quality and outperforms all reconstructions generated by every possible projection subset. As discussed in sec. 4.5 and sec. 10.6 this is a strong assumption that is not necessarily true [126]. However, this work concentrates on reconstructions obtained by significantly fewer projections than this reference and it appears reasonable to assume that the image quality difference is sufficiently high to neglect this factor. Both metrics are very prone to registration errors, which is completely avoided since subsamples from the same data set are used which leads to all possible reconstructions being already perfectly aligned (see also sec. 6.5.2). This is a considerable advantage to many practical studies, where it is often required to reposition the volume correctly. While this is often not very critical due to the high material contrast and good image quality for industrial CT, it becomes particular severe for medical investigations where the object shape is likely to change between two scans, so that often additional tracker points or more sophisticated methods are required [257].

6.5.1.1 Root-Mean-Square Error

Probably the most widely used and direct image quality indicator the root-mean-square error (RMSE) defined as

$$\text{RMSE}(\mathbf{A}, \mathbf{B}) = \sqrt{\frac{1}{n} \sum_{i=1}^{n} \left(\mathbf{A_i} - \mathbf{B_i}\right)^2}, \tag{6.3}$$

where n is the total number of voxels and $\mathbf{A_i}$, $\mathbf{B_i}$ denoting a particular pixel in the evaluation and reference volume, respectively. According to this definition the RMSE equals zero if both volumes are identical and can in theory reach arbitrary high values, which are, however, bound in practice by the dynamic range of the voxel elements. Other widely used metrics comprise the mean-squared error (MSE) and the peak signal-to-noise ratio (PSNR), which are in essence differently scaled versions of the RMSE.

The RMSE is symmetric and the standard criterion for image and signal quality assessment [258, 259] and serves as a widely established and accepted metric that allows comparison to the results of other studies. However, it also exhibits some disadvantages that can turn out problematic under certain circumstances. For instance, it has been pointed out by some researchers that the use of the RMSE inherently assumes that several strong implicit assumptions hold, which are typically not fulfilled. Furthermore, it correlates extremely poorly with the human perception [260], is very unstable with respect to registration errors, and cannot differentiate between different forms of image degradation [70, p. 7f].

6.5.1.2   Structural Similarity Index

Due to the drawbacks mentioned in sec. 6.5.1.1 a second metric is required to relate the obtained quality to the human image perception. This is generally a very demanding task and several evaluation approaches have been suggested with the manual rating performed by human test subjects being the most obvious one. However, this method is obviously not feasible for most applications owing to the numerous required evaluations and the linked high manual effort, so that alternatives are necessary [258]. In the last decades several sophisticated metrics based on models of the human visual system have been proposed [261]. While being typically rather complex and nonlinear [258] they have been shown to relate usually well with human performance [262]. Unfortunately, among other limitations [263] this complexity has turned out to be a severe drawback and has led some researchers to the conclusion that these metrics have become too complicated for practical applications and particularly for algorithm optimization purposes [264].

However, as a comparably simple metric not based on such models is the structural similarity index (SSIM), which was developed to overcome the typical limitations of pointwise difference metrics, has turned out to agree sufficiently well with human perception and is widely used today. The index is based on the assumption that the human visual system is highly adapted to extract structural information and uses the variation of it to quantify the degradation of image quality. To accomplish this, it separately evaluates luminance, contrast and combines it into a single figure of merit [263].

Given images $\mathbf{A}$ and $\mathbf{B}$ defined analogously to sec. 6.5.1.1, the luminance comparison function $l(\mathbf{A}, \mathbf{B})$ is given with [263]

$$l(\mathbf{A}, \mathbf{B}) = \frac{2\mu_A\mu_B + C_1}{\mu_A^2 + \mu_B^2 + C_1},$$

(6.4)

where μ_A, μ_B are the mean signal intensities of the images and C_1 is a constant to avoid instability if the denominator approaches zero. It is defined as $C_1 = (K_1 L)^2$, with L being

the dynamic pixel value range (e.g., 255 for 8 bit grayscale images) and K_1 a sufficiently small constant $\ll 1$. Next, the contrast comparison function $c(A, B)$ is defined as [263]

$$c(\mathbf{A}, \mathbf{B}) = \frac{2\sigma_A \sigma_B + C_2}{\sigma_A^2 + \sigma_B^2 + C_2}, \tag{6.5}$$

with σ_A and σ_B being the image standard deviations of the mean signal intensities and C_2 is defined analogously to the luminance comparison as $C_2 = (K_1 L)^2$, with L being the dynamic pixel value range and regularization parameter $K_2 \ll 1$. After subtracting the mean luminance and normalization of the contrast the signals $\sum_{i=1}^{n}(\mathbf{A_i} - \mu_A/\sigma_A)$ and $\sum_{i=1}^{n}(\mathbf{B_i} - \mu_B)/\sigma_B)$ are obtained and the structure comparison function $s(\mathbf{A}, \mathbf{B})$ can be defined, which is given by [263]

$$s(\mathbf{A}, \mathbf{B}) = \frac{\sigma_{AB} + C_3}{\sigma_A \sigma_B + C_3}, \tag{6.6}$$

with the regularization constant C_3 and σ_{AB} being the correlation coefficient, which is defined as

$$\sigma_{AB} = \frac{1}{n-1} \sum_{i=1}^{n} \left(\mathbf{A_i} - \mu_A\right)\left(\mathbf{B_i} - \mu_B\right), \tag{6.7}$$

with total number of pixels n. The three comparison functions can then be combined generally as

$$\mathrm{SSIM}(\mathbf{A}, \mathbf{B}) = l(\mathbf{A}, \mathbf{B})^{\alpha} \cdot c(\mathbf{A}, \mathbf{B})^{\beta} \cdot s(\mathbf{A}, \mathbf{B})^{\gamma}, \tag{6.8}$$

with weights $\alpha, \beta, \gamma > 0$. For simplification of the formula, these values are usually set to 1 and for the particular choice of $C_3 = C_2/2$ the final, typically encountered form of the structural similarity can be obtained as [263]:

$$\mathrm{SSIM}(\mathbf{A}, \mathbf{B}) = \frac{(2\mu_A \mu_B + C_1)(2\sigma_{AB} + C_2)}{(\mu_A^2 + \mu_B^2 + C_1)(\sigma_A^2 + \sigma_B^2 + C_2)}. \tag{6.9}$$

The SSIM is symmetric and reaches values between 0 and 1, with the latter only being feasible if both compared images are identical. Theoretically, also negative values are possible if one image is inversely correlated to the other one, which is typically not the case for real applications. In this work the regularization constants were selected to equal approx. 1 % of the typical attenuation value to prevent any relevant influence on the evaluation results. Furthermore, to calculate this metric a Gaussian-weighted sliding window with a standard deviation of 4 pixel and a two-sided search range of six standard deviations is used and averaged to obtain the final value of the SSIM.

It shall be noted that among other variations [264–267] an earlier version of the SSIM referred to as universal quality index (UQI) exists, for which all regularization constants are set to zero [259]. Both, the SSIM [12, 30, 92, 180, 192, 268–271] and the UQI [109, 181, 182, 272] have been previously used as image quality criterion for assessing CT volumes.

6.5.2 Reference Trajectories

While it is important to quantify the image quality with respect to the selected trajectory, it is also necessary to have a baseline reference to relate to. For this purpose several benchmark trajectories shown in fig. 6.3 and 6.4 have been defined that should
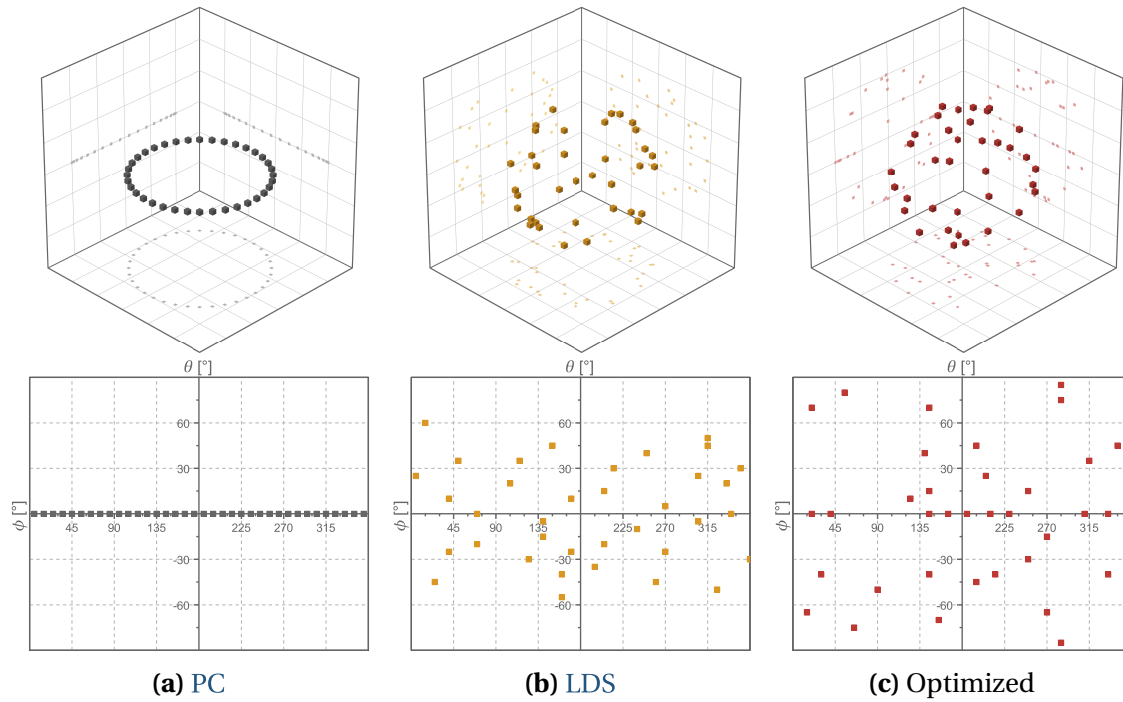
(a) PC **(b)** LDS **(c)** Optimized

Figure 6.3: The most frequently used trajectory designs in this work. Shown are source position representatives with 36 projections for the planar circle (PC, fig. 6.3a) and low-discrepancy spherical trajectory (LDS, fig. 6.3b), which are used as two- and three dimensional reference. For comparison an optimized trajectory (feature-based NPW MO with geometric weighting for the cylinder VOI of the batphantom) is shown in figure 6.3c.

be outperformed by a successfully optimized trajectory. Each benchmark trajectory depends on the selected number of projections, the implementation of the respective trajectory design and a shift parameter. While it is theoretically possible that a particular implementation of a benchmark trajectory outperforms all other designs by chance the shift parameter allows the generation of several trajectories with the same projection number and design that allow statistical analysis and diminishes the influence of such outliers.

To speed up the calculations, reference reconstructions were only performed at distinct projection numbers, which are defined in steps of four projections (i.e., 4, 8, 12, 16, …) until 72 projections, which equals all positions located in the horizontal plane. The step size was then first increased to ten until 200 projections and then to 100 until 2,400 projections. The finer step size for low numbers was selected since this region is of particular interest for this work and the rate of quality change is steepest in this region [11,12,126,130]. It shall be noted that not equally many shifted trajectories can be defined for each projection number with the proposed method. This means that fewer samples exist for higher projection counts, which increases the calculated standard error of the mean (SEM). However, this effect is mitigated to a certain degree since the direction dependency of a part is highest at low projection numbers [122] where more samples can be provided. Since the projection pool of available projections consists of a limited amount of discrete feasible poses some compromises at the definition of each design were necessary that will be briefly explained in the following while a detailed contemplation can be found in the literature [136].

(a) IC　　　　　　　　　　　　　　**(b)** HCA
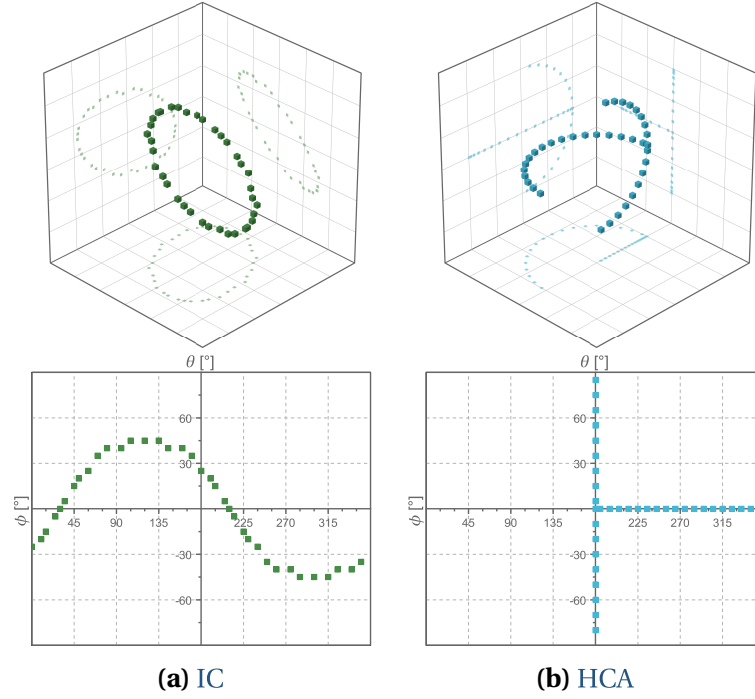
Figure 6.4: Acting as additional spherical reference trajectories, the inclined circle (IC) and half-circle and arc (HCA) trajectory are used together with the designs previously introduced in fig. 6.3 for benchmarking.

6.5.2.1　Planar Equidistant Trajectory

The most often used standard trajectory for industrial CT systems is a full planar circle (PC, fig. 6.3a) trajectory where all n projections are located in equiangular steps with azimuthal angle $\theta = 0°$. Consequently, a set consisting of $\lfloor 72/n \rfloor$ entries denoted as $s \in [0, 1, \ldots, \lfloor 72/n \rfloor - 1]$ shifted PC trajectories is defined by a start angle $\alpha_0(s) = s \cdot 5°$ that serves as offset parameter and an angular increment $\Delta\alpha = \lfloor 2\pi/n \rfloor$, where $\lfloor \cdot \rfloor$ denotes a rounding towards zero. The finest possible $\Delta\alpha$ equals 5°, which is considered to be sufficient, since it was shown that reconstructions stemming from small offsets yield similar results [122] so that an improved sampling would not provide further benefits.

Since the sampling is performed on discrete poses, $\alpha_0 < \Delta\alpha$ must hold to prevent defining identical evaluation subsets and the number of trajectories in each sets for a given projection number n decreases with increasing n. For values $n > 36$ only one trajectory can be defined, i.e., no error bars can be provided anymore for higher choices of n. It is important to highlight that with this definition projections can be added or removed from the set, i.e., each trajectory design does not necessarily contain all projections that are included in its realization with a smaller number of projections, which means that there is no need for the information content to increase monotonously with n. In particular for few projections this property can lead to jumps and a high standard error in the quality plots, which has also been observed in related work [131, 206]. Since 72 projections are located in the horizontal plane, this trajectory can only be defined until this number and no results are provided for higher projection numbers.

71

6.5.2.2 Low-Discrepancy Spherical Trajectory

The low-discrepancy spherical (LDS, fig. 6.3b) trajectory was motivated by statistical sampling point distributions for Monte Carlo simulations and serves as a three-dimensional equivalent to the PC trajectory. The definition of this design is more complex and outlined in a separate work [136] as well as in pseudocode in sec. C.3. In principle, the surface of a sphere is mapped onto a two-dimensional grid and samples according to the pseudorandom Halton-sequence are iteratively drawn which are then rounded to the nearest feasible position that is provided by the full projection dataset. The sequence starts at a multiple of an offset parameter and a correction term is included to compensate for pole clustering phenomena. After the desired number of samples is drawn, the plane is mapped back to the sphere surface and values for ϕ and θ are extracted. This design is defined in such a way that its information content increases monotonously and a uniform angular sampling is achieved, which leads to a smoother trend in the quality plots. This trajectory design can be calculated for arbitrary projection numbers.

6.5.2.3 Inclined Circle Trajectory

The inclined circle (IC, fig. 6.4a) is defined analogous to the PC trajectory. Instead of an angular offset parameter, the intersection point with the plane defined by $\theta = 0°$ is varied while the inclination angle is fixed at 45°. This trajectory can be interpreted as a PC where the investigated object is positioned with this angular tilt and can be defined until the same maximum number of projections.

6.5.2.4 Half-Circle and Arc Trajectory

For the generation of the half-circle and arc (HCA, fig. 6.4b) trajectory, half of the desired number of projections n is distributed equiangularily in a half circle and the other half in another half circle perpendicular to it, where both part trajectories are defined analogously to the PC trajectory. Results can in theory be provided for up to 70 projections, since 36 poses form a half circle, up to 35 ones are located on one vertical arc and one point appears double as intersection point. However, due to the defined step size only results for up to 68 projections are provided.

7 | Optimization Criterion

In sec. 3 expressions for the prewhitening and non-prewhitening model observer were derived. In this section the influence of the choice of MO and signal template will be evaluated. Furthermore, the weighting map as part of the final figure of merit was introduced in sec. 6.4.3. By variation of all three parameters (type of model observer, choice of template function, and use of geometric weighting) three important properties will by identified in this chapter that are considered to be essential in order to achieve high image quality and a stable trajectory optimization method. While modified versions of observer models have been proposed – for instance by the use of an additional noise source, an eye filter imitating a human observer or less calculation-heavy channelized MOs – these methods are beyond the scope of this work. The same is valid for two-dimensional (i.e., slice-wise operating) pendants. However, preliminary investigations [130] have included such variants as well and demonstrated inferior performance for trajectory optimization. While all plots in this work are color-coded (see tab. A.2 in the appendix), this property is particularly relevant to distinguish different parameter combinations as shown in this chapter.

7.1 Prewhitening and Non-Prewhitening Model Observer

As a first variation, the performance of the PW in relation to the NPW model observer is investigated. For this, the signal template ω was initially set uniformly to one. The resulting plots shown in fig. 7.1 consist of both resulting optimized trajectories together with the PC and LDS reference trajectory according to the workflow described in chapter 6. Image fidelity curves such as this one, which will be used frequently in the course of this work, are in particularly important for qualitative interpretation. The data are shown as quasi-continuous curves for better presentability, but are actually discrete as discussed in sec. 6.5. From the plots it is apparent that the PW MO performs significantly worse than the NPW MO for almost all projection numbers. It is known that the NPW MO shows basic agreement with the performance of human observers over a broad range of imaging conditions [190], while the PW model is usually used to quantify maximum achievable results [50, p. 829], turning it unsuitable for trajectory optimization. As a consequence, none of the MO-based methods outlined in sec. 5 make use of the PW model, but use exclusively the NPW observer.

Due to the poor results obtained with the PW MO it is excluded from further discussions for convenience. However, all parameter combinations were also performed with this model, which yielded, without exception, clearly inferior results to the NPW MO. Experimental findings are shown in sec. 8 and further results are provided in sec. D.2 for transparency. However, the performance of both optimized trajectories investigated in
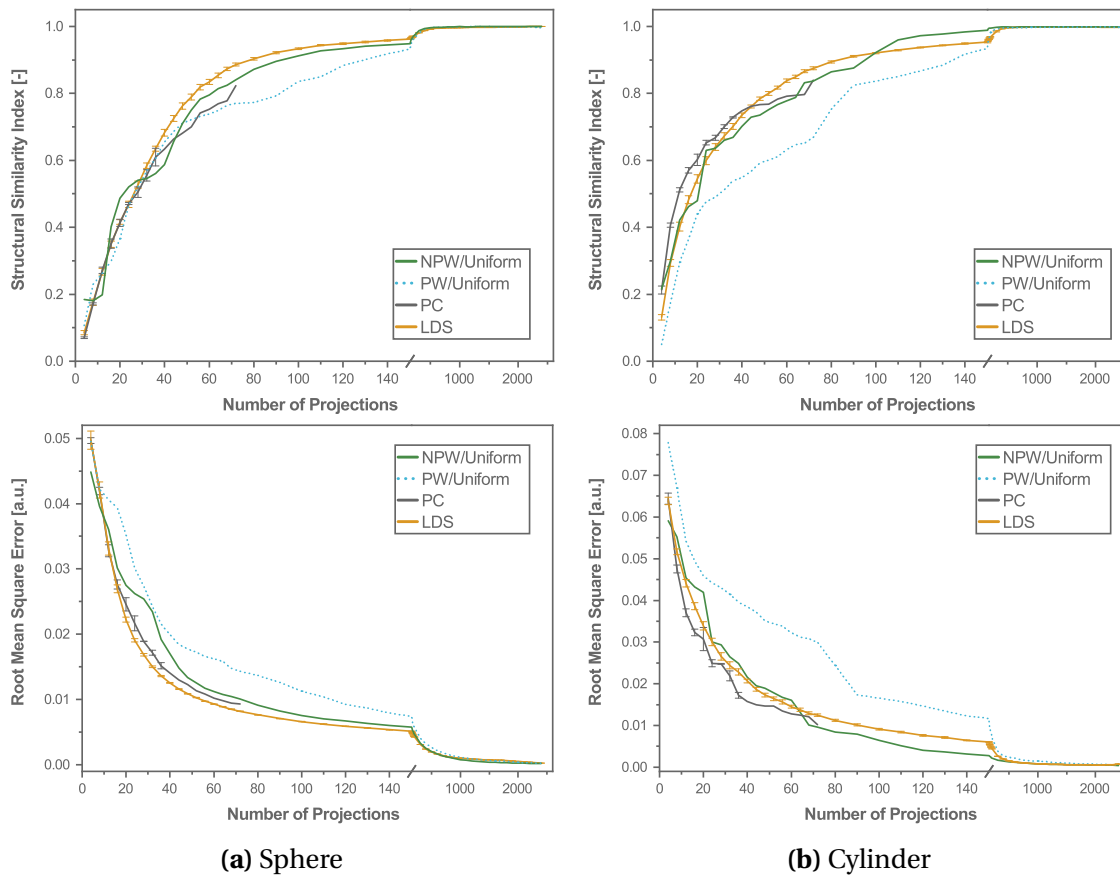
Figure 7.1: Comparison of results for the NPW and PW model observer for sphere (left, fig. 7.1a) and cylinder (right, fig. 7.1b). For most projection numbers the NPW clearly outperforms the PW. Nevertheless, in most cases the image quality of the reference trajectories is still better than both observer models.

this section is generally still very poor and outperformed by the LDS and for some projection ranges even the PC trajectory. These unsatisfactory results of the PW MO have already been shown in a separate work [130], which was restricted to planar trajectories.

7.2   Uniform and Feature-Specific Templates

Since the results using a uniform template are insufficient, a new optimization run was performed using a feature-derived template. For this, the sphere and cylinder object were defined on a voxel grid in binarized versions and used as signal templates for the optimization framework. In contrast, for more complex features in this work such templates were generated by cropping and thresholding the respective VOI from the full reconstruction (see sec. 6.4.1). By providing this additional input, the model observer gains access to a part-dependent signal template and does not rely solely on the information provided by the projection images and the location. As apparent from the results in fig. 7.2 this leads to a remarkable improvement of the optimization results. The use of feature-based templates does not only clearly outperform the trajectories related to the uniform one but results also in a similar or better image quality than the PC or LDS trajectory for a broad range of projections.

74

(a) Sphere   **(b)** Cylinder
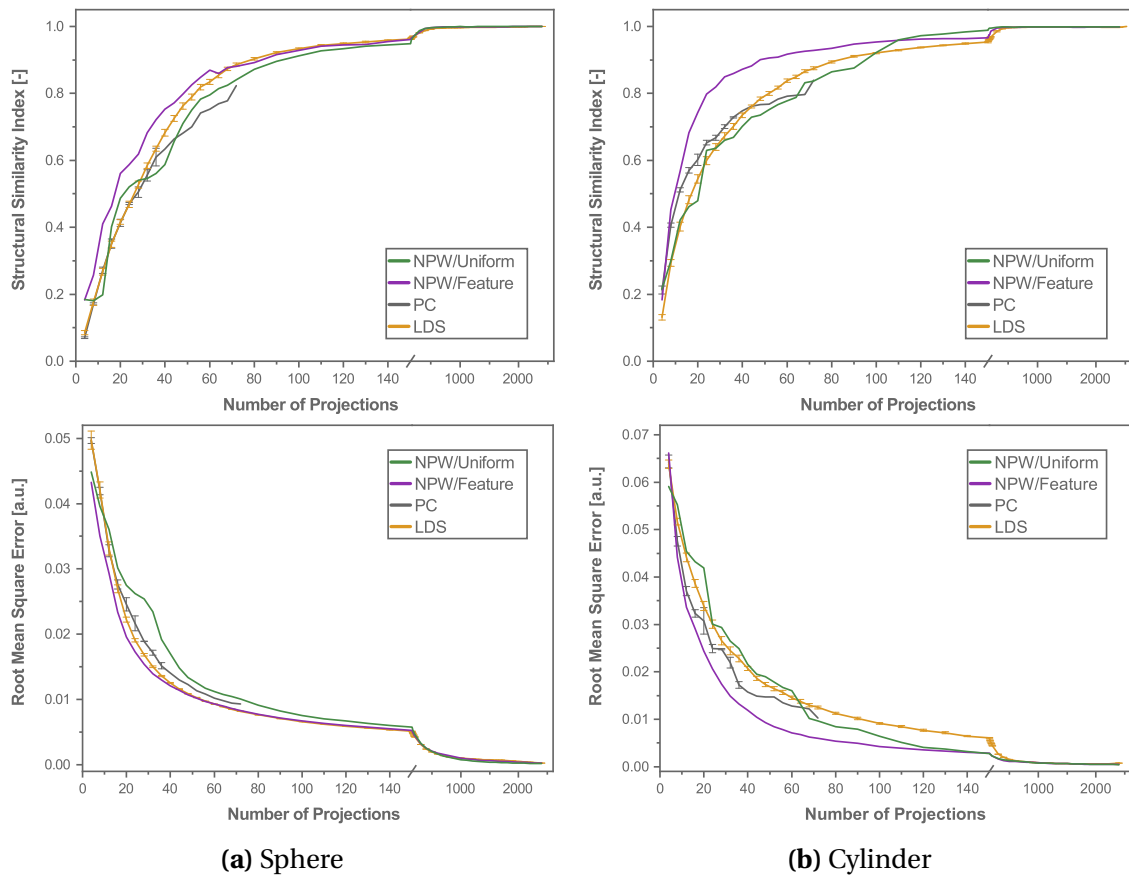
Figure 7.2: Comparison of uniform and feature-based NPW MO. The use of a part-specific template significantly improves the image quality associated with the optimized trajectory and performs equally well or better for all projection numbers than the benchmark.

The improvement can be seen as a direct result of the considerations of sec. 4.3. While the uniform template acts on the entire Fourier space, the feature-based MO assigns additional weight to the frequencies that are associated with the feature in the VOI and can cover these parts of the spectrum more efficiently. It shall be noted that the combination of NPW MO and feature-weighting is the typically used one for all MO-based trajectory optimization approaches in the literature [187–193, 195]. The only counter example is the work of Fischer et al. [22], for which good results have been reported using also a uniform template. Their results contradict the findings provided in fig. 7.2. This might be caused by the different reconstruction method used in their work, which is more appropriate with respect to the used predictor functions. It is also possible that the test parts used in their investigation coincidentally have few and clearly defined preferential directions, so that a purely SNR-based approach is sufficient by chance.

7.3 Influence of the Geometrical Weighting

In section 6.4.3 the geometric weighting method was introduced, which reduces the clustering of projections that is related to limited view angle artifacts and tries to enforce a more homogeneous distribution over the entire range of available positions.

75

(a) SSIM for Engine Part

(b) RMSE for Engine Part
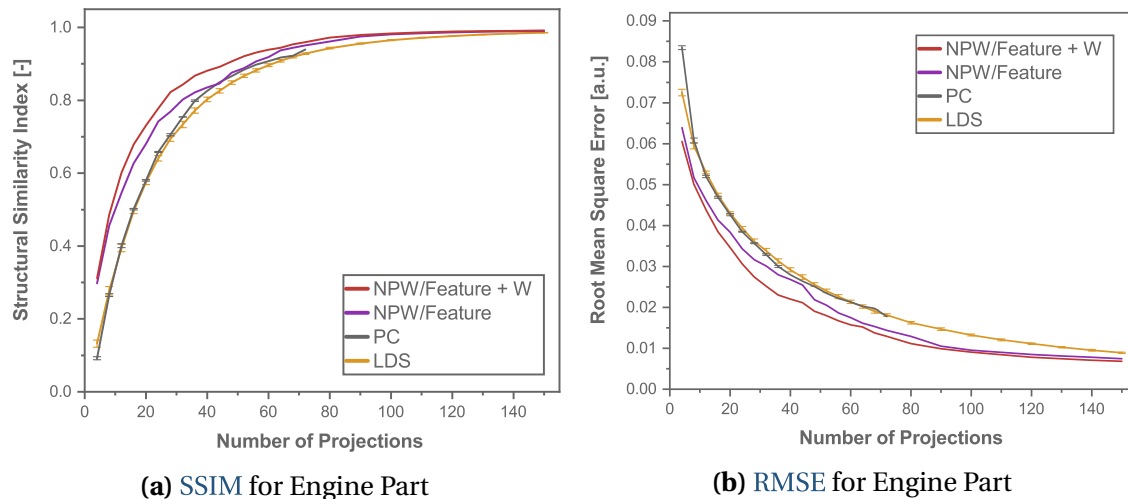
Figure 7.3: Optimization results for the KUKA robot engine using a NPW MO with and without geometric weighting function. While for signal templates without clear preferential direction angular variety is typically automatically achieved, the additional weighting step can further improve the image quality for other objects.

However, the results for a weighted NPW MO are almost identical to the outcome of the unweighted one (see sec. D.3 and 7.2), irrespective of the used evaluation metric. For all other parameter combinations, i.e., the uniformly weighted NPW MO (sec. D.1) as well as the PW MOs with uniform or feature-specific template (sec. D.2 and fig. 7.1) the geometric weighting clearly improves the results. In these cases the solely MO-based figure of merit did not perform well but the image quality improved when at least a certain degree of angular variety was achieved. As discussed in sec. 4.3 an infinite number of one-dimensional parallel tangents to a two-dimensional plane exists and consequently several solutions that are similarly correct. If the optimization using an MO is considered to find such tangents[1], the geometric weighting decides in favor of some (i.e., such that provide angular variety) of these possible solutions without introducing new ones. This might explain why the use of the weighting function typically does not reduce the outcome of the optimization but performs at least equally well.

However, as mentioned above the weighted and unweighted NPW MO performed almost equally which can be attributed to their relatively simple shape and lack of dominant edges. Due to this, for both VOIs angular variety is already achieved without the additional use of the geometric weighting, so that no difference is observable in image quality. In order to illustrate the beneficial effect of the geometric weighting, a different, more edge dependent datset was used. The optimizations concerning this example have been separately published and the interested reader is referred to the respective investigations [129] for more details concerning the workflow or the test objects. In the related work it was also shown that the image quality for both, VOIs located at the surface or within the part, can be improved by the proposed trajectory optimization. The new optimization task is an industrial robot, which features a round manipulation head and an engine VOI. For the investigation in this section the engine VOI was used, which features few, but very dominant edges. This feature was also used

---

[1]This is highly simplified since the MO consider more information than the location of edges in space, for instance the SNR. For the sake of a more illustrative explanation its validity is nevertheless assumed at this point.

in addition to the symmetric head VOI in sec. 10.5. As shown in fig. 7.3, the weighting function improves the image quality with respect to the unweighted model observer. This observation holds for all considered projection numbers. It shall be noted that a similar investigation as the one outlined in this section has recently been performed by other researchers [195], with their results being in agreement with the results provided in this section (see also sec. 7.4.3). As the weighted NPW MO with non-uniform feature template is considered the most promising parameter combination it will be the primary choice for the remaining part of this work.

7.4 Comparison to the State of the Art

Building on the results provided in the last sections, three important properties can be identified that are required to accomplish an effective trajectory optimization and achieve high image quality. Remarkably, it can be shown that almost all[2] existing approaches outlined in sec. 5.2 make directly or indirectly use of one or several of these characteristics as summarized in tab. 7.1. Since the criteria are implemented very differently in other trajectory optimization algorithms, a short overview will be provided in this section. Furthermore, as already outlined in sec. 5.1 and sec. 6.5.2, several standard trajectories exist that are occasionally applied for industrial CT imaging. Since the use of an optimized trajectory can only be reasonably justified if it offers an improvement to the status quo – which is given by part-independent designs – a comparison to the most frequently used ones that can be investigated with the proposed evaluation approach (chapter 6) is performed in sec. 7.4.4.

7.4.1 Contrast and Noise

The property of achieving a good SNR is probably the most straightforward one to be accomplished and is typically already used in industrial practice as CT operators usually attempt to achieve an object positioning that results in the lowest amount of material in the X-ray path. As such, the approach of Herl et al. considered the condition of a good SNR by introducing a gray value threshold in the projections, i.e., very high attenuating directions are per default excluded from possible solutions [175]. Similar methods aiming either towards minimizing the sum of attenuation values or the X-ray pathlength through the object (which is equivalent for monomaterial objects) are used by other algorithms [18, 160, 163–165]. Even simpler than those, Grace et al. defined regions of highly attenuating material and treated every ray passing through this area automatically as one with poor SNR that should be avoided [176]. Wu et al. made use of a figure of merit that was defined as the sum of all attenuation coefficients over the X-ray intersection length. As alternative, the so called spectral shift was proposed, which was defined as the discrepancy between the measured attenuation given a mono- and polychromatic source [170, 171]. However, this discrepancy will also be typically higher for long paths through the object, so that a similar result is achieved. Another formulation of this property is provided by Kano et al., who aimed to maximize the visible area of high density material in a single projection [166]. Since maximizing this

---

[2]If approaches based on the image quality quantification of reconstructed solution candidates are included, which can be reasoned as outlined in sec. 7.4.1, even all methods discussed in this work rely on these three criteria.

Table 7.1: Overview of the approaches from sec. 5.2 and the explicitly used properties for trajectory optimization. The numeration is derived and identical to tab. 5.2. While almost every method in the literature relies on at least one condition identified in this chapter, only method 13 and the one proposed in this work fully satisfy all criteria. Reconstruction-based image quality assessment was not considered as SNR-related method for this table.
[1] Not explicitly stated (see full text).
[2] Depending on detailed implementation and objective function.
[3] Assured by the side condition of a smooth trajectory.
[4] Assuming the use of an object-specific template function.

Approach	High SNR	High Fourier Coefficients	Angular Variety	Source
1	Yes	Yes	Partially[1]	[160]
2	No	Yes	Yes	[161]
3	Yes	No	Yes[2]	[18, 163–167]
4	Yes	No	Partially[3]	[170, 171]
5	Yes	No	Yes	[19, 175, 177]
6	Yes	No	Yes	[176]
7	No	No	Yes	[179]
8	Yes[2]	No	Partially[3]	[180–183]
9	No	No	No	[186]
10	Yes	Yes	Partially[3]	[187–191]
11	Yes	Yes	Partially[3]	[192, 193]
12	Yes	Yes[4]	No	[22]
13	Yes	Yes	Yes	[195]
14	No	Yes	Yes	[179]
15	No	No	No	[14, 15, 196]
16	No	No	Yes	[197]
17	No	Yes	No	[198]
Own	Yes	Yes	Yes	[129, 130, 199]

area also means that such highly attenuating materials are not located along the same X-ray path in this particular projection, long pathlengths of highly attenuating material are indirectly avoided.

As outlined in detail in chapter 3, all model observer based methods (approaches 10, 11, 12 and 13) are based on MTF and NPS and therefore reflect the SNR as well. Furthermore, it has been noted that a well-reasoned selection of projections is particularly important for high noise levels in imaging via MRI [131]. As part of one of the objective functions proposed by Hatamikia et al., the three-dimensional point spread function is applied, which is directly linked to the contrast and noise levels (see sec. 3.3). Other figures of merit for trajectory optimization are derived by comparing the reconstructed volume of a certain evaluation set to a reference reconstruction [180–182], which was used in this work solely for evaluation purposes. While it is reasonable that such an evaluation – that is similarly also used by other studies (for instance approach 14) – includes information concerning the SNR of the reconstructed projections, it does not directly target this property and is not considered in tab. 7.1.

7.4.2 High Fourier Coefficients

Contrary to the condition of a high SNR, this property is probably the least frequently used principle. Nevertheless, for instance, all model observer based methods use a matched filter that includes the part geometry and aims particularly towards including high components in Fourier space, which holds for approaches 10, 11, 13 and this work. As such, also the method of Fischer et al. holds this property. However, in their work the signal template was in some cases selected to be uniform in order to be suitable for arbitrary objects without further parameter adjustment [22]. The results provided in sec. 7.2 show that this choice is generally not recommended since significantly better results can be achieved by defining a template function.

The approach of Barkan et al. [198] uses the highest coefficients of a Ridgelet transform instead of the Fourier transformation for their optimization method, which is considered to result nevertheless in a similar effect. The first method proposed by Haque et al. (approach 14) backprojects each projection into the volume, applies a two-dimensional Fourier transform on it and sums the resulting entries parallel to the detector plane [179]. This is equivalent to finding projections that contain high Fourier coefficients over the entire frequency spectrum and – if the entire object and not just a small VOI is considered – acts as part-dependent Fourier weighting. The method is very similar to the concept of amplitude-summed Fourier coefficient (ASFC) maps that will be introduced in sec. 10.2. However, for the ASFC the object itself is considered, while the optimization approach is projection-based.

As alternative, some approaches optimize the acquisition trajectory by selecting projections that correspond to rays that are tangential to the object edges [160, 161], which is also equivalent to including high Fourier coefficients (see also sec. 4.3). For this purpose the Hough or wavelet transform have been applied, which are widely used in image science. The method proposed by Heinzl et al. and Amirkhanov et al. aims towards minimizing parts of the object for which the Tuy-Smith condition is not fulfilled, therefore avoiding cone beam artifacts for these regions [163, 164]. Consequently, this means that the acquisition angles are adjusted in such a way that in particular high Fourier coefficients are sampled. It shall be noted that the use of a criterion that exploits the property of high Fourier coefficients is considered to be unsuited without the additional use of a SNR-based figure of merit, since parts of the Fourier space that are lost due to very low SNR are treated as available, which can lead to severe artifacts and even decrease image quality to values lower than the part-independent reference trajectories.

7.4.3 Angular Variety

The geometric weighting introduced in sec. 6.4.3 and investigated in sec. 7.3 aims towards sampling the Fourier space as uniform and complete as possible with respect to the given number of projections. Some methods [189, 192] optimize one position per circular increment, for instance in order to achieve a smooth acquisition trajectory that can be mechanically implemented relatively uncomplicated for certain setups. Using the terminology of this work this procedure equals finding the best θ-coordinate for each available ϕ. It is obvious that angular variety – at least in the horizontal plane – is automatically achieved by such approaches. However, angular variety is not necessarily fulfilled in the vertical plane and related methods are indicated accordingly

in tab. 7.1. Contrary to this, the proposed trajectory design of Kingston et al. aims towards minimizing the degree of redundancy in adjacent projections for three spatial directions. The authors argue that their design fulfills a discrete version of the Tuy-Smith criterion (sec. 4.1), uses more information due to a more efficient apodization window, and tries to maximize isotropy in order to obtain a uniform resolution [23]. The geometric weighting function (sec. 6.4.3) targets all these properties as well, even though being probably less efficient than the more direct Tuy-based approaches. Similarly, for a switched source X-ray system it was found that a sampling pattern that generates a uniform ray density and angular distribution per voxel results in particularly good reconstruction results [273]. For planar trajectory optimization a related concept has been used in both approaches of Haque et al., which include a maximum angular step size to assure that a certain minimal spread over the plane of feasible projections is always achieved [179]. The method of Matz et al. also includes a weighting function that aims to avoid projection clustering [161].

As already mentioned in sec. 5.2, different further methods [175, 176, 195] have been developed to directly quantify the degree to which Tuy's condition is locally fulfilled, which was used in the trajectory optimization approach of Herl et al. High local values of this quantitative Tuy criterion result in similar properties like the geometric weighting function and angular variety can be achieved [175]. The approach of Herl et al. is of particular interest, since it was used later together with model observers and compared to a purely MO-based method, which is essentially the same investigation as carried out in sec. 7.3. For this particular optimization the opposed positions were not included in the projection pool, therefore avoiding the need for a separate treatment of such poses entirely. Their results confirm that the additional weighting provides better results [195], which is in agreement with the findings of this work. Furthermore, their method is considered to be the only other one that is able to fully optimize all three criteria shown in tab. 7.1.

Jørgensen et al. found that acquiring many angular projections is clearly beneficial, even if the SNR per projection needs to be lowered to achieve this [127] (see also sec. 4.5). Interestingly, these findings contradict the results of several other studies conducted by Sollmann et al. and Rayudu et al. [31–33]. A possible explanation is that these studies were performed for medical CT and are likely to differ considerably in the choice of imaging parameters. Unfortunately, since only the relative and not the total number of projections is reported, no direct comparison to the work of Jørgensen et al. is possible. However, it is not improbable that the benefits of achieving angular variety only become relevant for higher projection numbers when the most important parts of the Fourier space have already been sufficiently covered, which would explain the discrepancy if Sollmann et al. and Rayudu et al. used a higher number of projections as ground truth. In addition, Jørgensen et al. chose the "SophiaBeads" dataset [274] for their work, which comprises of a collection of spherical beads, together with a CS-based reconstruction method which is able to deal well with noisy data. Consequently, a high number of projections is necessary to obtain a reasonable edge contrast and their conclusions are likely influenced by the systematic bias of the test set and the reconstruction algorithm.

It is assumed that a high angular variety can also be beneficial for reducing artifacts stemming from defect detector pixels or inadequate calibration, since they are spread out over larger parts of the volume which makes them easier to compensate. For instance, the use of helical instead of planar designs has been suggested to mitigate the severity of ring artifacts [275]. Furthermore, Zhao et al describes image quality

improvements by selecting an odd projection number for a PC trajectory, which is caused by an improved sampling of the Fourier space (see also sec. 4.5). This even holds if the overall number of projections has to be slightly reduced to accomplish this pattern [126]. Similar results were found by Grace et al., where sinusoidal trajectories with odd frequency outperformed such with an even one due to the avoidance of opposite projections [178]. These findings suggest that for low projections numbers views located at opposite sides (i.e., spanning 180°) should be avoided, due to the information gain being comparably low, since they are related to identical points in Fourier space and are therefore redundant information. In addition to projections that are tangential to salient edges, Zheng et al. includes further projections from other directions [160]. Unfortunately, it is not further specified how these supplementary poses are selected, but it seems reasonable to assume that they fulfill a similar function. As last example, Venere et al. used an optimization method that assigns every possible acquisition pose after each iteration a certain probability to get selected in the next iteration, where the probability for adjacent projections to already selected ones vanishes [197]. This has a very similar effect as the geometric weighting and prevents projection clustering as well.

7.4.4 Performance of Common Trajectory Designs

For the optimization to be successful, the proposed trajectory must be able to outperform other designs that were defined without taking the shape of the part into consideration. As such, in sec. 6.5.2 four different benchmark trajectories were introduced. Figure 7.4 show the SSIM and RMSE values over the entire projection range, while exemplarily difference images between the full reconstruction and each design for 16 projections is shown in fig. 7.5. It is apparent that the optimized trajectory yields a significantly higher image quality for all investigated projection numbers, which is particularly obvious for the cylinder feature. The part-dependent ranking among the benchmark trajectories was discussed in detail in a separate publication [136], where also additional metrics were used for the evaluation.

While the image quality increases for most of the part even outside the defined VOIs as visible in fig. 7.5 it is important to outline that this is not necessarily always the case and a counterexample for this will be given in sec. 8.3. As an example, one might imagine an octahedral feature that is inscribed into a cube. The edges of both parts would barely coincide, which leads to different preferable trajectories for both objects so that the image quality of the entire object would be reduced by a respective trajectory while it is improved for the VOI or vise versa.

(a) Sphere

(b) Cylinder
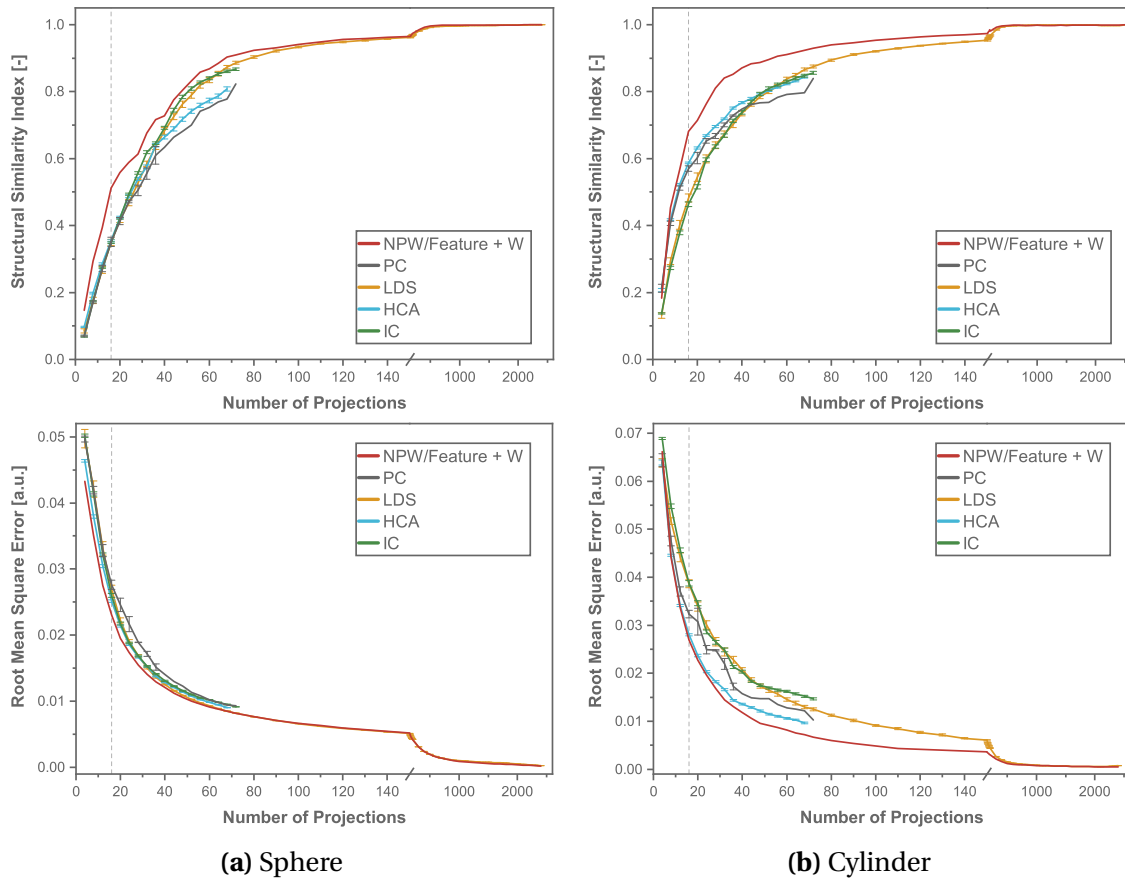
Figure 7.4: Comparison of the optimized and all feasible reference trajectories used in this work. For both features the optimized trajectory outperforms all other designs over the entire range of projections. Difference images for 16 projections are shown in fig. 7.5 as indicated.
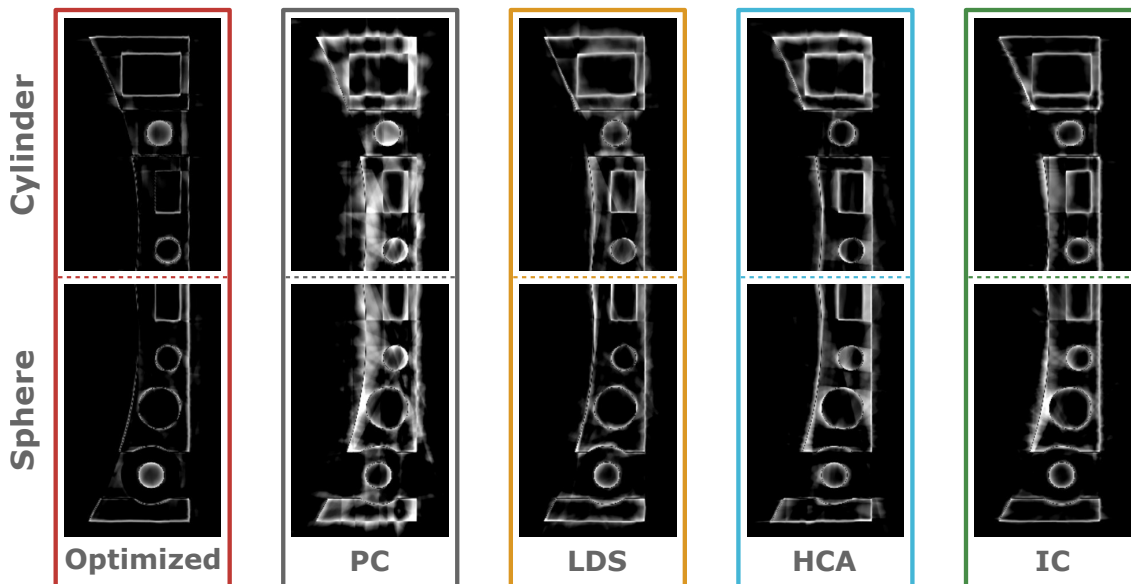
Figure 7.5: Absolute gray value differences of the reconstructions with 16 projections for a representative of each reference trajectory to the full reconstruction. The PC design performs poorest while the optimized trajectory clearly results in the lowest deviations.

Part III

Measurements and Experiments

8 | Experimental Verification

So far only simulated projections and data sets have been used for the evaluations. Since all imaging parameters are assumed to be ideal (see sec. 6.5) the findings of the previous investigations are clearly limited and need to be supplemented by experimental measurements. In particular, the influence of the polyenergetic X-ray tube emission spectrum, scattering effects, and noise could not be considered. To clarify if the trajectory optimization framework is also applicable to real-world data and in order to confirm the findings of the last sections, a CT-scan and optimization of the bat phantom was conducted and compared to the simulation-based results.

8.1 Generation of the Experimental Dataset

For the work presented in this chapter an experimental CT setup depicted in fig. 8.1 was used for the measurements. The system consists of a water cooled transmission micro-focus X-ray tube type XT9225-TED (*Viscom AG, Hannover, Germany*) with a tungsten target (shown on the left side). The highest attainable acceleration voltage is 225 kV and the maximum permitted target power is 120 W. The high-precision rotation stage where the object of investigation is placed uses air bearings (depicted in the center). As detector (right) a flat panel detector type XRD 1621 AN14 EHS (*PerkinElmer, Inc., Waltham, USA*) was utilized. It is equipped with a (2,048 × 2,048) pixel screen of (41 × 41) cm size and 200 µm pixel pitch. The scintillator layer is based on gadolinium oxysulfide.

The test part was milled using aluminum instead of iron-based alloys due to the limited acceleration voltage of the used X-ray tube and the small bars over both features were removed to facilitate manufacturing. Due to the poor commercial availability of aluminum balls of suitable size, steel-made sphere and cylinder features were used and glued into the frame. Since the CT setup was unable to offer all necessary axis for the movements related to a spherical trajectory, the part was mounted on an assembly of two tilting tables as shown in fig. 8.2. Since each table was only able to move up to 30° in each direction, a plastic wedge with an additional 30° angle was polymer-printed to reach a total range of motion of 90°. This part is X-ray transparent in comparison to the denser other materials and acts as intermediate layer to enable easy separation of bat phantom and mount.

The setup was scanned using a standard planar trajectory with 72 projections, resulting in a step size of 5°. Subsequently, the inclination angle was raised in 5° steps until 85°, yielding 14 additional scans. Next, the polymer wedge was flipped horizontally while the position of the bat phantom remained identical with respect to the assembly and the procedure was repeated, resulting in 35 separate circular scans with 72 projections each. Additionally, a single planar reference scan using 2,520 projections was
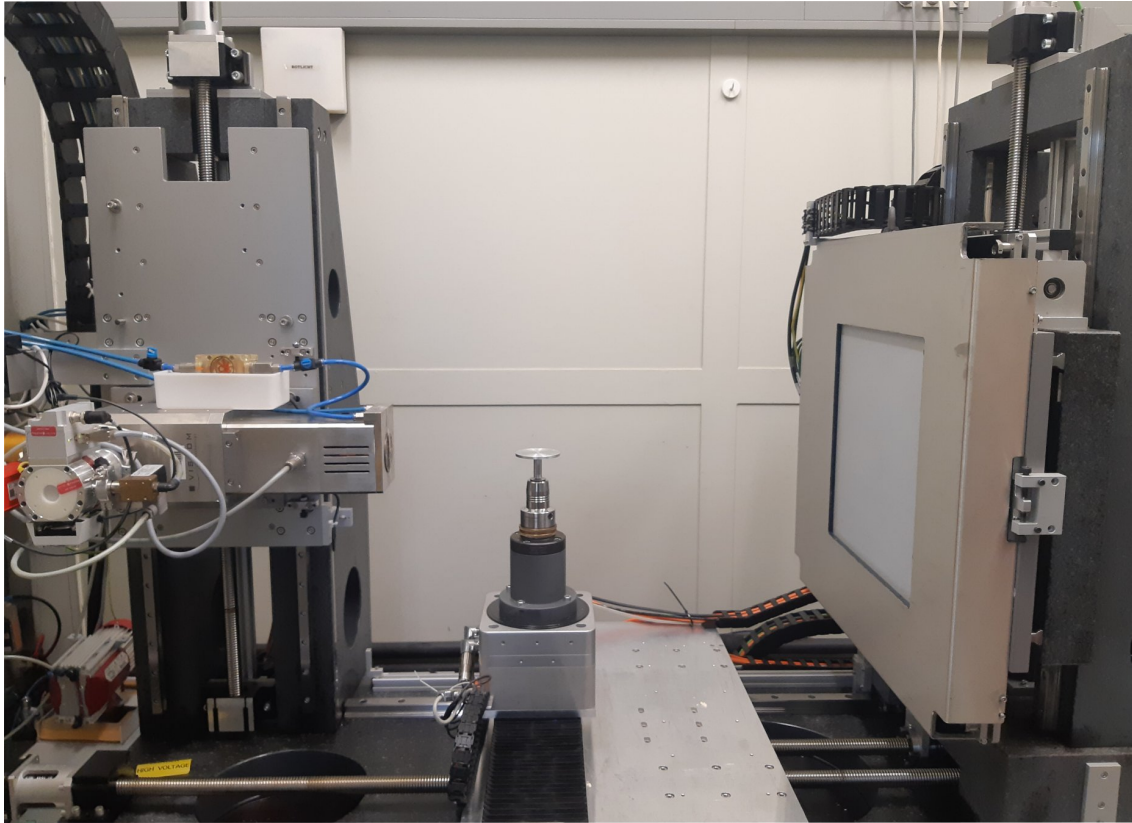
Figure 8.1: The industrial lab CT setup used for the experimental measurements in this chapter. Shown is the water-cooled transmission X-ray tube on the left side, the rotation stage in the center and the shielded detector on the right. The scanner has seven degrees of freedom, is installed on a vibration-damped granite bed and placed in a separate room with lead-reinforced walls for radiation protection.

performed in the untilted position, which was done as the first scan to prevent deviations to the shorter scan in horizontal position. All datasets with few projections were reconstructed separately using the SART algorithm, while the FDK method was used for the last scan, since it resulted in a better distinguishability of background and test object. The scans with a lower number of projections cannot be directly combined into a single dataset since their coordinate systems do not align and need to be rotated back with respect to the world coordinate system. Also, the rotation points of the tilting tables are unknown and located (unlike the simulations) somewhere outside of the center of the bat phantom, which introduces a linear shift to the volumes so that additional processing steps are necessary.

Subsequently, all reconstructed volumes were loaded into the commercial CT visualization and evaluation tool VGStudio MAX 3.4.3 (*Volume Graphics GmbH, Heidelberg, Germany*) where the surface of each individual bat phantom reconstruction was determined manually. To reduce the influence of potential positioning errors between the scans and to quantify the displacement that was introduced by tilting the setup, the built-in automatic registration method was used to align all volumes with respect to the reference scan with 2,520 projections. Next, the projection matrices, which describe the acquisition position relative to the CT setup coordinate system for each projection, were computed. Using the translational and rotational components determined in

(a) Resting Position at 0°   **(b)** Maximum Extension at 90°
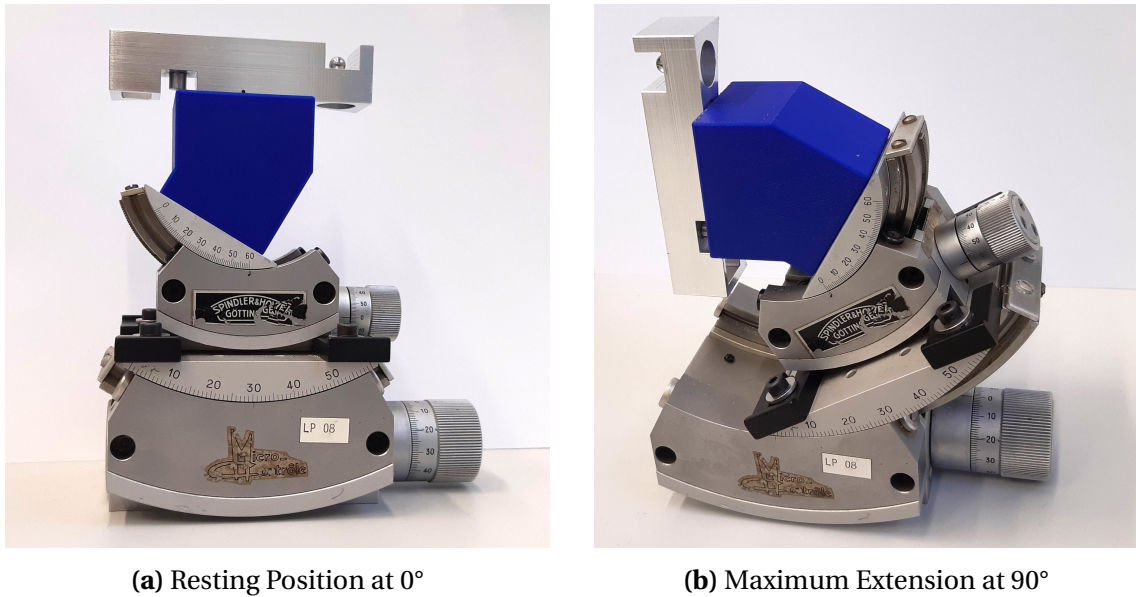
Figure 8.2: Manipulator setup for the experimental measurements. The test part can be rotated accurately between 0° (fig. 8.2a) and 90° (fig. 8.2b). The polymer wedge appears transparent compared to the other materials in the X-ray image and allows easy separation of tilting table and test part.

the registration step, the projection matrices for each scan were modified so that the reconstructed volume was aligned with the reference scan. These adjusted projection matrices were separately computed for each of the 34 tilted scans and stored together with the projection data as additional input files. In combination with the untilted scan, for which no change of projection matrices is necessary, the final dataset was obtained.

8.2 Differences to the Simulated Dataset

It is important to highlight that the dataset presented in this chapter is not identical – neither with respect to the acquisition poses nor the projections themselves – to the simulated projections of sec. 6.3. While the phantom was considered to be free floating without any mount or assembly for the simulations, the test part for the measurements was attached to the mount described above, which has to be positioned in the beam for some acquisition positions so that the image quality clearly deteriorates in such cases. For instance, if a very inclined angle as shown in fig. 8.2b is considered, projections taken from lateral direction will contribute very few information to the reconstruction in case of the cylinder, while the sphere feature remains unaffected. Furthermore, for the experimental data acquisition the bat phantom was tilted instead of the CT setup, which leads to a different distribution of acquisition poses. In case of the simulated dataset a singularity can be found (i.e., several projections rotated around the SOD axis at the identical acquisition position) at the poles located at $\theta = \pm 90°$, which is avoided by the sampling schema that spans between $\theta \in [-85°; \ldots; 85°]$. However, this does not hold for the experimental dataset, where such a situation occurs at $\phi = [0°; 180°]$. This problem is solved by an adjustment of the weighting function as described in sec. 7.3. Nevertheless, this solution leads to a systematic bias since projections located at the singularity are less likely to be included in the optimized trajectory after the first one

is selected, so that fewer projections are effectively available. In addition, projections located in the vertical plane were not acquired to fit the number of 2,520 projections which poses an additional bias as well. Last, as mentioned above, while the test part itself consists of aluminum, the features were made of steel and are therefore more absorbing. While this leads to slight horizontal artifacts around both features, which was observed even for the reconstruction using all available projections, it also increases the visibility of the features in the projections due to their enhanced contrast. Contrary to this, the simulated dataset was completely modeled as iron parts and the resulting higher attenuation is compensated by virtually increasing the energy of the monoenergetic X-ray spectrum (see fig. 6.2). Consequently, this dataset needs to be treated separately from the one defined in sec. 6.3 and previously generated results are not directly applicable, e.g., it is not possible to use the trajectory optimized on simulated data for the experimental measurements using the datasets generated for this work.

As planar reference scan for evaluation, the untilted scan with 72 projection was used, since all of these projections are contained in the optimization dataset. Unfortunately, it is not possible to define a meaningful spherical benchmark trajectory, since some projections are systematically impeded by the manipulator and manually removing those would improve the average SNR in the remaining projections, therefore biasing the results as well. It shall be noted that the method applied for generation of the dataset is only able to compensate for inaccuracies of the setup and discrepancies of nominal and actual position to a certain extent, since it relies heavily on the registration performance of VGStudio and the achieved image quality. However, while the geometric accuracy will obviously be worse compared to flawless simulations, the acquisition method is considered to be still more reliable than uncorrected measurements as conducted in sec. 9.

8.3   Evaluation of the Experimental Measurements

A trajectory optimization (parameters see chapter B) using different configurations was performed on the dataset described in sec. 8. The evaluation using the SSIM turned out to be problematic, since the calculated values did not coincide with the perceived image quality. It is known that the SSIM fails when applied to very blurred images [276], which is probably the reason for this issue, since, unlike the simulated data, the experimental measurements include scattering effects and noise. For comparison, the SSIM plots are shown in sec. D.4, while the reconstructed images are presented in sec. E.1.

Results using the RMSE, which turned out to be more representative for this dataset, are shown in fig. 8.3. Due to reasons outlined in sec. 8.1 only the planar circle is feasible as reference trajectory. However, the performance of the PC in comparison to the LDS for this part is known from the results provided in sec. 7 and it seems reasonable to assume a similar relation also for the experimental data. To prevent singularities, the geometric weighting was included in all cases (see sec. 7.3). This is not considered a disadvantage since almost no difference between weighted and unweighted model observers was observed in the simulations (see fig. D.3) and the weighting step only improved the results for other parts.

All in all, the results are in agreement with the simulations (see sec. 7 and fig. D.2): the PW model observers perform poorly while both NPW MOs reach better or equal image quality levels for all numbers of projections compared to the planar reference
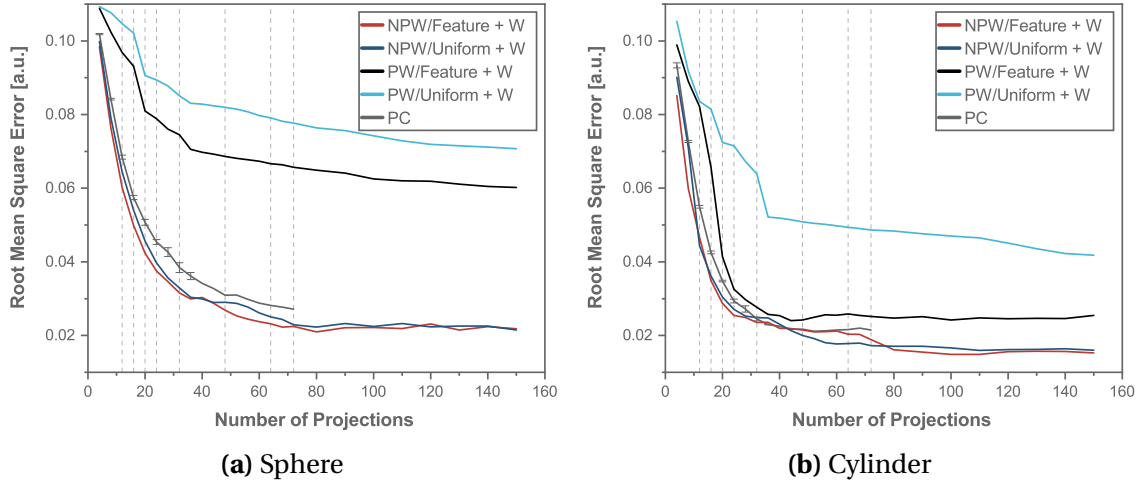
(a) Sphere **(b)** Cylinder

Figure 8.3: Quantitative results for the trajectory optimization with feature based and uniform template for the experimental data for both VOIs. A weighting function is necessary and used for all optimizations in order to avoid singularities. Both optimized NPW trajectories are better or equal to the planar reference trajectory for all projection numbers while the PW trajectories perform worse. Slices of the reconstructions using the indicated projection numbers are provided in sec. E.1.

trajectory. Unlike for the simulations, the optimization results for the cylinder are slightly worse than for the sphere in comparison to the reference trajectory, while feature-based and uniformly weighted NPW-optimizations perform comparably well. However, the differences are relatively small and in the order of the SEM of the reference trajectory.

Reconstructed images of the the planar circle and the optimized feature-based trajectory for 12 projections (first dashed line in fig. 8.3) are provided in fig. 8.4. The remaining reconstructed images indicated in fig. 8.3 are shown in sec. E.1. The qualitative visual comparison is in agreement with the quantitative findings and shows a clear improvement for the optimized trajectory. Additionally, the undersampling artifacts around both VOIs are almost entirely suppressed. However, the optimization of one VOI can lead to a decrease in image quality for another one, which has similarly been reported by other sources as well [190, 195]. This is particularly well visible in case of the cylinder optimization, where the right half of the artifact exhibits severe artifacts caused by a poor SNR. Considering the example mentioned in sec. 8.2, this is not surprising: a projection acquired from a position like depicted in fig. 8.2b shows a good visibility and contrast for one feature but in exchange for a very unfavorable acquisition position for the second one that is characterized by a high amount of material in the X-ray path that leads to a poor SNR. This was not visible to this extent for the simulated dataset, since no manipulator setup was necessary for the data generation so that both features were always similarly well visible.

As consequence, it can be deduced that the best potential for trajectory optimization is achieved if only few (ideally only one) VOIs of reasonably small size are optimized. Also, an optimization towards one part of the object can lead to image degradation in other regions. Both assumptions are assumed to hold irrespectively of the used optimization framework. While the measurements conducted in this chapter confirm
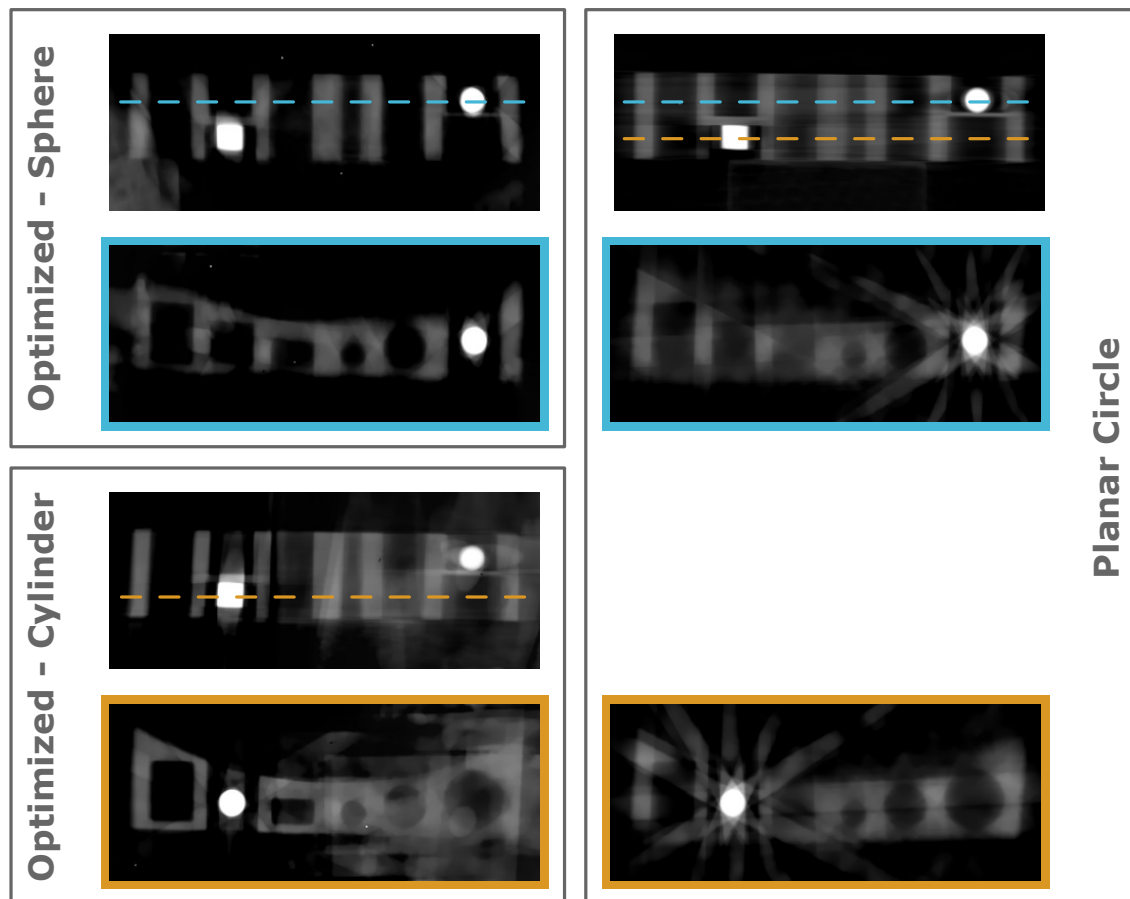
Figure 8.4: Visual comparison of the optimized trajectory towards the sphere (upper left) and the cylinder (lower left) and the reference PC trajectory (right). For each dataset an intersection plane and the horizontal cross section is provided (indicated with light blue and orange). For all depicted reconstructions 12 projections were used and the optimization was carried out using a weighted feature-based NPW MO. While the optimized trajectory shows clearly improved image quality and artifact suppression for each feature compared to the planar reference, in return the phantom area outside of the VOI shows severe artifacts, which is particularly visible in case of the cylinder optimization. Isolated white dots in the reconstructed images are caused by uncorrected defect detector pixels, i.e., by the acquisition setup, and not related to the optimization.

the former findings it was not possible to directly apply the simulation-based optimized trajectory to an experimental setup due to practical restrictions.

9 | Practical Application with Robotic Setup

After verifying the investigations stemming from simulations (chapter 7) with experimental data (chapter 8) the next logical step is to leave the laboratory setting and apply the optimization algorithm to an existing robotic CT setup. This chapter aims to provide a proof of concept that image quality improvements or a significant reduction of the projection number can be obtained for practical usage as well. As stated in sec. 5.3 robotic CT installations have emerged just in the recent years and are typically still not applicable for routine use. Furthermore, the used setup differs in many aspects from the simulated or laboratory conditions that all other results of this work are based on. Such differences are, for instance, limited accessibility, higher SOD and SDD and reduced positioning accuracy. In particular, only half-circle trajectories were feasible for image acquisition due to range of motion restrictions of the robots. The investigation provided in this chapter is considered to be the first trajectory optimization for an industrial robotic CT system using experimentally acquired data and was also published as a separate work [199], where further information is provided. The images used in this section are identical or modified versions to the ones used in the paper.

9.1   Setup and Inspection Task

The setup used for this work is the RoboCT-system of the car manufacturer BMW, which was developed together with the Fraunhofer institute and is depicted in fig. 9.1. Detailed information about the setup is available in the literature [225, 232] so that only a brief overview is provided here. While the entire installation comprises four cooperating industrial robots (Kuka Quantec extra KR90 R3100 HA, *Kuka AG, Augsburg, Germany*) with a position repeatability of ±0.04 mm [277] which are assembled on two linear axes, only two are used for this investigation, which will be focused on in the following. These are equipped with a Varex XRD 3025 detector (*Varex Imaging Corporation, Salt Lake City, Utah, USA*) and a Comet MXR-225VF X-ray tube (*COMET AG, Flamatt, Switzerland*). The setup is located in a closed area with radiation-shielded walls and provides enough space to fit the largest car models as a whole.

As test object a Siemens CSM12/24 industrial Ethernet switch (*Siemens AG, Munich, Germany*) as shown in fig. 9.2 was used, which has a base plate size of (90 × 70) mm and a height of approx. 60 mm. To provide a well-defined imaging task, the component was opened and a screw nut (size M6) was glued onto the lower circuit board (see fig. 9.2b), which acts as signal template and the surrounding volume as VOI for the optimization

91

Figure 9.1: Robotic CT system ("RoboCT") of the BMW AG. The setup for this work comprises two cooperative robots carrying the detector (left) and the source (right) as well as a mobile sample holder (middle). The latter is equipped with an X-ray transparent polystyrene block at the top on which the test part (see fig. 9.2) was fixated. Only the two robots in the foreground were used for this investigation.

algorithm. Both parts can be considered typical industrial items with many parallel and perpendicular surfaces. The inner electric components of the Ethernet switch are located in two separate height levels, but unevenly distributed in each horizontal plane. While the housing is made from plastic, these inner parts are significantly higher absorbing and can cause image degradationin some regions, so that it is considered to be well-suited as demonstration object for trajectory optimization.

9.2   Data Acquisition and Optimization Method

The test part was assembled onto an X-ray transparent polystyrene block that is located at the top of a movable stand as shown in fig. 9.1. Due to reduced accessibility and motion restrictions of the robots, only a limited space was available in horizontal direction for positioning of X-ray source and detector. In vertical direction, imaging of the metal parts of the assembly had to be avoided as well as collisions with the sample holder itself. Due to these constraints, the acquisition trajectory for generating the projection pool had to be restricted to 190° in horizontal and 135° in the vertical plane of which were 70° in inclining and 65° in declining direction to avoid colliding with the stand. Since the cone beam angle was determined to be maximal approx. 16.8° for the entire detector size of (354 × 304) mm, but the actual part being clearly smaller, this

(a) Industrial Ethernet Switch

(b) Open Part with Screw Nut Feature
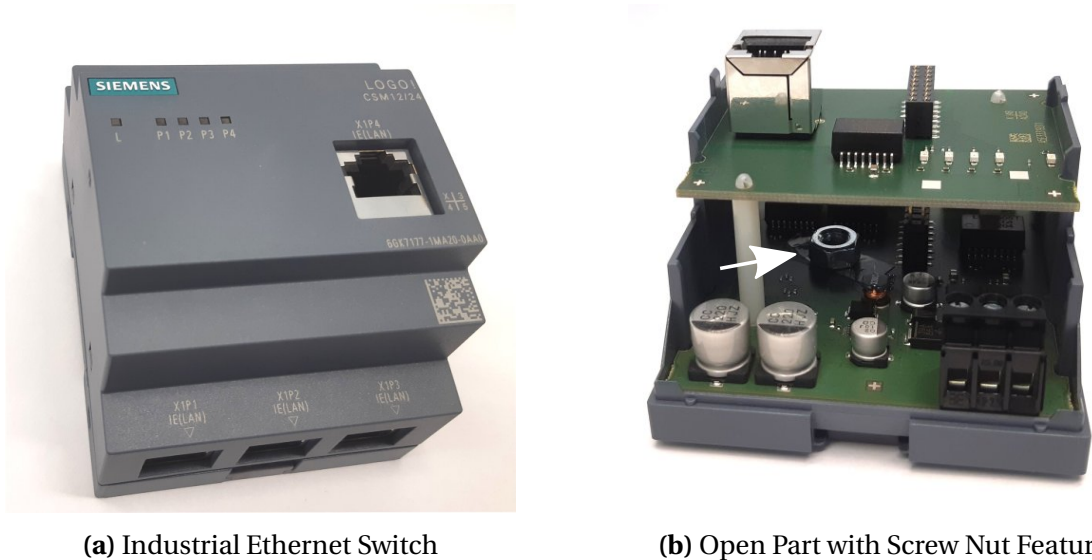
Figure 9.2: As test object for the investigation an industrial Ethernet switch was selected. While the housing (fig. 9.2a) is almost completely X-ray transparent with respect to the used imaging parameter (see sec. B.2), the inner electronic components are clearly more attenuating. A screw nut (white arrow) was glued into the lower circuit board as shown in the center of fig. 9.2b, which was used as feature for the optimization. Figure 9.2b is rotated by 180° relative to fig. 9.2a for better visibility.

trajectory is just at the border of acquiring the full Fourier space related to the horizontal plane, which is necessary to avoid cone beam artifacts in this direction. The angular sampling steps were uniformly set to 5°, resulting in 39 poses in the horizontal and 28 in the vertical direction, yielding overall 1092 projections available, which is significantly less than for other investigations in this work. Due to mechanical restrictions the orientation of source and detector relative to the test part had to be rotated by 180° for some projections, which was compensated by aligning the respective projections prior to further processing steps. Some partial trajectories had to be manually complemented by additional support movements to prevent collision with the sample holder. The imaging and volume parameters are provided in sec. B.

Analogous to sec. 7 and 8 an optimization using a weighted NPW MO was performed. Since other optimization parameters and models did not outperform this configuration as described in these sections they were omitted entirely for this investigation. For the acquired positions LDS and PC trajectories were computed analogous to the previous sections. However, since only less than a half sphere was available for reference definition and optimization, the PC trajectory was renamed to the more representative planar half circle trajectory (PHC) and both benchmark trajectories are shown with dashed lines to highlight the difference to former designs. However, also the acquisition positions of the optimized trajectory is located in a half-sphere due to this definition of the input projection set.

9.3   Evaluation Results for the Robotic Setup

Analogous to sec. 8, evaluations using the structural similarity index as image quality criterion have turned out to be problematic, so that the discussion concentrates on
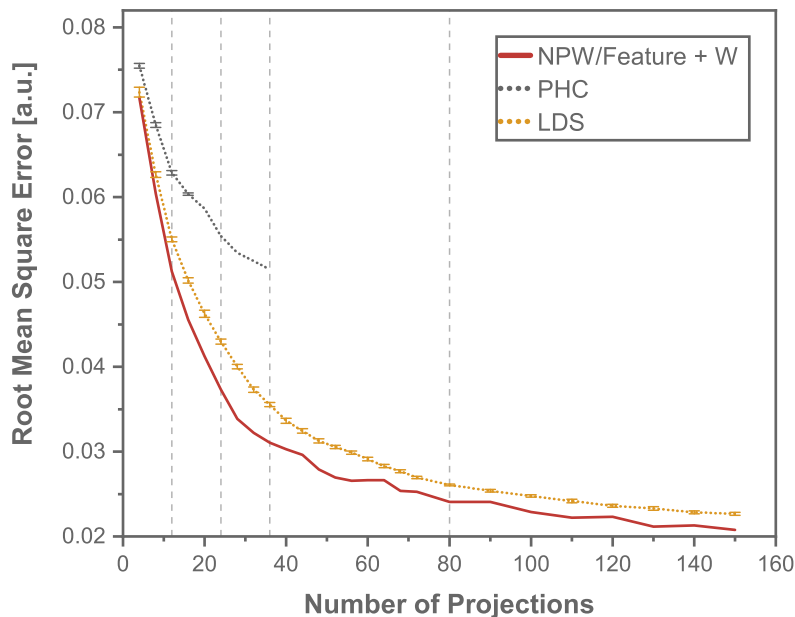
Figure 9.3: Optimization results for the RoboCT application. The optimized and LDS trajectories perform significantly better than the PHC reference. The curves for the reference trajectories are plotted in a dashed format to highlight that they are – unlike all other cases in this work – defined only in a half sphere due to the available poses in the projection pool. For all projection numbers the optimization approach, which was also restricted to the same feasible poses, is able to provide the best image quality.

the RMSE shown in fig. 9.3, while SSIM-plots are additionally provided in sec. D.5. Unfortunately, no values beyond 36 projections for the PHC can be provided due to the positions of the acquired projections. As apparent from the quality curves, the PHC performs poorly with respect to the LDS trajectory. As in former investigations, the optimized trajectory outperforms the LDS for all projection numbers. However, the improvements are much less than the transition from the planar PHC to the three-dimensional LDS trajectory. This is likely caused by the shape of the test object: the polymer housing is almost entirely X-ray transparent for the selected acceleration voltage, but the internal structure is arranged in two planar circuit boards that comprises highly absorbing electronic components. This leads to a systematic disadvantage for a planar trajectory, since effectively none of these dense objects can be avoided, which leads to a poor SNR even though the structure of the screw nut with many edges tangential to the horizontal and vertical plane would be well suited for such a design. Contrary, most of the absorbing structures are avoided if projections stemming from out-of-plane source positions are used. Since the circuit boards are an almost perfectly two-dimensional structure any arbitrary three-dimensional trajectory is assumed to improve the image quality with respect to the PHC. Additionally, the upper board is much smaller than the lower one, where the VOI is located, so that only few projections are affected by this structure. The optimized trajectory can only improve this result by achieving a more homogeneous image due to the geometric weighting and better edge contrast in the VOI due to the signal template used for calculating the observer model, which explains the comparably lower gain in image quality with respect to the LDS.

A cross-section view through representative reconstructed volumes for each trajectory using 12 projections is shown in fig. 9.4. The findings of fig. 9.3 can be confirmed

94
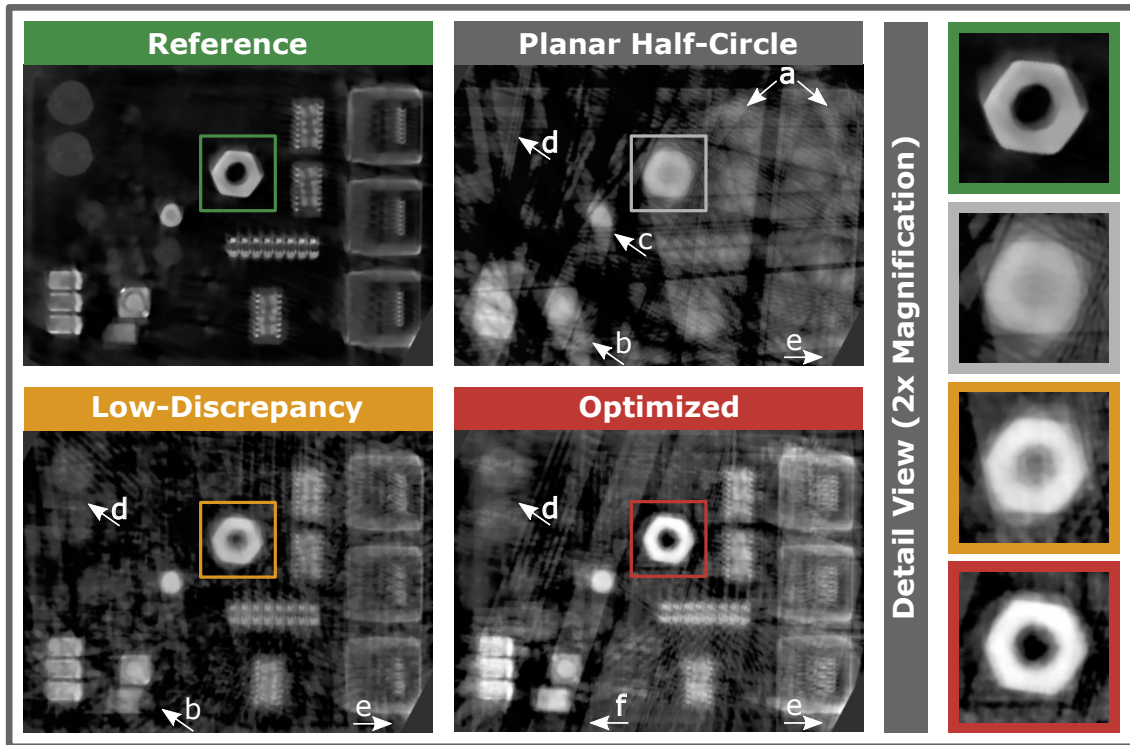
Figure 9.4: Exemplary volume cross sections through the center of the screw nut using all 1,092 poses for the reference reconstruction and 12 projections for all other depicted cases. As apparent from the overview images and in particular the magnified VOI, the optimized trajectory leads to clear improvements with respect to the LDS and especially the PHC design. As in the former experimental investigation (see fig. 8.4) the VOI image quality improvements lead to a slightly higher noise level in the remaining image. For arrow explanations see full text.

visually, i.e., LDS and optimized trajectory perform significantly better than the PHC, which is particularly well visible in the magnified VOIs. Further visual images for the other projection steps indicated in fig. 9.3 can be found in sec. E.2. As for the experimental investigation of sec. 8, the noise level for the overview image of the optimized trajectory appears slightly higher than for the reference trajectories, e.g., the LDS, while the image quality and edge detectability in the VOI improves. However, the difference is relativized for higher projection numbers as apparent from the cross-sections in sec. E.2.

The visual images provide further relevant details. For one, even in the reference image slight geometric distortions are visible. This is most likely caused by a discrepancy between assumed and actual positions of X-ray tube and detector for each projection. Due to practical limitations of the acquisition software, each acquired arc of the input dataset (i.e., positions with different θ but identical ϕ) was imaged separately in predefined steps. These predefined steps were also used for the optimization algorithm and all reconstructions. However, this approach does not allow the use of the actual setup positions but only the nominal ones. While this difference is typically negligible in practice for conventional industrial CT systems, it is much higher for robotic installations and should be taken into account [226, 233]. Furthermore, no software-based alignment or other correction methods were used, so that these geometrical errors are completely uncompensated and only the nominal geometry information was used.

Concerning image quality, the PHC performs poorly, which is apparent as well in the VOI, where the inner hole of the screw nut disappears due to low contrast. In particular, highly absorbing structures on the circuit board cannot be resolved as shown at arrow **a**. Also, the position of the lowest structure at **b** appears right instead of left of the one located higher in the image and the structure at **c** is not displayed round but angular, which can lead to false conclusions about the structure. While the low-absorbing round structures at **d** are visible in the optimized and LDS trajectory, it cannot be observed in the PHC reference at all. It is surprising that such low-contrast structures (as apparent in the full reference image) can already be resolved relatively well with only 12 projections. It shall be noted that the missing edge at **e** is no artifact, but is caused by the restricted and cubic reconstruction volume which ends at this part of the image. Last, as intended, it can be observed that the optimization algorithm aims towards acquiring projections parallel to edges of the feature template. This is well visible by the diagonal streaks at **f**, which are caused by rays passing the volume almost unobstructed in proximity to higher absorbing object parts.

Considering these aspects it can be concluded that it was possible to successfully apply the proposed optimization framework to a robotic CT installation for a practically relevant task and representative imaging conditions. It was shown that the adaptation of the acquisition trajectory towards spherical designs can clearly improve image quality with respect to the typically used planar half-circle trajectory and that a reasonable reconstruction result can be obtained even for relatively few projections if an iterative method is used. Due to the particular structure of the test part it is assumed that out-of-plane trajectories generally outperform the conventional planar design for the investigated object. Furthermore, it shall be noted that the test object is the only multi-material part used in this work. However, even though this restricts the potential for optimization in this case, the optimization method was able to define a trajectory design that is able to provide better imaging conditions than both reference trajectories for all considered projection numbers. Considering the RMSE as criterion, a similar quality can be achieved by the optimized trajectory with 16 compared to 36 projections for the PHC, i.e., only approx. 45 % of projections are necessary. Alternatively, if 36 projections are considered, the RMSE of the PHC can is determined to approx. 0.051 compared to 0.031 for the optimized trajectory, which equals a quality improvement by approx. 40 % for this particular object and projection number.

Part IV

Boundary Conditions, Limitations and Discussion

10 | Influence of Part and Setup Geometry

10.1 General Considerations

As discussed in sec. 4.3 the shape of the object greatly influences the distribution of high coefficients in Fourier space. Since a sparse representation in the frequency domain is necessary for successful trajectory optimization it stands to reason that not all items can benefit in the same degree from such an approach. For instance, it was found that the highest potential can be achieved by objects with few preferential directions [123]. In the extreme case, one can even imagine geometries that can be imaged with only two projections for both, parallel beam geometry (e.g., cuboid) and CBCT (e.g., deformed parallelepiped). However, in general it is much easier to construct a shape that can be imaged with a certain number of projections than quantifying how simple a particular profile is with respect to the trajectory optimization task.

Furthermore, due to the properties of the Fourier transform an edge of the object is not mapped to a single entry but an entire line through the origin located in Fourier space. The Fourier slice theorem (see sec. 2.3.1) states that the values in this domain cannot be measured individually but are located on such a line as well, since it corresponds to all the information inherent to a single projection, which is the smallest unit of information obtainable. Consequently, the more representative property with respect to the optimizability of a part is not the sparsity of its Fourier transform but its *angular* sparsity instead, which means that the Fourier space consists mostly of small values and the high components are concentrated on a few directions expressed in polar coordinates. Varga et al. proposed a measure to quantify the direction dependency of the reconstructions for a given part [122] which is likely linked to the optimizability. Unfortunately, to be applicable for the investigations in this work the method requires a high number of reconstructions and a similar size of samples per data point, which was not always feasible (e.g., between different trajectory designs or for PC trajectories with many projections) for the results provided in this work and was therefore omitted.

Instead, in sec. 10.2 an optimizability metric will be derived that aims to predict the potential for trajectory optimization. In order to validate the findings of the metric and to better evaluate experimental results, a simple quantitative quality indicator will be introduced in sec. 10.4.1. Furthermore, as result of an intermediate computation step to calculate the optimizability metric, the concept of summed Fourier coefficient plots is introduced, which tries to visualize the angular sparsity for a given object and can be used as a tool to identify valuable acquisition poses directly.

10.2 Definition of a Metric for Optimizability

Based on the considerations of sec. 10.1 a quantitative metric can be derived that expresses the angular sparsity – and as a consequence the optimization potential – quantitatively. To accomplish this, after a Fourier transform of the feature (i.e., the signal) that is to be optimized $\omega = \mathcal{F}(\Delta \mathbf{s})$, the coordinate system is changed to spherical coordinates and coefficients corresponding to different distances from the volume center but the same spacial direction are summed up. While typically for the quantification of signals the signal power is used (e.g., in sec. 4), the amplitude spectrum is applied instead as it is considered to be more representative due to its direct link to the original image and not the physical processes that lead to its generation. However, since the power spectrum equals the amplitude spectrum squared, this choice is eventually of minor importance since it just affects the scaling of the optimizability metric. Using the signal power as basis for the optimizability metric instead would disproportionately emphasize high valued coefficients, which distorts the quantitative values of the optimizability metric and shifts it to relatively high numbers.

This step produces a coefficient map that shows the direction of valuable projection poses with respect to the angles ϕ and θ. Exemplary these plots, which will be referred to as angular summed Fourier coefficient plot (ASFC-plot) in the following, are shown in fig. 10.1 for two objects that will be introduced in sec. 10.4. The values of the ASFC-plot can be used to calculate an angular histogram $\mathbf{h}(\Delta \mathbf{s})$. Using the notation introduced in sec. 4.2 these steps can be expressed as

$$\mathbf{h}(\Delta \mathbf{s}) = \mathcal{R}_{\phi,\theta}\left(\mathcal{F}(\Delta \mathbf{s})\right) = \mathcal{R}_{\phi,\theta}(\omega), \tag{10.1}$$

where $\mathcal{R}_{\phi,\theta}$ indicates an angular Radon transform for a single pixel detector. Note that this is a combination of Radon and Fourier transform applied to a part of the object, while the base $\mathbf{\Psi}_{\mathbf{CT}}$ suited for CT of eq. 4.7 is a combination of Radon and inverse Fourier transform to the Fourier-transformed object, which yields a similar matrix structure. Figuratively speaking, the ASFC-plot represents the information per spacial direction of the Fourier-transformed feature. Such maps can in principle be used to identity valuable angles for the trajectory optimization since these are located perpendicular to particular high entries in the plots and a framework based on this property will be proposed in sec. 11.2.1. Theoretically, it is also possible that one direction corresponds to more than one edge of the object, which would result in particular high values. A similar concept – but based on projections instead of the feature itself – has been previously proposed as figure of merit for a trajectory optimization algorithm [179] (see sec. 5.2, approach 14).

To quantify the sparsity of $\mathbf{h}(\Delta \mathbf{s})$, several metrics have been suggested in the past, for instance the Shannon entropy or the ℓ_1 norm that is frequently used as constraint in compressed sensing [106, 278, p. 89]. Taking use of one of these metrics, the optimizability Ξ is defined as the Gini coefficient of $\mathbf{h}(\Delta \mathbf{s})$, which is treated as one-dimensional vector so that

$$\Xi(\Delta \mathbf{s}) = \text{Gini}(\mathbf{h}(\Delta \mathbf{s})) = \text{Gini}(\mathcal{R}_{\phi,\theta}(\mathcal{F}(\Delta \mathbf{s}))), \tag{10.2}$$

which is a scalar value. The pseudocode for the calculation is given in sec. C.4. It shall be noted that an alternative implementation could be achieved by use of the Hankel transform, which is the special case of a Fourier transform with a radial symmetric kernel [36, p. 128f] that would improve the performance for the summation step. The Gini

coefficient, which is mainly known for its application to express disparities in economics, was selected as sparsity metric since it shows several beneficial properties compared to other metrics [279]. Particularly relevant for this application is the homogenity of degree 0, which means that a multiplication of the input vector for the Gini coefficient with a constant value α causes an scaling of the result with factor $\alpha^0 = 1$, i.e., the Gini coefficient is scale invariant and $\text{Gini}(\mathbf{a}) = \text{Gini}(\alpha\mathbf{a})$ is valid for an arbitrary distribution $\mathbf{a}$ [279]. As direct consequence, the template does not need to be defined in binarized form but can be given in arbitrary values (assuming a mono-material part) as long as the background is set to zero. Even more important, the result is theoretically independent of the volume size and the number of voxels containing the feature itself (see sec. 10.3), since the magnitude of the values of $\Delta\mathbf{s}$ and $\boldsymbol{\omega}$ are bounded and linked by Parseval's theorem (see sec. 3.7.2).

While the Gini coefficient ranges between 0 (perfect equality of all coefficients) and 1 (all coefficients except a single one are 0), the optimizability Ξ cannot reach 0. Because of the summation of angles in space and the feature being defined in a cubic volume the diagonal path through this space is longer than the side edges and more voxels are contained in comparison to those. Therefore, due to this systematic bias – even in the case of a dirac impulse $\boldsymbol{\delta}$ in object space, which leads to a Fourier Space with all elements having the same value – $\Xi(\boldsymbol{\delta})$ does not reach 0 but instead results in a value of approx. 0.41 for the considered volume size of $(91 \times 91 \times 91)$ voxels. However, the reverse effect does not exist: the Fourier transform of a completely filled volume $\Xi(\alpha\mathbf{I})$ with a constant factor α yields 1. Considering these extreme cases, the optimiziability Ξ can be normalized to cover the full range:

$$\overline{\Xi}(\boldsymbol{\omega}) = \frac{\Xi(\boldsymbol{\omega}) - \Xi(\boldsymbol{\delta})}{\Xi(\mathbf{I}) - \Xi(\boldsymbol{\delta})}, \tag{10.3}$$

yielding the normalized optimizability $\overline{\Xi} \in [0; 1]$. Higher values of $\overline{\Xi}$ indicate an angular sparse Fourier space and high potential for the trajectory optimization.

10.3 Limitations

It was stated in sec. 10.2 that the optimizability metric is independent from the volume size it is defined in and consequently the sampling resolution, which has, however, some limitations. Beside numerical inaccuracies due to the change of the coordinate system and subsequent summation, a too small resolution might also result in the loss of relevant feature properties, e.g., in case of curved transitions. Additionally, the obtainable angular resolution decreases for a coarser voxel grid. On the other hand, extremely large volumes can become computationally demanding, since the Gini coefficient needs to be computed in a single step and cannot be generated by combining precomputed smaller segments of the volume [280], so that parallelized computation is not feasible. To mitigate this effect it is recommended to explicitly compute the minimum and maximum obtainable optimizability metrics with test functions for each volume size and normalize subsequently using eq. 10.3. For this work the normalization test functions were a uniformly filled volume and a dirac impulse as indicated in eq. 10.3. The volume size was $(91 \times 91 \times 91)$ voxels with an angular resolution of 1°.

Furthermore, the optimizability metric is just an approximative indicator. For instance, a cube can be captured with the same number of projections, irrespective

(a) Octahedron (8 faces, $\overline{\overline{\Xi}} = 0.44$)

(b) Icosahedron (20 faces, $\overline{\overline{\Xi}} = 0.35$)
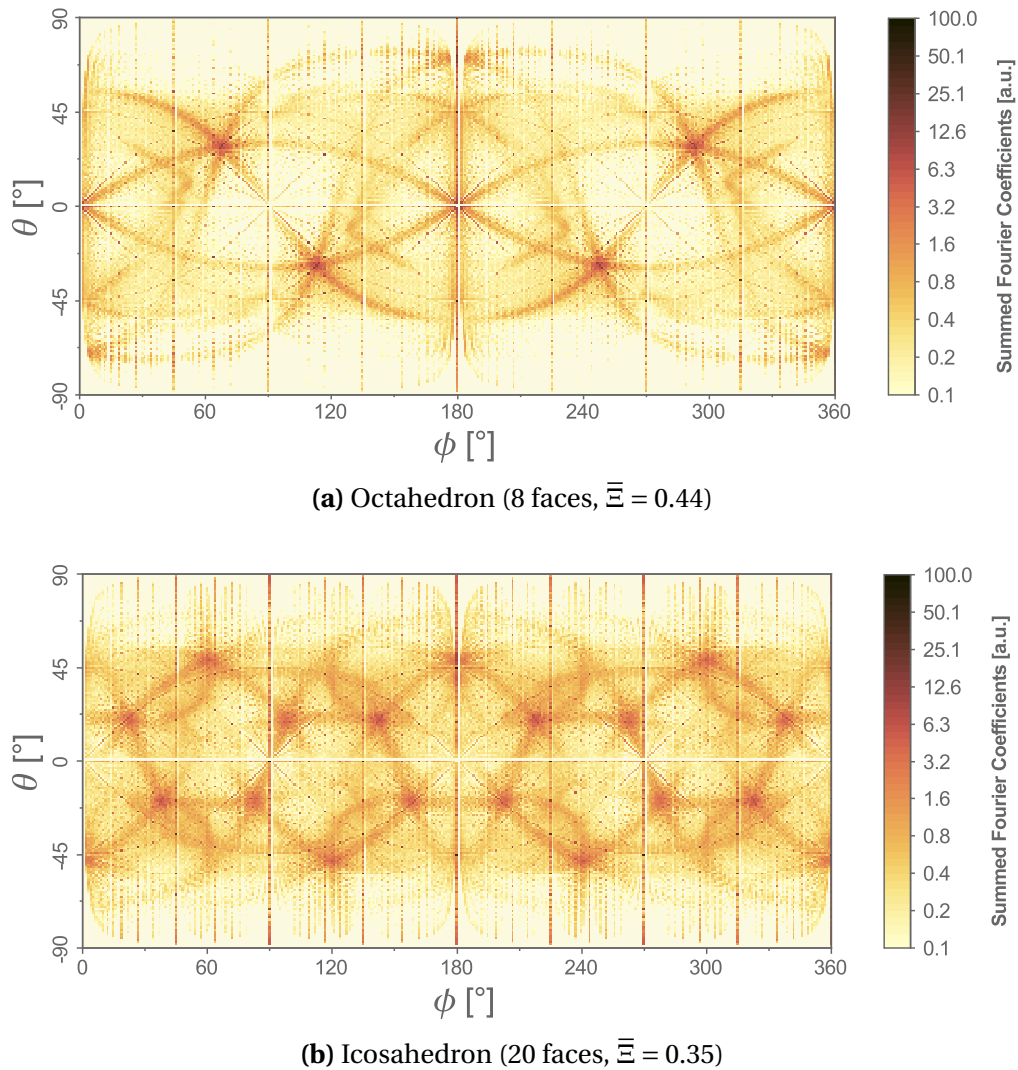
Figure 10.1: Exemplary ASFC-plots of summed Fourier coefficients for the octahedron (fig. 10.1a) and the icosahedron (fig. 10.1b). High coefficients indicate valuable acquisition directions, which correspond to the number of edges of the object and are symmetric due to geometric reasons. The angular distribution of these coefficients is less sparse for the icosahedron compared to the octahedron, which results in a lower value of the optimizability metric Ξ and corresponds to less improvements for the trajectory optimization. Plots for the remaining platonic solids are shown in sec. F.

of its size. However, the Fourier transform of differently sized objects differ and the distribution of coefficients does as well, which can lead to slightly varying values for otherwise almost identical objects. This property justifies the normalization towards the theoretical extreme values instead of using practically more representative test functions. Furthermore, the rotation of the object in space can influence the result of the optimizability metric as well to a certain degree due to the voxel discretization of the volume. This inaccuracy can be reduced by a finer voxel grid for the cost of a higher computational effort.

As mentioned in sec. 10.2 the ASFC-plots can be used to identify valuable angles that can be used for trajectory optimization. However, this does strictly speaking only hold if a parallel beam setup is used, since the Fourier transform does not consider the
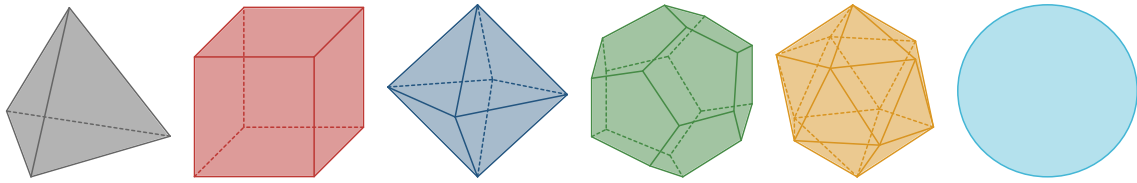
Figure 10.2: Overview of the Platonic solids used for the investigation. From left to right: tetrahedron (4 faces), cube (hexaeder, 6 faces), octahedron (8 faces), dodecahedron (12 faces), icosahedron (20 faces) and sphere.

diverging rays caused by the cone beam angle. This assumption can be approximately fulfilled if the object is centered in the middle of the rotary stage and the VOI is considerably small (see also sec. 10.4.2 for further discussion). It shall also be noted that modern robot-based systems are able to scan in a virtual parallel beam mode, which is achieved by the postprocessing of several acquired images [281]. Furthermore, even though the concept of ASFC-plots corresponds well with subjective intuition, only the information of the amplitude spectrum is taken into account. In addition to the limitations and drawbacks mentioned above, also several extensions and adaptions are conceivable, which will be discussed in sec. 11.2.2.

10.4 Simulative Verification via Platonic Solids

To investigate the suitability of a part with respect to trajectory optimization six test parts have been defined. These are the six regular Platonic solids depicted in fig. 10.2 that were selected due to their high symmetry, their spatial expansion, and their well defined increasing complexity; i.e., the increasing number of edges. The test objects were scaled so that they are inscribed into the sphere to reduce size-dependent effects.

10.4.1 Parallel Beam Configuration

Figure 10.3 shows the normalized optimizability values for each test object. As expected, the optimizability decreases with increasing number of faces of each body, where the sphere is considered to have an infinite number of faces. However, the value for the tetrahedron is unusually low and on the same level as the more complex octahedron, which appears to be implausible at the first glance. The explanation comprises a close look at the symmetry of the Platonic solids: for the cube, octahedron, dodecahedron and icosahedron two planes are always parallel to each other, while this is not the case for tetrahedron and sphere. Consequently, the cube has only three unique faces compared to four for the tetrahedron, which results in a higher optimizability value for the former.

Also counter-intuitively, the tetrahedron (4 faces) reaches the same value as the octahedron (8 faces). However, this can be explained by a similar argument as both bodies have each four unique planes. Moreover, in this particular case, under an appropriate orientation those faces overlap as illustrated in fig. 10.4. This suggests that both parts can not only be similarly well optimized but the optimized trajectories should even coincide. As logical consequence, the ASFC-plots appear identical for both bodies (compare fig. F.1 and fig. F.3).
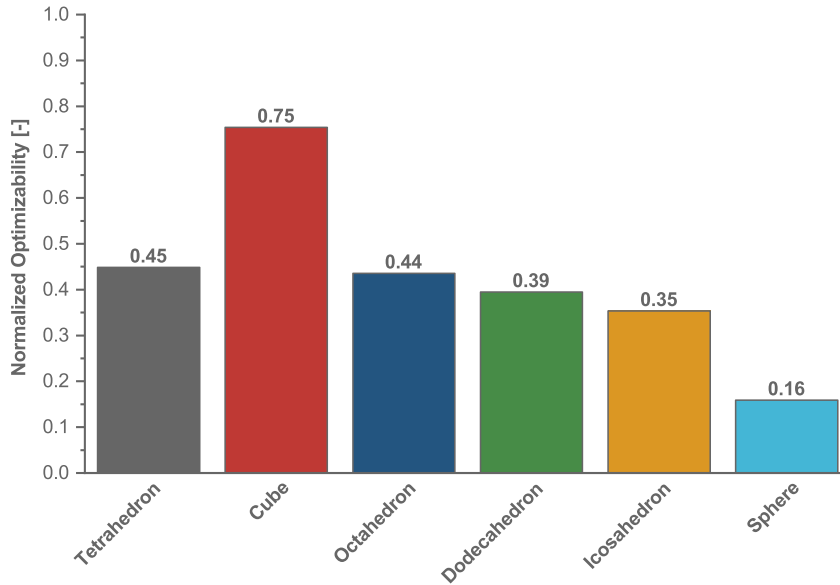
Figure 10.3: Calculated normalized optimizability for all platonic solids. Due to the planes of the cube being aligned in only three different spacial directions, the calculated value is higher compared to the tetrahedron that spans four directions. Even though having double as many faces, the octahedron yields the identical value since only the same four spatial directions are covered (see fig. 10.4).

To confirm these considerations, datasets for each part were generated analogous to the workflow described in sec. 6.3, using Aluminum as material. Since the simulation tool does not permit parallel beam geometry, the source-object distance was increased until an effective half cone beam angle of maximum 1.2° was reached, which is considered to be negligible in the following. Analogous to the workflow proposed in sec. 6.5, sets of ten LDS reference trajectories were generated and averaged. Additionally, a feature-based optimization using a NPW MO with geometrical weighting was performed for each Platonic solid. Since the test parts are the only objects in the simulation, the optimization VOI was enlarged to $(91 \times 91 \times 91)$ voxel in order to fit the entire part. As an empirical figure of merit for the optimizability per projection number the image quality ratio IQR is defined as the ratio of the RMSE of the LDS reference to the optimized trajectory:

$$IQR = \frac{RMSE_{LDS}}{RMSE_{optimized}}, \tag{10.4}$$

where values higher than 1 correspond to an improved image quality compared to the reference (i.e., a successful optimization) and for values lower than 1 the optimization algorithm failed. The LDS trajectory was chosen as reference, since the optimized trajectory comprises poses located in three spatial directions, while using e.g., the PC as reference would result in a systematic error due to its planar design. A drawback of the simple definition of the IQR is a dependency on the volume filling of the evaluated part. Reconstructions with a small number of acquired projections typically lead to smeared out attenuation values over larger parts of the volume, since few samples are averaged over the domain. This is particularly well visible for FDK reconstructions, where few projections result in typical, well visible streaks through the volume, but also other methods such as the SART algorithm used for this investigation exhibit a similar
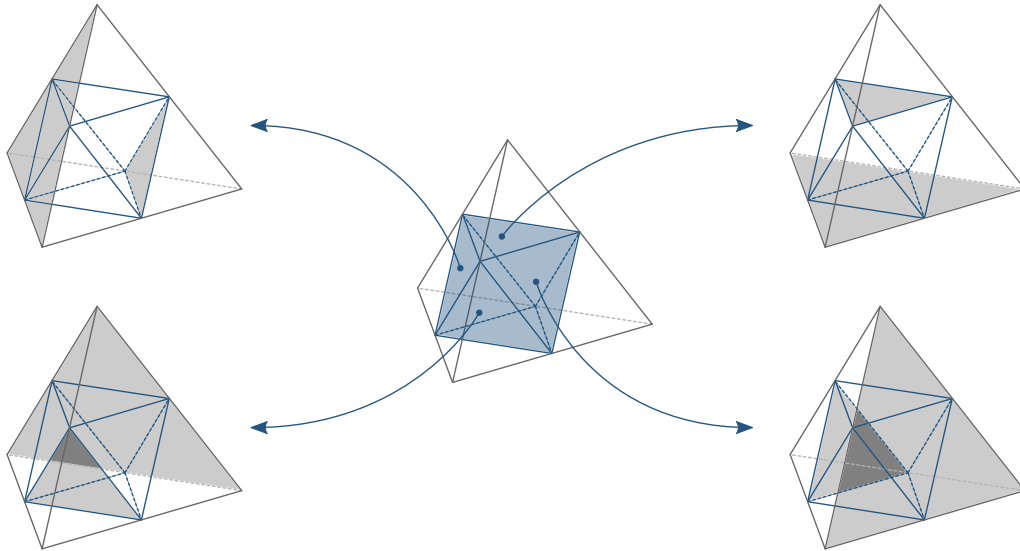
Figure 10.4: For an octahedron (blue) inscribed into a tetrahedron (gray) as depicted in the center, four of the eight octahedron faces match the faces of side planes of the tetrahedron, while the other four ones are aligned parallel to them as shown schematically on the left and right. Since no additional plane directions are introduced, the optimizability index $\bar{\Xi}$ is identical for both figures (see fig. 10.3), even though the number of edges differ by a factor of two. Given parallel beam geometry, both features can theoretically be reconstructed with the same minimum number of projections and even the identical trajectory, while the octahedron requires double as many for a cone beam setup. The sizes of the depicted objects do not correspond to their actual size for the simulation, since both were inscribed into a sphere (see sec. 10.4).

behavior. For bodies on the left side of fig. 10.2 this leads to particular high RMSE values, since the volume filling of e.g., tetrahedron or cube is comparably small so that smeared out attenuation values are compared to the very low air values of the environment and subsequently squared, which increases the effect. For Platonic solids with high volume filling, the effect is smaller, since the VOI contains less air. As result the IQR values of test objects with low volume can be slightly worse than such for larger parts.

The resulting IQR curves for all Platonic solids are shown in fig. 10.5 where the error bars were omitted since they are barely visible due to the scale adjustment. The improvement is in agreement with the calculated optimizability values (see fig. 10.3): as expected, the cube, which showed the highest optimizability reaches very high IQR values higher than 3, while a lower $\bar{\Xi}$ correlates with a lower IQR. In theory, the curves corresponding to test parts with few unique planes should also incline earlier than others (e.g., the cube at 3 and tetrahedron and octahedron at 4 projections, even though this would not be distinguishable due to the sampling resolution in steps of 2 projections). However, this is not observed, most likely due to the insufficiently fine 5°-discretization of the available poses and the normalization with respect to the LDS design. Due to performance limitations only the first 72 projections were calculated for each geometry. However, based on the typical shape of the image quality curves (see sec. 7) it appears reasonable to assume that the IQR of all test parts will quickly converge to 1 for higher projection numbers.
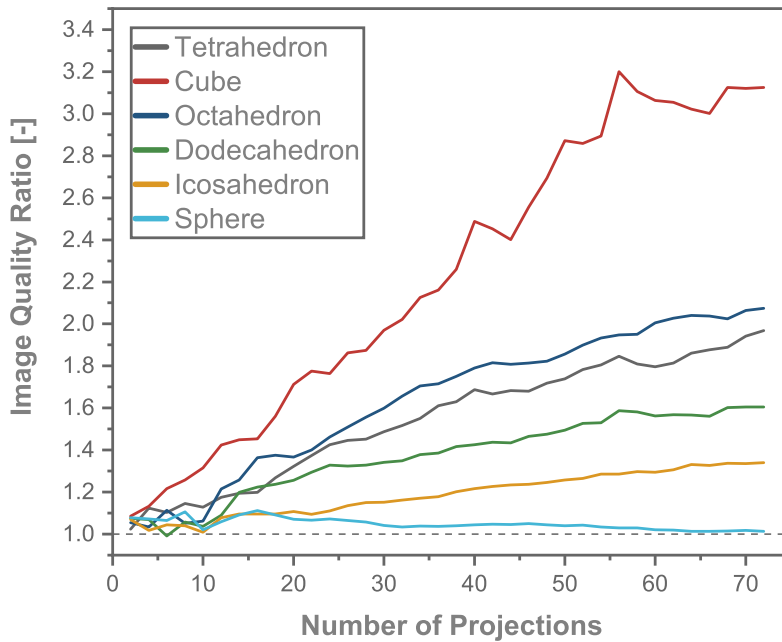
Figure 10.5: Image quality ratios for the parallel beam geometry case. All test parts show improved image quality compared to the LDS benchmark trajectory (equal performance indicated by a ratio of 1) and behave like predicted by the optimizability metric in fig. 10.3. For higher projection numbers all curves would converge towards 1.

10.4.2 Cone Beam Configuration

Most discussions in this work were conducted with a parallel beam geometry for convenience and since the derivation for cone beam can be performed analogously. However, the use of a CBCT setup has a direct practical consequences. The cone beam angle generally depends on the CT geometry and the size of the investigated part or the detector. Typically, the HCA is not explicitly predetermined in practice but derives from the application because other geometry parameters as the SDD cannot be selected arbitrarily since the VOI of the part needs to fit the screen and higher SDDs lead to longer scan times due to the inverse square law of radiation. While a single projection image captured via parallel beam setup appears to be a line in Fourier space (see fig. 2.4), it resembles a wedge for CBCT, where the opening angle equals the HCA [99]. Analogously, obtaining a cone beam projection can be imagined as acquiring several partial images from different angles, with each of them projecting to another position on the detector plane [36, p. 265f].

It can be intuitively shown that the proposed optimizability metric (sec. 10.2) cannot be directly applied for CBCT since the phase spectrum is not taken into account. Both Fourier-transformed figures in fig. 10.6 have the same amplitude spectra, therefore resulting in the same values for $\bar{\bar{\Xi}}$. However, the left example (fig. 10.6a) can be almost perfectly recovered[1] by only one projection if the upper and lower edges – which would

---

[1]In practice, this is only approximately true as a shift to higher attenuation coefficients for the lateral rays can be observed in fig. 10.6c. This is caused by the reconstruction algorithm that weights each ray by the sum of voxels in the reconstructed volume that it passes through. In this example the volume is rectangular and ends abruptly at both horizontal sides, which means that less voxels are used to weight the respective rays and the lateral voxel values are considered to be higher.

(a) Positive Example

(b) Negative Example

(c) Reconstruction of 10.6a

(d) Reconstruction of 10.6b
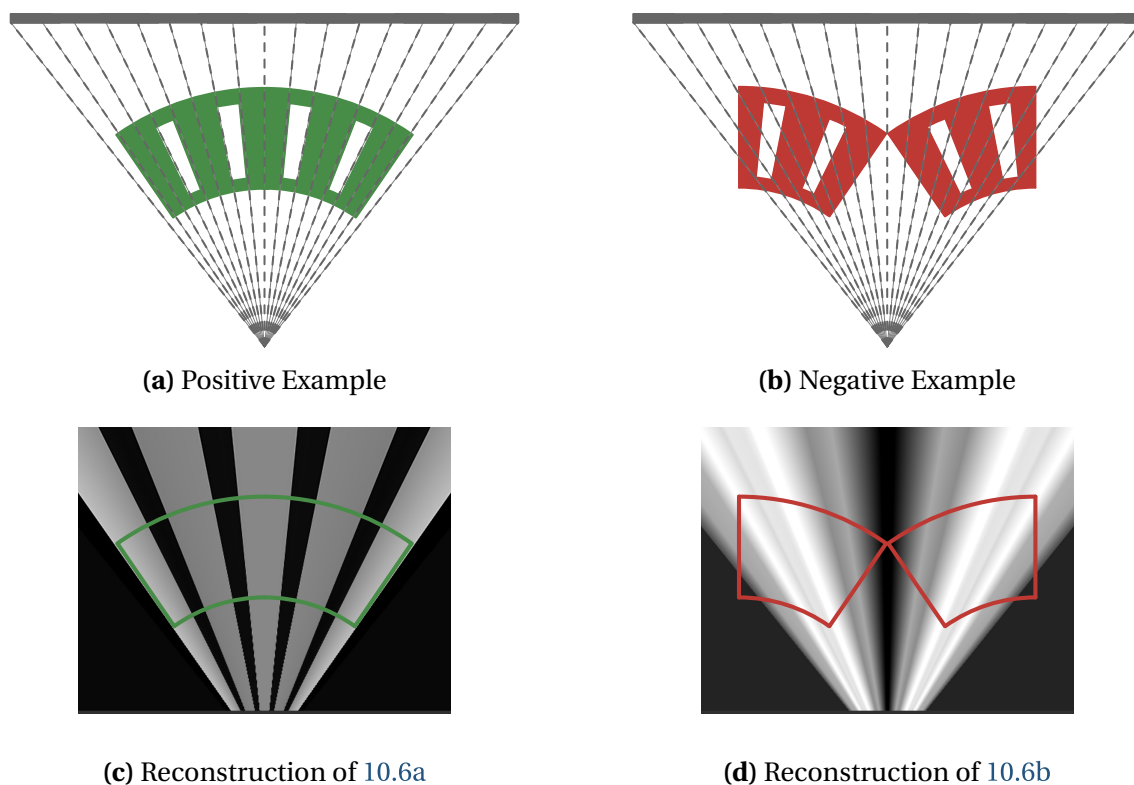
Figure 10.6: The amplitude and power spectra of the Fourier-transformed test parts in 10.6a and 10.6b are identical. Nevertheless, the first part can be almost perfectly reconstructed from a single projection (fig. 10.6c) while this is not possible for the second one (fig. 10.6d). This effect is caused by the cone beam geometry of the setup, which is not taken into account by the Fourier transform.

require adding significantly more projections – are not of interest, which is not feasible for the second part (fig. 10.6b).

While in this example the CBCT geometry can be considered to be beneficial since fig. 10.6d cannot be obtained with a parallel beam setup, the opposite effect is also possible and even more likely to occur. Since the number of faces increase with each Platonic solid, it appears reasonable to assume that the number of faces determine the optimizability of the part for the CBCT case, irrespective of any symmetries. This is exemplary illustrated in fig. 10.7. Analogous to fig. 4.2, the Fourier transform of the object would result in a very sparse representation that allows imaging by a parallel beam setup with only two projections for the entire part or with only a single one if solely the grid pattern needs to be resolved. Unfortunately, this is not feasible if a CBCT setup is used instead, since only a single ray (marked green) is parallel to one part of the lattice at the same time. One can imagine cases where the angle between the edges corresponds to the HCA (e.g., fig. 10.6), which are in favor of the cone beam setup. However, in practice for typical industrial items most edges are parallel or perpendicular to each other and will only seldom coincide with this angle by chance. In such cases the optimizability can be qualitatively determined by counting the edges of the part (fewer edges are better optimizable) instead of using the metric introduced in sec. 10.2.

To further investigate the influence of the CBCT quantitatively, the steps described in sec. 10.4.1 were repeated where SDD and SOD were decreased while the magnification was kept constant, resulting in a wide half cone beam angle of approx. 22°. The results

(a) First Necessary Angle   **(b)** Third Necessary Angle
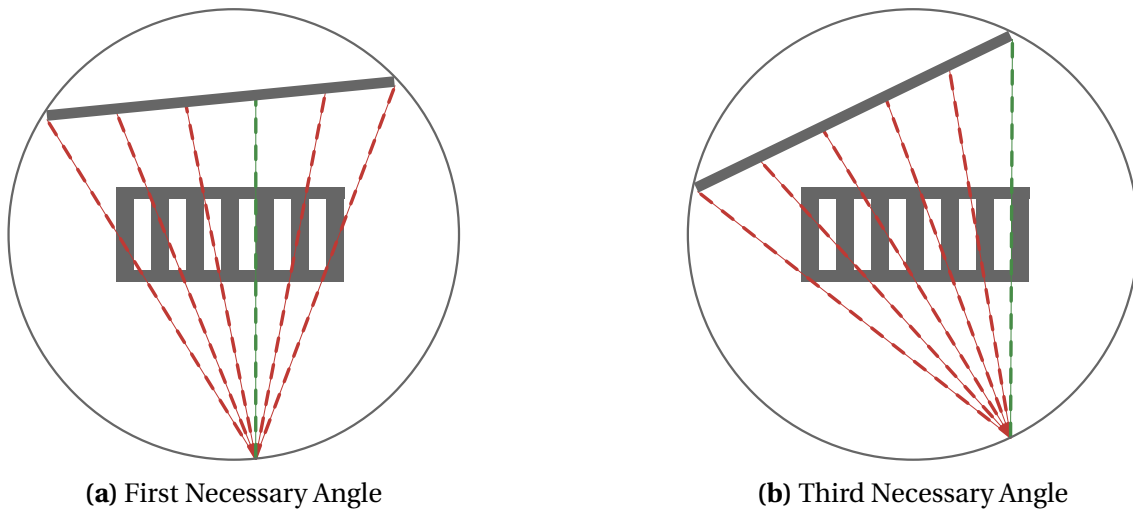
Figure 10.7: For a parallel beam setup, the vertical part of the grid could be imaged with a single projection. However, since the rays of a cone beam setup diverge, each edge needs to be captured separately as shown for the first (fig. 10.7a) and the third left edge (fig. 10.7b) of the lattice (counted from inside to outside, aligned ray marked green). As a result, significantly more projections are necessary for this example with a cone beam geometry compared to a parallel beam setup to obtain a reasonable reconstruction.

are shown in fig. 10.8. As expected, unlike in the parallel beam configuration, the performance of the tetrahedron (4 faces) appears now better than the cube (6 faces) due to its lower total number of planes. Also, the IQR values are generally lower, since one projection is now necessary for each plane, assuming that no two planes span precisely the cone beam angle.

Surprisingly, the optimized trajectory for all test bodies except the first two performs very poorly, with all IQR values being below 1.1 and even lower than 1 for a broad range. This is not linked to the optimizability of the parts; instead, the setup geometry violates the assumption of a small cone beam angle. The problem is illustrated in fig. 10.9. Exemplarily shown is the central section plane of a tetrahedron (green) and an dodecahedron, which is a regular hexaeder (red). As described in sec. 10.9 both are inscribed into a sphere (gray). As described in sec. 6.4.2, the Fisher information matrix used for the optimization is calculated based on a single evaluation point **E**, which is the central voxel of the VOI. For convenience the VOI is shown centered in the principal ray between source and detector. Modulation transfer function and noise power spectrum are predicted for the evaluation point and considered to be identical for each voxel in the VOI; this is equivalent to the assumption of a small VOI, where image characteristics do not change considerably, including the cone beam angle. This is an approximation, resulting in the angular errors α and β for each test object. These errors depend on the effective size of each object (i.e., the distance between evaluation point and outer edge) and the SOD, where smaller objects or larger SDDs lead to smaller errors α' and β' as indicated on the right side. It is apparent that the angular error for the given setup approaches the half cone beam angle for larger VOIs and therefore larger test objects, resulting in a very poor result of the optimization algorithm for such. For the smaller cube and tetrahedron objects the error is also smaller, so that still reasonable results can be obtained, while it is worst per definition for the sphere. Theoretically, this problem could be avoided by evaluating at each voxel position in the VOI. However, this would
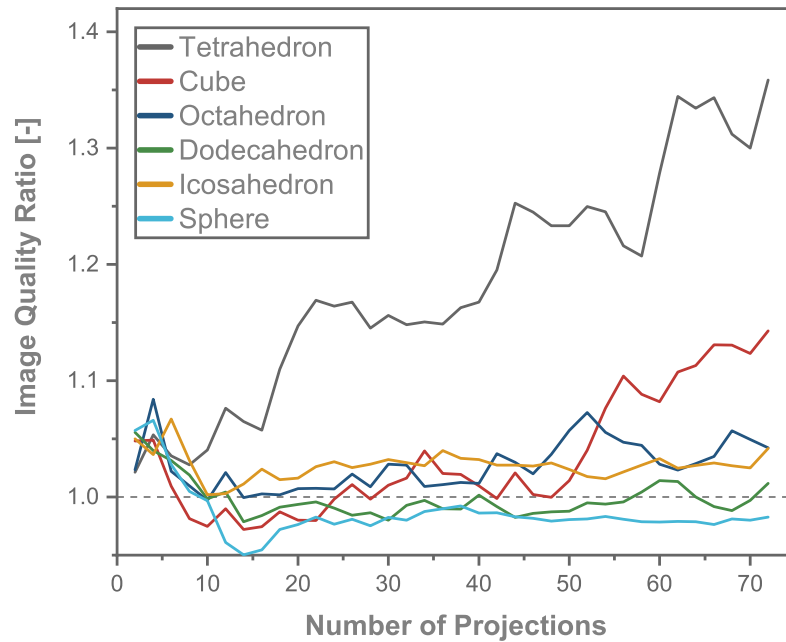
Figure 10.8: Image quality ratios for a wide half cone beam angle of 22°. The total achievable image quality ratio is greatly reduced and the relative performance of cube (6 faces) and tetrahedron (4 faces) change compared to the parallel beam case (fig. 10.5) since the overall number of planes becomes relevant instead of the number of unique faces. For the remaining, larger test objects the optimization algorithm fails as the IQR drops below 1; for a discussion see main text and fig. 10.9.

linearly increase the computational time; for this case with a size of (91 × 91 × 91) voxel the calculation would take approx. 750,000 times longer, which is clearly not feasible for practical use.

10.5   Industrial Example Applications

In section 10.4 the validity of the optimizability predictions have been investigated using artificial, mathematically defined test objects that correspond to extreme cases. In the following, an example application for the industrial parts introduced in sec. 7.3 will be used to demonstrate that the metric can also be applied to more realistic cases. While further details concerning this dataset have been previously published in a separate work [129], considerations concerning the optimizability have not been conducted in this paper and will be added in the following. Further details about this dataset are also summarized in sec. B.

As VOIs, an electric engine and the manipulation head of an industrial robot is considered. The former contains sharp, clearly defined edges and reaches a normalized optimizability of $\bar{\bar{\Xi}} = 0.80$. Contrary, the head part is round and highly symmetric, yielding a lower value of $\bar{\bar{\Xi}} = 0.71$. Both are very high values compared to the Platonic solids of sec. 10.4, which is probably a result of the smaller VOI ((49 × 49 × 49) voxels opposed to (91 × 91 × 91) voxels) that results in a coarser reachable angular resolution leading to a sparser distribution of the summed Fourier coefficients (see sec. 10.3).

IQR plots for both VOIs are shown in fig. 10.10 together with reconstructed slices for 16 projections. The comparably low projection number was selected since differences
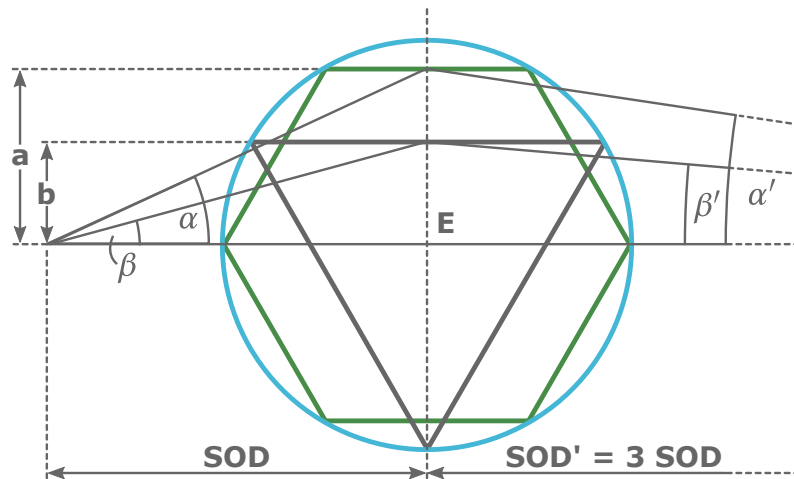
Figure 10.9: Influence of the CT setup and object shape, exemplarily depicted for horizontal cross sections of tetrahedron (gray) and dodecahedron (green), which are inscribed into the boundary sphere (light blue), together with their effective half-VOI sizes **a** and **b**. For performance reasons the optimization algorithm assumes a VOI-centered X-ray beam path passing through the evaluation point **E**. Low SDDs or large objects (**a**) result in a wide half cone beam (left side) and the angular errors α and β increase. Contrary, for smaller features (**b**) or higher SDDs a narrower half cone beam angle results (right), which leads to negligible angular errors α' and β'.

are better visible for few projections; additional reconstructions for more projections are provided in the related work [129]. As predicted by the optimizability metric, the IQR is higher for the engine, reaching values of approx. 1.5, while comparably low values around 1.2 are obtained for the head VOI. Both findings are also confirmed by the visual impression of the reconstructed volume slices. The IQR decreases after approx. 80 projections, while the head values are mostly constant over a longer range. In contrast, most Platonic solids have not reached the plateau in the investigated range until 72 projections in sec. 10.4.1. The optimized trajectory also outperforms the LDS reference for all projection numbers.

This example demonstrates that the optimizability metric derived in sec. 10.2 is capable to qualitatively predict how well a certain feature can be optimized even for complicated VOIs. The highest empirically obtained IQR values are approx. 3.2 in the extreme case of the cube (fig. 10.5) and 1.5 for the more realistic industrial part. This corresponds to a decrease of the RMSE of approx. 70 % and 35 %, respectively.

10.6   Relevant Projection Ranges for the Bat Phantom

Due to the considerations of chapter 4 this work concentrates on trajectory optimization with less than approx. 150 projections. However, for the simulated bat phantom optimized trajectories over almost the entire range up to 2,400 (of a set of 2,520) projections have been generated, so that these results are available for further analysis. The optimizability values were calculated as $\bar{\Xi} = 0.70$ for sphere and $\bar{\Xi} = 0.85$ for the cylinder, where the VOIs were of size (49 × 49 × 49) voxels as for the industrial parts in sec. 10.5. The IQR values are shown in fig. 10.11 and are in agreement with the optimizability values. In particular, the sphere reaches their first plateau at IQR values of approx. 1.2,
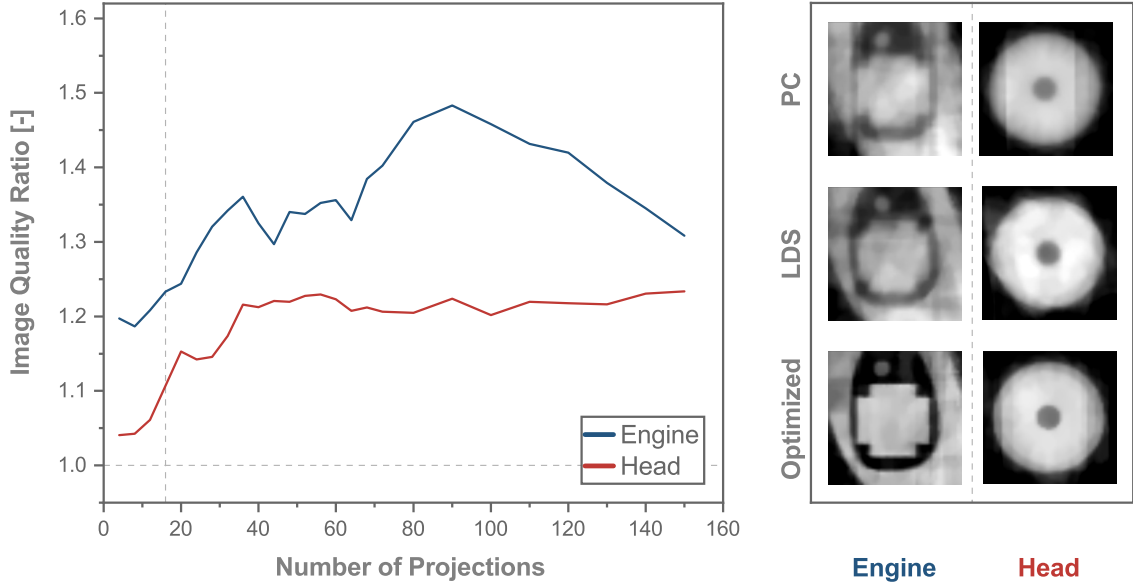
Figure 10.10: Image quality ratios (left) for the industrial example parts: as predicted by the optimizability values, the engine VOI ($\bar{\bar{\Xi}} = 0.80$) includes several salient edges and has consequently more potential for improvement via trajectory optimization than the round and symmetric head part ($\bar{\bar{\Xi}} = 0.71$). This is also obvious in the reconstructions (right) as shown exemplarily for 16 projections, where the image quality clearly improves for the engine but changes barely noticeable (to a human observer) for the head VOI.

which is identical for the head VOI ($\bar{\bar{\Xi}} = 0.71$) for which a similar optimizability was calculated. Interestingly, apart from the first, sharp IQR peak under 200 projections both features show a second peak towards very high projection numbers. This peak differs in magnitude, spread and location between both test objects and exceeds the primary peak clearly for the sphere. Since the IQR at 2,520 projections is 1 per definition, the second peak for the cylinder has to be even more narrow than the first one.

These findings suggest that apart from the optimization for low projection numbers on which this work concentrates on, there also exists a second range closer to the full projection set as proposed in sec. 4.5 where the adjustment of the trajectory is worthwhile. While the absolute RMSE difference of the second peak is negligible compared to the first one, where differences can typically be seen with the bare eye, the relative improvement in the high projection region can even surpass the potential in the first region in relative numbers. Such considerations could be relevant for metrological investigations using industrial CT scans. All of the left out projections are located opposite to already included ones or along the longest X-ray path in case of the sphere, with most of them being concentrated at the poles, i.e., the algorithm tries to achieve an angular uniform sampling pattern. Interestingly, the same distribution can be found at the much lower projection numbers at approx. 1,600 projections which indicates that the Fourier space is already completely sampled at this point and adding further projections only affects the noise. Since the dataset was generated by simulations with perfect detectors the only source of noise is given by the photon statistics determined by the attenuation values of the object, which is not critical in vertical direction and leads to preferable positions at the poles. The conclusion is that the extended plateau between approx. 1,600 projections to 2,000 projections arises due to the addition of pole-located projections that provide few further information and the decrease in image quality

111
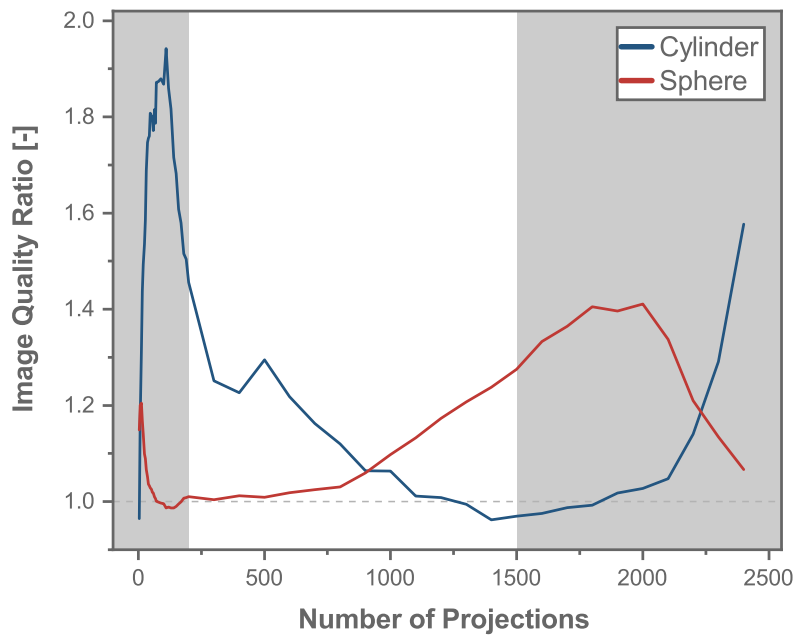
Figure 10.11: Image quality ratios for the bat phantom VOIs. While this work mostly concentrates on the region with low projection numbers, also a second range was identified where the optimized approach clearly outperforms the reference trajectory (both approximate ranges highlighted). The location of this second maximum is part-dependent and even higher than the first peak for the sphere.

for higher numbers is caused by including low-contrast ones in the horizontal plane. For the cylinder the result is similar, but most missing projections can be found in the regions outside the horizontal or vertical plane, since these correspond to the least important directions in Fourier space. In this case a homogeneous angular projection distribution seems to be less relevant and the distinct peak at high numbers corresponds to poses related to the longest X-ray path. Both results appear reasonable and are in accordance with the properties outlined in chapter 7. The high projection peaks could be more efficiently identified by adapting the trajectory optimization algorithm so that projections are successively removed from the full set. However, it is not yet clear if the resulting trajectory is identical to the ones shown here, which were generated by adding projections to the solution set. Furthermore, it is crucial to bear in mind that this discussion is based on the assumption that the best image quality is achieved by the full reconstruction with 2,520 projections as outlined in sec. 6.5.1, which is just a simplification to facilitate this analysis. It appears reasonable to assume that reference-less metrics like the Shannon entropy are better suited to assure representative image quality assessment in the high projection domain which, however, is beyond the scope of this work.

11 | Discussion and Outlook

While this work aims towards providing a set of tools and methods to facilitate and evaluate trajectory optimization for industrial CT, still several limitations apply and many questions that are important for its practical usage are yet unanswered. In sec. 11.1 an overview of such will be provided, while suggestions for further development are discussed in sec. 11.2. In general, the structure is organized with respect to the priority of each item, i.e., most relevant points are listed first.

11.1   Limitations and Open Questions

The framework proposed in this work is still far from being applicable for industrial routine and several points have to be clarified before a large scale application can reasonably take place. Probably the most pressing question that could not been answered in this work due to reasons outlined in part III, is how well optimizations based on simulations and measured projection data coincide (sec. 11.1.1). The clarification of this point is imperative for a broader use of trajectory adjustment methods, since time-consuming and costly experiments could be avoided in the workflow. Practical problems related to the adjustment of the setup (sec. 11.1.2) and mechanical optimizations of the path (sec. 11.1.3) are further limitations that should be solved in subsequent steps. The next question to be addressed should be how many projections are actually necessary to obtain a sufficient image quality (sec. 11.1.6). However, in order to give an accurate answer it is essential to first develop more reliable image quality metrics (sec. 11.1.4) and investigate their impact onto the POD (sec. 11.1.5) to avoid overlooking certain kinds of defects. Last, the influence of the inspected object geometry (sec. 11.1.7) and the consequences of spatially varying image properties (sec. 11.1.8) should be analyzed to gather experience on how to use such optimization methods and how much adjusted workflows can benefit in practice.

11.1.1   Transferability between Simulations and Test Objects

While the results presented in this work suggest that the input projections for the optimization framework can either stem from simulations (sec. 6.3) or experimental measurements (sec. 8 and 9), it is not yet clear if results performed on the former can directly be used for real world applications. Since the generation of synthetic datasets is significantly cheaper and easier than real measurements, it is desirable to evaluate to which extent simulation parameters need to agree with the measurement setup to obtain reliable results. Solving these questions would allow to optimize and refine a trajectory based solely on digital data (e.g., via CAD) so that no expensive measurements

need to be conducted at all before productive use. Furthermore, most of the experiments in this work were conducted using noise-free simulations of primitives (sphere and cylinder) or simple geometrical shapes (Platonic solids) that are not representative for typical industrial items in all aspects. For instance, the evaluations using the image quality ratio (IQR) in sec. 10.5 showed that the highest optimizability for such objects is achieved at much lower projection numbers than for other test bodies. Furthermore, the potential was much lower and decreased earlier, but showed benefits for symmetric parts over a longer projection range. For future developments it would be desirable to evaluate certain properties with more diverse geometrical shapes – preferably in form of predefined test datasets – to obtain more robust results.

11.1.2   Practical Routine Implementation

While the results presented in this work suggest that trajectory optimization has a high potential for many industrial scenarios, its realization requires that the proposed design can also be implemented swiftly in practice. Consequently, the uncomplicated mechanical realization of the respective movements, for instance of the source-detector system, needs to be easily adjustable in a shop floor environment. Unfortunately, setups offering the necessary flexibility and DOFs have only recently been developed (see sec. 5.3) and the technology is still in its infancy, which turns the detailed trajectory definition into a demanding and time-consuming task that needs to be performed manually in many small steps. In particular, adjusting the setup with respect to geometrical restrictions, accessibility and collision avoidance is still a major obstacle for its routine usage. To allow for trajectory optimization in a productive context it is essential to first facilitate the uncomplicated selection and adaptations of the proposed design [195].

11.1.3   Spatial Constraints and Smooth Trajectories

For the course of this work it was assumed that all positions on a sphere around the part can be reached by the acquisition setup. While this condition can be investigated by the use of simulation tools, it is clearly not feasible in practice due to kinematic and spatial constraints, so that the input data set was reduced accordingly for the experimental measurements (see sec. 8). In practice, such movement restrictions also apply for most medical [182, 191] and industrial setups [240] and in extreme cases only a two-dimensional trajectory optimization is possible. Particularly problematic with respect to spatial constraints are robotic installations, where often an accessibility of less than 180° can be achieved [230]. It seems reasonable to assume that such restrictions will also diminish the improvements that can be obtained by adjusting the acquisition poses. It shall also be noted that a smoothly connected trajectory as result of the optimization framework would generally be desirable, which was not investigated in this work to reduce the overall complexity. While some work has been performed towards generating a smooth and continuous curve as side condition of the optimization [190] it has also been shown that this can have a significant negative impact onto the achievable image quality when compared to discontinuous designs as used in this work [195]. However, for such trajectories the unproductive positioning time is also reduced, which increases the overall acquisition speed so that more projections can be generated in the same amount of time, which can improve image quality for a given time budget.

11.1.4 Robust Image Quality Indicators

Currently, no generally accepted image quality metric for reconstructed volumes exist that can be reliably applied to all use cases (see sec. 6.5.1). In preliminary investigations [136] for this work, five different image quality metrics have been considered in particular (RMSE, SSIM, mutual information, Shannon entropy and Fourier shell correlation). However, the evaluation of experimental data has still turned out to be demanding (see sec. 8). One reason is probably that the reconstructed volume represents a mathematically derived, highly artificial image defined in three dimensions, while most quality measures were developed for natural two-dimensional images. A universally applicable, stable and volume-defined image quality metric for CT data would clearly facilitate the evaluation of optimized trajectories and appears also relevant for other use cases and related future investigations.

11.1.5 Influence onto Probability of Detection

As repeatedly outlined in this work, features do typically not contain frequencies of the entire Fourier space, but span only a limited part of it. While this lays the foundation for trajectory optimization, several geometries that need to be detected are not known beforehand and not including the mandatory projections for related angles could lead to a significantly more difficult or even impossible detection of such. The incapability of resolving features and discontinuities that are not tangential to acquired poses [121] is particularly problematic for near-2D or 1D geometries like cracks [282], delaminations or interface layers (e.g., adhesive bonds). Furthermore, defect detection is a complicated task including many influence factors and even though a flaw is clearly visible in one part of the test piece, it might become less recognizable in other parts of the volume due to varying imaging properties and influence of the part geometry [283]. Currently, it is unclear how trajectory optimization approaches influence the probability of detection of such geometries; however, there is strong evidence [284] that these methods should not be used if certain kinds of flaws (e.g., very directed ones) need to be detected since they might disappear in the reconstructed images. In any case profound knowledge of the imaging task, likely flaws and the part as such are strongly required to safely apply trajectory optimization algorithms on a routine basis.

11.1.6 Definition of the Termination Criterion

For the course of this work the explicit definition of a termination criterion for the optimization algorithm was entirely avoided by repeating the calculation for different projection numbers, which results in the quality plots that were extensively used, e.g., in sec. 7. However, in practice it is typically not feasible to determine a projection number that leads to a sufficient image quality before the optimization step. One possibility would be to repeatedly reconstruct the optimized trajectory at different projection numbers and compare it to a reference like performed in this work. The termination criterion could then be defined as the number of projections that lead to an image quality that reaches a predefined threshold or does not change considerably anymore over a certain range; this corresponds to finding a plateau in the quality curves. Since a certain image quality does typically not have sufficient expressive value on its own, it would be desirable to link the probability of detection of certain kinds of flaws – which

is usually the property that one is eventually interested in – to a certain image quality value, combined with further properties of the object. This seems reasonable, since the concepts of POD and receiver operating characteristic curve (ROC) are related (see sec. 3.5). Unfortunately, these criteria would increase the computational costs of the algorithm due to the necessary but unproductive reconstruction steps so that alternative definitions are preferable. A more efficient method would be to determine the termination condition with respect to the optimizability value defined in sec. 10.2, which is computationally cheap and can be calculated before the expensive and time-consuming optimization, therefore allowing to decide if the effort is actually worthwhile. While a very first step towards such a criterion has been made in sec. 10.4 by qualitatively linking the image quality ratio to the optimizability, still significantly more work is required to define a feasible and reliable termination criterion that can be applied in practice.

11.1.7 Geometry Influence Investigation via Part Libraries

As outlined at various parts of this work (e.g., sec. 4.3), the potential of trajectory optimization approaches depends heavily on the definition of the imaging task and the shape of the object to be investigated. While this has been covered in sec. 10 for particular geometries, most experiments in this work have been conducted with only few test bodies due to computational constraints. In order to obtain more accurate and representative results it would be desirable to optimize not just few parts but entire databases of various different shapes and compare the outcome. Unfortunately, such a broad investigation was beyond the scope of this work since it requires significantly more measurements, time and computational power. However, for the easier case of discrete tomography problems such evaluations are often feasible and have been performed in most of the work presented in sec. 5.2.2.

11.1.8 Practical Impact of Spatially Varying Image Properties

Since the density of X-ray paths crossing a particular voxel varies over the geometry of the object, trajectory optimization can lead to spatially inhomogeneous image properties like noise, contrast or resolution [23] (see also sec. 4.5). While this is generally a desirable mechanism since the goal of the method is to improve these characteristics for the VOI, it is imaginable that the image degradation in other parts of the volume (see fig. 8.4) can lead to confusion for human observers or ultimately wrong conclusions. Furthermore, it is known that uncompensated, nonuniform resolution can lead to geometric distortions that impede image registration and the direct comparison of features at different locations within one image is not feasible for such cases [285, 286]. However, it is yet unclear to what extent these effects are relevant for practical trajectory optimization applications.

11.2 Further Work

11.2.1 Adaptations of the Optimization Approach

As stated in sec. 11.1, several questions are still unanswered, but also further developments to improve the performance of the trajectory optimization approach are also imaginable. Certainly by far the most important improvement would be to reduce the complexity of the method (sec. 11.2.1.1) to become independent of the predictor functions (sec. 6.4.2) and therefore avoid the necessity of costly parameter sweeps for the regularization parameter. Next, clarifying what the inspection task actually is can turn out to be very demanding and will usually require expert knowledge. Some approaches are imaginable that allow more flexibility in the task definition and extend its use to new application scenarios, which are discussed in sec. 11.2.1.2. While several methods, such as simulation-based refinement steps (sec. 11.2.1.3) or an extension of the parameter space (sec. 11.2.1.4) are possible to improve the outcome of the trajectory optimization, also advances concerning the computational speed are feasible. Such comprise, for instance, simplifications in form of partial trajectories instead of single projections (sec. 11.2.1.5) and reductions of the problem towards lower dimensions (sec. 11.2.1.6) or even a discrete formulation (sec. 11.2.1.7). While such optimizations are usually of relatively low relevance if sufficient calculation power can be provided (e.g., via cloud-based computation services), these approaches can become important if online optimizations (sec. 11.2.1.8) are required. However, such methods are usually less relevant in industrial practice, due to the existence of repeated inspection workflows and the broad availability of geometrical object data.

11.2.1.1 Simplified Framework

The optimization framework (see fig. 6.1) proposed in this work is generally complex and intertwines various effect by use of a model observer. Furthermore, the prediction framework is highly dependent on a (in advance typically unknown) regularization parameter and can even introduce a certain chaotic behavior in some cases. Consequently, a drastic simplification of the approach is desirable; a suggestion for such is depicted in fig. 11.1, which combines several already existing approaches. In sec. 10 it was demonstrated that the potential of the trajectory optimization is particularly high if the VOI to be optimized is relatively small. Taking advantage of this, a reconstruction stage of this small local volume can be included in the optimization loop, which becomes computational feasible by a high degree of parallelization and replaces the prediction framework. The relevant optimization properties can be assessed by separate metrics instead of the MO. For the image quality, for instance, a figure of merit like the RMSE or SSIM used in this work could be used. In fact, for a very similar framework promising results have been reported using either SSIM, FSIM or a averaged PSF (see sec. 5.2) [180–182]. Also, noise-quantifying metrics like the Shannon entropy or edge-based metrics are conceivable. The ASFC maps introduced in sec. 10.2 are a helpful method to identify valuable poses with respect to the part to be optimized, since these are located perpendicular to points with particular high summed Fourier coefficients in the diagram (termed Fourier weighting in fig. 11.1). Last, the geometric weighting proposed in this work can still be used to enforce a high coverage of the Fourier space. However, more direct methods of accomplishing this goal have been
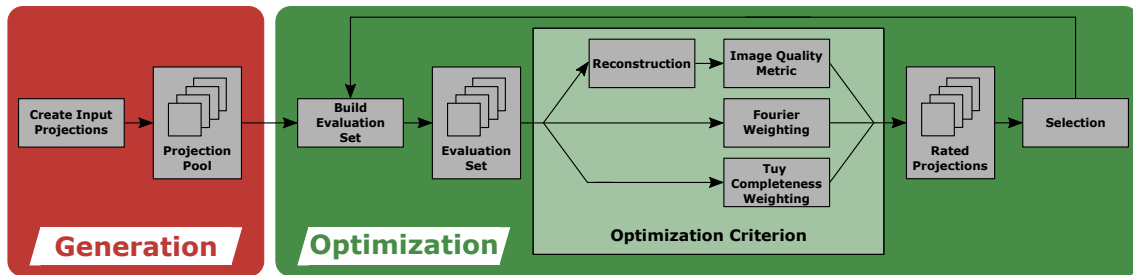
Figure 11.1: Proposed simplified framework for the trajectory optimization. For small VOIs and a high degree of parallelization of the main loop the reconstruction stage becomes computationally feasible and can replace the prediction framework. Separate assessment and pooling of the different optimization properties reduces the overall complexity considerably.

proposed, so that a weighting based on, for instance, the local Tuy criterion [174, 175] or a combination of sampling density and data incoherence [30] might be preferable.

11.2.1.2 Practical Signal Template Definition

The definition of a signal template ω as described in sec. 6.4.1 has been relatively straightforward for this work, since VOI and object of interest were always clearly defined. Furthermore, in all cases only one relatively small VOI was considered to reduce the computational cost. However, the task definition can be problematic in practice, since often the shape, type, and location of potential errors are not known in the first place. While in the course of this work, trajectory optimization has been suggested primarily for repeated scanning of known objects (e.g., inline-CT), where one is typically already familiar with the object, also different other application scenarios are conceivable, where the imaging task cannot be defined directly. Typically, expert knowledge will be required to define areas where defects might occur. Detailed information concerning flaw types and sizes are necessary to adapt the VOI and template definition accordingly. Alternatively, e.g., for additive manufacturing or machine tools, production parameters may be available that support specifying the task. As shown in sec. 8.3, it is important to select these parameters carefully, since image degradation in other parts of the object can occur. Furthermore, it is possible to define several VOIs of similar importance with distinct templates and combine their separate detectability values into a single figure of merit. While several possible combination strategies for this have been proposed [190], it shall be noted that the use of too many separate VOIs is not recommended, since it reduces the potential of the optimization method as discussed in sec. 8.3. However, it not impossible that the optimized trajectory with such a task definition is still able to outperform a conventional planar trajectory in some cases. The framework can also be relatively easy extended to predict MTF, NPS, and the result of the computed MO for several evaluation points. While this increases the computational burden almost linearly, it would also allow the investigation of larger VOIs, since the influence of the cone beam error (sec. 10.4.2) can be mitigated by the use of several separate evaluation voxels and the recombination of the predicted quality properties into a single metric. As extreme case, one might even define the entire geometry as task template and use the complete volume as VOI, which of course is computationally not feasible at the moment and might yield insufficient results due to the huge VOI size. An

alternative, computationally less demanding attempt for such scenarios is the method of Haque et al. [179], which has been outlined in sec. 5.2.

11.2.1.3 Refinement via Simulation and Parameter Sweeps

A fundamental problem of the proposed optimization method is its formulation as selection problem, i.e., the achievable solution depends on the number of the input projections, which in return depend on the angular resolution of the simulation. While the 5°-steps used in this work have turned out to be sufficient for most cases, it seems likely that a finer sampling could lead to an improved solution. For instance, in case of the platonic solids theoretically the IQR plots should rise at the distinct number of edges for each test body, which was not observed and is believed to be caused by the insufficient angular resolution. However, increasing the size of the input stack would lead to a higher computational cost and higher time demands. As compromise, the framework could be modified, so that additional projections are simulated on-the-fly for spatial position areas that have been found to be valuable, e.g., starting with explorative 5° steps and refining to 1° or less for regions corresponding to high values of the figure of merit. Since the simulation is relatively fast if most degradation mechanisms (e.g., scattering) are not considered and the projection size can be reduced to the relevant part that backprojects into the VOI, the additional computational and time demands are believed to be well manageable. It is also possible to replace the simulation framework entirely by few initial measurements of the object and optimize iteratively on the reconstructed result of this estimate as suggested, for instance, by approach 17 in sec. 5.2. Similarly, the regularization parameter sweep could subsequently be improved by refining the step size for values and projection numbers providing good results.

11.2.1.4 Extension of Parameter Space

In this work only the source position defined by its two angular coordinates has been optimized. However, a CT system is a complex setup with many additional parameters that could be considered as well for the optimization, making the appropriate choice of the acquisition trajectory only one of several possible improvement methods which can be combined to further reduce scan times; a review of related automation methods is provided in the literature [287]. For instance, approaches aiming at determining suitable imaging parameters (e.g., prefilter, tube voltage or current) have been proposed for several applications [165, 288]. As mentioned in sec. 4.3 and suggested for a similar framework [190], additionally adjusting the SOD, SDD, or rotation center could lead to better results since a projection can be selected tangential to more than one non-parallel edge, and the SNR can be improved while imaging a sufficiently large fraction of the VOI at the same time. Furthermore, the image quality assessment and prediction used to compute model observers can also be extended towards other factors. For fixed trajectories, this has already been performed for tube current modulation [87, 289], the FDK filter kernel [289], the regularization parameter for an iterative reconstruction [87, 88], and further parameters [290]. However, such augmentations are often more demanding for many reconstruction algorithms, which can lead to new artifacts or higher computational demands. Also, due to time and performance restrictions, more powerful hardware is necessary to further extend the parameter space of the optimization framework.

11.2.1.5 Optimization of Partial Trajectories

One possible simplification to increase the computational performance is to optimize not in steps of single projections but of projection sets instead. For instance, grouping acquisition positions and treating them as an inseparable set can reduce complexity clearly and similar approaches have already been suggested [181]. While this will probably slightly decrease the outcome in terms of achievable image quality, an appropriate choice of these subsets can also fulfill further side conditions so that the efficient filling of the Fourier space (sec. 7.3) is achieved without additional calculations. Alternatively, instead of selecting partial trajectories, one might think of cases where only one projection of each set is permitted. For instance, splitting the evaluation dataset in arc subsets with constant ϕ and only allowing one pose of each set, automatically results in a smooth trajectory that is easier to implement on mechanical setups. In practice, particularly for robot-guided CT systems, it is often not feasible to obtain projections from more than approx. 180° of the horizontal plane. Consequently, it appears reasonable for such cases to adapt the input projection set to contain only images from slightly more than a half sphere in order to sample the entire Fourier space due to cone-beam effects (see sec. 4.1). This restriction would speed up the computations by a factor of approximately two and avoids the necessity to weight projections that are opposed on the sphere while probably still yielding good results (see also sec. 9).

11.2.1.6 Reducing Dimensionality

A problem for most methods proposed in this work is that the computational burden increases significantly if the considered volume sizes are getting larger. In principle it is possible to combine several pixels or voxels of an image or volume (e.g., via building the average or median) into a new one with reduced resolution and perform the optimization and computational steps on this one instead. This method, referred to as binning, can greatly reduce the dimensionality of the problem and increase performance. Unfortunately, there is a certain threshold until which this approach is feasible. For binary tomography similar volume sizes as used in this work have been found to provide acceptable results [291]. While it is yet unclear if this finding is directly applicable for CT with multiple gray values, methods of this kind appear promising to tackle practical problems caused by large volumes or detectors with a high number of pixels and reduce calculation times.

11.2.1.7 Reduction to Discrete Problem

Unlike in the medical field, the objects scanned by industrial CT systems typically consist of only few different materials. In many relevant cases (e.g., parts produced via additive manufacturing) only a distinction between air and a much denser material needs to be performed. In such situations, the task can be formulated as discrete tomography problem, which is considerably easier and allows additional trajectory optimization approaches (see sec. 5.2.2 for an overview) that require fewer projections than conventional CT [210]. Furthermore, the reconstruction can be performed faster and more efficiently, which is particularly interesting for future methods (e.g., the one proposed in fig. 11.1) and specialized algorithms for such cases are available [203, 205, 207, 292].

11.2.1.8   On-the-Fly Optimization

The method proposed in this work requires a description of the part geometry (e.g., as CAD file) to compute projection candidates for the optimization step. However, it is possible to acquire a small number of (e.g., equiangularly distributed) projections in an initial scan, reconstruct them and use the result as initial guess instead of the part geometry. Subsequently the optimization is performed and these steps can be repeated multiple times. While the feasibility of such an approach has been demonstrated for a different optimization framework [198], its performance is yet unknown for larger dimensions and very complex geometries. Furthermore, it shall be noted that in most industrial application scenarios for trajectory optimization – for instance the repeated measurement of similar parts – the geometry is typically already available [22] so that on-the-fly methods are only necessary in a limited amount of cases.

11.2.2   Extension of the Optimizability Metric

The optimizability metric derived in sec. 10.2 is only valid for parallel beam geometry, which is usually not or only approximately fulfilled by most setups. Consequently, an augmentation towards CBCT appears reasonable (sec. 11.2.2.1). It could further be related to other properties that are relevant in industrial practice, which would increase its expressive value as a predictor if trajectory optimization can be applied well to a given scenario (sec. 11.2.2.2). Also, the concept of ASFC maps has been found to be helpful and could be further developed towards new use cases or optimization algorithms as outlined in sec. 11.2.2.3.

11.2.2.1   Adaptation for Cone Beam Geometry

A drawback of the optimizability metric is that it is only accurate for approximately parallel X-ray beams. While it is feasible to adapt the computation so that the divergence of a cone beam setup and the feature's off-center position is considered, this does not allow the direct use of the fast Fourier transform as efficient calculation method. However, such an adjustment would be beneficial for practical usage and to obtain more representative information than just counting the faces of a part for the CBCT case, which can be considered more a rule of a thumb than a detailed analysis.

11.2.2.2   Link to Practically Relevant Properties

To provide more accurate and economically more relevant information than the interval between zero and one in which the optimizability metric is defined (eq. 10.3), it would be desirable to link the total number of saved projections or the image improvement for a given number of projections to a value of this figure of merit. However, this would likely require to include additional parameters such as the cone beam angle or further information about the imaging conditions and would probably be very complex. Also, a link to the probability of detection would be desirable in the long term, which might, however, even more demanding to determine.

11.2.2.3 Combination with Attenuation Map

Furthermore, the optimizability was investigated with respect to the Fourier space representation of the object, but without taking further important properties like the SNR into account. Analogous to the ASFC plots, an attenuation map based on the summed material attenuation values in one spatial direction could be determined. By combining this second representation with the ASFC map a modified map could be computed that is not only more representative if used for the search of valuable acquisition poses but could also result in a more precise optimizability value. Based on these considerations, a simplified optimization framework is proposed in sec. 11.2.1.1. For the sake of completeness, it shall also be noted that the sparsity of the transformed feature space can not only be exploited for optimized acquisition (for instance for compressed sensing approaches) but as well for data compression and storage [108]. Consequently, the optimizability metric could, in theory, also be used to quantify the degree of compressibility (see also sec. 4.2).

11.2.3 Faster Image Acquisition

While most approaches for performance advances suggested in this section concentrate on the use of algorithms considering a limited amount of data, additionally also other enhancements are conceivable that directly increase the imaging speed of the CT system. Such concepts comprise better hardware (ref. 11.2.3.1), post-processing algorithms (sec. 11.2.3.2) or an automatic choice of appropriate imaging parameters (sec. 11.2.3.3). Supplementary to the improved instrumentation, also the implementation of mechanical adjustments, such as continuous image acquisition (sec. 11.2.3.4) or the use of several X-ray sources and detectors (sec. 11.2.3.5) can improve the overall scan speed.

11.2.3.1 Improved X-ray Tubes and Detectors

The usage of X-ray tubes with a higher output power and photon flux is generally an effective method to reduce detector exposure time for a given SNR so that remarkable enhancements in scan speed can be obtained if used in combination with fast read-out electronics. Unfortunately, this is typically linked to a higher thermal load to the target, so that larger focal spots are required that inherently lead to image blurring. To mitigate this effect, alternative tube designs such as liquid metal jet [293] or line focus [294] based configurations have been proposed that are able to achieve a higher photon flux while retaining a comparably small focus. Other, less common, methods comprise synchrotron light sources [295] and pulsed flash X-ray tubes [27], which are more complex in handling and therefore only applicable for special cases.

11.2.3.2 Compensation for Blurred or Noisy Projections

Instead of tackling the issue of increased focal spots using improved hardware, an alternative is extensive software-based post-processing. Recently, such an approach using convolutional neural networks was proposed to resharpen blurry projection images. The method allowed the operation with a higher photon flux, while maintaining a comparable image quality, so that the acquisition was feasible almost three times faster than a conventional scan [296, 297]. The reverse is also imaginable: images are

obtained by reduced detector exposure times, which leads to noisy but sharp projections that can subsequently be enhanced, e.g., by other machine learning algorithms. For this method, scan time reductions of over 60 % have been reported [268]. A third viable option is to perform the denoising operation on the reconstructed volume instead of the projection data [298]. Such approaches are in particular attractive since they can be applied independently from other optimization methods.

11.2.3.3   Modulation of Imaging Parameters

Higher part thicknesses or denser materials lead to a decrease in SNR, which makes related acquisition poses less favorable as shown in this work. Furthermore, in particular for very different path lengths or multi-material objects it can be difficult to balance the applied X-ray energy due to limitations of the dynamic detector range [155]. As a consequence, X-ray tubes with current modulation and variable voltage selection are available for medical imaging, which are able to adjust several parameters for each projection accordingly to obtain a uniform SNR, while delivering an as low as possible radiation dose to the patient [299]. Applying a similar concept to industrial CT by dynamically changing the exposure time for each projection instead of the tube parameters seems reasonable. While fast power-switching of the tube is generally demanding, the comparably slow rotation and acquisition speed of industrial CT systems simplify the use of such methods compared to medical setups [21]. While some work has been performed on automatically determining preferable acquisition parameters [288], also augmentations towards dynamic settings are conceivable. Such a modulated system would be able to acquire projections more efficiently from directions with a short X-ray pathlength, while making better use of the dynamic detector resolution simultaneously. The concept could also be extended to different other imaging parameters like pixel binning or tube voltage. It shall also be mentioned that the binning of detector elements reduces the effective pixel pitch, which results in less required projections according to eq. 4.2 at the cost of decreased resolution.

11.2.3.4   Acquisition in Continuous Motion

For this work, the projection images were acquired in distinct positions with the source-detector system standing still. However, it is also common to generate images without stopping the setup but in a continuous motion movement instead, which is more time-efficient. While this is not always viable for most application scenarios in this work based on separated projection positions, it can be a reasonable choice for connected and smooth trajectories (see sec. 11.1.3) in the future.

11.2.3.5   Simultaneous Acquisition by Multiple Sources

In theory, a straightforward method to increase the speed of data acquisition is the usage of several separate source-detector systems (or parts thereof, e.g., for electron beam CT) instead of a single one and a wide range of such setups has been proposed [300]. While such methods can increase the scanning speed remarkably, also the setup becomes much more complex and expensive. For many inspection scenarios like robot-based CT, particularly spatial restrictions make it very difficult or even impossible to increase the number of X-ray sources or detectors at all. As a consequence, this method seems yet to

be a viable option only for special applications, for instance airport baggage scanners [24], but might provide a valuable concept in some cases, given further technological advancements.

11.2.4 Further Improvement Methods

In addition to the approaches suggested so far, also several methods can be applied that combine trajectory optimization with already existing concepts, leveraging the advantages of both techniques. For instance, the usage of modern iterative reconstruction algorithms is not only reasonable as stand-alone method, but can be used to further improve the image quality of sparsely sampled trajectories (sec. 11.2.4.1). Similarly, interpolating the missed out projections can enhance the achievable image fidelity significantly, even though its value as inspection modality might be reduced (sec. 11.2.4.2). Since CT or radiography is only a single modality, the combination with different other NDT techniques can help to obtain more information about a given part (sec. 11.2.4.3) and can further be used as additional input for data fusion or specialized reconstruction algorithms (sec. 11.2.4.4). All these methods are comparably relevant since they satisfy different application scenarios.

11.2.4.1 Advanced Reconstruction Methods

While the SART reconstruction (see sec. 2.3.3) used in this work has previously demonstrated good results for undersampled and non-uniform data [36, 55, p. 201], modified versions are available that have been reported to perform even better under certain conditions [230, 301]. Furthermore, over the last decades a myriad of different reconstruction methods for various applications and conditions has been developed. For instance, CS-inspired methods (e.g., such based on total-variation minimization) have turned out to be well-suited for scenarios where only a very limited number of projections is available [21, 210, 302], which could provide better results than the algorithm used in this work, if applied and tuned properly. As an example for such, prior image constrained compressed sensing (PICCS) has been reported to provide accurate results using only about 20 projections [303]. Recently, several machine learning based reconstruction methods have been proposed that are also able to deal well with sparse information [304]. Particularly for inline-CT, Janssens et al. proposed such an algorithm, referred to as neural network Hilbert transform based filtered backprojection (NN-hFBP) that is able to provide reasonable results with relatively few projections in less than a second [305]. It was later extended with an automatic defect-recognition method [306]. Similarly, Pereira et al. suggested a method for sparse inline-laminography [270] and Russ et al. presented a fast reconstruction algorithm for non-circular acquisition orbits [271]. A non-exhaustive overview of CBCT reconstruction algorithms developed before 1990 [307], iterative methods already implemented by major vendors [308] as well as performance evaluations for several iterative [309] and machine learning based [269] methods for sparse projection data are provided in the literature.

11.2.4.2 Sinogram Interpolation

The use of few projections can lead to view alising artifacts if a backprojection-type reconstruction algorithm is used [310]. While typically iterative methods are better

suited for such cases [55], these approaches are still preferable under some conditions due to their lower computational complexity. A possibility to reduce arising artifacts for such applications is to interpolate within the incomplete sinogram (see fig. 2.4) in order to restore the missing parts, which has been proposed already in the 1970s [103, 311]. Even rather simple approaches like linear interpolation can already reduce streak artifacts greatly [312] and further work based on the sinc-interpolation has been performed [313, 314]. Unfortunately, it was also shown that both methods inherently lead to slightly blurred images due to low-pass filtering [315]. Instead of interpolation, it has also been suggested to obtain the missing projections by forward-projecting the limited view reconstruction and subsequently applying several filtering and post processing steps. It is also possible to forward-project instead of using actually measured positions and use the deviation to those for artifact suppression [310]. Other methods based on displacement functions [20], a sine-wave approximation referred to as warp [316] or directional interpolation [317] have been suggested as well and lately machine-learning based methods have increasingly gained attention [318]. Recently, Wei et al. proposed an advanced framework that combines several methods and includes an additional refinement step [319]. A good overview of further approaches can be found in the literature [316]. Sinogram-based image enhancement methods have also been successfully applied for metal artifact reduction [320] as well as compensation for undersampled PET [321] and SPECT [322] data. It shall be noted, however, that – if applicable with enough samples – trajectory optimization is generally preferable to such interpolation based artifact compensation methods, since there is no guarantee that the restored data are identical with the real data [176] as discussed in sec. 11.1.5. This is particularly relevant if important discontinuities like flaws or voids occur, while adjusted trajectories might be able to acquire information from this region.

11.2.4.3 Combination with Further NDT Modalities

While this work focuses on the use of CT for non-destructive inspection, also further modalities are of interest in the context of trajectory optimization. For one, it has been shown that other X-ray based methods, such as dark field [194] and likely also phase contrast CT can benefit from such approaches due to the improved SNR, which can be relevant, e.g., for dynamic imaging of biological processes [323] as mentioned in chapter 1. But also robotic inspection systems are generally well suited for the use with additional sensors. For instance, a system recently entered the market that can be equipped with further capabilities, such as optical surface scanning, thermography, air-coupled ultrasound and even more exotic applications like X-ray fluorescence imaging and diffraction or absorption spectroscopy due to the use of photon-counting detectors [281]. The additional information obtained from such sources can then further be used for data fusion [324, 325] or the generation of a digital twin of the inspected part.

11.2.4.4 A Priori Knowledge

One often encounters the situation that preliminary information for the specimen is available, originating for instance from earlier scans, blueprints or other imaging modalities. This information can be used via data-fusion to improve the final image, which is particularly beneficial to reduce artifacts that arise if only view projections or such originating from a limited angle are available [324, 326, 327]. Also, often only

image differences between scans are of major interest, for instance in industrial defect recognition (e.g., inline-CT of many similar parts) or medical follow-up scans. In such cases, one is actually only interested in smaller changes, for which an even sparser representation is possible than for the entire scan and modified reconstruction methods are available that aim to provide particularly efficient solutions to this problem [21].

12 | Overview and Conclusion

12.1 Summary

This work started with a brief overview of the basics of CT imaging (sec. 2) and the statistical theory required for the methodology (sec. 3). In sec. 4 preliminary considerations were discussed regarding the influence of projection numbers and ranges as well as their practical implications. Furthermore, based on compressed sensing and signal theory it was outlined why trajectory optimization is feasible at all and a more detailed definition of the problem was provided. Relevant preliminary investigations in the literature were gathered in sec. 5.

Based on such previous work, in sec. 6 the methodology was outlined, which comprises an algorithm to optimize a trajectory with respect to a given part and without performing any expensive reconstructions. Furthermore, the framework allows direct evaluation of the resulting trajectory and comparison to conventional designs. The optimization criterion of the algorithm was refined in sec. 7 and used to identify three important properties. First, the signal-to-noise ratio needs to be maximized. This was achieved by reducing the noise level by avoiding projections that correspond to highly attenuating parts of the object and favoring those that result in a good visibility of the relevant parts of the volume. Furthermore, it appears important to sample the Fourier space as completely and homogeneously as possible, where directions corresponding to high coefficients of the Fourier-transformed VOI are most important. It was shown that most state-of-the-art approaches directly or indirectly aim to include these properties in their respective implementation.

The feasibility of the optimization framework and confirmation of the simulation-based findings was demonstrated using experimentally acquired data in sec. 8. It was additionally shown that an optimization towards one VOI can lead to a decrease in image quality in other regions of the part. As a consequence, it seems reasonable to assume that trajectory optimization works best for few and small VOIs. Both taken assumptions are considered to hold independently of the optimization algorithm used. To demonstrate that the method can be applied in practice and for multi-material parts, a feasibility study using a robot-based CT platform was conducted. Several minor adaptations were necessary to meet the requirements for this setup particularly with respect to the limited accessibility and range of motion. Due to the specific object geometry the planar reference trajectory was clearly outperformed by spherical designs, while the optimized trajectory performed best for all investigated projections numbers. This is considered to be the first successful proof-of-concept of a part-specific trajectory optimization for a robotic industrial CT system.

In section 10 the practical relevant influence of the part geometry was investigated. By quantifying the sparsity of the angular Fourier coefficient distribution of the Fourier-transformed object, an optimizability metric, denoted as Ξ, was derived as predictor of the trajectory optimization potential for a given part in case of parallel X-rays. The metric was validated using artificial (sec. 10.4) and more realistic (sec. 10.5) examples. The concept of ASFC maps was introduced, which are a side product of the calculation of Ξ and can be used to identify valuable angles that are of interest for trajectory optimization. To compare with experimental in silico observations, the image quality ratio (IQR) was defined to quantify the optimizability if an already optimized trajectory design is available. With this second metric it is possible to additionally identify particularly valuable ranges of projections. Evaluations based on the given examples suggest that at least two of these ranges exist, being located in the domain of very few and close to all feasible projections. Furthermore, these projection ranges were found to be highly part dependent and confirm the assumptions given in sec. 4.5. Last, it was shown that for typical industrial parts a low cone-beam angle is preferable and that the optimization framework can fail when a too large angle or VOI is selected.

12.2   Conclusion

Circular standard trajectories typically used for industrial CT are suboptimal, since they are defined without consideration of the particular object and inspection task. Furthermore, in practice the application of such common approaches is often impeded by motion restrictions and artifacts associated with poor radiolucency, which holds especially for flexible setups or large parts. To improve performance with respect to image quality and throughput of evolving versatile CT scanners and leverage the effect of optimized sampling patterns, this work aimed to identify valuable acquisition poses and evaluate the practical consequences of such adapted trajectories.

The investigations and examples provided in this thesis have demonstrated that trajectory optimization methods have remarkable potential. This goes particularly for often encountered scenarios like low cone beam angles or large distances between X-ray source and detector. But also demanding imaging situations, which are characterized by highly attenuating and low-contrast objects in close proximity to each other can benefit from such approaches, which has also been suggested by similar work [191]. Additionally, irregularly shaped or large components with strongly differing aspect ratios can benefit greatly. Most of these conditions typically appear in the inspection of industrial items and especially for CT systems with many degrees of freedom. Considering a spherical trajectory as reference and for noise- and artifact-free simulations of typical industrial items, image quality improvements (according to the RMSE criterion) in the range of 35 % to 70 % were evident (sec. 10.5). Furthermore, it seems reasonable to expect even higher gains for more realistic imaging conditions. In the first representative investigation for an implementation on a robot-based CT scanner, it was possible to achieve quality enhancements on the order of 40 %, which is equivalent to a measurement time reduction by approx. 55 % compared to the conventional planar standard trajectory (sec. 9). While this work has focused on relatively few projections (fewer than about 150 images), where the highest gains in image fidelity can be expected, further results have been presented which suggest that relevant advances can also be reached for very high projection numbers (see sec. 10.6).

While these findings clearly show the potential of the proposed methodology, it needs to be stressed that trajectory optimization is by no means a universal remedy that can be carelessly applied. Instead, profound knowledge of the inspected object and the imaging task is imperative for reasonable and consistent results. While, correctly used, the optimized trajectories performed in no observed case worse than the standard approach, several practically relevant questions are yet unclear and require further investigation (see sec. 11.1). Furthermore, while it has been shown that not all parts and problems benefit equally from such methods, first steps towards the assessment of inspection scenarios with respect to their suitability for beneficial trajectory adjustments have been suggested (sec. 10). It also needs to be stressed that in practice, the choice of the acquisition trajectory is not solely guided by the problem itself, but also depends on further criteria. Such can be, for instance, accessibility, the available setup and its specifications (e.g., positioning accuracy or permitted inspection volume), time demand, accomplishable adjustments in the shop floor environment and many other factors.

Trajectory optimization techniques combined with iterative reconstruction algorithms could pose a remedy for the limitations in achievable cycle times of current CT setups that prevent their broad usage in industrial mass inspection. However, inline-CT can only have any practical impact if an automated analysis of the scan data is available [328] and it is embedded in a comprehensive inspection framework. This may comprise many individual parts that range from sample handling mechanisms and real-time defect recognition to data fusion, storage and reporting routines. As such, optimization approaches as proposed in this work should not be considered an isolated concept. Instead, they must rather be understood as a part of the journey towards a wider and more economical use of industrial CT systems and a highly sustainable method of non-destructive inspection.

Bibliography

[1]   Villarraga-Gómez, H., Herazo, E., and Smith, S., "X-Ray computed tomography: from medical imaging to dimensional metrology," *Precision Engineering*, vol. 60, pp. 544–569, 2019.

[2]   Kruth, J. P., Bartscher, M., Carmignato, S., Schmitt, R., De Chiffre, L., and Weckenmann, A., "Computed tomography for dimensional metrology," *CIRP Annals*, vol. 60, no. 2, pp. 821–842, 2011. Available Online: http://www.sciencedirect.com/science/article/pii/S0007850611002083

[3]   Weckenmann, A. and Krämer, P., "Computed tomography in quality control: Chances and challenges," *Proceedings of the Institution of Mechanical Engineers, Part B: Journal of Engineering Manufacture*, vol. 227, no. 5, pp. 634–642, 2013. Available Online: http://journals.sagepub.com/doi/abs/10.1177/0954405413479849

[4]   De Chiffre, L., Carmignato, S., Kruth, J. P., Schmitt, R., and Weckenmann, A., "Industrial applications of computed tomography," *CIRP Annals - Manufacturing Technology*, vol. 63, no. 2, pp. 655–677, 2014. Available Online: http://www.sciencedirect.com/science/article/pii/S0007850614001930

[5]   Thompson, A., Maskery, I., and Leach, R. K., "X-Ray computed tomography for additive manufacturing: a review," *Measurement Science and Technology*, vol. 27, no. 7, p. 072001, 2016. Available Online: http://stacks.iop.org/0957-0233/27/i=7/a=072001

[6]   Bauer, F., Schrapp, M., and Szijarto, J., "Accuracy analysis of a piece-to-piece reverse engineering workflow for a turbine foil based on multi-modal computed tomography and additive manufacturing," *Precision Engineering*, vol. 60, pp. 63–75, 2019. Available Online: https://www.sciencedirect.com/science/article/pii/S014163591830816X

[7]   Kolb, C. G., Zier, K., Grager, J.-C., Bachmann, A., Neuwirth, T., Schmid, S., Haag, M., Axtner, M., Bayerlein, F., Grosse, C. U., and Zaeh, M. F., "An investigation on the suitability of modern nondestructive testing methods for the inspection of specimens manufactured by laser powder bed fusion," *SN Applied Sciences*, vol. 3, no. 7, p. 713, 2021. Available Online: https://doi.org/10.1007/s42452-021-04685-3

[8]   Kiefel, D., "Quantitative Porositätscharakterisierung von CFK-Werkstoffen mit der Mikro-Computertomografie," Thesis, 2017.

[9] Ciliberti, G. A., Janello, P., Jahnke, P., and Keuthage, L., "Potentials of full-vehicle CT scans within the automotive industry," *World Conference on Non-Destructive Testing (WCNDT 2016), Munich, Germany*, 2016.

[10] Buratti, A., Grozmani, N., and Schmitt, R., "Optimisation of the number of projections in industrial X-ray computed tomography for dimensional measurements on multimaterial workpieces," *EUSPEN 2018, Venice*, 2018.

[11] Buratti, A., Ben Achour, S., Isenberg, C., and Schmitt, R., "Frequency-based method to optimize the number of projections for industrial computed tomography," *6th Conference on Industrial Computed Tomography, Wels, Austria (iCT 2016)*, 2016.

[12] Villarraga-Gómez, H. and Smith, S., "Effect of the number of projections on dimensional measurements with X-ray computed tomography," *Precision Engineering*, 2020.

[13] Nagy, A. and Kuba, A., "Reconstruction of binary matrices from fan-beam projections," *Acta Cybernetica*, vol. 17, 2006.

[14] Kazantsev, I. G., "Information content of projections," *Inverse Problems*, vol. 7, no. 6, pp. 887–898, 1991. Available Online: http://dx.doi.org/10.1088/0266-5611/7/6/010

[15] Kazantsev, I. G., "Information content of projections in few-views tomography," *Proceedings of SPIE*, vol. 1843, 1992. Available Online: https://doi.org/10.1117/12.131878

[16] Butzhammer, L. and Hausotte, T., "Effect of iterative sparse-view CT reconstruction with task-specific projection angles on dimensional measurements," *9th Conference on Industrial Computed Tomography, Padova, Italy (iCT2019)*, 2019.

[17] Schmitt, R. and Niggemann, C., "Einfluss der Bauteilorientierung auf die Messunsicherheit bei dimensionellen Computertomografie Messungen," *iCT 2010 (Industrielle Computertomografie Tagung)*, pp. 221–226, 2010. Available Online: http://www.shaker.de/de/content/catalogue/index.asp?lang=de&ID=8&ISBN=978-3-8322-9418-2

[18] Grozmani, N., Buratti, A., and Schmitt, R. H., "Investigating the influence of workpiece placement on the uncertainty of measurements in industrial computed tomography," *9th Conference on Industrial Computed Tomography, Padova, Italy (iCT2019)*, 2019.

[19] Villarraga-Gómez, H., Amirkhanov, A., Heinzl, C., and Smith, S., "Assessing the effect of sample orientation on dimensional X-Ray computed tomography through experimental and simulated data," *Measurement*, vol. 178, p. 109343 (23p), 2021.

[20] Zeng, G., "Sparse-view tomography via displacement function interpolation," *Visual Computing for Industry, Biomedicine, and Art*, vol. 2, 2019.

[21] Abbas, S., Min, J., and Cho, S., "Super-sparsely view-sampled cone-beam CT by incorporating prior data," *Journal of X-ray Science and Technology*, vol. 21, no. 1, pp. 71–83, 2013.

[22] Fischer, A., Lasser, T., Schrapp, M., Stephan, J., and Noël, P., "Object specific trajectory optimization for industrial X-ray computed tomography," *Scientific Reports*, vol. 6, p. 19135, 2016.

[23] Kingston, A. M., Myers, G. R., Latham, S. J., Recur, B., Li, H., and Sheppard, A. P., "Space-filling X-Ray source trajectories for efficient scanning in large-angle cone-beam computed tomography," *IEEE Transactions on Computational Imaging*, 2018.

[24] Warnett, J. M., Titarenko, V., Kiraci, E., Attridge, A., Lionheart, W. R. B., Withers, P. J., and Williams, M. A., "Towards in-process X-Ray CT for dimensional metrology," *Measurement Science and Technology*, vol. 27, no. 3, p. 035401, 2016. Available Online: http://dx.doi.org/10.1088/0957-0233/27/3/035401

[25] Schromm, T. M. and Grosse, C. U., "Automatic generation of cross sections from computed tomography data of mechanical joining elements for quality analysis," *SN Applied Sciences*, vol. 3, no. 11, p. 832, 2021. Available Online: https://doi.org/10.1007/s42452-021-04806-y

[26] Zwanenburg, E. A., Williams, M. A., and Warnett, J. M., "Review of high-speed imaging with lab-based X-Ray computed tomography," *Measurement Science and Technology*, vol. 33, no. 1, p. 012003, 2021. Available Online: http://dx.doi.org/10.1088/1361-6501/ac354a

[27] Moser, S., Nau, S., Salk, M., and Thoma, K., "In situ flash X-Ray high-speed computed tomography for the quantitative analysis of highly dynamic processes," *Measurement Science and Technology*, vol. 25, no. 2, p. 025009, 2014. Available Online: http://dx.doi.org/10.1088/0957-0233/25/2/025009

[28] Cramer, A., Hecla, J., Wu, D., Lai, X., Boers, T., Yang, K., Moulton, T., Kenyon, S., Arzoumanian, Z., Krull, W., Gendreau, K., and Gupta, R., "Stationary computed tomography for space and other resource-constrained environments," *Scientific Reports*, vol. 8, no. 1, p. 14195, 2018. Available Online: https://doi.org/10.1038/s41598-018-32505-z

[29] Thompson, W., Lionheart, W., Morton, E., Cunningham, M., and Luggar, R., "High speed imaging of dynamic processes with a switched source X-ray CT system," *Measurement Science and Technology*, vol. 26, 2015.

[30] Abbas, S., Lee, T., Shin, S., Lee, R., and Cho, S., "Effects of sparse sampling schemes on image quality in low-dose CT," *Medical Physics*, vol. 40, no. 11, p. 111915, 2013. Available Online: https://doi.org/10.1118/1.4825096

[31] Sollmann, N., Mei, K., Riederer, I., Probst, M., Löffler, M., Kirschke, J., Noël, P., and Baum, T., "Low-dose MDCT: Evaluation of the impact of systematic tube current reduction and sparse sampling on the detection of degenerative spine diseases," *European radiology*, vol. 31, 2020.

[32] Sollmann, N., Mei, K., Hedderich, D. M., Maegerlein, C., Kopp, F. K., Löffler, M. T., Zimmer, C., Rummeny, E. J., Kirschke, J. S., Baum, T., and Noël, P. B., "Multi-detector CT imaging: Impact of virtual tube

current reduction and sparse sampling on detection of vertebral fractures," *European Radiology*, vol. 29, no. 7, pp. 3606–3616, 2019. Available Online: https://doi.org/10.1007/s00330-019-06090-2

[33] Rayudu, N. M., Anitha, D. P., Mei, K., Zoffl, F., Kopp, F. K., Sollmann, N., Löffler, M. T., Kirschke, J. S., Noël, P. B., Subburaj, K., and Baum, T., "Low-dose and sparse sampling MDCT-based femoral bone strength prediction using finite element analysis," *Archives of Osteoporosis*, vol. 15, no. 1, p. 17, 2020. Available Online: https://doi.org/10.1007/s11657-020-0708-9

[34] Mulkens, T. H., Bellinck, P., Baeyaert, M., Ghysen, D., Van Dijck, X., Mussen, E., Venstermans, C., and Termote, J. L., "Use of an automatic exposure control mechanism for dose optimization in multi-detector row CT examinations: Clinical evaluation," *Radiology*, vol. 237, no. 1, pp. 213–23, 2005.

[35] Röntgen, W. C., "Ueber eine neue Art von Strahlen (Vorläufige Mittheilung)," *Sonderabbdruck aus den Sitzungsberichten der Würzburger Physik.-medic. Gesellschaft*, 1895.

[36] Buzug, T. M., *Computed Tomography*. Berlin, Heidelberg: Springer-Verlag, 2008.

[37] Webb, S., "A brief history of tomography and CT," *Proceedings of the 7th Asian and Oceanian Congress of Radiology*, p. 429, 1995.

[38] Carmignato, S., Dewulf, W., and Leach, R., *Industrial X-ray Computed Tomography*. Springer International Publishing, 2018.

[39] Chen, G., Leng, S., and Mistretta, C., "A novel extension of the parallel-beam projection-slice theorem to divergent fan-beam and cone-beam projections," *Medical Physics*, vol. 32 3, pp. 654–65, 2005.

[40] Zhao, S. R., Jiang, D., Yang, K., and Yang, K., "Generalized fourier slice theorem for cone-beam image reconstruction," *Journal of X-Ray Science and Technology*, vol. 23, pp. 157–88, 2015.

[41] Kutsaev, S. V., Agustsson, R., Arodzero, A., Boucher, S., Burstein, P., and Smirnov, A. Y., "X-ray sources for adaptive radiography and computed tomography," *AIP Conference Proceedings*, vol. 2160, no. 1, p. 050014, 2019. Available Online: https://aip.scitation.org/doi/abs/10.1063/1.5127706

[42] du Plessis, A., le Roux, S. G., and Guelpa, A., "Comparison of medical and industrial X-Ray computed tomography for non-destructive testing," *Case Studies in Nondestructive Testing and Evaluation*, vol. 6, pp. 17–25, 2016. Available Online: http://www.sciencedirect.com/science/article/pii/S2214657116300302

[43] Russo, P., *Handbook of X-ray Imaging*. CRC Press, 2018.

[44] Encyclopædia Britannica, "Electromagnetic Spectrum," 2017, accessed on 23.3.2021. Available Online: https://www.britannica.com/science/electromagnetic-spectrum

[45] Bhat, M., Pattison, J., Bibbo, G., and Caon, M., "Diagnostic X-ray spectra: A comparison of spectra generated by different computational methods with a measured spectrum," *Medical physics*, vol. 25, pp. 114–20, 1998.

[46] Berger, M., Hubbell, J., Seltzer, S., Chang, J., Coursey, J., Sukumar, R., Zucker, D., and Olsen, K., *XCOM: Photon Cross Sections Database, NIST Standard Reference Database 8 (XGAM)*. Gaithersburg, USA: National Institute of Standards and Technology (NIST), 2010, accessed on 8.3.2021. Available Online: https://www.nist.gov/pml/xcom-photon-cross-sections-database

[47] Podgorsak, E. B., *Radiation Physics for Medical Physicists*, 2nd ed. Berlin, Heidelberg: Springer-Verlag, 2010.

[48] Shultis, J. and Richard, E., *Fundamentals of Nuclear Science and Engineering*. CRC Press Inc, 2002.

[49] Körner, M., Weber, C. H., Wirth, S., Pfeifer, K.-J., Reiser, M. F., and Treitl, M., "Advances in digital radiography: Physical principles and system overview," *RadioGraphics*, vol. 27, no. 3, pp. 675–686, 2007. Available Online: https://doi.org/10.1148/rg.273065075

[50] Barrett, H. H. and Myers, K. J., *Foundations of Image Science*. Hoboken, New Jersey: Wiley-Interscience, 2004, vol. 1.

[51] Radon, J., "Über die Bestimmung von Funktionen durch ihre Integalwerte längs gewisser Mannigfaltigkeiten," *Berichte über die Verhandlungen der Königlich-Sächsischen Akademie der Wissenschaften zu Leipzig*, no. 69, pp. 262–277, 1917.

[52] Herman, G. T., *Image Reconstruction from Projections*. Academic Press, 1980.

[53] Feldkamp, L., Davis, L. C., and Kress, J., "Practical cone-beam algorithm," *J. Opt. Soc. Am*, vol. 1, pp. 612–619, 1984.

[54] Shepp, L. A. and Logan, B. F., "The fourier reconstruction of a head section," *IEEE Transactions on Nuclear Science*, vol. 21, no. 3, pp. 21–43, 1974.

[55] Beister, M., Kolditz, D., and Kalender, W. A., "Iterative reconstruction methods in X-ray CT," *Physica Medica*, vol. 28, no. 2, pp. 94–108, 2012. Available Online: http://www.sciencedirect.com/science/article/pii/S112017971200004X

[56] Yu, G., Li, L., Gu, J., and Zhang, L., "Total variation based iterative image reconstruction," *Computer Vision for Biomedical Image Applications (CVBIA)*, pp. 526–534, 2005.

[57] Sorzano, C. O. S., Marabini, R., Boisset, N., Rietzel, E., Schröder, R., Herman, G. T., and Carazo, J. M., "The effect of overabundant projection directions on 3D reconstruction algorithms," *Journal of Structural Biology*, vol. 133, no. 2, pp. 108–118, 2001. Available Online: https://www.sciencedirect.com/science/article/pii/S1047847701943382

[58] Andersen, A. H. and Kak, A. C., "Simultaneous algebraic reconstruction technique (SART): A superior implementation of the ART algorithm," *Ultrasonic Imaging*, vol. 6, no. 1, pp. 81–94, 1984. Available Online: https://www.sciencedirect.com/science/article/pii/0161734684900087

[59] Kak, A. C. and Slaney, M., *Principles of Computerized Tomographic Imaging*. Society for Industrial and Applied Mathematics, 2001. Available Online: https://doi.org/10.1137/1.9780898719277.ch7

[60] Xu, F., Xu, W., Jones, M., Keszthelyi, B., Sedat, J., Agard, D., and Mueller, K., "On the efficiency of iterative ordered subset reconstruction algorithms for acceleration on GPUs," *Computer Methods and Programs in Biomedicine*, vol. 98, no. 3, pp. 261–270, 2010. Available Online: https://www.sciencedirect.com/science/article/pii/S0169260709002521

[61] McDonough, R. N. and Whalen, A. D., *Detection of Signals in Noise*. Elsevier, 1995, vol. 2. Available Online: https://app.knovel.com/hotlink/toc/id:kpDSNE000A/detection-signals-in/detection-signals-in

[62] Marcum, J. I., "A statistical theory of target detection by pulsed radar," *The Research Memorandum*, 1947. Available Online: https://www.rand.org/pubs/research_memoranda/RM754.html

[63] Mertins, A., *Signaltheorie*, 3rd ed. Springer Vieweg, 2013.

[64] Arens, T., Hettlich, F., Karpfinger, C., Kockelkorn, U., Lichtenegger, K., and Stachel, H., *Mathematik*, 4th ed. Springer Spektrum, 2018.

[65] Welvaert, M. and Rosseel, Y., "On the definition of signal-to-noise ratio and contrast-to-noise ratio for fMRI data," *PloS One*, vol. 8, no. 11, pp. e77 089–e77 089, 2013. Available Online: https://pubmed.ncbi.nlm.nih.gov/24223118https://www.ncbi.nlm.nih.gov/pmc/articles/PMC3819355/

[66] Verdun, F. R., Racine, D., Ott, J. G., Tapiovaara, M. J., Toroi, P., Bochud, F. O., Veldkamp, W. J. H., Schegerer, A., Bouwman, R. W., Giron, I. H., Marshall, N. W., and Edyvean, S., "Image quality in CT: From physical measurements to model observers," *Phys Med*, vol. 31, no. 8, pp. 823–843, 2015.

[67] Williams, C. S. and A., B. O., *Introduction to the Optical Transfer Function*. New York: Wiley, 2002.

[68] Chen, Z. and Ning, R., "Three-dimensional point spread function measurement of cone-beam computed tomography system by iterative edge-blurring algorithm," *Physics in Medicine and Biology*, vol. 49, no. 10, pp. 1865–1880, 2004. Available Online: http://dx.doi.org/10.1088/0031-9155/49/10/003

[69] Wolbarst, A. B., Karellas, A., Krupinski, E. A., and William R., H., *Advances in Medical Physics 2010*. Medical Physics Publishing Corporation, 2010, vol. 3.

[70] Sharp, P., Barber, D. C., Brown, D. G., Burgess, A. E., Metz, C. E., Myers, K. J., Taylor, C. J., Wagner, R. F., Brooks, R., Hill, C. R., Kuhl, D. E., Smith, M. A., Wells, P., and Worthington, B., "ICRU report 54," *Journal of the International Commission*

on Radiation Units and Measurements, vol. os28, no. 1, 2016. Available Online: https://doi.org/10.1093/jicru/os28.1.Report54

[71] Yendiki, A. and Fessler, J. A., "Analysis of observer performance in known-location tasks for tomographic image reconstruction," *IEEE Transactions on Medical Imaging*, vol. 25, no. 1, 2006.

[72] Barrett, H. H., Yao, J., Rolland, J. P., and Myers, K. J., "Model observers for assessment of image quality," *Proc Natl Acad Sci U S A*, vol. 90, no. 21, pp. 9758–65, 1993.

[73] Wickens, T. D., *Elementary Signal Detection Theory*. Oxford University Press USA, 2001.

[74] Berens, A. P., "NDE reliability data analysis," *ASM Handbook*, vol. 17, no. 9, 1989.

[75] Wagner, R. F. and Brown, D. G., "Unified SNR analysis of medical imaging systems," *Physics in Medicine and Biology*, vol. 30, no. 6, pp. 489–518, 1985. Available Online: http://dx.doi.org/10.1088/0031-9155/30/6/001

[76] Müller-Wichards, D., *Transformationen und Signale*, 2nd ed. Springer-Vieweg, 2013.

[77] Pineda, A. R., Tward, D. J., Gonzalez, A., and Siewerdsen, J. H., "Beyond noise power in 3D computed tomography: the local NPS and off-diagonal elements of the fourier domain covariance matrix," *Med Phys*, vol. 39, no. 6, pp. 3240–52, 2012.

[78] Smith, W. E. and Barrett, H. H., "Hotelling trace criterion as a figure of merit for the optimization of imaging systems," *Journal of the Optical Society of America A*, vol. 3, no. 5, pp. 717–725, 1986. Available Online: http://josaa.osa.org/abstract.cfm?URI=josaa-3-5-717

[79] Rencher, A. C. and Christensen, W. F., *Methods of Multivariate Analysis*, 3rd ed. John Wiley & Sons, Inc., 2012.

[80] Ohm, J.-R. and Lüke, H. D., *Signalübertragung*. Berlin, Heidelberg: Springer Vieweg, 2014, vol. 12.

[81] Turin, G. L., "An introduction to matched filters," *IRE Trans. Inf. Theory*, vol. 6, pp. 311–329, 1960.

[82] Platiša, L., Goossens, B., Vansteenkiste, E., Park, S., Gallas, B. D., Badano, A., and Philips, W., "Channelized hotelling observers for the assessment of volumetric imaging data sets," *Journal of the Optical Society of America A*, vol. 28, no. 6, pp. 1145–1163, 2011. Available Online: http://josaa.osa.org/abstract.cfm?URI=josaa-28-6-1145

[83] Gagne, R. M., Gallas, B. D., and Myers, K. J., "Toward objective and quantitative evaluation of imaging systems using images of phantoms," *Med Phys*, vol. 33, no. 1, pp. 83–95, 2006.

[84] Racine, D., Ryckx, N., Ba, A., Becce, F., Viry, A., Verdun, F. R., and Schmidt, S., "Task-based quantification of image quality using a model observer in abdominal CT: a multicentre study," *European Radiology*, vol. 28, no. 12, pp. 5203–5210, 2018. Available Online: https://doi.org/10.1007/s00330-018-5518-8

[85] Tseng, H.-W., Fan, J., Kupinski, M. A., Sainath, P., and Hsieh, J., "Assessing image quality and dose reduction of a new X-Ray computed tomography iterative reconstruction algorithm using model observers," *Medical Physics*, vol. 41, no. 7, p. 071910, 2014. Available Online: https://doi.org/10.1118/1.4881143

[86] Othman, N., Simon, A.-C., Montagu, T., Berteloot, L., Grévent, D., Habib Geryes, B., Benkreira, M., Bigand, E., Capdeville, S., Desrousseaux, J., Farman, B., Garnier, E., Gempp, S., Nigoul, J.-M., Nomikossoff, N., and Vincent, M., "Toward a comparison and an optimization of CT protocols using new metrics of dose and image quality part I: Prediction of human observers using a model observer for detection and discrimination tasks in low-dose CT images in various scanning conditions," *Physics in Medicine and Biology*, vol. 66, no. 11, p. 115003, 2021. Available Online: http://dx.doi.org/10.1088/1361-6560/abfad8

[87] Gang, G. J., Siewerdsen, J. H., and Webster Stayman, J., "Task-driven optimization of CT tube current modulation and regularization in model-based iterative reconstruction," *Physics in medicine and Biology*, vol. 62, no. 12, pp. 4777–4797, 2017. Available Online: https://pubmed.ncbi.nlm.nih.gov/28362638https://www.ncbi.nlm.nih.gov/pmc/articles/PMC5738673/

[88] Gang, G. J., Siewerdsen, J. H., and Stayman, J. W., "Task-driven optimization of fluence field and regularization for model-based iterative reconstruction in computed tomography," *IEEE Transactions on Medical Imaging*, vol. 36, no. 12, pp. 2424–2435, 2017.

[89] Đedović, E., Faj, D., and Bokulić, T., "Computed tomography protocols optimization using non-prewhitening model observer," *International Physics Conference in Bosnia and Herzegovina (PHYCONBA 2020)*, vol. 1814, 2020.

[90] Frey, E. C., Gilland, K. L., and Tsui, B. M., "Application of task-based measures of image quality to optimization and evaluation of three-dimensional reconstruction-based compensation methods in myocardial perfusion SPECT," *IEEE Trans Med Imaging*, vol. 21, no. 9, pp. 1040–50, 2002.

[91] Richard, S. and Samei, E., "Quantitative breast tomosynthesis: From detectability to estimability," *Medical Physics*, vol. 37, no. 12, pp. 6157–6165, 2010. Available Online: https://doi.org/10.1118/1.3501883

[92] Han, M., Shim, H., and Baek, J., "Low-dose CT denoising via convolutional neural network with an observer loss function," *Med Phys*, vol. 48, no. 10, pp. 5727–5742, 2021.

[93] Zhao, C. and Kanicki, J., "Task-based modeling of a 5k ultra-high-resolution medical imaging system for digital breast tomosynthesis," *IEEE Trans Med Imaging*, vol. 36, no. 9, pp. 1820–1831, 2017.

[94]   K. Tuy, H., "An inversion formula for cone-beam reconstruction," *SIAM Journal on Applied Mathematics*, vol. 43, no. 3, pp. 546–552, 1983.

[95]   Noo, F., Clack, R., and Defrise, M., "Cone-beam reconstruction from general discrete vertex sets using radon rebinning algorithms," *IEEE Transactions on Nuclear Science*, vol. 44, pp. 1309–1316, 1997.

[96]   Jacobsen, C., "Relaxation of the crowther criterion in multislice tomography," *Optics Letters*, vol. 43, no. 19, pp. 4811–4814, 2018. Available Online: https://pubmed.ncbi.nlm.nih.gov/30272746https://www.ncbi.nlm.nih.gov/pmc/articles/PMC6410570/

[97]   Nyquist, H., "Certain topics in telegraph transmission theory," *Transactions of the American Institute of Electrical Engineers*, vol. 47, no. 2, pp. 617–644, 1928.

[98]   Shannon, C. E., "Communication in the presence of noise," *Proceedings of the IEEE*, vol. 86, no. 2, pp. 447–457, 1998.

[99]   Zhao, S. R., Yang, K., and Yang, K., "Fan beam image reconstruction with generalized fourier slice theorem," *Journal of X-ray Science and Technology*, vol. 22, pp. 415–436, 2014.

[100] Brooks, R. A. and Di Chiro, G., "Principles of computer assisted tomography (CAT) in radiographic and radioisotopic imaging," *Physics in Medicine and Biology*, vol. 21, no. 5, pp. 689–732, 1976.

[101] Noo, F., Defrise, M., Clackdoyle, R., and Kudo, H., "Image reconstruction from fan-beam projections on less than a short scan," *Physics in Medicine and Biology*, vol. 47, no. 14, pp. 2525–2546, 2002. Available Online: http://dx.doi.org/10.1088/0031-9155/47/14/311

[102] Crowther, R. A., DeRosier, D. J., and Klug, A., "The reconstruction of a three-dimensional structure from projections and its application to electron microscopy," *Proceedings of the Royal Society A: Mathematical, Physical and Engineering Sciences*, vol. 317, no. 1530, pp. 319–340, 1970. Available Online: https://doi.org/10.1098/rspa.1970.0119

[103] Lewitt, R. M., Bates, R. H. T., and Peters, T. M., "Image reconstruction from projections: II: Modified backprojection methods," *Optik*, vol. 50, no. 2, pp. 85–109, 1978.

[104] Rattey, P. and Lindgren, A., "Sampling the 2-D radon transform," *IEEE Transactions on Acoustics, Speech, and Signal Processing*, vol. 29, no. 5, pp. 994–1002, 1981.

[105] Wagner, R. F., Brown, D. G., and Pastel, M. S., "Application of information theory to the assessment of computed tomography," *Med Phys*, vol. 6, no. 2, pp. 83–94, 1979.

[106] Brunton, S. L. and Kutz, J. N., *Data-Driven Science and Engineering: Machine Learning, Dynamical Systems, and Control*. Cambridge: Cambridge University Press, 2019. Available Online: https://www.cambridge.org/core/books/datadriven-science-and-engineering/77D52B171B60A496EAFE4DB662ADC36E

[107] Foucart, S. and Rauhut, H., *A Mathematical Introduction to Compressive Sensing*. New York: Birkhäuser, Springer Science+Business Media, 2010.

[108] Stock, A. M., Herl, G., Sauer, T., and Hiller, J., "Edge-preserving compression of CT scans using wavelets," *Insight - Non-Destructive Testing and Condition Monitoring*, vol. 62, pp. 345–351, 2020.

[109] Lee, M. S., Kim, H. J., Cho, H. S., Hong, D. K., Je, U. K., Oh, J. E., Park, Y. O., Lee, S. H., Cho, H. M., Choi, S. I., and Koo, Y. S., "Compressed-sensing (CS)-based 3D image reconstruction in cone-beam CT (CBCT) for low-dose, high-quality dental X-ray imaging," *Journal of the Korean Physical Society*, vol. 63, no. 5, pp. 1066–1071, 2013. Available Online: https://doi.org/10.3938/jkps.63.1066

[110] Graff, C. G. and Sidky, E. Y., "Compressive sensing in medical imaging," *Applied Optics*, vol. 54, no. 8, pp. C23–C44, 2015. Available Online: http://ao.osa.org/abstract.cfm?URI=ao-54-8-C23

[111] Yang, F. Q., Zhang, D. H., Huang, K. D., Shi, W. L., and Wang, X. Y., "Scattering estimation for cone-beam CT using local measurement based on compressed sensing," *IEEE Transactions on Nuclear Science*, vol. 65, no. 3, pp. 941–949, 2018.

[112] Ye, J. C., "Compressed sensing MRI: a review from signal processing perspective," *BMC Biomedical Engineering*, vol. 1, no. 1, p. 8, 2019. Available Online: https://doi.org/10.1186/s42490-019-0006-z

[113] Lustig, M., Donoho, D., and Pauly, J. M., "Sparse MRI: The application of compressed sensing for rapid MR imaging," *Magnetic Resonance in Medicine*, vol. 58, no. 6, pp. 1182–1195, 2007.

[114] Emil, Y. S., Jakob, H. J., and Xiaochuan, P., "Sampling conditions for gradient-magnitude sparsity based image reconstruction algorithms," *Proceedings of SPIE*, vol. 8313, 2012. Available Online: https://doi.org/10.1117/12.913307

[115] Candes, E. J., Romberg, J., and Tao, T., "Robust uncertainty principles: Exact signal reconstruction from highly incomplete frequency information," *IEEE Transactions on Information Theory*, vol. 52, no. 2, pp. 489–509, 2006.

[116] Jørgensen, J. S., Sidky, E. Y., and Pan, X., "Quantifying admissible undersampling for sparsity-exploiting iterative image reconstruction in X-ray CT," *IEEE Transactions on Medical Imaging*, vol. 32, no. 2, pp. 460–473, 2013.

[117] Jørgensen, J. S. and Sidky, E. Y., "How little data is enough? phase-diagram analysis of sparsity-regularized X-ray computed tomography," *Philosophical Transactions of the Royal Society A: Mathematical, Physical and Engineering Sciences*, vol. 373, no. 2043, p. 20140387, 2015. Available Online: https://doi.org/10.1098/rsta.2014.0387

[118] Manohar, K., Brunton, B. W., Kutz, J. N., and Brunton, S. L., "Data-driven sparse sensor placement for reconstruction: Demonstrating the benefits of exploiting known patterns," *IEEE Control Systems Magazine*, vol. 38, no. 3, pp. 63–86, 2018.

[119] Sarkar, V., Shi, C., Rassiah-Szegedi, P., Diaz, A., Eng, T., and Papanikolaou, N., "The effect of a limited number of projections and reconstruction algorithms on the image quality of megavoltage digital tomosynthesis," *J Appl Clin Med Phys*, vol. 10, no. 3, pp. 155–172, 2009.

[120] Russ, J. C. and Neal, F. B., *The Image Processing Handbook*, 7th ed. Boston: CRC Press, 2016.

[121] Quinto, E., "Singularities of the X-ray transform and limited data tomography in $\mathbb{R}^2$ and $\mathbb{R}^3$," *SIAM Journal on Mathematical Analysis*, vol. 24, no. 5, pp. 1215–1225, 1993. Available Online: https://doi.org/10.1137/0524069

[122] Varga, L., Balázs, P., and Nagy, A., "Direction-dependency of binary tomographic reconstruction algorithms," *Graphical Models*, vol. 73, no. 6, pp. 365–375, 2011. Available Online: http://www.sciencedirect.com/science/article/pii/S1524070311000245

[123] Dabravolski, A., Batenburg, K. J., and Sijbers, J., "Dynamic angle selection in X-ray computed tomography," *Nuclear Instruments and Methods in Physics Research Section B: Beam Interactions with Materials and Atoms*, vol. 324, pp. 17–24, 2014. Available Online: http://www.sciencedirect.com/science/article/pii/S0168583X14000986

[124] Barrett, H. H. and Gifford, H., "Cone-beam tomography with discrete data sets," *Phys Med Biol*, vol. 39, no. 3, pp. 451–76, 1994.

[125] Yan, B., Zhang, W., Li, L., Zhang, H., and Wang, L., "Quantitative study on exact reconstruction sampling condition by verifying solution uniqueness in limited-view CT," *Physica Medica: European Journal of Medical Physics*, vol. 32, no. 10, pp. 1321–1330, 2016. Available Online: https://doi.org/10.1016/j.ejmp.2016.07.094

[126] Zhao, Z., Gang, G., and Siewerdsen, J., "Noise, sampling, and the number of projections in cone-beam CT with a flat-panel detector," *Medical physics*, vol. 41, p. 061909, 2014.

[127] Jørgensen, J., Coban, S. B., Lionheart, W., and Withers, P., "Effect of sparsity and exposure on total variation regularized X-ray tomography from few projections," *4th International Conference on Image Formation in X-ray Computed Tomography, Bamberg, Germany*, 2016.

[128] Gang, G. J., Lee, J., Stayman, J. W., Tward, D. J., Zbijewski, W., Prince, J. L., and Siewerdsen, J. H., "Analysis of fourier-domain task-based detectability index in tomosynthesis and cone-beam CT in relation to human observer performance," *Medical Physics*, vol. 38, no. 4, pp. 1754–1768, 2011. Available Online: https://doi.org/10.1118/1.3560428

[129] Bauer, F., Goldammer, M., and Große, C. U., "Scan time reduction by fewer projections - an approach for part-specific acquisition trajectories," *World Conference on Non-Destructive Testing (WCNDT2020), Incheon, South Korea*, 2022.

[130] Bouhaouel, F., Bauer, F., and Grosse, C. U., "Task-specific acquisition trajectories optimized using observer models," *10th Conference on Industrial Computed Tomography (iCT 2020)*, 2020.

[131] Placidi, G., Alecci, M., and Sotgiu, A., "Theory of adaptive acquisition method for image reconstruction from projections and application to EPR imaging," *Journal of Magnetic Resonance, Series B*, vol. 108, no. 1, pp. 50–57, 1995. Available Online: http://www.sciencedirect.com/science/article/pii/S1064186685711016

[132] Xuanhao, Z., Lijuan, S., Bo, W., and Bing, P., "Effect of the number of projections in x-ray CT imaging on image quality and digital volume correlation measurement," *Measurement*, vol. 194, p. 111061, 2022. Available Online: https://www.sciencedirect.com/science/article/pii/S026322412200327X

[133] Zhao, C., Herbst, M., Ritschl, L., Vogt, S., Kappler, S., Siewerdsen, J. H., and Zbijewski, W., "Advanced scan trajectories for chest tomosynthesis on robotic X-ray systems," *6th International Conference on Image Formation in X-ray Computed Tomography (CT Meeting 2020), Regensburg*, 2020.

[134] Abbas, S., Park, M., Min, J., Kim, H. K., and Cho, S., "Sparse-view computed laminography with a spherical sinusoidal scan for nondestructive testing," *Optics Express*, vol. 22, no. 15, pp. 17 745–17 755, 2014. Available Online: http://www.opticsexpress.org/abstract.cfm?URI=oe-22-15-17745

[135] Herbst, M., Schebesch, F., Berger, M., Fahrig, R., Hornegger, J., and Maier, A., "Improved trajectories in C-Arm computed tomography for non-circular fields of view," *Proceedings of the Third International Conference on Image Formation in X-ray Computed Tomography, Salt Lake City, USA*, pp. 274–278, 2014.

[136] Bauer, F., Goldammer, M., and Grosse, C. U., "Selection and evaluation of spherical acquisition trajectories for industrial computed tomography," *Proceedings of the Royal Society A: Mathematical, Physical and Engineering Sciences*, vol. 477, no. 2250, p. 20210192, 2021. Available Online: https://doi.org/10.1098/rspa.2021.0192

[137] Katsevich, A., "Image reconstruction for the circle and line trajectory," *Physics in Medicine and Biology*, vol. 49, no. 22, pp. 5059–5072, 2004. Available Online: http://dx.doi.org/10.1088/0031-9155/49/22/003

[138] Katsevich, A., "Image reconstruction for the circle-and-arc trajectory," *Physics in Medicine and Biology*, vol. 50, pp. 2249–65, 2005.

[139] Zeng, G. and Gullberg, G., "A cone-beam tomography algorithm for orthogonal circle-and-line orbit," *Physics in Medicine and Biology*, vol. 37, pp. 563–77, 1992.

[140] Tang, X. and Ning, R., "A cone beam filtered backprojection (CB-FBP) reconstruction algorithm for a circle-plus-two-arc orbit," *Med Phys*, vol. 28, no. 6, pp. 1042–55, 2001.

[141] Lu, Y. B., Yang, J. S., Emerson, J. W., Mao, H., Zhou, T., Si, Y. Z., and Jiang, M., "Cone-beam reconstruction for the two-circles-plus-one-line trajectory," *Physics in Medicine and Biology*, vol. 57, no. 9, p. 19, 2012.

[142] Zhicong, Y., Guenter, L., Frank, D., Yanfei, M., Joachim, H., and Frédéric, N., "Extended ellipse-line-ellipse trajectory for long-object cone-beam imaging with a mounted C-Arm system," *Physics in Medicine and Biology*, vol. 61, no. 4, p. 1829, 2016. Available Online: http://stacks.iop.org/0031-9155/61/i=4/a=1829

[143] Noo, F., Clack, R., White, T. A., and Roney, T. J., "The dual-ellipse cross vertex path for exact reconstruction of long objects in cone-beam tomography," *Physics in Medicine and Biology*, vol. 43, no. 4, pp. 797–810, 1998.

[144] Zhuang, T., Zambelli, J., Nett, B., Leng, S., and Chen, G.-H., "Exact and approximate cone-beam reconstruction algorithms for C-Arm based cone-beam CT using a two-concentric-arc source trajectory," *Proceedings of SPIE – the International Society for Optical Engineering*, vol. 6913, pp. 691321–691321, 2008. Available Online: https://pubmed.ncbi.nlm.nih.gov/19287507https://www.ncbi.nlm.nih.gov/pmc/articles/PMC2654769/

[145] Noo, F., Pack, J., and Heuscher, D., "Exact helical reconstruction using native cone-beam geometries," *Physics in Medicine and Biology*, vol. 48, pp. 3787–818, 2004.

[146] Yu, Z., Noo, F., Dennerlein, F., Lauritsch, G., and Hornegger, J., "FDK-Type reconstruction algorithms for the reverse helical trajectory," *IEEE Nuclear Science Symposium Conference Record*, pp. 3980–3985, 2011.

[147] Ritschl, L., Kuntz, J., Fleischmann, C., and Kachelrieß, M., "The rotate-plus-shift C-Arm trajectory. part I. complete data with less than 180 degree rotation," *Medical Physics*, vol. 43, no. 5, pp. 2295–2302, 2016. Available Online: https://doi.org/10.1118/1.4944785

[148] Kuntz, J., Ritschl, L., Knaup, M., and Kachelriess, M., "The rotate-plus-shift C-Arm trajectory. part II. exact reconstruction from less than 180 degree rotation," *Medical Physics*, vol. 43, no. 5, pp. 2303–2310, 2016. Available Online: https://doi.org/10.1118/1.4944786

[149] Yang, H. Q., Li, M. H., Koizumi, K., Kudo, H., and Ieee, "Closed sinusoid trajectory for C-Arm CT imaging," *IEEE Nuclear Science Symposium Conference Record*, vol. 1-6, pp. 3480–3484, 2006.

[150] Andrew, M. K., Glenn, R. M., Shane, J. L., Heyang, L., Jan, P. V., and Adrian, P. S., "Optimized X-Ray source scanning trajectories for iterative reconstruction in high cone-angle tomography," *Proceedings of SPIE*, vol. 9967, 2016. Available Online: https://doi.org/10.1117/12.2238297

[151] Wu, W. W., Yu, H. Y., Cong, W. X., and Liu, F. L., "Theoretically exact backprojection filtration algorithm for multi-segment linear trajectory," *Physics in Medicine and Biology*, vol. 63, no. 1, p. 14, 2018.

[152] Hewei, G., Li, Z., Zhiqiang, C., Yuxiang, X., Jianping, C., and Zhihua, Q., "Direct filtered-backprojection-type reconstruction from a straight-line trajectory," *Optical Engineering*, vol. 46, no. 5, pp. 1–11, 2007. Available Online: https://doi.org/10.1117/1.2739624

[153] Gao, H., Zhang, L., Chen, Z., Xing, Y., Xue, H., and Cheng, J., "Straight-line-trajectory-based X-ray tomographic imaging for security inspections: System design, image reconstruction and preliminary results," *IEEE Transactions on Nuclear Science*, vol. 60, no. 5, pp. 3955–3968, 2013.

[154] Levine, M. S., Sidky, E. Y., and Pan, X., "Consistency conditions for cone-beam CT data acquired with a straight-line source trajectory," *Tsinghua science and technology*, vol. 15, no. 1, pp. 56–61, 2010. Available Online: https://pubmed.ncbi.nlm.nih.gov/20559455https://www.ncbi.nlm.nih.gov/pmc/articles/PMC2886312/

[155] Chen, P., Han, Y., and Gui, Z., "CT scanning imaging method based on a spherical trajectory," *PLOS ONE*, vol. 11, no. 3, p. e0149779, 2016. Available Online: https://doi.org/10.1371/journal.pone.0149779

[156] Zhao, C., Herbst, M., Vogt, S., Ritschl, L., Kappler, S., Siewerdsen, J. H., and Zbijewski, W., "A robotic X-ray cone-beam CT system: Trajectory optimization for 3D imaging of the weight-bearing spine," *SPIE Medical Imaging*, vol. 10948, 2019. Available Online: https://doi.org/10.1117/12.2513433

[157] Russ, T., Abdelrehim, A., Bauer, D. F., Hatamikia, S., Schad, L., Zöllner, F., and Chung, K., "CBCT image quality and dose simulations for arbitrary source-detector trajectories with GATE," *Poster at the EuroSafe Imaging 2020 Conference*, 2020. Available Online: https://epos.myesr.org/poster/eurosafe/eurosafeimaging2020/ESI-05719

[158] Zhang, Y., Li, Z., Zhao, J., Zhou, L., Wang, M., Wang, B., and Ma, Y., "Sparing sensitive organ by optimizing cone beam CT gantry rotation," *Poster at the Proceedings of the American Society for Radiation Oncology*, vol. 99, no. 2, pp. E746–E747, 2017. Available Online: https://www.redjournal.org/article/S0360-3016(17)33450-8/fulltext

[159] Tuy, H., "Reconstruction of a three-dimensional object from a limited range of views," *Journal of Mathematical Analysis and Applications*, vol. 80, no. 2, pp. 598–616, 1981. Available Online: http://www.sciencedirect.com/science/article/pii/0022247X81901268

[160] Zheng, Z. and Mueller, K., "Identifying sets of favorable projections for few-view low-dose cone-beam CT scanning," *Fully Three-dimensional Image Reconstruction in Radiology and Nuclear Medicine (Fully3D), Potsdam, Germany*, p. 480, 2011. Available Online: http://www.fully3d.org/2011/program.html

[161] Matz, A., Holub, W., and Schielein, R., "Trajectory optimization in computed tomography based on object geometry," *11th Conference on Industrial Computed Tomography, Wels, Austria (iCT 2022)*, 2022.

[162] Barrett, J. F. and Keat, N., "Artifacts in CT: Recognition and avoidance," *RadioGraphics*, vol. 24, no. 6, pp. 1679–1691, 2004. Available Online: https://doi.org/10.1148/rg.246045065

[163] Heinzl, C., Kastner, J., Amirkhamov, A., Gröller, E., and Gusenbauer, C., "Optimal specimen placement in cone beam X-ray computed tomography," *NDT & E International*, vol. 50, pp. 42–49, 2012. Available Online: https://www.sciencedirect.com/science/article/pii/S096386951200062X

[164] Amirkhanov, A., Heinzl, C., Reiter, M., and Gröller, E., "Visual optimality and stability analysis of 3DCT scan positions," *IEEE Trans Vis Comput Graph*, vol. 16, no. 6, pp. 1477–86, 2010.

[165] Reisinger, S., Kasperl, S., Franz, M., Hiller, J., and Schmid, U., "Simulation-based planning of optimal conditions for industrial computed tomography," *International Symposium on Digital Industrial Radiology and Computed Tomography, 20-22 June 2011, Berlin, Germany (DIR 2011)*, 2011.

[166] Kano, T. and Koseki, M., "Optimization of multi-axis control for metal artifact reduction in X-Ray computed tomography," *9th Conference on Industrial Computed Tomography, Padova, Italy (iCT2019)*, 2019.

[167] Grozmani, Natalia amd Chupina, D. and Schmitt, R. H., "Investigation of the independence of the best assembly orientations with respect to X-Ray source parameters in industrial computed tomography," *10th Conference on Industrial Computed Tomography, Wels, Austria (iCT 2020)*, 2020.

[168] Herl, G., Hiller, J., and Sauer, T., "Artifact reduction in X-ray computed tomography by multipositional data fusion using local image quality measures," *9th Conference on Industrial Computed Tomography, Padova, Italy (iCT2019)*, 2019.

[169] Tan, Y., Ohtake, Y., and Suzuki, H., "Scan angle selection and volume fusion for reducing metal artifacts by multiple X-Ray CT scanning," *Precision Engineering*, vol. 74, pp. 384–395, 2021. Available Online: https://www.sciencedirect.com/science/article/abs/pii/S0141635921001896

[170] Wu, P., Sheth, N., Sisniega, A., Uneri, A., Han, R., Vijayan, R., Vagdargi, P., Kreher, B., Kunze, H., Kleinszig, G., Vogt, S., Lo, S. F., Theodore, N., and Siewerdsen, J. H., "Method for metal artifact avoidance in C-arm cone-beam CT," *Proceedings of SPIE*, vol. 11312, 2020. Available Online: https://doi.org/10.1117/12.2549840

[171] Wu, P., Sheth, N., Sisniega, A., Uneri, A., Han, R., Vijayan, R., Vagdargi, P., Kreher, B., Kunze, H., Kleinszig, G., Vogt, S., Lo, S. F., Theodore, N., and Siewerdsen, J. H., "C-Arm orbits for metal artifact avoidance (MAA) in cone-beam CT," *Physics in Medicine and Biology*, vol. 65, no. 16, p. 165012, 2020. Available Online: http://dx.doi.org/10.1088/1361-6560/ab9454

[172] Lee, S., Cho, G., and Wang, G., "Artifacts associated with implementation of the grangeat formula," *Medical physics*, vol. 29 12, pp. 2871–80, 2002.

[173] Maier, A., Kugler, P., Lauritsch, G., and Hornegger, J., "Discrete estimation of data completeness for 3D scan trajectories with detector offset," *Bildverarbeitung für die Medizin 2015*, pp. 47–52, 2015.

[174] Liu, B., Bennett, J., Wang, G., De Man, B., Zeng, K., Yin, Z., Fitzgerald, P., and Yu, H., "Completeness map evaluation demonstrated with candidate next-generation cardiac CT architectures," *Medical physics*, vol. 39, pp. 2405–16, 2012.

[175] Herl, G., Hiller, J., and Maier, A., "Scanning trajectory optimisation using a quantitative tuy-based local quality estimation for robot-based X-ray computed tomography," *Nondestructive Testing and Evaluation*, pp. 1–17, 2020. Available Online: https://doi.org/10.1080/10589759.2020.1774579

[176] Grace, J. G., Jeffrey, H. S., and Stayman, J. W., "Non-circular CT orbit design for elimination of metal artifacts," *Proceedings of SPIE*, vol. 11312, 2020. Available Online: https://doi.org/10.1117/12.2550203

[177] Ito, T., Ohtake, Y., and Suzuki, H., "Orientation optimization and jig construction for X-Ray CT scanning," *10th Conference on Industrial Computed Tomography, Wels, Austria (iCT 2020)*, 2020.

[178] Gang, G. J., Russ, T., Ma, Y., Toennes, C., Weiss, C. R., Siewerdsen, J. H., Schad, L. R., and Stayman, J. W., "Metal-tolerant noncircular orbit design and implementation on robotic C-Arm systems," *6th International Conference on Image Formation in X-Ray Computed Tomography (CT Meeting 2020), Regensburg*, 2020.

[179] Haque, M. A., Ahmad, M. O., Swamy, M. N. S., Hasan, M. K., and Lee, S. Y., "Adaptive projection selection for computed tomography," *IEEE Transactions on Image Processing*, vol. 22, no. 12, pp. 5085–5095, 2013.

[180] Hatamikia, S., Biguri, A., Kronreif, G., Russ, T., Kettenbach, J., and Birkfellner, W., "Short scan source-detector trajectories for target-based CBCT," *42nd Annual International Conference of the IEEE Engineering in Medicine & Biology Society (EMBC)*, pp. 1299–1302, 2020.

[181] Hatamikia, S., Biguri, A., Kronreif, G., Kettenbach, J., Russ, T., Furtado, H., Shiyam Sundar, L. K., Buschmann, M., Unger, E., Figl, M., Georg, D., and Birkfellner, W., "Optimization for customized trajectories in cone beam computed tomography," *Medical Physics*, 2020.

[182] Hatamikia, S., Biguri, A., Kronreif, G., Figl, M., Russ, T., Kettenbach, J., Buschmann, M., and Birkfellner, W., "Toward on-the-fly trajectory optimization for C-Arm CBCT under strong kinematic constraints," *PLoS ONE*, vol. 16, 2021.

[183] Hatamikia, S., Biguri, A., Kronreif, G., Russ, T., Kettenbach, J., and Birkfellner, W., "Collision avoidance trajectories for on-line trajectory optimization in C-Arm CBCT," *16th International Meeting on Fully 3D Image Reconstruction in Radiology and Nuclear Medicine*, 2021. Available Online: https://arxiv.org/abs/2110.04143

[184] Brierley, N., Bellon, C., and Lazaro Toralles, B., "Optimized multi-shot imaging inspection design," *Proceedings of the Royal Society A: Mathematical, Physical and Engineering Sciences*, vol. 474, no. 2216, p. 20170319, 2018. Available Online: https://doi.org/10.1098/rspa.2017.0319

[185] Brierley, N., "Optimised inspection of complex geometries," *12th European Conference on Non-Destructive Testing (ECNDT), Gothenburg*, 2018.

[186] Suth, D., Berg, M., Kretzer, C., Waldyra, A., Sukowski, F., and Schielein, R., "Automatic scan planning for CT scans," *11th Conference on Industrial Computed Tomography, Wels, Austria (iCT 2022)*, 2022.

[187] Stayman, J. W. and Siewerdsen, J. H., "Task-based trajectories in iteratively reconstructed interventional cone-beam CT," *12th Fully3D Meeting (International Conference on Fully Three-Dimensional Image Reconstruction in Radiology and Nuclear Medicine)*, p. 257–260, 2013.

[188] Ouadah, S., Jacobson, M., Stayman, J. W., Ehtiati, T., Weiss, C., and Siewerdsen, J. H., "Task-driven orbit design and implementation on a robotic c-arm system for cone-beam CT," *Proceedings of SPIE*, vol. 10132, p. 101320H, 2017. Available Online: http://www.ncbi.nlm.nih.gov/pmc/articles/PMC5627522/

[189] Stayman, J. W., Gang, G. J., and Siewerdsen, J. H., "Task-based optimization of source-detector orbits in interventional cone beam CT," *Fully Three-dimensional Image Reconstruction in Radiology and Nuclear Medicine (Fully3D)*, 2015.

[190] Stayman, J. W., Capostagno, S., Gang, G. J., and Siewerdsen, J. H., "Task-driven source-detector trajectories in cone-beam computed tomography: I. theory and methods," *J Med Imaging (Bellingham)*, vol. 6, no. 2, p. 025002, 2019.

[191] Sarah, C., Joseph, W. S., Matthew, W. J., Tina, E., Clifford, R. W., and Jeffrey, H. S., "Task-driven source–detector trajectories in cone-beam computed tomography: II. application to neuroradiology," *Journal of Medical Imaging*, vol. 6, no. 2, pp. 1–11, 2019. Available Online: https://doi.org/10.1117/1.JMI.6.2.025004

[192] Thies, M., Zäch, J.-N., Gao, C., Taylor, R., Navab, N., Maier, A., and Unberath, M., "A learning-based method for online adjustment of C-arm cone-beam CT source trajectories for artifact avoidance," *International Journal of Computer Assisted Radiology and Surgery*, vol. 15, 2020.

[193] Zaech, J.-N., Gao, C., Bier, B., Taylor, R., Maier, A., Navab, N., and Unberath, M., "Learning to avoid poor images: Towards task-aware C-arm cone-beam CT trajectories," *Medical Image Computing and Computer Assisted Intervention (MICCAI 2019)*, pp. 11–19, 2019.

[194] Theodor Cheslerean, B., Franz, P., and Tobias, L., "Task-driven acquisition in anisotropic X-ray dark-field tomography," *Proceedings of SPIE*, vol. 11072, 2019. Available Online: https://doi.org/10.1117/12.2534831

[195] Herl, G., Hiller, J., Thies, M., Zaech, J.-N., Unberath, M., and Maier, A., "Task-specific trajectory optimisation for twin-robotic X-Ray tomography," *IEEE Transactions on Computational Imaging*, vol. PP, pp. 1–1, 2021.

[196] Kazantsev, I., "An algebraic approach to projection data informativity in computerized tomography," *Zeitschrift für Angewandte Mathematik und Mechanik (ZAMM)*, vol. 76, 1996.

[197] Venere, M., Liao, H., and Clausse, A., "A genetic algorithm for adaptive tomography of elliptical objects," *IEEE Signal Processing Letters*, vol. 7, no. 7, pp. 176–178, 2000.

[198] Barkan, O., Weill, J., Dekel, S., and Averbuch, A., "A mathematical model for adaptive computed tomography sensing," *IEEE Transactions on Computational Imaging*, vol. 3, no. 4, pp. 551–565, 2017.

[199] Bauer, F., Forndran, D., Schromm, T., and Grosse, C. U., "Practical part-specific trajectory optimization for robot-guided inspection via computed tomography," *Journal of Nondestructive Evaluation*, vol. 41, no. 3, p. 55, 2022. Available Online: https://doi.org/10.1007/s10921-022-00888-9

[200] Varga, L., Balázs, P., and Nagy, A., "Projection selection dependency in binary tomography," *Acta Cybernetica*, vol. 20, no. 1, pp. 167–187, 2011.

[201] Dines, K. A. and Lytle, R. J., "Computerized geophysical tomography," *Proceedings of the IEEE*, vol. 67, no. 7, pp. 1065–1073, 1979.

[202] Herman, G. T. and Kuba, A., "Discrete tomography in medical imaging," *Proceedings of the IEEE*, vol. 91, no. 10, pp. 1612–1626, 2003.

[203] Batenburg, K. J. and Sijbers, J., "DART: A practical reconstruction algorithm for discrete tomography," *IEEE Transactions on Image Processing*, vol. 20, no. 9, pp. 2542–2553, 2011.

[204] Schüle, T., Schnörr, C., Weber, S., and Hornegger, J., "Discrete tomography by convex–concave regularization and D.C. programming," *Discrete Applied Mathematics*, vol. 151, no. 1, pp. 229–243, 2005. Available Online: http://www.sciencedirect.com/science/article/pii/S0166218X05001320

[205] Lin, Y.-t., Ortega, A., and Dimakis, A., "Sparse recovery for discrete tomography," *IEEE International Conference on Image Processing*, pp. 4181–4184, 2010.

[206] Varga, L., Balázs, P., and Nagy, A., "Projection selection algorithms for discrete tomography," *Advanced Concepts for Intelligent Vision Systems (CompIMAGE 2010)*, pp. 390–401, 2010.

[207] Varga, L., Balázs, P., and Nagy, A., "Projection selection dependency in binary tomography," *Acta Cybernetica*, vol. 20, no. 1, pp. 167–187, 2011.

[208] Lékó, G. and Balázs, P., "Sequential projection selection methods for binary tomography," *Computational Modeling of Objects Presented in Images. Fundamentals, Methods, and Applications (CompIMAGE 2018)*, pp. 70–81, 2019.

[209] Pap, G., Lékó, G., and Grósz, T., "A reconstruction-free projection selection procedure for binary tomography using convolutional neural networks," *Image Analysis and Recognition*, pp. 228–236, 2019.

[210] Batenburg, K. J., Palenstijn, W. J., Balázs, P., and Sijbers, J., "Dynamic angle selection in binary tomography," *Computer Vision and Image Understanding*, vol. 117, no. 4, pp. 306–318, 2013. Available Online: http://www.sciencedirect.com/science/article/pii/S1077314212001774

[211] Varga, L., Nyúl, L., Nagy, A., and Balazs, P., "Local and global uncertainty in binary tomographic reconstruction," *Computer Vision and Image Understanding*, vol. 129, 2014.

[212] Lékó, G., Balázs, P., and Varga, L. G., "Projection selection for binary tomographic reconstruction using global uncertainty," *Image Analysis and Recognition (ICIAR 2018)*, pp. 3–10, 2018.

[213] Lékó, G., Domány, S., and Balázs, P., "Uncertainty based adaptive projection selection strategy for binary tomographic reconstruction," *Computer Analysis of Images and Patterns (CAIP 2019)*, pp. 74–84, 2019.

[214] Vogel, J., Lasser, T., Gardiazabal, J., and Navab, N., "Trajectory optimization for intra-operative nuclear tomographic imaging," *Medical Image Analysis*, vol. 17, no. 7, pp. 723–731, 2013. Available Online: http://www.sciencedirect.com/science/article/pii/S1361841513000625

[215] Presenti, A., Sijbers, J., den Dekker, A. J., and De Beenhouwer, J., "CAD-based defect inspection with optimal view angle selection based on polychromatic X-Ray projection images," *9th Conference on Industrial Computed Tomography (iCT2019)*, 2019.

[216] Alice, P., Jan, S., and Jan De, B., "Dynamic angle selection for few-view X-Ray inspection of CAD based objects," *Proceedings of SPIE*, vol. 11072, 2019. Available Online: https://doi.org/10.1117/12.2534894

[217] Presenti, A., Sijbers, J., and De Beenhouwer, J., "Dynamic few-view X-Ray imaging for inspection of CAD-based objects," *Expert Systems with Applications*, vol. 180, p. 115012, 2021. Available Online: https://www.sciencedirect.com/science/article/pii/S095741742100453X

[218] Kazankova, O., Bartscher, M., Matern, D., and Neuschaefer-Rube, U., "Neues röntgenbasiertes Verfahren für dimensionelle Messungen und dessen Anwendungen," *DACH-Jahrestagung 2019*, 2019. Available Online: https://www.ndt.net/search/docs.php3?id=24596

[219] Kitslaar, P., Marquering, H., Jukema, W., Koning, G., Nieber, M., Vossepoel, A., Bax, J., and Reiber, J., "Automated determination of optimal angiographic viewing angles for coronary artery bifurcations from CTA data," *Proceedings of SPIE*, vol. 6918, 2008.

[220] Bi, J., Grass, M., and Schäfer, D., "Optimization of acquisition trajectories for 3D rotational coronary venography," *Int J Comput Assist Radiol Surg*, vol. 5, no. 1, pp. 19–28, 2010.

[221] Garcia, J., Movassaghi, B., Casserly, I., Klein, A., Chen, S. Y., Messenger, J., Hansgen, A., Wink, O., Groves, B., and Carroll, J., "Determination of optimal viewing regions for X-Ray coronary angiography based on a quantitative analysis of 3D reconstructed models," *The international journal of cardiovascular imaging*, vol. 25, pp. 455–62, 2009.

[222] Wink, O., Kemkers, R., Chen, S. Y., and Carroll, J. D., "Intra-procedural coronary intervention planning using hybrid 3-dimensional reconstruction techniques," *Acad Radiol*, vol. 10, no. 12, pp. 1433–41, 2003.

[223] Chen, S. J. and Carroll, J. D., "3-D reconstruction of coronary arterial tree to optimize angiographic visualization," *IEEE Transactions on Medical Imaging*, vol. 19, no. 4, pp. 318–336, 2000.

[224] Dumay, A. C. M., Reiber, J. H. C., and Gerbrands, J. J., "Determination of optimal angiographic viewing angles: Basic principles and evaluation study," *IEEE Transactions on Medical Imaging*, vol. 13, no. 1, pp. 13–24, 1994.

[225] Holub, W., Brunner, F., and Schön, T., "RoboCT – application for in-situ inspection of join technologies of large scale objects," *International Symposium on Digital Industrial Radiology and Computed Tomography (DIR 2015), Ghent, Belgium*, 2019.

[226] Landstorfer, P., Hiller, J., and Herbst, M., "Investigation of positioning accuracy of industrial robots for robotic-based X-ray computed tomography," *9th Conference on Industrial Computed Tomography, Padova, Italy (iCT2019)*, 2019.

[227] Blumensath, T., O'Brien, N., and Wood, C. E., "Calibration of robotic manipulator systems for cone-beam tomography imaging," *IEEE Transactions on Nuclear Science*, vol. 65, no. 7, pp. 1384–1393, 2018.

[228] Kang, R., Probst, G., Vlaeyen, M., Fei, G., Guerrero, P., Haitjema, H., Slaets, P., and Dewulf, W., "Geometric qualification for robot CT with flexible trajectories," *11th Conference on Industrial Computed Tomography, Wels, Austria (iCT 2022)*, 2022.

[229] Klein, P. and Herold, F., "Comparison of reconstruction methods for computed tomography with industrial robots using automatic object position recognition," *19th World Conference on Non-Destructive Testing*, 2016.

[230] Vienne, C. and Costin, M., "Adapted acquisition trajectory and iterative reconstruction for few-views CT inspection," *8th Conference on Industrial Computed Tomography, Wels, Austria (iCT2018)*, 2018.

[231] Landstorfer, P., Herl, G., and Hiller, J., "Investigation of non-circular scanning trajectories in robot-based industrial X-ray computed tomography of multi-material objects," *16th International Conference on Informatics in Control, Automation and Robotics*, pp. 518–522, 2019.

[232] Holub, W., Hassler, U., Schorr, C., Maisl, M., Janello, P., and Jahnke, P., "XXL-micro-CT comparative evaluation of microscopic computed tomography for macroscopic objects," *Digital Industrial Radiology and Computed Tomography (DIR 2015), Ghent, Belgium*, 2015.

[233] Hess, J., Eberhorn, M., Hofmann, M., and Luxa, M., "Advanced reconstruction techniques applied to an on-site CT system," *2nd International Symposium on NDT in Aerospace*, 2010.

[234] Banjak, H., Costin, M., Vienne, C., and Kaftandjian, V., "X-ray computed tomography reconstruction on non-standard trajectories for robotized inspection," *19th World Conference on Non-Destructive Testing*, 2016.

[235] Universal Medical Systems, Inc., "Homepage of manufacturer," 2021, http://www.veterinary-imaging.com/equimagine-robotic-ct.php, Accessed on 11.06.2021. Available Online: http://www.veterinary-imaging.com/equimagine-robotic-ct.php

[236] Fieselmann, A., Steinbrener, J., Jerebko, A. K., Voigt, J. M., Scholz, R., Ritschl, L., and Mertelmeier, T., "Twin robotic X-ray system for 2D radiographic and 3D cone-beam CT imaging," *SPIE Medical Imaging*, vol. 9783, p. 6, 2016.

[237] Krumm, M., Sauerwein, C., Hämmerle, V., Heile, S., Schön, T., Jung, A., and Sindel, M., "Rapid robotic X-ray computed tomography of large assemblies in automotive production," *8th Conference on Industrial Computed Tomography 2018, Wels, Austria (iCT 2018)*, 2018.

[238] FACC, "Web Page," 2019, accessed on 11.06.2021. Available Online: https://www.facc.com/BEyond-Blog/FACC-entwickelt-innovative-Pruefrobotik

[239] Dedyaeva, P., Krohne, K., and Herold, F., "Digital twin for region-of-interest computed tomography of additive manufactured components using an industrial robot," *11th Conference on Industrial Computed Tomography, Wels, Austria (iCT 2022)*, 2022.

[240] De Samber, B., Renders, J., Elberfeld, T., Maris, Y., Sanctorum, J., Six, N., Liang, Z., De Beenhouwer, J., and Sijbers, J., "FleXCT: a flexible X-ray CT scanner with 10 degrees of freedom," *Optics Express*, vol. 29, 2021.

[241] Butzhammer, L. and Hausotte, T., "Complex 3D scan trajectories for industrial cone-beam computed tomography using a hexapod," *Measurement Science and Technology*, 2021. Available Online: http://iopscience.iop.org/article/10.1088/1361-6501/ac08c4

[242] North Star Imaging, Inc., "Homepage of manufacturer," 2021, https://4nsi.com/innovations/robotix, Accessed on 11.06.2021. Available Online: https://4nsi.com/innovations/robotix

[243] Wood, C., O'Brien, N., Denysov, A., and Blumensath, T., "Computed laminography of CFRP using an X-ray cone beam and robotic sample manipulator systems," *IEEE Transactions on Nuclear Science*, vol. 66, no. 3, pp. 655–663, 2019. Available Online: https://eprints.soton.ac.uk/415613/

[244] Krimmel, S., "Limited view angle tomography for single material objects in non-destructive testing with X-rays," PhD Thesis, 2006.

[245] Hiller, J., Landstorfer, P., Marx, P., and Herbst, M., "Evaluation of the impact of faulty scanning trajectories in robot-based X-ray computed tomography," *Measurement Science and Technology*, vol. 32, no. 1, p. 015401, 2020. Available Online: http://dx.doi.org/10.1088/1361-6501/abaf2a

[246] Bellon, C. and Jaenisch, G., "aRTist - analytical RT inspection simulation tool," *International Symposium on Digital Industrial Radiology and Computed Tomography (DIR 2007)*, 2007. Available Online: http://www.ndt.net/article/dir2007/papers/s1.pdf

[247] Gang, G. J., Stayman, J. W., Zbijewski, W., and Siewerdsen, J. H., "Task-based detectability in CT image reconstruction by filtered backprojection and penalized likelihood estimation," *Medical Physics*, vol. 41, no. 8Part1, p. 081902, 2014. Available Online: https://doi.org/10.1118/1.4883816

[248] Siewerdsen, J. H., Cunningham, I. A., and Jaffray, D. A., "A framework for noise-power spectrum analysis of multidimensional images," *Med Phys*, vol. 29, no. 11, pp. 2655–71, 2002.

[249] Brunner, C. C., Renger, B., Hoeschen, C., and Kyprianou, I. S., "Investigation of a method to estimate the MTF and NPS of CT towards creating an international standard," *Proc.SPIE*, vol. 7961, 2011. Available Online: https://doi.org/10.1117/12.877657

[250] Friedman, S. N., Fung, G. S. K., Siewerdsen, J. H., and Tsui, B. M. W., "A simple approach to measure computed tomography (CT) modulation transfer function (MTF) and noise-power spectrum (NPS) using the american college of radiology (ACR) accreditation phantom," *Medical Physics*, vol. 40, no. 5, p. 051907, 2013. Available Online: https://doi.org/10.1118/1.4800795

[251] Fessler, J. A., "Mean and variance of implicitly defined biased estimators (such as penalized maximum likelihood): Applications to tomography," *IEEE Transactions on Image Processing*, vol. 5, no. 3, pp. 493–506, 1996.

[252] Fessler, J. A. and Rogers, W. L., "Spatial resolution properties of penalized-likelihood image reconstruction: Space-invariant tomographs," *IEEE Trans Image Process*, vol. 5, no. 9, pp. 1346–58, 1996.

[253] Fessler, J. A. and Rogers, W. L., "Resolution properties of regularized image reconstruction methods," *Technical Report No. 297, Communications and Signal Processing Laboratory*, 1996. Available Online: https://citeseerx.ist.psu.edu/viewdoc/download?doi=10.1.1.447.2649&rep=rep1&type=pdf

[254] Stayman, J. W. and Fessler, J. A., "Efficient calculation of resolution and covariance for penalized-likelihood reconstruction in fully 3-D SPECT," *IEEE Transactions on Medical Imaging*, vol. 23, no. 12, pp. 1543–1556, 2004.

[255] Company Homepage of the Siemens Healthineers AG, "CERA – Software for High-quality CT Imaging," 2020, https://www.oem-products.siemens-healthineers.com/software-components, Accessed on 20.11.2020. Available Online: https://www.oem-products.siemens-healthineers.com/software-components

[256] Wang, W., Gang, G. J., Siewerdsen, J. H., and Stayman, J. W., "Spatial resolution and noise prediction in flat-panel cone-beam CT penalized-likelihood reconstruction," *Proc SPIE Int Soc Opt Eng*, vol. 10573, 2018.

[257] Uneri, A., Otake, Y., Wang, A. S., Kleinszig, G., Vogt, S., Khanna, A. J., and Siewerdsen, J. H., "3D-2D registration for surgical guidance: Effect of projection view angles on registration accuracy," *Physics in Medicine and Biology*, vol. 59, no. 2, pp. 271–287, 2014. Available Online: https://pubmed.ncbi.nlm.nih.gov/24351769https://www.ncbi.nlm.nih.gov/pmc/articles/PMC4927006/

[258] Thung, K. and Raveendran, P., "A survey of image quality measures," *International Conference for Technical Postgraduates (TECHPOS)*, pp. 1–4, 2009.

[259] Zhou, W. and Bovik, A. C., "A universal image quality index," *IEEE Signal Processing Letters*, vol. 9, no. 3, pp. 81–84, 2002.

[260] Wang, Z. and Bovik, A. C., "Mean squared error: Love it or leave it? a new look at signal fidelity measures," *IEEE Signal Processing Magazine*, vol. 26, no. 1, pp. 98–117, 2009.

[261] Eskicioglu, A. M. and Fisher, P. S., "Image quality measures and their performance," *IEEE Transactions on Communications*, vol. 43, no. 12, pp. 2959–2965, 1995.

[262] Sheikh, H. R., Sabir, M. F., and Bovik, A. C., "A statistical evaluation of recent full reference image quality assessment algorithms," *IEEE Transactions on Image Processing*, vol. 15, no. 11, pp. 3440–3451, 2006.

[263] Wang, Z., Bovik, A., Sheikh, H., Member, S., and Simoncelli, E., "Image quality assessment: From error measurement to structural similarity," *IEEE Transactions on Image Processing*, vol. 13, 2003.

[264] Wang, Z., Simoncelli, E. P., and Bovik, A. C., "Multiscale structural similarity for image quality assessment," *The Thrity-Seventh Asilomar Conference on Signals, Systems & Computers*, vol. 2, pp. 1398–1402 Vol.2, 2003.

[265] Chaofeng, L. and Alan, C. B., "Three-component weighted structural similarity index," *Proceedings of SPIE*, vol. 7242, 2009. Available Online: https://doi.org/10.1117/12.811821

[266] Guan-Hao, C., Chun-Ling, Y., Lai-Man, P., and Sheng-Li, X., "Edge-based structural similarity for image quality assessment," *IEEE International Conference on Acoustics Speech and Signal Processing ICASSP*, vol. 2, pp. II–II, 2006.

[267] Zhou, W. and Simoncelli, E. P., "Translation insensitive image similarity in complex wavelet domain," *IEEE International Conference on Acoustics Speech and Signal Processing ICASSP*, vol. 2, pp. ii/573–ii/576 Vol. 2, 2005.

[268] Alsamadony, K., Yildirim, E., Glatz, G., Bin Waheed, U., and Hanafy, S., "Deep learning driven noise reduction for reduced flux computed tomography," *Sensors*, vol. 21, p. 1921, 2021.

[269] Leuschner, J., Schmidt, M., Ganguly, P., Andriiashen, V., Coban, S., Denker, A., Bauer, D., Hadjifaradji, A., Batenburg, K., Maass, P., and van Eijnatten, M., "Quantitative comparison of deep learning-based image reconstruction methods for low-dose and sparse-angle CT applications," *Journal of Imaging*, vol. 7, p. 44, 2021.

[270] Pereira, L. F. A., Beenhouwer, J. d., Kastner, J., and Sijbers, J., "Extreme sparse X-Ray computed laminography via convolutional neural networks," *2020 IEEE 32nd International Conference on Tools with Artificial Intelligence (ICTAI)*, pp. 612–616, 2020.

[271] Russ, T., Wang, W., Golla, A.-K., Bauer, D., Tivnan, M., Tönnes, C., Ma, Y., Reynolds, T., Hatamikia, S., Schad, L., Zöllner, F., Gang, G., and Stayman, J., "Fast reconstruction of non-circular CBCT orbits using CNNs," *16th International Meeting on Fully 3D Image Reconstruction in Radiology and Nuclear Medicine, Leuven, Belgium*, 2021.

[272] Bian, J., Siewerdsen, J. H., Han, X., Sidky, E. Y., Prince, J. L., Pelizzari, C. A., and Pan, X., "Evaluation of sparse-view reconstruction from flat-panel-ddtector cone-beam CT," *Physics in Medicine and Biology*, vol. 55, no. 22, pp. 6575–6599, 2010. Available Online: https://pubmed.ncbi.nlm.nih.gov/20962368https://www.ncbi.nlm.nih.gov/pmc/articles/PMC3597413/

[273] Thompson, W. M., "Source firing patterns and reconstruction algorithms for a switched source, offset detector CT machine," PhD Thesis, 2010.

[274] Coban, S. B. and McDonald, S. A., "SophiaBeads dataset project," 2021, http://dx.doi.org/10.5281/zenodo.16474, Accessed on 16.09.2021. Available Online: http://dx.doi.org/10.5281/zenodo.16474

[275] Pelt, D. M. and Parkinson, D. Y., "Ring artifact reduction in synchrotron X-Ray tomography through helical acquisition," *Measurement Science and Technology*, vol. 29, no. 3, p. 9, 2018.

[276] Guan-Hao, C., Chun-Ling, Y., Lai-Man, P., and Sheng-Li, X., "Edge-based structural similarity for image quality assessment," *2006 IEEE International Conference on Acoustics Speech and Signal Processing Proceedings*, vol. 2, pp. II–II, 2006.

[277] GmbH, K. D., "Technical datasheet for KR 90 R3100 extra HA," accessed on 28.3.2022. Available Online: https://www.kuka.com/-/media/kuka-downloads/imported/6b77eecacfe542d3b736af377562ecaa/0000208694_de.pdf

[278] Candès, E. J., Romberg, J. K., and Tao, T., "Stable signal recovery from incomplete and inaccurate measurements," *Communications on Pure and Applied Mathematics*, vol. 59, no. 8, pp. 1207–1223, 2006.

[279] Hurley, N. and Rickard, S., "Comparing measures of sparsity," *IEEE Transactions on Information Theory*, vol. 55, pp. 4723–4741, 2009.

[280] Zonoobi, D., Kassim, A., and Venkatesh, Y., "Gini index as sparsity measure for signal reconstruction from compressive samples," *IEEE Journal of Selected Topics in Signal Processing*, vol. 5, pp. 927–932, 2011.

[281] Ghita, M., Uher, J., Boháčová, J., and Kadeřábek, R., "Arbitrary path CT by multi-robot imaging platform (RadalyX)," *11th Conference on Industrial Computed Tomography, Wels, Austria (iCT 2022)*, 2022.

[282] Siltanen, S., Kolehmainen, V., Järvenpää, S., Kaipio, J. P., Koistinen, P., Lassas, M., Pirttilä, J., and Somersalo, E., "Statistical inversion for medical X-ray tomography with few radiographs: I. general theory," *Phys Med Biol*, vol. 48, no. 10, pp. 1437–63, 2003.

[283] Brierley, N., Nye, B., and McGuinness, J., "Mapping the spatial performance variability of an X-ray computed tomography inspection," *NDT & E International*, vol. 107, p. 102127, 2019. Available Online: https://www.sciencedirect.com/science/article/pii/S096386951930132X

[284] Herman, G. T. and Davidi, R., "Image reconstruction from a small number of projections," *Inverse Problems*, vol. 24, no. 4, p. 045011, 2008. Available Online: http://dx.doi.org/10.1088/0266-5611/24/4/045011

[285] Stayman, J. W. and Fessler, J. A., "Compensation for nonuniform resolution using penalized-likelihood reconstruction in space-variant imaging systems," *IEEE Transactions on Medical Imaging*, vol. 23, no. 3, pp. 269–284, 2004.

[286] Stayman, J. W. and Fessler, J. A., "Regularization for uniform spatial resolution properties in penalized-likelihood image reconstruction," *IEEE Trans Med Imaging*, vol. 19, no. 6, pp. 601–15, 2000.

[287] Hashem, N., Pryor, M., Haas, D., and Hunter, J., "Design of a computed tomography automation architecture," *Applied Sciences*, vol. 11, p. 2858, 2021.

[288] Buratti, A., Ferrucci, M., Achour, S. B., Dewulf, W., and Schmitt, R. H., "An analytical method for optimizing imaging parameters in industrial X-Ray computed tomography for dimensional measurements on multimaterial workpieces," *SPIE Optical Engineering + Applications*, vol. 9967, p. 7, 2016.

[289] Gang, G. J., Stayman, J. W., Ehtiati, T., and Siewerdsen, J. H., "Task-driven image acquisition and reconstruction in cone-beam CT," *Physics in Medicine and Biology*, vol. 60, no. 8, pp. 3129–3150, 2015. Available Online: http://www.ncbi.nlm.nih.gov/pmc/articles/PMC4539970/

[290] Prakash, P., Zbijewski, W., Gang, G. J., Ding, Y., Stayman, J. W., Yorkston, J., Carrino, J. A., and Siewerdsen, J. H., "Task-based modeling and optimization of a cone-beam CT scanner for musculoskeletal imaging," *Med Phys*, vol. 38, no. 10, pp. 5612–29, 2011.

[291] Lékó, G. and Balázs, P., "Scale invariance in projection selection using binary tomography," *Fundamenta Informaticae*, vol. 172, pp. 129–142, 2020.

[292] Li, M., Yang, H., and Kudo, H., "An accurate iterative reconstruction algorithm for sparse objects: Application to 3D blood vessel reconstruction from a limited number of projections," *Physics in Medicine and Biology*, vol. 47, no. 15, pp. 2599–2609, 2002. Available Online: http://dx.doi.org/10.1088/0031-9155/47/15/303

[293] Larsson, D. H., Lundström, U., Westermark, U. K., Arsenian Henriksson, M., Burvall, A., and Hertz, H. M., "First application of liquid-metal-jet sources for small-animal imaging: High-resolution CT and phase-contrast tumor demarcation," *Medical Physics*, vol. 40, no. 2, p. 021909, 2013.

[294] Bartzsch, S. and Oelfke, U., "Line focus X-ray tubes - a new concept to produce high brilliance X-Rays," *Physics in Medicine and Biology*, vol. 62, no. 22, pp. 8600–8615, 2017.

[295] Günther, B., Gradl, R., Jud, C., Eggl, E., Huang, J., Kulpe, S., Achterhold, K., Gleich, B., Dierolf, M., and Pfeiffer, F., "The versatile X-Ray beamline of the munich compact light source: Design, instrumentation and applications," *Journal of Synchrotron Radiation*, vol. 27, pp. 1395–1414, 2020.

[296] Yuki, R., Ohtake, Y., and Suzuki, H., "Deblurring X-ray transmission images using convolutional neural networks to achieve fast CT scanning," *10th Conference on Industrial Computed Tomography, Wels, Austria (iCT 2020)*, 2020.

[297] Yuki, R., Ohtake, Y., and Suzuki, H., "Acceleration of X-Ray computed tomography scanning with high-quality reconstructed volume by deblurring transmission images using convolutional neural networks," *Precision Engineering*, vol. 73, pp. 153–165, 2022. Available Online: https://www.sciencedirect.com/science/article/pii/S0141635921002129

[298] Hendriksen, A., Bührer, M., Leone, L., Merlini, M., Viganò, N., Pelt, D., Marone, F., Di Michiel, M., and Batenburg, K., "Deep denoising for multi-dimensional synchrotron X-Ray tomography without high-quality reference data," *Scientific Reports*, vol. 11, 2021.

[299] Papadakis, A. E. and Damilakis, J., "Automatic tube current modulation and tube voltage selection in pediatric computed tomography: A phantom study on radiation dose and image quality," *Investigative Radiology*, vol. 54, no. 5, 2019. Available Online: https://journals.lww.com/investigativeradiology/Fulltext/2019/05000/Automatic_Tube_Current_Modulation_and_Tube_Voltage.2.aspx

[300] Neculaes, V., Edic, P., Frontera, M., Caiafa, A., Wang, G., and De Man, B., "Multi-source X-ray and CT: Lessons learned and future outlook," *IEEE Access*, vol. 2, pp. 1–1, 2015.

[301] Lu, Y., Zhao, J., and Wang, G., "Few-view image reconstruction with dual dictionaries," *Physics in medicine and Biology*, vol. 57, pp. 173–89, 2011.

[302] Sen Sharma, K., Jin, X., Holzner, C., Narayanan, S., Liu, B., Wang, D., Agah, M., Wang, L., Yu, H., and Wang, G., "Experimental studies on few-view reconstruction for high-resolution micro-CT," *J Xray Sci Technol*, vol. 21, no. 1, pp. 25–42, 2013.

[303] Chen, G., Tang, J., and Leng, S., "Prior image constrained compressed sensing (PICCS): a method to accurately reconstruct dynamic CT images from highly undersampled projection data sets," *Medical Physics*, vol. 35 2, pp. 660–3, 2008.

[304] Han, Y. and Ye, J. C., "Framing u-net via deep convolutional framelets: Application to sparse-view CT," *IEEE Transactions on Medical Imaging*, vol. 37, 2017.

[305] Janssens, E., De Beenhouwer, J., Van Dael, M., De Schryver, T., Van Hoorebeke, L., Verboven, P., Nicolai, B., and Sijbers, J., "Neural network hilbert transform based filtered backprojection for fast inline X-Ray inspection," *Measurement Science and Technology*, vol. 29, no. 3, p. 034012, 2018. Available Online: http://dx.doi.org/10.1088/1361-6501/aa9de3

[306] Janssens, E., Sijbers, J., Dierick, M., and De Beenhouwer, J., "Fast detection of cracks in ultrasonically welded parts by inline X-Ray inspection," *9th Conference on Industrial Computed Tomography, Padova, Italy (iCT2019)*, 2019.

[307] Smith, B., "Cone-beam tomography. recent advances and a tutorial review," *Optical Engineering - OPT ENG*, vol. 29, 1990.

[308] Willemink, M. J. and Noël, P. B., "The evolution of image reconstruction for CT – from filtered back projection to artificial intelligence," *European radiology*, vol. 29, no. 5, pp. 2185–2195, 2019. Available Online: https://pubmed.ncbi.nlm.nih.gov/30377791https://www.ncbi.nlm.nih.gov/pmc/articles/PMC6443602/

[309] Mishra, D., Longtin, J. P., Singh, R. P., and Prasad, V., "Performance evaluation of iterative tomography algorithms for incomplete projection data," *Applied Optics*, vol. 43, no. 7, pp. 1522–1532, 2004. Available Online: http://ao.osa.org/abstract.cfm?URI=ao-43-7-1522

[310] Galigekere, R. R., Wiesent, K., and Holdsworth, D. W., "Techniques to alleviate the effects of view aliasing artifacts in computed tomography," *Medical Physics*, vol. 26, no. 6, pp. 896–904, 1999. Available Online: https://doi.org/10.1118/1.598606

[311] Brooks, R. A., Weiss, G. H., and Talbert, A. J., "A new approach to interpolation in computed tomography," *Journal of Computer Assisted Tomography*, vol. 2, no. 5, 1978. Available Online: https://journals.lww.com/jcat/Fulltext/1978/11000/A_New_Approach_to_Interpolation_in_Computed.10.aspx

[312] Weiss, G. H., Talbert, A. J., and Brooks, R. A., "The use of phantom views to reduce CT streaks due to insufficient angular sampling," *Physics in Medicine and Biology*, vol. 27, no. 9, pp. 1151–1162, 1982. Available Online: http://dx.doi.org/10.1088/0031-9155/27/9/005

[313] Körner, L., Lawes, S. D. A., Bate, D., Newton, L., Senin, N., and Leach, R., "Increasing throughput in X-ray computed tomography measurement of surface topography using sinogram interpolation," *Measurement Science and Technology*, vol. 30, p. 125002, 2019.

[314] Körner, L., Lawes, S., Newton, L., Senin, N., Bate, D., and Leach, R., "Sinogram interpolation to decrease acquisition time in X-ray computed tomography measurement of surface topography," *9th Conference on Industrial Computed Tomography, Padova, Italy (iCT2019)*, 2019.

[315] Galigekere, R. R., Wiesent, K., Mertelmeier, T., and Holdsworth, D. W., "On intermediate view estimation in computed tomography," *Circuits, Systems and Signal Processing*, vol. 19, no. 4, pp. 279–299, 2000. Available Online: https://doi.org/10.1007/BF01200889

[316] Kalke, M. and Siltanen, S., "Sinogram interpolation method for sparse-angle tomography," *Applied Mathematics*, vol. 05, pp. 423–441, 2014.

[317] Kim, H.-G. and Yoo, H., "Image enhancement for computed tomography using directional interpolation for sparsely-sampled sinogram," *Optik*, vol. 166, pp.

227–235, 2018. Available Online: http://www.sciencedirect.com/science/article/pii/S0030402618304777

[318] Dong, J., Fu, J., and He, Z., "A deep learning reconstruction framework for X-Ray computed tomography with incomplete data," *PLOS ONE*, vol. 14, no. 11, p. e0224426, 2019. Available Online: https://doi.org/10.1371/journal.pone.0224426

[319] Wei, H., Schiffers, F., Würfl, T., Shen, D., Kim, D., Katsaggelos, A., and Cossairt, O., "2-Step sparse-view CT reconstruction with a domain-specific perceptual network," *ArXiv*, vol. abs/2012.04743, 2020. Available Online: https://arxiv.org/abs/2012.04743

[320] Kiwan Jeon, P. and Suk, H., "A curvelet based sinogram correction method for metal artifact reduction," *9th Conference on Industrial Computed Tomography, Padova, Italy (iCT2019)*, 2019.

[321] Shojaeilangari, S., Schmidtlein, C. R., Rahmim, A., and Ay, M. R., "Recovery of missing data in partial geometry PET scanners: Compensation in projection space vs image space," *Medical Physics*, vol. 45, no. 12, pp. 5437–5449, 2018. Available Online: https://pubmed.ncbi.nlm.nih.gov/30288762https://www.ncbi.nlm.nih.gov/pmc/articles/PMC6329391/

[322] Riviere, P. J. L. and Pan, X., "Few-view tomography using roughness-penalized nonparametric regression and periodic spline interpolation," *IEEE Transactions on Nuclear Science*, vol. 46, no. 4, pp. 1121–1128, 1999.

[323] Gradl, R., Dierolf, M., Hehn, L., Gunther, B., Kutschke, D., Yang, L., Moller, W., Stoeger, T., Kimm, M., Haas, H., Roiser, N., Pfeiffer, D., Donnelley, M., Jud, C., Gleich, B., Parsons, D., Achterhold, K., Schmid, O., Pfeiffer, F., and Morgan, K. S., "Dynamic x-ray imaging at the munich compact light source," *Microscopy and Microanalysis*, vol. 24, no. S2, pp. 350–351, 2018. Available Online: https://www.cambridge.org/core/article/dynamic-xray-imaging-at-the-munich-compact-light-source/AD49C18567A319FBC7B4B3CA25692E12

[324] Schrapp, M., Goldammer, M., Stephan, J., Chimenti, D. E., Bond, L. J., and Thompson, D. O., "Artifact reduction in industrial computed tomography via data fusion," *AIP Conference Proceedings*, vol. 1581, no. 1, pp. 1961–1966, 2014. Available Online: http://aip.scitation.org/doi/abs/10.1063/1.4865064

[325] Coello, E., Sperl, J. I., Bequé, D., Benz, T., Scherer, K., Herzen, J., Sztrókay-Gaul, A., Hellerhoff, K., Pfeiffer, F., Cozzini, C., and Grandl, S., "Fourier domain image fusion for differential x-ray phase-contrast breast imaging," *Eur J Radiol*, vol. 89, pp. 27–32, 2017.

[326] Schrapp, M., Scharrer, T., Goldammer, M., J. Rupitsch, S., Sutor, A., Ermert, H., and Lerch, R., "Artifact reduction in non-destructive testing by means of complementary data fusion of X-Ray computed tomography and ultrasonic pulse-echo testing," *Measurement Science and Technology*, vol. 24, no. 12, p. 125403, 2013. Available Online: http://stacks.iop.org/0957-0233/24/i=12/a=125403

[327] Fedrigo, M., Wenger, A., and Hoeschen, C., "Investigating tomographic reconstruction with a priori geometrical information," *Journal of X-ray Science and Technology*, vol. 20, no. 1, pp. 1–10, 2012.

[328] Hassler, U., Oeckl, S., and Bauscher, I., "Inline CT methods for industrial production," *International Symposium on NDT in Aerospace, 2008, Fürth, Germany (AeroNDT 2008)*, 2008.

[329] Pruim, R. J., Welch, R. P., Sanna, S., Teslovich, T. M., Chines, P. S., Gliedt, T. P., Boehnke, M., Abecasis, G. R., and Willer, C. J., "Locuszoom: Regional visualization of genome-wide association scan results," *Bioinformatics*, vol. 26, no. 18, pp. 2336–7, 2010.

[330] Crameri, F., Shephard, G. E., and Heron, P. J., "The misuse of colour in science communication," *Nature Communications*, vol. 11, no. 1, p. 5444, 2020. Available Online: https://doi.org/10.1038/s41467-020-19160-7

[331] Drath, P., *Leitfaden für den Gebrauch des Internationalen Einheitensystems*. Braunschweig: Physikalisch-Technische Bundesanstalt, 1996.

[332] Deutsches Institut für Normung, *DIN 1338:2011-03: Writing and Typesetting of Formulae*, 2011.

List of Figures

List of Tables

List of Acronyms

ART	Algebraic Reconstruction Technique
ASFC	Angular Summed Fourier Coeffients
AUC	Area under the Curve
BKE	Background Known Exactly
CAD	Computer-Aided Design
CBCT	Cone Beam Computed Tomography
CNR	Contrast-to-Noise Ratio
CS	Compressed Sensing
CT	Computed Tomography
DOF	Degree of Freedom
DQE	Detective Quantum Efficiency
FBP	Filtered Backprojection
FDK	Reconstruction Algorithm Developed by Feldkamp, Davis and Kress
FFT	Fast Fourier Transform
FIM	Fisher Information Matrix
FNF	False Negative Fraction
FPF	False Positive Fraction
FSIM	Feature Similarity Index
FWHM	Full Width at Half Maximum
HCA	Half-Circle-and-Arc Trajectory
IC	Inclined Circle Trajectory
IQR	Image Quality Ratio
JPEG	Joint Photographic Experts Group (Data Format)
LDS	Low Discrepancy Spherical Trajectory
MO	Model Observer
MPEG	Moving Picture Experts Group (Data Format)
MRI	Magnetic Resonance Imaging
MSE	Mean Squared Error

MTF	Modulation Transfer Function
NDT	Non-Destructive Testing
NEQ	Noise-Equivalent Quanta
NN-hFBP	Neural Network Hilbert Transform Based Filtered Backprojection
NPS	Noise Power Spectrum
NPW	Non-Prewhitening (Model Observer)
OTF	Optical Transfer Function
PC	Planar Circle Trajectory
PET	Positron Emission Tomography
PHC	Planar Half Circle Trajectory
PICCS	Prior Image Constrained Compressed Sensing
POD	Probability of Detection
PSF	Point Spread Function
PSNR	Peak Signal-to-Noise Ratio
PW	Prewhitening (Model Observer)
RMSE	Root Mean Square Error
ROC	Receiver Operating Characteristic Curve
SART	Simultaneous Algebraic Reconstruction Technique
SDD	Source-Detector Distance
SEM	Standard Error of the Mean
SIRT	Simultaneous Iterative Reconstruction Technique
SKE	Signal Known Exactly
SNR	Signal-to-Noise Ratio
SOD	Source-Object Distance
SPECT	Single Photon Emission Computed Tomography
SSIM	Structural Similarity Index
SVD	Singular Value Decomposition
TNF	True Negative Fraction
TPF	True Positive Fraction
UQI	Universal Image Quality Index
VOI	Volume of Interest

List of Symbols

$\mathbf{A}$	System Matrix, Evaluation Image
$\mathbf{B}$	Reference Image
C	Contrast (Modulation), Regularization Constant
$\mathbf{C_n}$	Noise Correlation Matrix
D	Detector Size
$\mathbf{D}$	Measured Pixel Values
$E_{\max}$	Maximum Photon Energy
F	Imaged Object (Fourier Space)
$\mathbf{H}$	Angular Histogram Matrix
I	X-Ray Beam Intensity
I_0	Initial X-Ray Beam Intensity
I_{m}	Measured X-Ray Beam Intensity
$\mathbf{I}$	Identity Matrix
$\mathbf{K_n}$	Noise Covariance Matrix
N	Number of Photons, Number of Projections
N_{ideal}	Number of Photons (Ideal Detector)
N_{real}	Number of Photons (Real Detector)
P_{noise}	Noise Power
P_{signal}	Signal Power
$\mathbf{R}$	Quadratic Regularization Matrix
T	Observed Time Interval
d	Size of Smallest Resolvable Feature
$d', \mathbf{d}'$	Detectability Index
$\mathbf{e_j}$	Position Vector of the VOI (Kronecker Delta Notation)
$f, \mathbf{f}$	Imaged Object (Object Space)
$\tilde{\mathbf{f}}$	Reconstructed Object (Object Space)
$\mathbf{g}, \mathbf{g_{CT}}$	Measured Data
h_{ϕ}	Filtered Projection (Radon Space)
$\mathbf{h}$	Angular Histogram
$n, \mathbf{n}$	Noise
p	Probability Density Function
$p_{\phi}, \mathbf{p}$	Imaged Object (Radon Space), Projection
s	Signal
$\mathbf{s}$	Sparse Vector Representation
$\mathbf{s_b}$	Background Signal
$\mathbf{s_f}$	Feature Signal

t	Time, Test Statistic, Number of Pixel Elements
t_c	Scalar Test Threshold
$\mathbf{w}$	Linear Discriminant
$\mathbf{\Gamma}$	Weighting Factor Matrix
$\Delta\mathbf{s}$	Signal Difference (Object Space)
$\Delta\xi$	Pixel Pitch (Object Space)
Λ	Likelihood Ratio
Ξ	Optimizability
$\overline{\Xi}$	Normalized Optimizability
$\mathbf{\Phi}$	Measurement Matrix, Rotation Angle Matrix (Azimuth)
$\mathbf{\Phi_N}$	Set of Measurement Matrices Containing N Projections
$\mathbf{\Phi_{opt}}$	Optimized Measurement Matrix
$\mathbf{\Psi}$	Sparse Transform Basis
$\mathbf{\Psi_t}$	Tailored Transform Basis
β	Regularization Parameter
γ	Weighting Factor
$\boldsymbol{\delta}$	Dirac Impulse Vector
$\theta, \mathbf{\Theta}$	Rotation Angle (Altitude)
λ, λ'	Log-Likelihood Ratio
λ_p	Photon Wavelength
μ	Combined Attenuation Coefficient, Expectation Value
μ_{cs}	Attenuation Coefficient from Coherent Scattering
μ_{is}	Attenuation Coefficient from Incoherent Scattering
μ_{pa}	Attenuation Coefficient from Photoelectric Absorption
μ_{pp}	Attenuation Coefficient from Pair Production
ν_{max}	Maximum Obtainable Frequency
ν_q	Pixel Pitch (Fourier Space)
ξ	Lateral Pixel Offset
σ_λ	Observer Standard Deviation
σ_n	Noise Standard Deviation
ϕ	Rotation Angle (Azimuth)
$\omega, \boldsymbol{\omega}$	Signal Template

List of Publications and Further Work

List of Supervised Theses

- Eck, Simon: "Untersuchung von Defekterkennungswahrscheinlichkeiten in der unterabgetasteten Röntgen-Computertomographie", Master's Thesis at the Department of Applied Sciences and Mechatronics (Munich University of Applied Sciences), submitted at 20.03.2020.

- Bouhaouel, Fehmi: "Evaluation of Observer Model Performance in Sparsely Sampled Cone Beam Computed Tomography", Master's Thesis at the Chair of Non-Destructive Testing (Technical University of Munich), submitted at 1.5.2019. Available online at https://mediatum.ub.tum.de/1487613.

- Pršeš, Kenan: "Development of a Method for Quality Assurance of Additive Manufactured Parts by Laser Metal Deposition based on 3D Visualization of Process Data", Interdisciplinary Project at the Chair of Non-Destructive Testing (Technical University of Munich), submitted at 19.09.2018.

List of Invention Disclosures and Patents

- "Bestimmung von optimierten Messpositionen in der Computertomographie", Patent, 2021.

- "Algorithmus zur gleichmäßigen Verteilung von Punkten auf einer diskretisierten Kugeloberfläche", Invention Disclosure, 2020.

Publications Related to this Dissertation

- Bauer, F., Forndran, D., Schromm, T., and Grosse, C. U., "Practical Part-specific Trajectory Optimization for Robot-Guided Inspection via Computed Tomography", *Journal of Nondestructive Evaluation*, vol. 41, no. 3, p. 55, 2022.

- Bauer, F., Goldammer, M., and Grosse, C. U., "Selection and Evaluation of Spherical Acquisition Trajectories for Industrial Computed Tomography", *Proceedings of the Royal Society A: Mathematical, Physical and Engineering Sciences*, vol. 477, no. 2250, p. 20210192, 2021.

- Bauer, F., Goldammer, M., and Grosse, C. U., "Scan Time Reduction by Fewer Projections – an Approach for Part-Specific Acquisition Trajectories", *World Conference on Non-Destructive Testing (WCNDT 2020)*, Incheon, South Korea, 2022, submitted.

- Bouhaouel, F., Bauer, F., and Grosse, C. U., "Task-Specific Acquisition Trajectories Optimized Using Observer Models", *10th Conference on Industrial Computed Tomography (iCT2020)*, Wels, Austria, 2020.

Publications not Directly Related to this Dissertation

- Reuter, T., Plotzki, D., de Oliveira, F. B., Wohlgemuth, F., Bauer, F., Ballach, F., Kimmig, W., Wagner, G., Watzl, C., Weiß, D., and Hausotte, T., "Numerical Measurement Uncertainty Evaluation for Computed Tomography Using Simulations – A first Approach to Build a Digital Twin", *Technisches Messen*, vol. 89, no. 10, 2022.

- Wildfeuer, L., Wassiliadis, N., Karger, A., Bauer, F., and Lienkamp, M., "Tear-Down Analysis and Characterization of a Commercial Lithium-Ion Battery for Advanced Algorithms in Battery Electric Vehicles", *Journal of Energy Storage*, vol 48, 2022.

- Bauer, F., Schrapp, M., and Szijarto, J., "Accuracy Analysis of a Piece-to-Piece Reverse Engineering Workflow for a Turbine Foil based on Multi-Modal Computed Tomography and Additive Manufacturing", *Precision Engineering*, vol. 60, pp. 63-75, 2019.

- Bauer, F., Schrapp, M., and Szijarto, J., "Error Investigations for a CT and Additive Manufacturing based Reverse Engineering Workflow", *9th Conference on Industrial Computed Tomography (iCT2019)*, Padova, Italy, 2019.

Appendix

A | Remarks Concerning Notation and Stylistic Elements

The overall color scheme (e.g., in graphs or figures) used in this work was originally inspired by the "LocusZoom" color map [329], which has been strongly modified and extended for this work and is shown in fig. A.1. Differing from this, the heat maps and Fourier-transformed image representations use the "lajolla" color map, which was scientifically derived and optimized for human perception [330]. Although compromises were necessary, particular care was given to coherently apply colors. Whenever possible, the color coding used in this work refers to the systematic listed in tab. A.2. In derogation of this, the cover page and formal elements use the color schema of the Technical University of Munich to maintain a uniform layout on several pages.

Table A.1: Color palette used for this work. Color codes are given in RGBA format as hexadecimal numbers with the alpha-channel taking values between 0 and 255.

Color						
RGBA	bf3934ff	235580ff	478c47ff	db9723ff	44b6d6ff	8d2eadff
Color						
RGBA	bf393480	23558066	478c4780	db972380	44b6d666	8d2ead66
Color						
RGBA	000000ff	666666ff	808080ff	b3b3b3ff	ccccccff	ffffffff

Table A.2: Typical color encoding for continuous or dotted curves in the quality plots and different style elements of this work.

Color	Trajectory (continuous)	Trajectory (dotted)	Platonic Solid	Domain
	PC	PHC	Tetrahedron	Object
	LDS	half-sphere LDS	Icosahedron	Fourier
	NPW/Uniform, IC	N/A	Dodecahedron	N/A
	NPW/Feature	N/A	N/A	N/A
	NPW/Uniform + W	N/A	Octahedron	N/A
	NPW/Feature + W	N/A	Cube	Radon
	PW/Uniform + W, HCA	PW/Uniform	Sphere	N/A
	PW/Feature + W	PW/Feature	N/A	N/A

As convention for the notations, following nomenclature is applied: lower case Greek and Latin letters are used to denominate scalar parameters, while bold ones are applied for vectors and upper case bold ones for matrices. Operators and transforms are expressed via calligraphic capital letters (e.g., $\mathcal{F}$ for the Fourier transform). Matrix and vector indices are typically used as a part of the variable name (e.g., $\mathbf{K_n}$ for the noise covariance matrix) but are sporadically also used as indexing variables if fit, for instance for the pseudocode in sec. C. The overall notation style follows the recommendations of the German National Metrology Institute [331] and the DIN 1338 [332] whenever reasonable in order to stay concise.

B | Overview of Test Parts and Imaging Parameters

B.1 Reconstructed Volume Sizes

Table B.1: Complete and VOI-sizes of the reconstructed volumes.

Dataset	Volume Size [voxel]	VOI-Size [voxel]	Voxel Size [μm]
Bat Phantom (Simulation)	$512 \times 512 \times 512$	$49 \times 49 \times 49$	100
Bat Phantom (Experiment)	$512 \times 512 \times 512$	$49 \times 49 \times 49$	250
Platonic Solids (Parallel Beam)	$512 \times 512 \times 512$	$91 \times 91 \times 91$	600
Platonic Solids (Cone Beam)	$512 \times 512 \times 512$	$91 \times 91 \times 91$	600
KUKA Robot	$512 \times 512 \times 512$	$49 \times 49 \times 49$	100
RoboCT	$512 \times 512 \times 512$	$91 \times 91 \times 91$	200

B.2 Imaging Parameters

Table B.2: Acquisition parameters for the datasets. All pixels and voxels are isotropic. Due to the selected detector definition in the simulations no meaningful exposure time or current can be provided.

Dataset	SOD [mm]	SDD [mm]	Detector Size [mm] (binning)	Pixel Size [µm]	Voltage [kV] (spectrum)	Current [µA]	Exposure [ms] (samples)	Prefilter [mm] (material)
Bat Phantom (Simulation)	100	200	512 × 512 (–)	200	150 (mono)	N/A	N/A (N/A)	none (–)
Bat Phantom (Experiment)	350	700	2,048 × 2,048 (–)	200	220 (poly)	200	250 (8)	0.5 (copper)
Platonic Solids (Parallel Beam)	1,000	2,000	512 × 512 (–)	800	250 (mono)	N/A	N/A (N/A)	none (–)
Platonic Solids (Cone Beam)	50	100	512 × 512 (–)	800	150 (mono)	N/A	N/A (–)	none (–)
KUKA Robot	100	200	512 × 512 (–)	200	250 (mono)	N/A	N/A (–)	none (–)
RoboCT	600	1,200	2,480 × 2,976 (4 × 4)	100	150 (poly)	1,300	600 (3)	none (–)

B.3   Design Drawing of the Bat Phatom

C | Algorithms and Code

C.1   Pseudocode of the Geometric Weighting Function

Algorithm 1: Implementation of the geometric weighting function, which is explained in detail in sec. 6.4.3. For comprehensibility, the empirically determined weighting zone ranges are exemplary used that were also applied in the final implementation, while the weights were selected as described in the main text.

Input: Index of the selected projection out of all possible projections n in optimization iteration $j \in [0; n-1]$ as dynamically built vector $\mathbf{p_j}$

Result: Weighting map $\mathbf{\Gamma_{jw}}$ consisting of n weights w for each iteration j

$\mathbf{\Gamma_{jw}} \leftarrow \mathbf{1}$ // inititalize matrix with all weights equal to one

for $j > 0$ **do**

     the optimization loop is performed at this point (see alg. 2)

     $\mathbf{\Gamma_{jw}} \leftarrow \mathbf{\Gamma_{(j-1)w}}$ // initialize with weights from previous iteration

     $\mathbf{\Gamma_{j(w=p_j)}} \leftarrow 0$ // selected iteration solution has zero weight

     for all $w \neq \mathbf{p_j}$ entries of $\mathbf{\Gamma_{jw}}$ **do**

         $a \leftarrow \sphericalangle \left(\mathbf{p_j}, \mathbf{\Gamma_{jw}}\right)$ // calculate difference angle in degrees

         if $a \leq 1°$ **then**

            $\gamma \leftarrow \gamma_{\text{close}}$ // assign close weighting factor

         else if $1° < a \leq 15°$ **then**

            $\gamma \leftarrow \gamma_{\text{adjacent}}$ // assign adjacent weighting factor

         else if $172.5° \leq a \leq 187.5°$ **then**

            $\gamma \leftarrow \gamma_{\text{opposed}}$ // assign opposed weighting factor

         else

            $\gamma \leftarrow 1$ // assign no weighting factor to other entries

         if $\gamma < \mathbf{\Gamma_{(j-1)w}}$ **then**

            $\mathbf{\Gamma_{jw}} \leftarrow \gamma$ // apply weighting factor only if stricter rule than the previous one

         end

     end

end

C.2 Pseudocode for the Model Observer based Optimization Framework

Algorithm 2: Model observer-based trajectory optimization algorithm including prediction part for a NPW MO. For the calculation of $\mathbf{d'^2}$ element-wise multiplication applies and a trapezoidal approximation was used to compute the integrals. In derogation of the usual notation convention used in this work $\mathbf{d'^2}$ denotes here a matrix of dimension $m \times n$. The weighting step is only indicated and its detailed implementation is described in alg. 1.

Input: Evaluation projection set containing n projections including their associated projection matrices; part volume of the feature $\Delta\mathbf{s}$ with position (a, b, c), regularization strength β

Result: Subset containing $m < n$ projections of the input projection set

$\boldsymbol{\omega} \leftarrow \mathcal{F}(\Delta\mathbf{s})$ // calculate FFT of $\Delta\mathbf{s}$

$\mathbf{R} \leftarrow \mathbf{0}$ // calculate quadratic regularization matrix $\mathbf{R}$

foreach $(-1, -1, -1) \leq (i, j, k) \leq (1, 1, 1)$ **do**

    $\mathbf{R_{a+i,b+j,c+k}} \leftarrow -1/\sqrt{i^2 + j^2 + k^2}$

end

$\mathbf{R_{abc}} \leftarrow -\ell_1(\mathbf{R})$

for all n projections **do**

    reshape projection pixel values into diagonal matrix $\mathbf{D_n}$

    calculate VOI-part of the system matrix $\mathbf{A}$

    $\mathbf{FIM_n} \leftarrow \mathbf{A}^{\mathrm{T}}\mathbf{D_n}\mathbf{A}$ // calculate Fisher information matrix $\mathbf{FIM_n}$

end

$\boldsymbol{\Gamma} \leftarrow \mathbf{1}$ // inititalize geometrical weights $\boldsymbol{\Gamma}$ (line vector) as equal to one

$i \leftarrow 0$ // start optimization loop

$\mathbf{d'^2} \leftarrow \mathbf{0}$

for $i < m$ **do**

    for all n projections **do**

        $\mathbf{MTF_n} \leftarrow |\mathcal{F}(\mathbf{FIM_n})|/|\mathcal{F}(\mathbf{FIM_n} + \beta\mathbf{R})|$ // estimate $\mathbf{MTF_n}$

        $\mathbf{NPS_n} \leftarrow |\mathcal{F}(\mathbf{FIM_n})|/|\mathcal{F}(\mathbf{FIM_n} + \beta\mathbf{R})|^2$ // estimate $\mathbf{NPS_n}$

        $\mathbf{d'^2_{in}} \leftarrow \left(\iiint (\mathbf{MTF_n} \cdot \boldsymbol{\omega})^2\right)^2 / \iiint \left(\mathbf{NPS_n} \cdot (\mathbf{MTF_n} \cdot \boldsymbol{\omega})^2\right)$ // calculate NPW MO

        $\mathbf{d'^2_{in}} \leftarrow \mathbf{d'^2_{in}} \cdot \boldsymbol{\Gamma_{in}}$ // apply geometrical weights for iteration and projection

    end

    add projection n_0 with heighest value in $\mathbf{d'^2_i}$ to solution

    for all n projections **do**

        assure $\mathbf{d'^2_{jn_0}} \leftarrow 0 \forall j > i$ // remove projection from evaluation set

        calculate $\boldsymbol{\Gamma_{jn}} \forall j > i$ // update geometrical weights for next iterations

    end

    $i \leftarrow i + 1$

end

C.3 Pseudocode for Generation of Low Discrepancy Spherical Reference Trajectories

Algorithm 3: Calculation of the low-discrepancy spherical trajectory (LDS) with correction term for pole clustering compensation. This code was previously published as part of a separate work [136].

Input: List of feasible poses defined by (ϕ, θ) pairs, number of desired samples in trajectory, offset parameter ω
Result: LDS trajectory defined by (ϕ, θ) pairs
load list of possible (ϕ, θ) pairs
calculate $\phi_{\min}, \phi_{\max}, \Delta\phi, \theta_{\min}, \theta_{\max}, \Delta\theta$
for all ϕ, θ **do**
    $\phi_k \leftarrow \phi_k - \phi_{\min}; \theta_k \leftarrow \theta_k - \theta_{\min}$ // shift
    $\phi_k \leftarrow \lfloor \phi_k / \Delta\phi \rfloor; \theta_k \leftarrow \lfloor \theta_k / \Delta\theta \rfloor$ // scale
end
$i \leftarrow \theta_{\min}$
for $i < \theta_{\max}$ **do**
    $\eta_i \leftarrow 0$ // create empty bin vector η_i
    $\xi_i \leftarrow \left\lfloor \frac{1}{\cos(\pi i / 180)} \right\rfloor$ // create bin thresholds ξ_i
    $i \leftarrow i + \Delta\theta$
end
$j \leftarrow 0$
while j < desired number of samples **do**
    $(\phi_{\text{test}}, \theta_{\text{test}}) \leftarrow (j + \omega)$-th Halton-sample   // offset ω controls start position
    $(\phi_{\text{test}}, \theta_{\text{test}}) \leftarrow (\phi_{\text{test}}, \theta_{\text{test}}) \cdot (\phi_{\max}, \theta_{\max})$ // scale to fit range of positions
    $\eta_{\phi_{\text{test}}} \leftarrow \text{modulo}(\eta_{\phi_{\text{test}}} + 1; \xi_i)$ // fill bin
    if $\eta_{\phi_{\text{test}}} = 0$ **then**
       if $(\phi_{\text{test}}, \theta_{\text{test}})$ is not already in solution set **then**
          add combination $(\phi_{\text{test}}, \theta_{\text{test}})$ to solution set
       end
    end
    $j \leftarrow j + 1$
end
for all ϕ, θ in solution set **do**
    $\phi_l \leftarrow \phi_l \cdot \Delta\phi; \theta_l \leftarrow \theta_l \cdot \Delta\theta$ // scale back
    $\phi_l \leftarrow \phi_l + \phi_{\min}; \theta_l \leftarrow \theta_l + \theta_{\min}$ // shift back
end

C.4 Pseudocode for the Optimizability Metric

Algorithm 4: Calculation of the unnormalized optimizability metric, which can be normalized using eq. 10.3. The metric yields a value that indicates how much optimization potential the respective feature has by quantifying the sparsity of the Fourier-transformed feature.

Input: 3D Volume of the Feature to be Optimized in Object Space $\Delta \mathbf{s}$
Result: Unnormalized Optimizability Metric $\Xi(\boldsymbol{\omega})$
load volume $\Delta \mathbf{s}$ of size $(k_{max}, l_{max}, m_{max})$
$\Delta\phi \leftarrow 1; \Delta\theta \leftarrow 1$ // define angular step size, e.g., 1°
$\boldsymbol{\omega} \leftarrow \mathcal{F}(\Delta \mathbf{s})$ // calculate FFT of $\Delta \mathbf{s}$
$\boldsymbol{\Phi} \leftarrow \mathbf{0}; \boldsymbol{\Theta} \leftarrow \mathbf{0}$
foreach $(0,0,0) \leq (k,l,m) < (k_{max}, l_{max}, m_{max})$ **do**
    $\boldsymbol{\Phi}_{\mathbf{abc}} \leftarrow \phi(k,l,m)$ // calculate spherical coordinate angle for Φ
    $\boldsymbol{\Theta}_{\mathbf{abc}} \leftarrow \theta(k,l,m)$ // calculate spherical coordinate angle for Θ
end
$\mathbf{S}^{\phi} \leftarrow [0, \Delta\phi, 2 \cdot \Delta\phi, \ldots, 360 - \Delta\phi]$ // define histogram step vector $\mathbf{S}^{\phi}$
$\mathbf{S}^{\theta} \leftarrow [-90, -90 + \Delta\theta, -90 + 2 \cdot \Delta\theta, \ldots, 90 - \Delta\theta]$ // define histogram step vector $\mathbf{S}^{\theta}$
$\mathbf{H} \leftarrow \mathbf{0}$
$i \leftarrow 0$ // loop over all possible directions
for $i < (360/\Delta\phi)$ **do**
    $j \leftarrow 0$
    for $j < (180/\Delta\theta)$ **do**
        $\xi \leftarrow 0$
        foreach $(0,0,0) \leq (k,l,m) < (k_{max}, l_{max}, m_{max})$ **do**
            if $\left(\mathbf{S}_{\mathbf{i}}^{\phi} \leq \boldsymbol{\Phi}_{\mathbf{klm}} < \mathbf{S}_{\mathbf{i+1}}^{\phi}\right)$ && $\left(\mathbf{S}_{\mathbf{j}}^{\theta} \leq \boldsymbol{\Theta}_{\mathbf{klm}} < \mathbf{S}_{\mathbf{j+1}}^{\theta}\right)$ **then**
                $\xi \leftarrow \xi + \boldsymbol{\omega}_{\mathbf{klm}}$ // sum all Fourier coefficients on a line
            end
            $\mathbf{H}_{\mathbf{ij}} \leftarrow \xi$ // save all summed coefficients in the histogram matrix $\mathbf{H}$
        end
        $j \leftarrow j + 1$
    end
    $i \leftarrow i + 1$
end
$\mathbf{H}_{\mathbf{n}}' \leftarrow \mathbf{H}_{\mathbf{ij}}$ // reshape into line vector with n_{max} elements
sort $\mathbf{H}'$ ascendingly
$v \leftarrow \ell_1(\mathbf{H}_{\mathbf{n}}')$ // v is the sum over all n_{max} elements of $\mathbf{H}'$
$\eta \leftarrow 0; k \leftarrow 0$ // calculate Gini coefficient of $\mathbf{H}'$
for $k < n_{max}$ **do**
    $\eta \leftarrow \eta + (\mathbf{H}_{\mathbf{k}}'/v) \cdot (n_{max} - k + 0.5) \cdot (1/n_{max})$
    $k \leftarrow k + 1$
end
$\Xi \leftarrow 1 - 2\eta$

D | Supplementary Image Quality Plots

D.1 Bat Phantom – Uniform Template With and Without Weighting Function for the Non-Prewhitening Model Observer
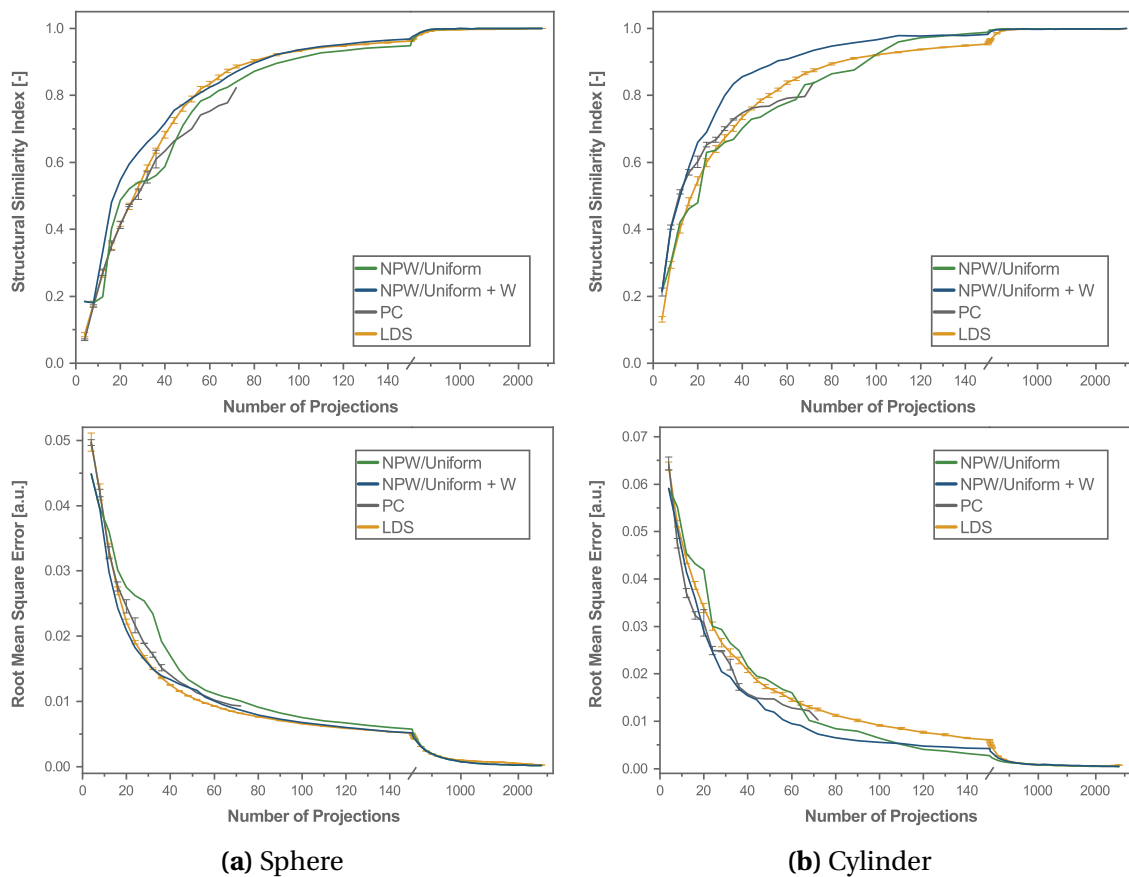

(a) Sphere

(b) Cylinder

Figure D.1: Comparison of weighted and unweighted uniform NPW model observer.

D.2 Bat Phantom – Additional Results for the Prewhitening Model Observer
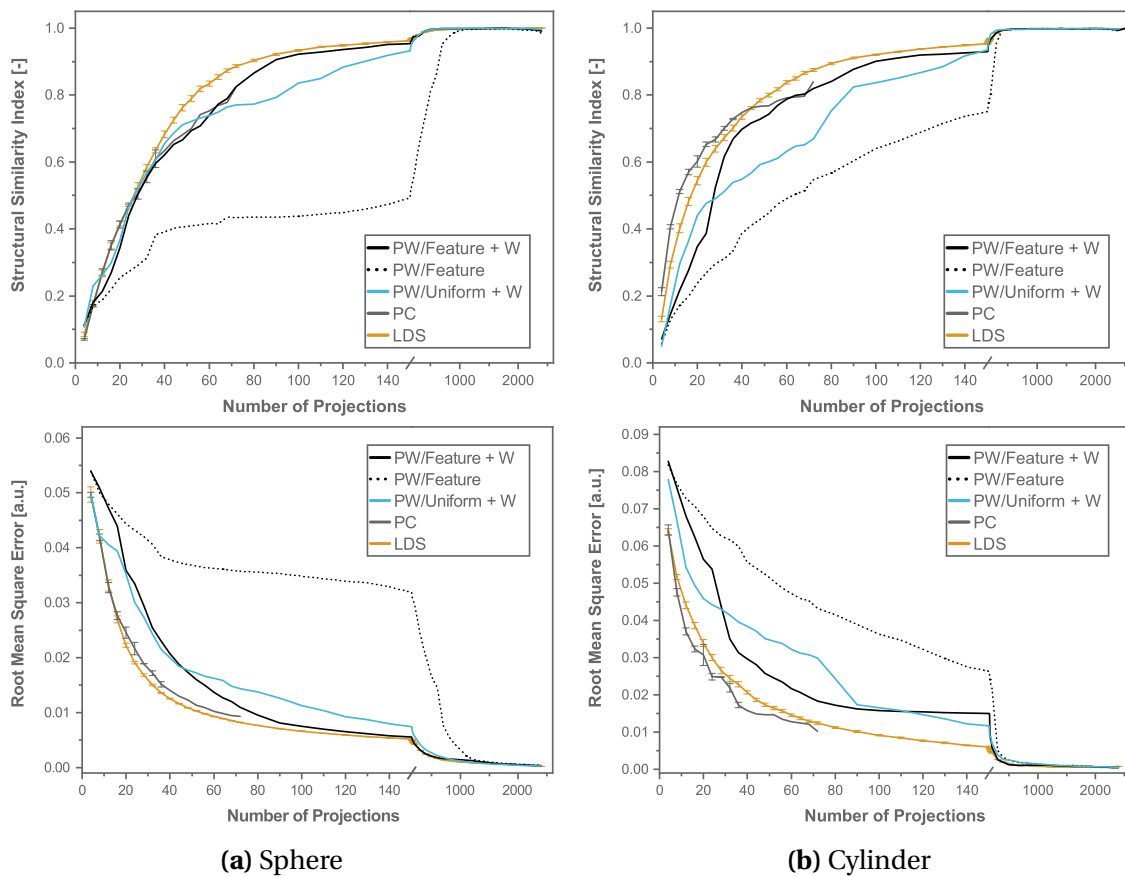

(a) Sphere

(b) Cylinder

Figure D.2: Results for the prewhitening model observer with additional parameter combinations.

D.3 Bat Phantom – NPW Model Observer With and Without Geometric Weighting Function

(a) Sphere

(b) Cylinder
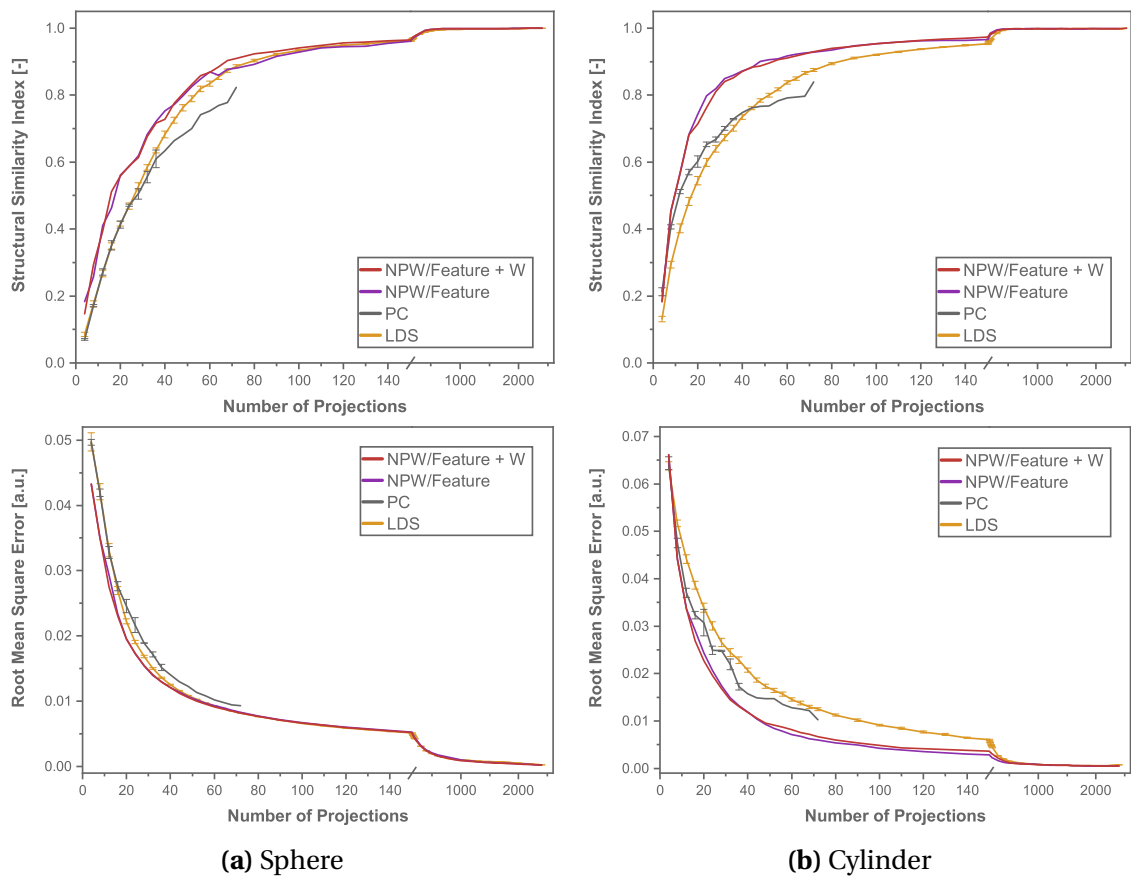
Figure D.3: Comparison of NPW MOs with and without geometric weighting.

D.4 Bat Phantom – Experimental Structural Similarity Plot

(a) Sphere

(b) Cylinder
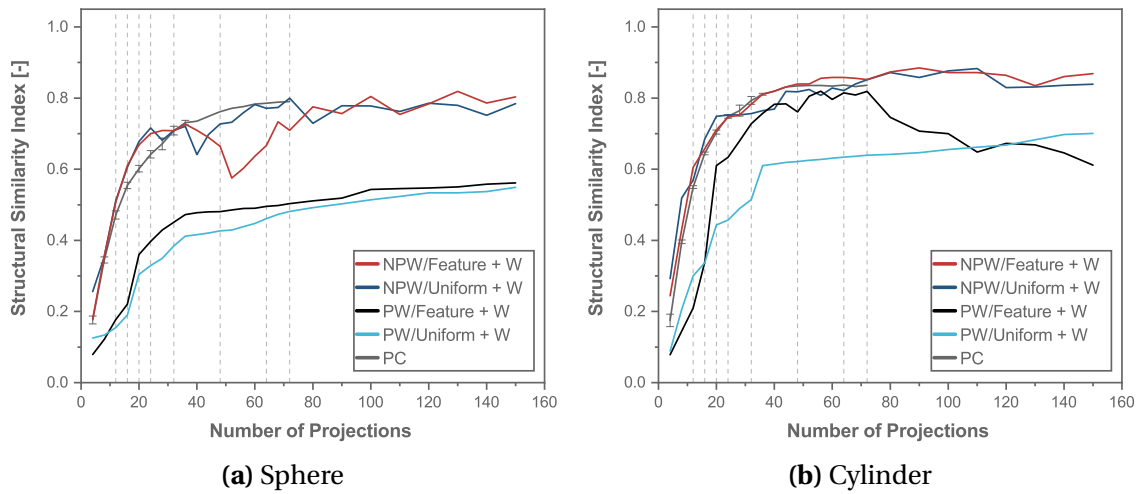
Figure D.4: Structural similarity values for the experimental measurements shown in fig. 8.3. The values are unreliable due to the high noise level as outlined in sec. 8. Slices of the reconstructions using the indicated projection numbers are provided in sec. E.1.

D.5 RoboCT – Experimental Structural Similarity Plot
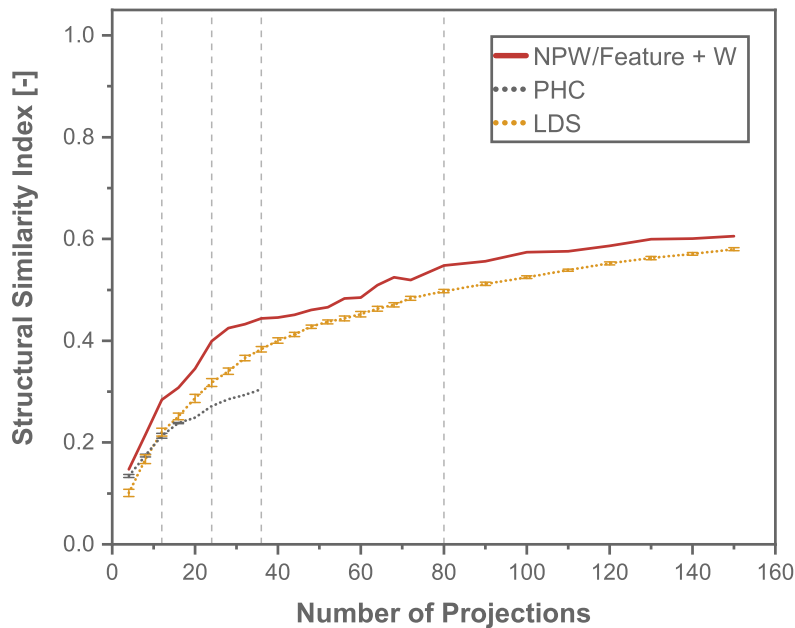
Figure D.5: SSIM plot for the RoboCT application that has turned out to be less reliable than the evaluation via RMSE, which is provided in fig. 9.3

E | Reconstruction Images

E.1 Bat Phantom – Experimental
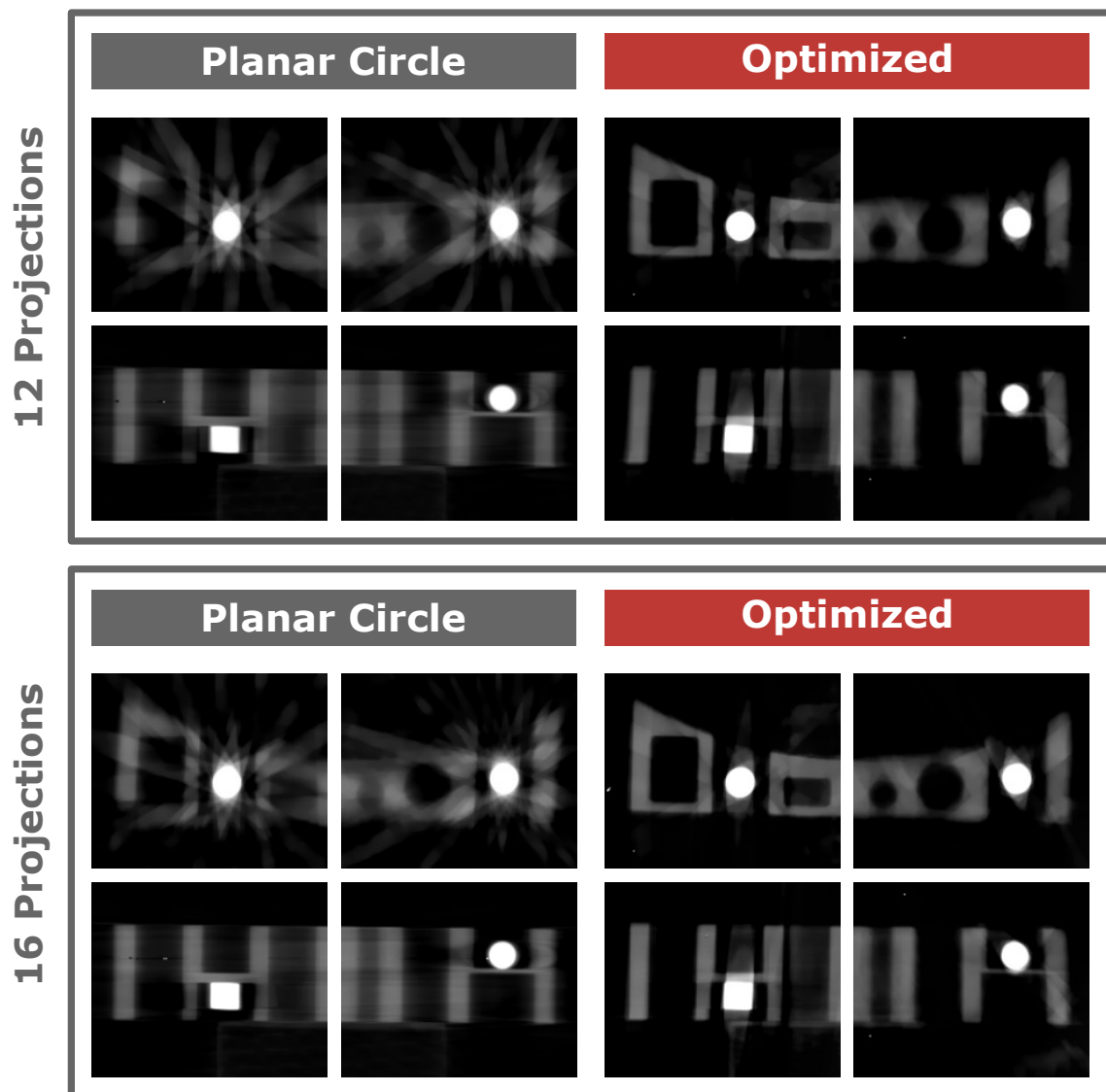
Figure E.1: Reconstructions of the bat phantom with equidistant and optimized trajectories using experimental data and 12 or 16 projections. For the optimization a weighted feature-based NPW model observer was used.
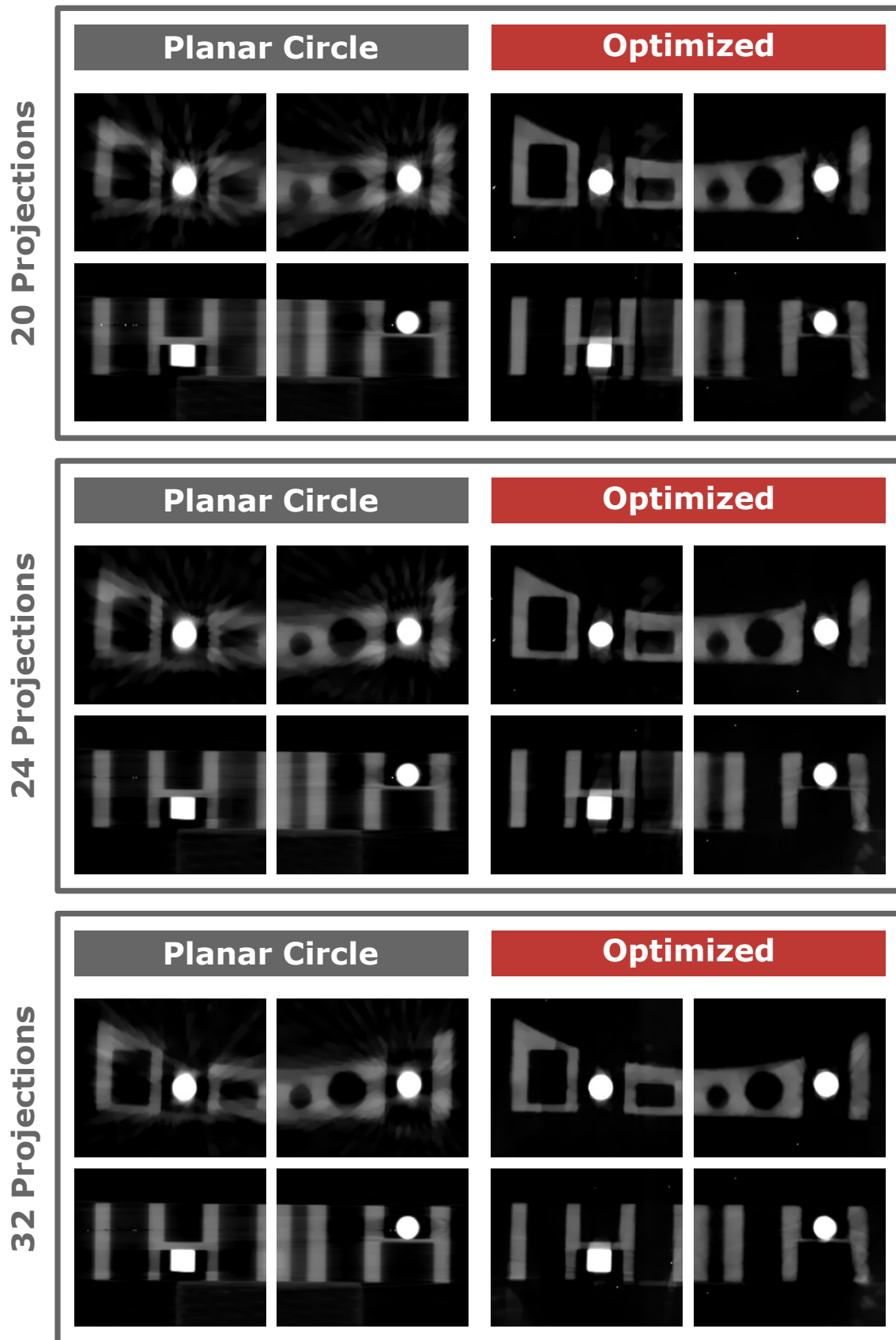
Figure E.2: Reconstructions of the bat phantom with equidistant and optimized trajectories using experimental data and 20, 24 or 32 projections. For the optimization a weighted feature-based NPW model observer was used.
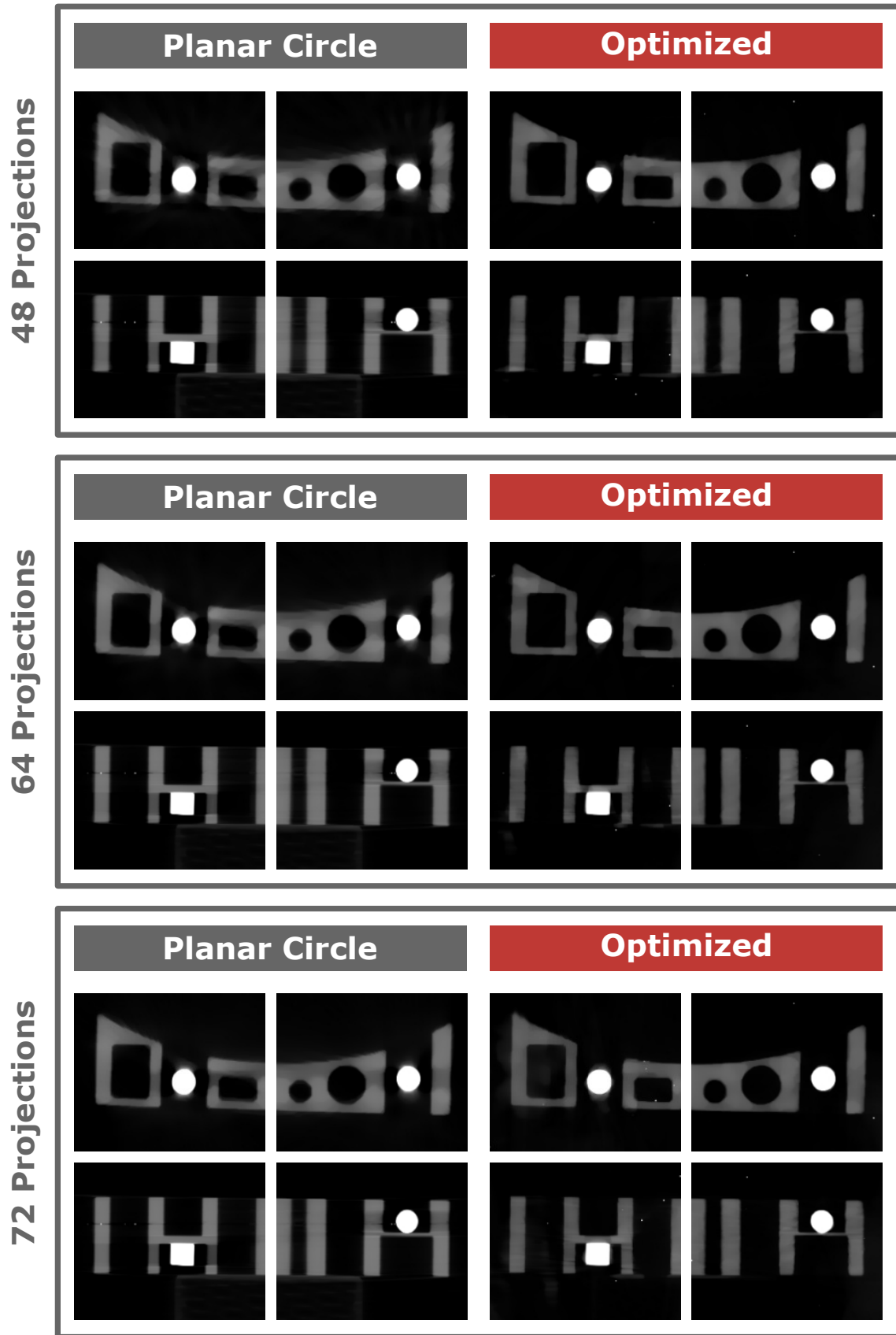
Figure E.3: Reconstructions of the bat phantom with equidistant and optimized trajectories using experimental data and 48, 64 or 72 projections. For the optimization a weighted feature-based NPW model observer was used.

E.2 RoboCT

12 Projections
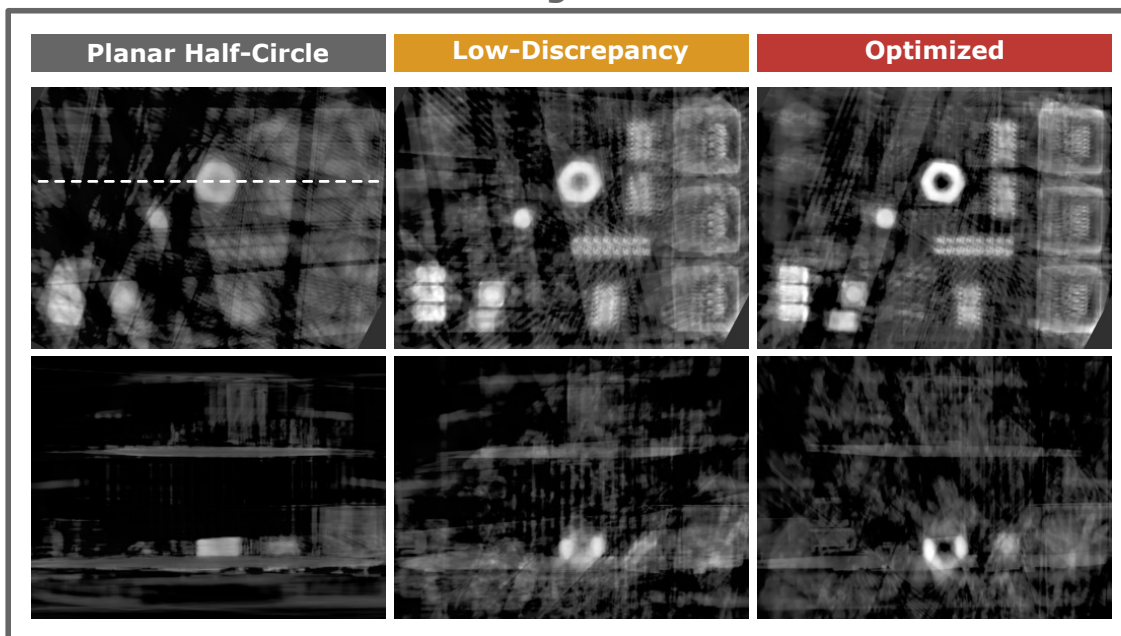
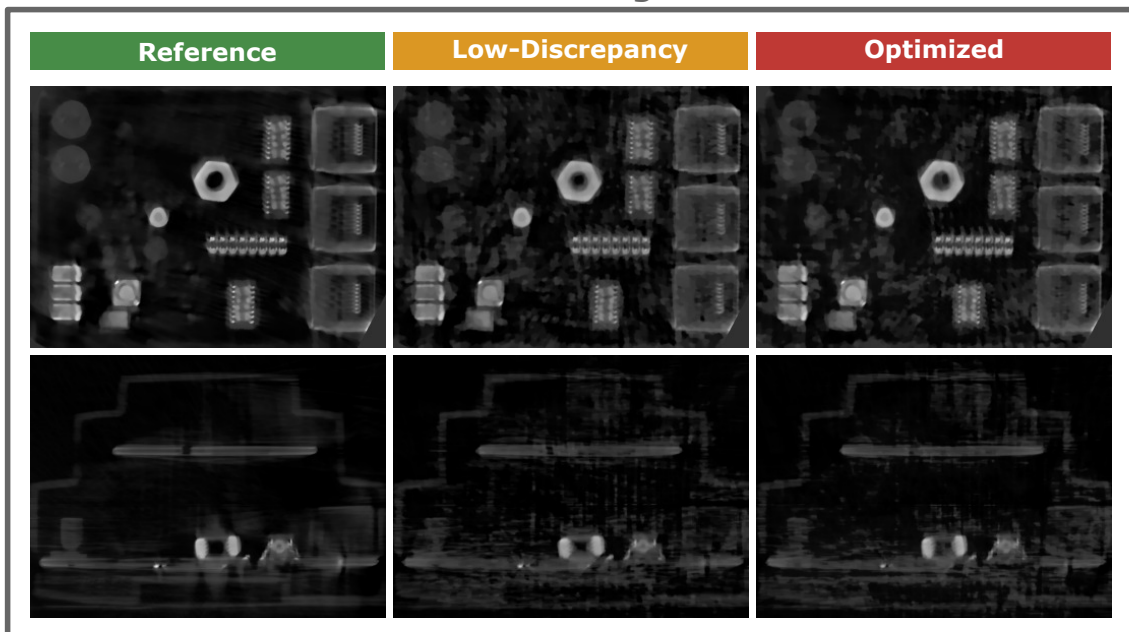**Figure E.4:** Reconstruction images of the RoboCT dataset for 12 projections. For the optimization a weighted feature-based NPW model observer was used. The plane of the intersection images in the lower row is exemplarily indicated in the first image.

24 Projections
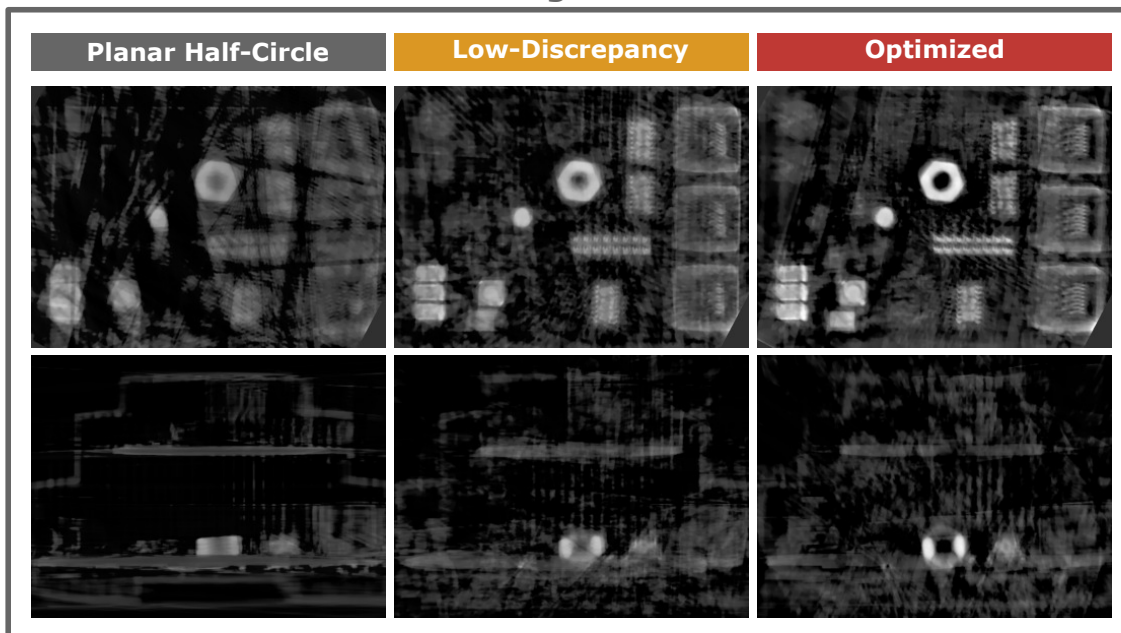
Figure E.5: Reconstruction images of the RoboCT dataset for 24 projections. For the optimization a weighted feature-based NPW model observer was used.

36 Projections
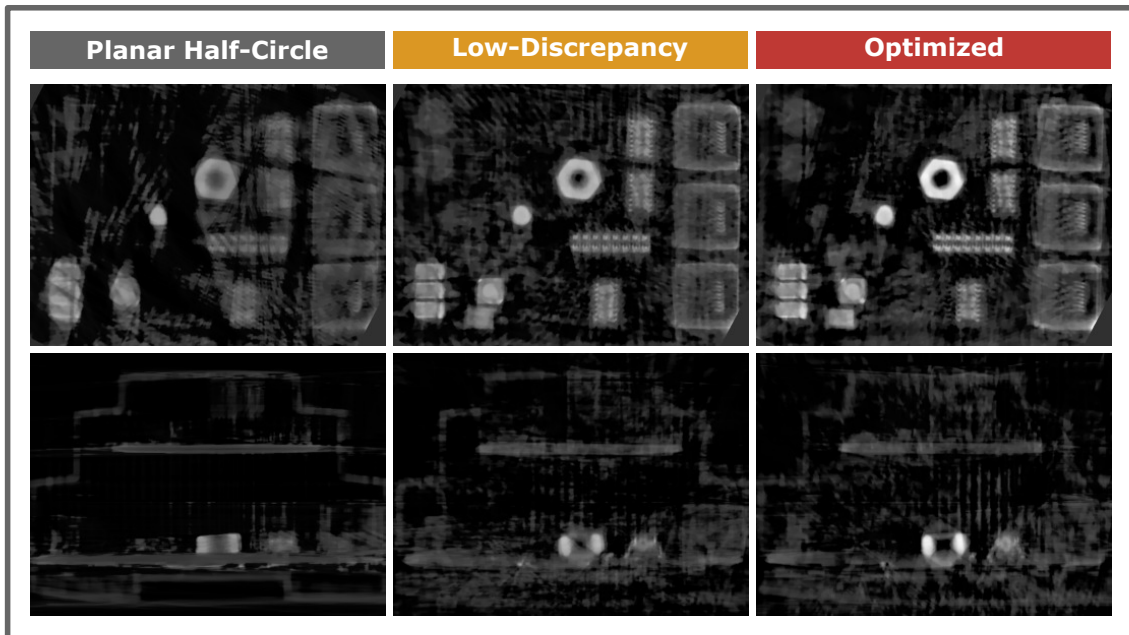
Figure E.6: Reconstruction images of the RoboCT dataset for 36 projections. For the optimization a weighted feature-based NPW model observer was used.

1092/80 Projections

Figure E.7: Reconstruction images of the RoboCT dataset for 80 projections and the reference reconstruction using all 1,092 projections. For the optimization a weighted feature-based NPW model observer was used.

F | ASFC Plots for the Platonic Solids
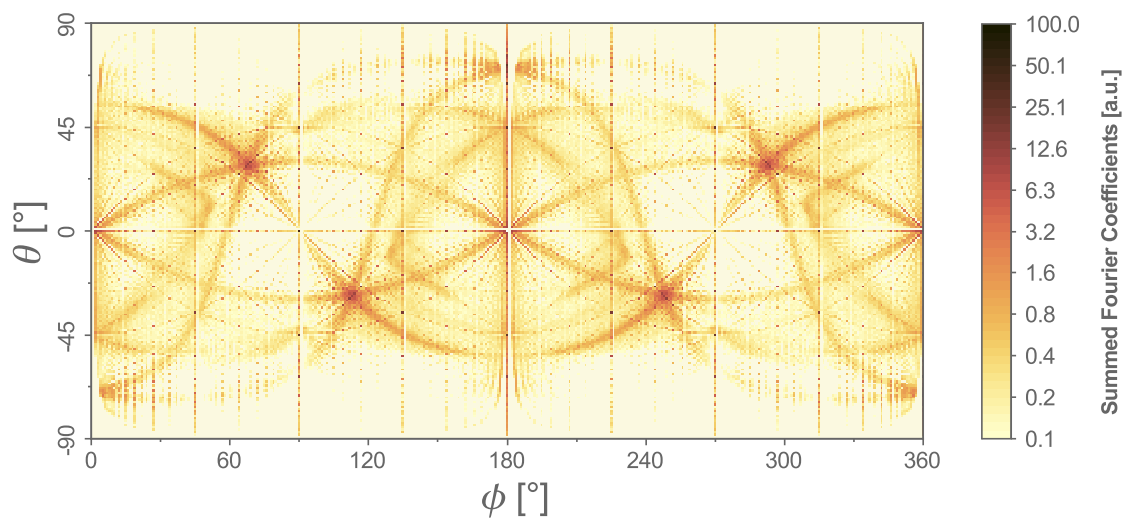
Figure F.1: Plot of summed Fourier coefficients for the tetrahedron (4 faces, $\bar{\bar{\Xi}} = 0.45$).
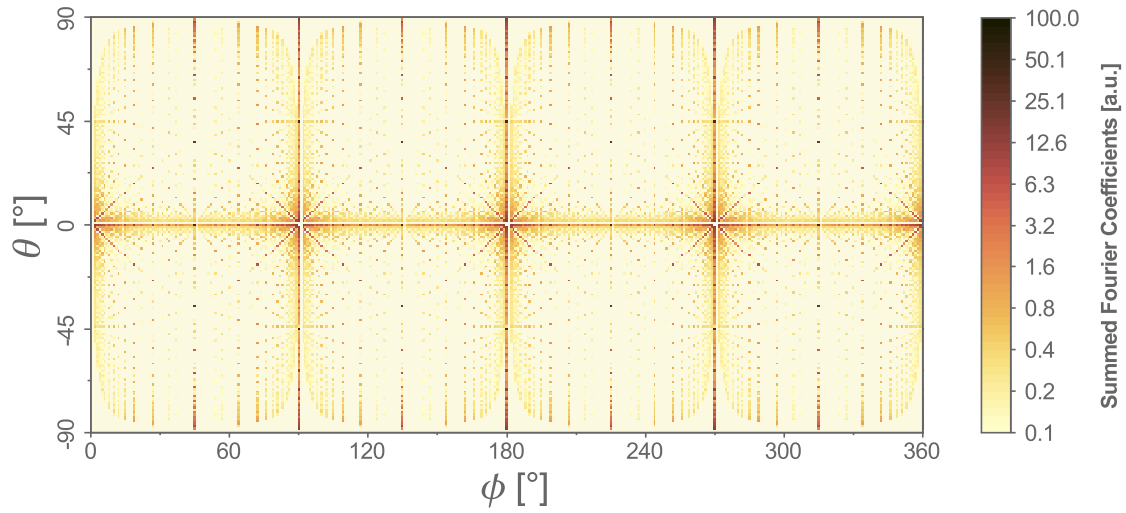
Figure F.2: Plot of summed Fourier coefficients for the cube (6 faces, $\bar{\bar{\Xi}} = 0.75$).
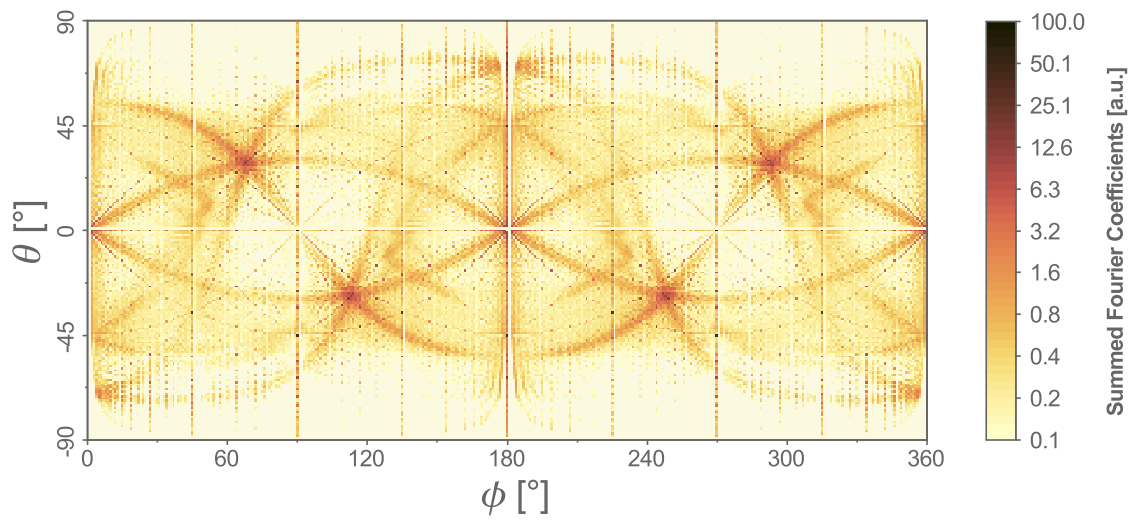

Figure F.3: Plot of summed Fourier coefficients for the octahedron (8 faces, $\bar{\bar{\Xi}} = 0.44$).
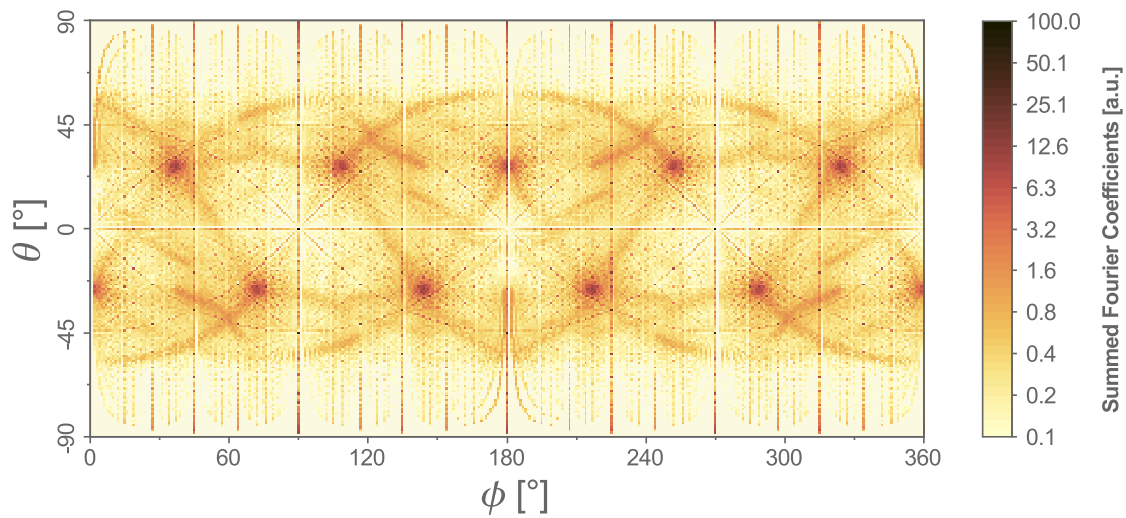

Figure F.4: Plot of summed Fourier coefficients for the dodecahedron (12 faces, $\bar{\bar{\Xi}} = 0.39$).
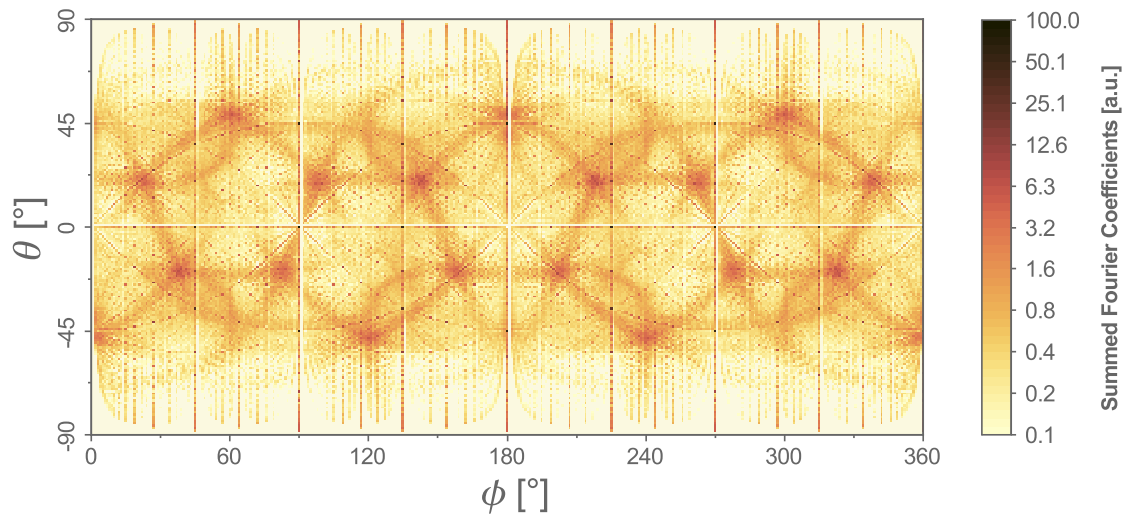
194

Figure F.5: Plot of summed Fourier coefficients for the icosahedron (20 faces, $\bar{\bar{\Xi}} = 0.35$).
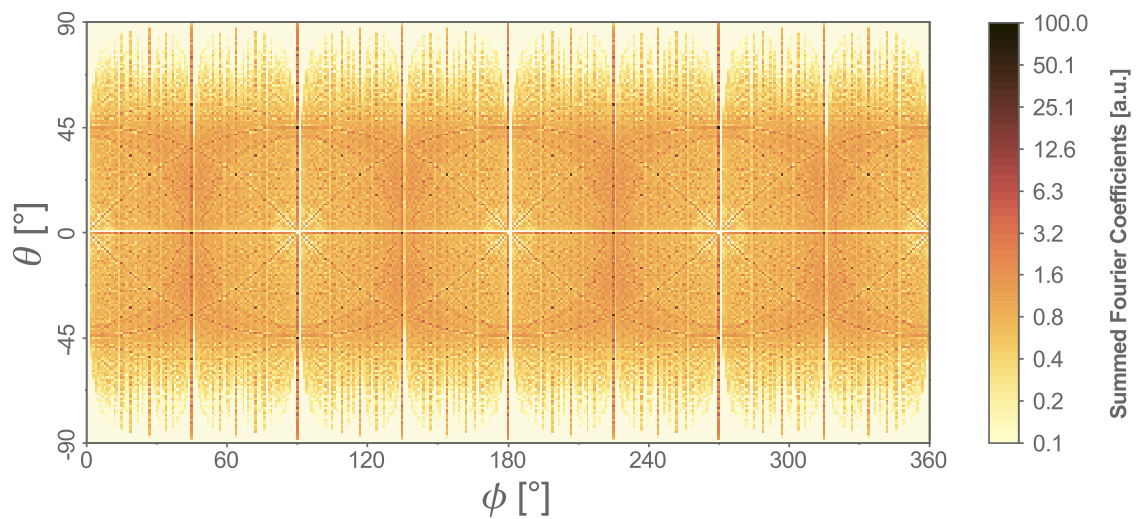

Figure F.6: Plot of summed Fourier coefficients for the sphere (infinite number of faces, $\bar{\bar{\Xi}} = 0.16$).

195